Development of a Josephson Parametric Amplifier for the Preparation and Detection of Nonclassical States of Microwave Fields

by

Manuel Angel Castellanos Beltran

B.S., Tecnológico de Monterrey, 2002

A thesis submitted to the

Faculty of the Graduate School of the

University of Colorado in partial fulfillment

of the requirements for the degree of

Doctor of Philosophy

Department of Physics

2010

This thesis entitled:
Development of a Josephson Parametric Amplifier for the Preparation and Detection of Nonclassical States of Microwave Fields
written by Manuel Angel Castellanos Beltran
has been approved for the Department of Physics

_____

Prof. Konrad W. Lehnert

_____

Prof. James K. Thompson

Date _____

The final copy of this thesis has been examined by the signatories, and we find that both the content and the form meet acceptable presentation standards of scholarly work in the above mentioned discipline.

Castellanos Beltran, Manuel Angel (Ph.D., Physics)

Development of a Josephson Parametric Amplifier for the Preparation and Detection of Nonclassical States of Microwave Fields

Thesis directed by Prof. Konrad W. Lehnert

Recent innovations in the technology of superconducting circuits have made it possible to create nonclassical states of microwave light fields. These states are usually associated with the subject of quantum optics. The ability to manipulate quantum states of microwave light fields holds out the promise of building dense integrable circuits to process quantum information electrically. However, a major difficulty lies in the fact that there is no general purpose method of efficiently measuring the quantum state of a microwave field. In this thesis, I describe the development of an amplifier, based on a Josephson parametric amplifier. This new parametric amplifier enables this kind of efficient measurement. Although parametric amplifiers are narrowband (only amplifying signals in a narrow frequency range around a central frequency), I have developed an amplifier whose central frequency is widely tunable (a full octave, 4–8 GHz), greatly improving its usefulness. I have studied the gain, bandwidth, dynamic range, and added noise of the amplifier. I have shown that when operated in a particular manner, known as degenerate mode, the parametric amplifier adds less noise than the noise associated with the quantum fluctuations of the electromagnetic vacuum. In addition, its gain is large enough to ensure that the amplified vacuum noise overwhelms the noise added by conventional amplifiers that follow the parametric amplifier. Together, these two features make it possible to measure either the phase or amplitude of a microwave signal where the dominant uncertainty comes from the quantum noise of the signal itself. In addition, a degenerate parametric amplifier also prepares particular nonclassical states called squeezed states. Our parametric amplifier prepares squeezed states, which have

(in one of its quadratures) noise with a variance less than one tenth that of the vacuum noise. I have employed the parametric amplifier in two experiments that require its ability to make efficient measurements. First, I used the parametric amplifier to determine the full density matrix of a squeezed state generated by a second parametric amplifier. Second, I used the amplifier to enable a measurement of position with precision better than the value at the standard quantum limit. These demonstrations are powerful evidence that we have indeed realized a general-purpose quantum-efficient method of measuring microwave fields.

Dedication

Para mi esposa Kassi y mis papás que siempre me apoyaron en todas mis empresas

Acknowledgements

In these last seven years, I have had the opportunity of meeting and working with great people. First I would like to thank my advisor Konrad Lehnert who taught me all I know about low-temperature and microwave measurements, and some more I already forgot. His passion and dedication to science always surprised and encouraged me. Also, I would like to thank Dan Dessau and Jim Shepard for encouraging me to come to Boulder for grad school. I also had the pleasure of working with a few great post-docs such as Dan Schmidt, Cindy Regal, John Teufel, François Mallet and Tobias Donner. I want to specially thank John Teufel for all his help; it didn't matter what he was doing, any time I had a question he would take the time to answer it (as long as I asked him in the right way: "John, you are an expert in INSERT ANYTHING HERE, ..."). It was also a pleasure to work with the other graduate students in the lab, Nathan Flowers-Jacobs Jennifer Harlow and Hsiang-Sheng Ku, although some times we fought for cables and equipment we had to share. I also would like to thank Hsiang-Sheng Ku for checking some of the early chapters of this thesis. Our collaborators from NIST, Kent Irwin, Gene Hilton and Leila Vale, made and helped us design the second generation of devices. I also had helpful conversations with (and borrowed multiple microwave components from) Joe Aumentado and Lafe Spietz, from NIST as well. To all this people (and others I am forgetting) thank you for your help.

Finally, these past years would not have been the same without the support of all my friends and family. I first want to thank my wife Kassi whose support helped

me through all the most difficult parts of my graduate career. Thank you for all your patience and understanding especially the times I was running the experiments, when I would spend (a lot) more time with Konrad than with you. I also want to thank my best friend Luis Miaja Ávila with whom I came to Boulder, first as an undergrad exchange student, and then as a graduate student. I want to thank my parents and siblings for all their help and support. It was great to have my brother Nacho live in Boulder with me in the last couple of years. To all my family and friends, thank you as I would not be where I am, or who I am, without you.

Contents

Chapter

Figures

Figure

Chapter 1

Introduction

The theory of quantum mechanics emerged to explain primarily macroscopic degrees of freedom, such as atoms and molecules. In the past thirty years there have been increasingly successful attempts to build macroscopic electrical circuits that nonetheless behave quantum mechanically. Recently, this trend has only accelerated with the emergence of the field of quantum information. This field seeks to exceed classical bounds on communication, cryptography, and other information processing tasks.

In contrast to microscopic degrees of freedom, these quantum electrical circuits are excited by much smaller energies. The transition frequencies between the eigenstates lie in the microwave rather than optical part of the electromagnetic spectrum. Because the energy of a microwave photon is so small, detecting fields at the level of single photons is one of the major problems that need to be solved to store and process quantum information with electrical circuits. In this thesis I address this measurement problem. I developed a method of measuring microwave fields where the quantum fluctuations in the microwave field are the dominant source of noise: in this sense, a measurement operating at the single photon level. The key element in our measurement scheme is an amplifier called the Josephson parametric amplifier (JPA), which is capable of amplifying a signal, in principle, without adding any noise.

At the microwave frequencies we will discuss in this thesis (4–8 GHz), there is not a quantum-limited photodetector such as in optics as the energy per photon

of a microwave signal is too small to be individually detected in the same way as an optical photon. Therefore, the detection of weak microwave signals needs to be preceded by amplification. The process of amplification usually consists of the task of weakly coupling many microscopic degrees of freedom (for example, the electrons of a transistor) to an input signal, and channeling energy from those microscopic degrees to the input signal. However, amplification is usually accompanied by the unfortunate addition of noise to the signal (Fig. 1.1a). Most of the time, this added noise will come from the lack of control of each individual microscopic degree of freedom. However, even in the case when the control is ideal, quantum mechanics may impose limits on the minimum added noise of an amplifier depending on the kind of amplification that is performed.

In this thesis, I will be only interested in linear amplifiers. Linear amplifiers are those whose output is linearly related to its input signal. I will be mostly interested in phase-sensitive amplifiers, whose response depends on the phase of the input signal and which can circumvent the quantum limit on the noise added by phase insensitive amplifiers. One simple way to understand the concept of a phase sensitive amplifier is to first define the quadratures of a signal. In general, we can decompose a voltage signal with frequency components close to a frequency ω_o as

$$V_s(t) = 2V_0 \left[X_1(t)\cos(\omega_o t) + X_2(t)\sin(\omega_o t)\right] \tag{1.1}$$

where X_1 and X_2 are the quadratures of the signal. A phase sensitive amplifier amplifies the quadrature components of the signal by different amounts. I will discuss only a specific type of phase-sensitive amplifier, one that will only amplify one of the quadratures and de-amplify the other one.

The quantum noise associated with amplification has been discussed extensively by several authors [1–3]. The quantum fluctuations limit the ultimate performance of any amplifier and hence these fluctuations play an important role in high-precision

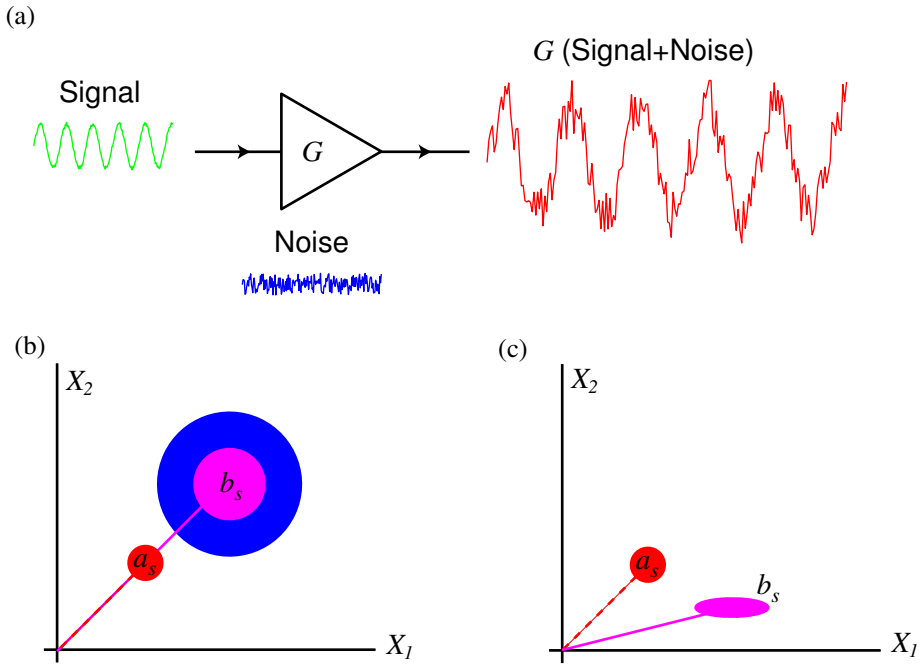

Figure 1.1: (a) In general, the amplification process will degrade the signal to noise ratio by adding certain amount of noise to the signal before amplifying it. (b) Quantum mechanics places a restriction on the minimum amount of this added noise when the amplifier amplifies both quadratures of the signal. When an amplifier achieves this limit, it is said to be quantum limited. (c) On other hand, if the amplifier is a phase-sensitive amplifier, and only amplifies one of the quadratures, then it can do that ideally without adding any noise.

measurements. The exact manifestation of this quantum limit depends on the actual amplification process. Quantum mechanics does not impose any restriction on the ultimate precision of a single measured quantity (for example, position or momentum of a particle), but only in the combined precision of two conjugate variables [4]. The typical case that interests us is a sinusoidal signal with the information encoded in the amplitude or phase. If we care about the information contained in both quadratures, Eq. (1.1), then we would need to use a linear phase-insensitive amplifier (Fig. 1.1b), and the minimum amount of noise (in energy units) that an amplifier must add to a signal at frequency ω_s is

$$E_N = \frac{\hbar\omega_s}{2}$$

where E_N is the noise that the amplifier adds to the signal before being amplified (Fig. 1.1a). This is often called the standard quantum limit of amplifiers and applies only to phase-insensitive amplifiers. However, if one is only interested in the information contained in one of the quadratures, the situation is very different (Fig. 1.1c). In this case, there is no restriction on the added noise of the amplifier. Essentially, as long as the information in one of the components of the signal is lost, the information contained in the other quadrature can be amplified with no degradation of the signal to noise ratio. In the ideal case, these amplifiers can be built from a system with a single well-controlled degree of freedom (the resonant-mode of a microwave circuit). Another interesting consequence of the behavior of phase sensitive amplifiers is that while one of the quadratures is noiselessly amplified, the other one can be squeezed. That is, the fluctuations at the output of the amplifier would be smaller than those fluctuations at the input, even if at the input there were only vacuum fluctuations. Such squeezed states are nonclassical states of light.

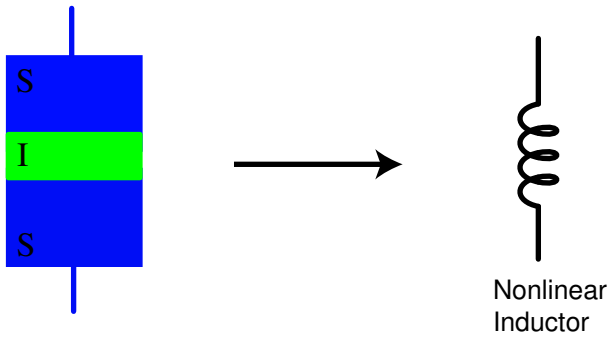

Figure 1.2: A Josephson tunnel junction consists of two superconductors separated by a small insulating barrier. For the most part, we will treat the Josephson junction as a nonlinear inductor.

In this thesis, I will describe how we built a microwave amplifier with the best reported noise-performance ever achieved. Its noise performance is so good and it can be operated at high enough gains that it is now possible to measure microwave signal where the dominant noise source is the quantum fluctuations of that microwave signal

itself. In addition, we have shown that it is a practical, useable amplifier which can be integrated with other low temperature microwave experiments.

The way we approached this problem of fabricating an ultra-low noise microwave amplifier was by creating a parametric amplifier using Josephson junctions (Fig. 1.2). Josephson junctions play a key role in the fabrication of low-noise microwave amplifiers, being the only nonlinear dissipationless element usable at microwave frequencies. The name parametric amplifier is associated with a class of amplifying and frequency-converting devices that use the properties of nonlinear or time-varying reactances. If a reactive parameter oscillates at twice the resonance frequency, energy can be pumped into (or out of) the input mode, realizing an amplifier. In practice, this time dependence is often generated through a nonlinear reactance, either inductance or capacitance. If the nonlinear reactance is proportional to the intensity rather than the amplitude of the mode, then an intense pump tone applied at the resonance frequency ω automatically creates the necessary 2ω parametric oscillation. In analogy with optics, we describe this effect as a Kerr nonlinearity. The nonlinear current-dependent inductance of a Josephson junction provides such a Kerr nonlinearity. By detecting only one quadrature of a signal, degenerate parametric amplifiers can add even less noise than the minimum required by quantum mechanics when detecting both quadratures. [5].

We are not the first group to study these kind of amplifiers. Josephson parametric amplifiers have already been operated with near quantum-limited sensitivity [6] and have been used to squeeze both thermal and vacuum noise [6–8]. However, in spite of these promising results they were not widely adopted since they suffer from two main disadvantages: a small dynamic range and narrow band gain. Furthermore, compelling applications that would benefit from a lower-noise microwave amplifier have only recently been developed: with the advent of quantum information processing using superconducting circuits [9, 10], or microwave-cavity optomechanics [11], there is now a need for practical amplifiers that operate at the limits imposed by quantum mechanics.

Also in contrast with the previous work where the JPA was only tested but never used to measure something else, we operated our JPA in two low-temperature experiments that require its unprecedented sensitivity. First, I efficiently reconstruct the quantum state of a nonclassical microwave signal. Second, I collaborate with other members of my lab to measure the position of an object with precision better than the quantum zero-point motion of that object.

While the devices that I create and study are practical amplifiers, we have also tested their performance in creating nonclassical states of the microwave field: squeezed states. In fact, the nonclassical microwave fields whose quantum state I reconstructed using my amplifier were themselves created by another JPA. These nonclassical states are useful resources for quantum information processing. The continuation of the work that I started during my Ph.D. will use the nonclassical state to process quantum information.

Thesis overview

In the succeeding chapters I will explore the operating principles of these devices, present a few design criteria for their construction and discuss two particular areas of application. This thesis is organized as follows. In chapter 2, I will describe the theoretical aspects related to the quantum description of microwave circuits, including quantum network theory and input-output theory. I will also discuss the origin of the limits on amplification as well as the generation of squeezed states using a degenerate parametric amplifier, a type of phase-sensitive amplifier. In chapter 3, I will treat very generally a type on nonlinear oscillators called Duffing oscillators. I will describe, in general terms, what a Josephson junction is and discuss how an electrical resonator with a Josephson junction embedded in it behaves, within some limit, like a Duffing oscillator. I will then describe how the theory discussed in chapter 2 can be used to analyze the behavior of the Josephson resonator as a degenerate parametric amplifier. In chapter 4,

I discuss some of the previous and present work regarding the use of Josephson junctions for parametric amplifiers. In chapter 5, I will describe the design and implementation of the amplifier, including a brief discussion of microwave resonators using distributed circuits. In previous chapters, the analysis of the JPA has been done assuming an ideal behavior, that is without including the possibility of loss in the system. In this chapter I also discuss the effects of loss on the performance of a JPA. In chapter 6, I will describe the experiments done to characterize the samples that we have measured. This includes the linear and nonlinear behavior of the cavities, and the performance of the nonlinear resonators as amplifiers, including gain, bandwidth, noise properties and saturation behavior. I will also describe the measurement of quadrature squeezing, but using a commercial microwave amplifier. Therefore, even though the inferred squeezing is about 10 dB, the real squeezing at the microwave detector at room temperature is only 2%. In chapter 7, I will discuss how we try to increase the sensitivity of our microwave homodyne measurement by using another JPA as a pre-amplifier for the chain of commercial amplifiers used in the experiment. This allows us to detect real (rather than inferred) squeezing of 37% and to perform what is called in the optics community Wigner-function reconstruction. In chapter 8, I will also use a JPA to increase the sensitivity of a microwave interferometer used to detect the motion of a nanowire. By using the JPA, our interferometer is less than a factor of 4 away from being shot-noise limited. Finally, I provide the conclusions of this thesis in chapter 9 as well as some directions for the future of these experiments.

Chapter 2

Quantization of electrical circuits and amplifiers

The theory of parametric amplification is intimately related to the theory of coupled modes of resonant systems. So our study begins with the study of the simplest resonant system: the simple harmonic oscillator (SHO). In our case, our SHO consist of circuits made out of microfabricated structures, such as for example a parallel LC-oscillator as shown in figure 2.1a. Quantum mechanics has been generally associated with the description of microscopic particles such as electrons and atoms. Nevertheless, recently the concept of macroscopic quantum (mesoscopic) systems has been used to describe systems that have an intermediate status between the realms of microscopic particles and classical macroscopic objets [12]. By macroscopic I mean that these systems contain a large number of microscopic particles and have been fabricated according to certain specifications. However, their behavior is described in terms of variables that consist of collective degrees of freedom that behave quantum-mechanically. For typical values and dimensions, the components that make up these systems can have resonances of a few gigahertz and dimensions of 1-100 microns. Because the centimeter-long wavelength of the probing microwave excitation is much larger than the circuits, we are well into the lumped element limit.[1] The state of the circuit in figure 2.1a can be specified by only two collective degrees of freedom: the charge Q in the capacitor and flux Φ

[1] We can also fabricate SHO out of microwave cavities. In that case the dimension of the circuit is too big to be in the lumped element limit. However, we still characterize the behavior in terms of single collective excitations.

in the inductor. In order to probe the quantum mechanical behavior of such a simple circuit, we need to cool it down to milliKelvin temperatures such that $k_B T \ll \hbar\omega_0$. However, this last condition is not enough to guarantee that the collective degrees of freedom Φ and Q need to be treated as a quantum variables; the separation between the different energy levels $\Delta E/\hbar$ must be bigger than their width γ (Fig. 2.1b). This condition means that the quality factor $\mathcal{Q}$ of the LC oscillator needs to satisfy $\mathcal{Q} \gg 1$, a constraint on the damping (and the coupling to the external world) of the oscillator [12].

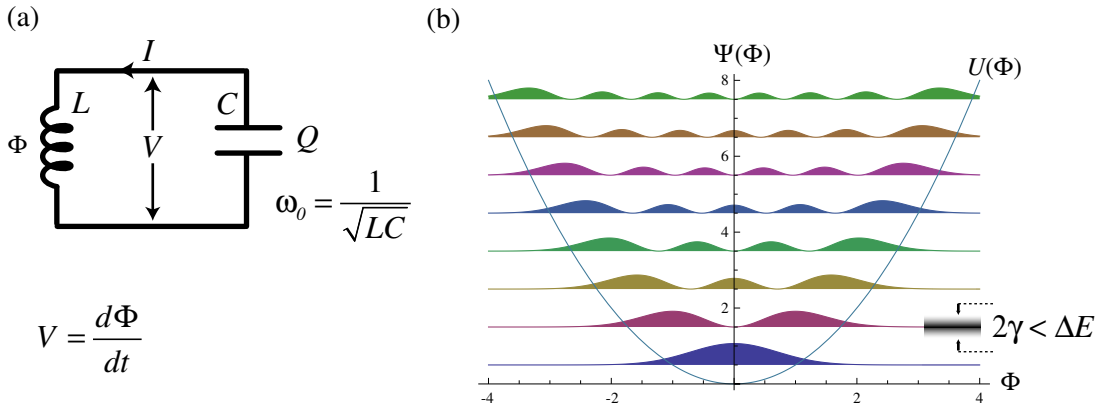

Figure 2.1: (a) Circuit representation of our simple harmonic oscillator. The system coordinates Φ and Q are used to specify the state of the system. (b) One required condition to observe the quantum nature of a system is that the width of the different energy states need to be smaller than their separation $\mathcal{Q} = \frac{\Delta E/\hbar}{2\gamma} \gg 1$.

In this chapter I will develop the classical and quantum description of electrical circuits, including a quantum description of dissipation. I will begin by studying a dissipationless classical and quantum lumped element circuit. Then I will give a description of transmission lines in the classical and quantum mechanical regime. This description will allow me to model dissipation as a semi-infinite transmission line –a model that is compatible with quantum mechanics. I will then discuss a method that describes how to treat quantum-mechanically the coupling of an arbitrary system (in this case, a SHO) to the external world called Input-Output theory (IOT). Finally, in the third part of the chapter, I will discuss the quantum limits for both phase-insensitive and

phase-sensitive amplifiers. These limits emerge from the simple constraint that both the input and output modes must satisfy the appropriate commutation relations. I will finish this part with a small description of the squeezed states generated by a degenerate parametric amplifier, a kind of phase-sensitive amplifier.

2.1 Electrical simple harmonic oscillator

2.1.1 Classical normal mode description of a LC-resonator

We will begin by deriving classical and quantum equations of motion for the simple circuit in figure 2.1. More complex circuits can described as combinations of this simple circuit. The Lagrangian of the circuit shown in figure 2.1a is

$$\begin{aligned} \mathcal{L} &= \frac{1}{2}CV^2 - \frac{1}{2}LI^2, \\ &= \frac{1}{2}C\left(\frac{d\Phi}{dt}\right)^2 - \frac{1}{2}\frac{\Phi^2}{L}, \end{aligned} \tag{2.1}$$

where in the second line the Lagrangian is expressed in terms of the generalized coordinate Φ. In analogy to the mechanical case of a SHO, the electrostatic energy plays the role of the kinetic energy, while the magnetic energy plays the role of the potential energy. From Eq. (2.1), we can derive the canonical conjugate momentum of Φ given by

$$\frac{\partial \mathcal{L}}{\partial \dot{\Phi}} = C\frac{d\Phi}{dt} = Q.$$

Using the canonical conjugate momentum Q, we can obtain the Hamiltonian

$$H = \frac{1}{2}\frac{\Phi^2}{L} + \frac{1}{2}\frac{Q^2}{C} \tag{2.2}$$

and the Hamiltonian form of the equations of motion for this simple oscillator:

$$\begin{aligned} \frac{dQ}{dt} &= -\frac{\partial H}{\partial \Phi} = -\frac{\Phi}{L}, \\ \frac{d\Phi}{dt} &= \frac{\partial H}{\partial Q} = \frac{Q}{C}. \end{aligned} \tag{2.3}$$

Since the signs of the coupling coefficients in Eqs. (2.3) are opposite, it follows that the system will oscillate with energy periodically exchanged between the electric and magnetic fields. Solving the equations of motion (EOM) for the LC-resonator is very simple however one thing to notice is that Eqs. (2.3) are coupled. The simple oscillator can be described by two decoupled first-order differential equations. This is the *normal mode form* of EOM [13]. One way to derive this form is to find the linear combinations of the Hamiltonian equations that will decouple them. First, we define the complex variables a and a^*:

$$a = \frac{1}{2\sqrt{L}}(\Phi + iZ_rQ), \tag{2.4}$$
$$a^* = \frac{1}{2\sqrt{L}}(\Phi - iZ_rQ),$$

where $Z_r = \sqrt{\frac{L}{C}}$. Replacing (2.4) in (2.3) yields

$$(\frac{d}{dt} + i\omega_0)a = 0 \tag{2.5}$$

and its complex conjugate (c.c.). The choice of normalization constants for the normal modes will become apparent shortly.

Eqs. (2.5) and its complex conjugate are the two first-order decoupled differential equations that I was looking for. They are said to be the *normal mode form* and describe the resonator equally as well as Eqs. (2.3). The quantities $a(t)$ and $a^*(t)$ are the normal mode amplitudes and are basically the classical version of the the operators $\hat{a}$ and $\hat{a}^\dagger$ often used to study the quantum mechanical version of the simple harmonic oscillator (SHO). They are linear combinations of the generalized coordinate and momentum (in this case flux of the inductor and charge in the capacitor) and can be pictured as two counterrotating phasors of constant length. The magnitudes of these phasors are normalized so that the sum of their squares gives the total energy stored in the system.

That is,

$$E = \frac{1}{2}\frac{\Phi(t)^2}{L} + \frac{1}{2}\frac{Q(t)^2}{C}, \tag{2.6}$$

$$= |a(t)|^2 + |a^*(t)|^2. \tag{2.7}$$

Furthermore, $|a|^2$ and $|a^*|^2$ represent the energy stored in the a and a^* modes respectively. Since both V and I are real variables, $|a|^2 = |a^*|^2$, and the energy stored in each mode is equal. The solutions of the normal modes are just

$$a(t) = a(0)e^{-i\omega t}, \tag{2.8}$$

$$a^*(t) = a^*(0)e^{i\omega t}, \tag{2.9}$$

where

$$a(0) = \frac{1}{2\sqrt{L}}\left(\Phi(0) + iZ_rQ(0)\right) = \sqrt{\frac{E}{2}}\exp\left[i\arctan\left(\frac{Z_rQ(0)}{\Phi(0)}\right)\right]$$

with E being the total energy.

Although it may seem artificial to call a and a^* different normal modes, this separation of modes offers the advantage of visualizing $\Phi(t) + iZ_rQ(t)$ and its c.c. as two different counterrotating phasors; this will be useful when we analyze parametric processes in coupled resonators. As we will see, modes that rotate in the same sense in non-degenerate parametric amplifiers will couple more effectively than modes that rotate in opposite senses; for degenerate parametric amplifiers, we only have one resonant circuit, and in that case the coupling of modes will be between the a and a^* mode [13]. Therefore dividing modes up in this fashion will aid in understanding and simplifying more involved coupled systems.

2.1.2 Description of the problem in quantum mechanics language

We can quantize the system of figure 2.1a following the usual procedure for canonical quantization [12, 14, 15]; Q and Φ become operators satisfying the commutation

relations:

$$[\hat{\Phi}, \hat{Q}] = i\hbar. \tag{2.10}$$

In analogy to the classical we define the quantum operator for the normal modes in term of the charge and flux operators

$$\hat{a} = \sqrt{\frac{1}{2\hbar Z_r}}(\hat{\Phi} + iZ_r\hat{Q}), \tag{2.11}$$
$$\hat{a}^\dagger = \sqrt{\frac{1}{2\hbar Z_r}}(\hat{\Phi} - iZ_r\hat{Q}).$$

The normalization factor in this case is slightly different than in Eq. (2.4) to be consistent with the usual quantum mechanical definitions for these operators. They satisfy the bosonic commutation relations

$$[\hat{a}, \hat{a}^\dagger] = 1.$$

Replacing this expression in the Hamiltonian for the system (2.2) we obtain the familiar expression for the Hamiltonian of the quantum SHO:

$$H = \frac{\hbar\omega}{2}(\hat{a}\hat{a}^\dagger + \hat{a}^\dagger\hat{a}) = \hbar\omega(a^\dagger a + \frac{1}{2}). \tag{2.12}$$

In order to simplify the notation, I will drop the hat on the operators, unless the distinction between classical c-numbers and quantum mechanical operator is not obvious from the context.

2.2 Transmission line theory

The main difference between circuit theory and transmission line theory is electrical size. For circuit theory, the main assumption is that the physical dimension of the circuit network is much smaller than the wavelength of the electrical signal used to drive the circuit. In a transmission line, the length of the network is large enough that the voltages and currents can vary in magnitude and phase over its length. In the systems we will be studying, there will be a combination of sizes in the building blocks that will

require us to make use of both circuit and transmission line theory. In the first part for this section I will first derive the equations of motion of a classical transmission line and then introduce quantum mechanics following the procedure for canonical quantization.

2.2.1 Classical analysis of transmission lines

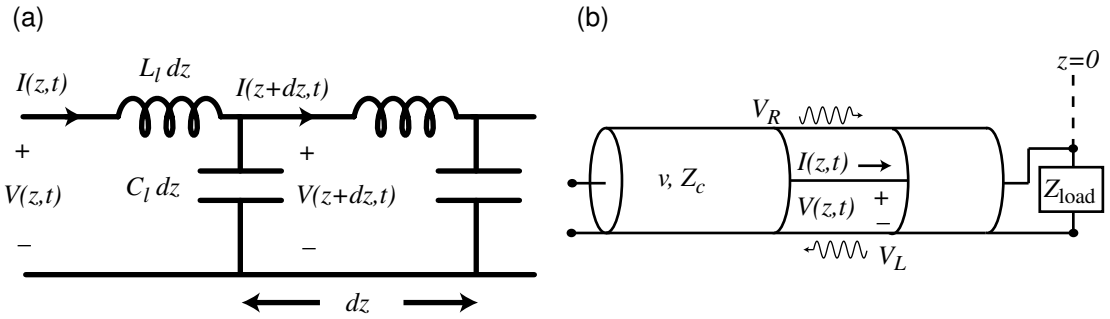

Figure 2.2: (a) Lumped element equivalent circuit of a lossless transmission line; the inductance and capacitance of the circuit shown are given by $L_l dz$ and $C_l dz$ respectively, where L_l is the inductance per unit length, C_l the capacitance per unit length and dz the infinitesimal length the section of transmission line. (b) A transmission line terminated at $z = 0$ by a load of impedance Z_{load}. Current I and voltage V are indicated as defined in the main text in terms of the right and left traveling voltage waves V_R and V_L.

Fields inside a transmission line satisfy the 1-D wave equation. We can derive this result by modeling the transmission line as a series of lumped element circuits of length dz, as shown in figure 2.2a, where C_l and L_l is the capacitance and inductance per unit length. Applying Kirchhoff's voltage and current law on one of the cells results into the derivations of the so called telegrapher equations [16]:

$$\begin{aligned} \frac{\partial V(z,t)}{\partial z} &= -L_l \frac{\partial I(z,t)}{\partial t}, \\ \frac{\partial I(z,t)}{\partial z} &= -C_l \frac{\partial V(z,t)}{\partial t}. \end{aligned} \tag{2.13}$$

Combining these equations, we can derive the 1-D wave equation for both voltages and currents with a propagating velocity of $v = \sqrt{1/L_l C_l}$:

$$\frac{\partial^2 V(z,t)}{\partial z^2} = \frac{1}{v^2} \frac{\partial^2 V(z,t)}{\partial t^2}. \tag{2.14}$$

We know that the solution for the wave equation can be decomposed into a left-traveling part and a right-traveling part:

$$\begin{aligned} V(z,t) &= V_R(t-\frac{z}{v}) + V_L(t+\frac{z}{v}), \\ I(z,t) &= \frac{1}{Z_c}\{V_R(t-\frac{z}{v}) - V_L(t+\frac{z}{v})\}, \end{aligned} \tag{2.15}$$

where Z_c is the characteristic impedance of the transmission line given by $Z_c = \sqrt{L_l/C_l}$, and relates the voltage and current on the line as:

$$Z_c = \frac{V_R}{I_R} = -\frac{V_L}{I_L}.$$

V_L and V_R are arbitrary functions of their argument and they represent signals being launched in the transmission line.

For an infinite transmission line, the right and left-traveling waves are independent; however, when at some coordinate z (that for our convenience, we will define this point as $z = 0$) the transmission line is terminated by some circuit then these solutions are not independent (Fig. 2.2b). They both have to fulfill certain boundary condition imposed by the circuit with a frequency dependant impedance $Z_{\text{load}}(\omega)$:

$$Z_{\text{load}} = \frac{V(z=0,\omega)}{I(z=0,\omega)}. \tag{2.16}$$

The instantaneous net power flow transported by the transmission line is given by

$$P = \frac{1}{Z_c}(V_R(z,t)^2 - V_L(z,t)^2) \tag{2.17}$$

where our convention is that positive carried power goes to the right. So far our description of a transmission line has been completely classical. In the next section we will treat it as a quantum system.

2.2.2 Quantization of a lossless transmission line

Before quantizing the system consisting of a transmission line, we will write its Hamiltonian and Lagrangian. We will see that an infinite transmission line can be

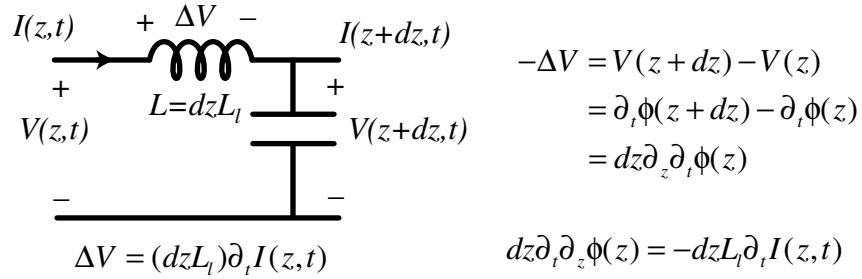

Figure 2.3: The relation between the current $I(z,t)$ and the generalized flux variable $\phi(z,t)$ is described.

studied as a collection of an infinite number of independent harmonic oscillators and hence it can be easily quantized.[2] Using the generalized flux variable defined as [3, 12]

$$\phi(z,t) \equiv \int_{-\infty}^{t} dt' V(z,t') \tag{2.18}$$

where $V(z,t') = \frac{\partial\phi(z,t)}{\partial t}$ is the local voltage of a transmission line at position z and at time t'. The relation between the current $I(z,t)$ and $\phi(z,t)$ is derived in figure 2.3 and is given by

$$I(z,t) = -\frac{1}{L_l}\frac{\partial\phi(z,t)}{\partial z}.$$

Then the Lagrangian density for a transmission line is

$$\mathfrak{L} = \frac{C_l}{2}\left(\frac{\partial\phi(z,t)}{\partial t}\right)^2 - \frac{1}{2L_l}\left(\frac{\partial\phi(z,t)}{\partial z}\right)^2. \tag{2.19}$$

Using Eq. (2.19), it can be shown using the Euler-Lagrange equation that ϕ satisfies a 1-D wave equation:

$$\frac{\partial^2\phi(z,t)}{\partial z^2} = \frac{1}{v^2}\frac{\partial^2\phi(z,t)}{\partial t^2}. \tag{2.20}$$

The momentum conjugate variable of the flux $\phi(z,t)$ is the charge density $q(z,t)$:

$$\frac{\delta\mathfrak{L}}{\delta\partial_t\phi} = C_l\frac{\partial\phi}{\partial t} = C_l V(z,t) = q(z,t)$$

[2] The only difference between the quantization of electromagnetic modes of vacuum in free space and the ones studied here that in our case photons do not carry a polarization label and travel in one dimension yielding a different density of states as a function of frequency [3].

from which we can then derive the Hamiltonian density:

$$\mathcal{H} = \frac{1}{2L_l}\left(\frac{\partial\phi(z,t)}{\partial z}\right)^2 + \frac{1}{2C_l}q(z,t)^2. \tag{2.21}$$

We have already stated that since the fields in the transmission line satisfy the wave equation, then their solutions consist of left and right-traveling waves (2.15). We can introduce quantum mechanics into the analysis of the transmission line again following the usual procedure of canonical quantization:

$$[\phi(z',t), q(z,t)] = i\hbar\delta(z-z'),$$
$$[q(z,t), q(z',t)] = [\phi(z,t), \phi(z',t)] = 0.$$

We can fourier expand these fields following the same procedure described in Refs. [3, 15, 17]. The only distinction is that I have chosen to use the voltage $V(z,t) = q(z,t)/C_l$ as my quantized field variable so that our analysis follows closely the language used in microwave theory

$$\begin{aligned} V_R(z,t) &= \sqrt{\frac{\hbar Z_c}{2}}\int_0^\infty \frac{d\omega}{2\pi}\sqrt{\omega}(a_R(\omega)e^{-i\omega(t-z/v)} + \text{H.c.}), \\ V_L(z,t) &= \sqrt{\frac{\hbar Z_c}{2}}\int_0^\infty \frac{d\omega}{2\pi}\sqrt{\omega}(a_L(\omega)e^{-i\omega(t+z/v)} + \text{H.c.}), \end{aligned} \tag{2.22}$$

where H.c. stands for Hermitian conjugate, and the operators $a_L(\omega)$ and $a_R(\omega)$ are the annihilation operators for the signal quanta propagating to the left and to the right, respectively. They satisfy the standard commutation relations for a 1-D scalar field given below, where we have used the convention from Ref. [3, 18]:

$$[a_\alpha(\omega), a_{\alpha'}(\omega')] = 0, \tag{2.23}$$

$$[a_\alpha(\omega), a^\dagger_{\alpha'}(\omega')] = 2\pi\delta(\omega-\omega')\delta_{\alpha,\alpha'}, \tag{2.24}$$

$$\langle a^\dagger_\alpha(\omega')a_{\alpha'}(\omega)\rangle = \frac{1}{\exp(\frac{\hbar\omega}{k_BT})-1}2\pi\delta(\omega-\omega')\delta_{\alpha,\alpha'}, \tag{2.25}$$

$$\langle\{a_\alpha(\omega), a^\dagger_{\alpha'}(\omega')\}\rangle = \coth(\frac{\hbar\omega}{2k_BT})2\pi\delta(\omega-\omega')\delta_{\alpha,\alpha'}, \tag{2.26}$$

where α and α' stand for either R or L. Using expressions (2.22)-(2.24) and replacing the field operators into the expression of the Hamiltonian density (2.21), we can derive our expression for the Hamiltonian of an infinite transmission line:

$$H = \int_{-\infty}^{\infty} dz\mathcal{H} = \int_{0}^{\infty} \frac{d\omega}{2\pi}\hbar\omega[a_L^{\dagger}(\omega)a_L(\omega) + a_R^{\dagger}(\omega)a_R(\omega)] \tag{2.27}$$

where I have dropped a constant term that arises from the commutation relations. Eq. (2.27) shows what I mentioned above: a transmission line can be modeled as a system composed of an infinite number of harmonic oscillators.

Once we have quantized the fields inside a transmission line, we can calculate statistical values for some important quantities. For a given thermal state, V_R and V_R^2 have the following expectation values:

$$\langle V_R \rangle = 0, \tag{2.28}$$

$$\langle V_R^2 \rangle = \int_B \frac{d\omega}{2\pi} S_{V_R V_R} = Z_c \int_B \frac{d\omega}{2\pi} \frac{\hbar\omega}{2} \coth(\frac{\hbar\omega}{2k_B T}), \tag{2.29}$$

where $S_{V_R V_R}$ is the symmetrized spectral density of right traveling voltage signal, and the integration has been limited to the bandwidth B_ω of the measuring instrument. We observe then that a thermal state with temperature T has a noise power per unit bandwidth of $\frac{\hbar\omega}{2}\coth(\frac{\hbar\omega}{2k_B T})$ propagating to the right and to the left along the transmission line. We can use the previous results to estimate the voltage fluctuations generated by a resistor [3]. In order to do that, let's consider the example of a transmission line terminated with a resistor at one end. The terminating resistor acts as a black body emitting thermal noise down the transmission line. If the resistor is held at temperature T it will bring the transmission line modes into equilibrium at the same temperature. Consider figure 2.2b where the load Z_{load} is replaced by a resistor like the one shown in figure 2.4. We can derive the voltage noise of a resistor by considering the voltage noise at the open termination of a transmission line with $Z_c = R$. For the open termination of the transmission line, the left and right moving signals are not independent, but $V_R = V_L$,

so that the voltage at the end is given by

$$V = V_R + V_L = 2V_R$$

and thus, using Eqs. (2.29), we have

$$S_{VV}(\omega) = 4S_{V_R,V_R}(\omega) = 4Z_c\frac{\hbar\omega}{2}\coth(\frac{\hbar\omega}{2k_BT}). \tag{2.30}$$

It is these fluctuations from a resistor that will allow us to calibrate the noise added by our amplifier in chapter 6.

Another important point is that transmission lines can act as a simple resistor in which instead of dissipating energy, it carries it away as propagating waves. This effective dissipation is a consequence of its semi-infinite length and since it has a conservative Hamiltonian, it can be used to treat dissipation within a quantum theory framework [3, 12, 15]. This model for resistors (called Nyquist model [19]) is completely equivalent to modeling dissipation as coupling to a thermal bath or reservoir with an infinite number of harmonic oscillators [20].

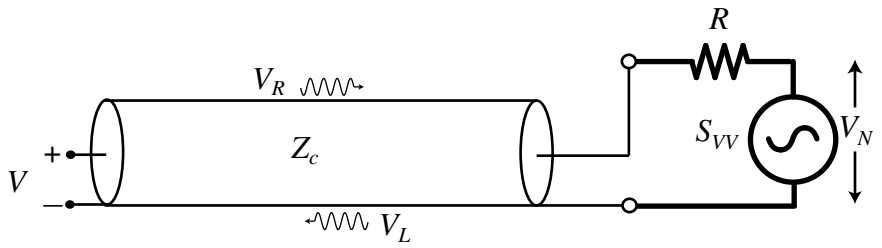

Figure 2.4: A noisy resistor R is coupled to a transmission line with a characteristic impedance of Z_c. The noise of the resistor is modeled as a voltage source with a spectral density given by S_{VV}.

2.3 Input-Output theory

In this section I will consider the problem of coupling a system, e.g. a simple harmonic oscillator, to the fields of a transmission line using Input-Output theory (IOT).

IOT is an approximate method that solves an important problem: how to calculate the quantum statistical properties of both, the field inside a cavity and the field exiting the cavity given the input field. In this section I will first treat the useful example of coupling a simple harmonic oscillator, in the form of an LC resonator, to external signals coming from a transmission line. Due to its simplicity, I can solve this problem exactly using quantum network theory [15].[3] Then I will explain a series of approximations made to the EOM that allows us to cast them into a form identical to the EOM derived in quantum optics books for a cavity coupled a reservoir modeled as a collection of infinite harmonic oscillators [22]. This serves as a prelude for the next part of this section where I describe another more direct approach of quantizing systems coupled to thermal baths in a language more akin to that of quantum optics.

2.3.1 Harmonic oscillator coupled to a transmission line

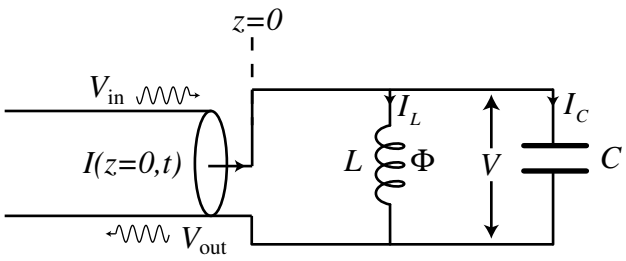

Figure 2.5: A SHO in the form of an LC resonator is coupled to a transmission line. The resonator is described using as generalized coordinates the flux Φ of the inductor and the charge Q of the capacitor.

The system analyzed is the one shown in figure 2.5. It consist of an LC resonator coupled to a transmission line. The equations of motion can be derived using current

[3] Quantum network theory was developed as quantum extension of the classical theory of electrical networks and as a quantum extension of linear response theory in the context of electrical circuits. It allows us to study fluctuations entering a system as input signal fields from a transmission line [15, 21]

conservation law[4] :

$$\begin{aligned} -I(z=0,t) + I_L(t) + I_C(t) &= 0, & (2.31)\\ -I(z=0,t) + \frac{\Phi}{L} + \frac{d(CV)}{dt} &= 0, & (2.32)\\ -I(z=0,t) + \frac{\Phi}{L} + C\frac{d^2\Phi}{dt^2} &= 0. & (2.33) \end{aligned}$$

Now, using expressions (2.15), we can solve for $I(z=0,t) = I(t)$ in terms of the internal $V(z=0,t)$ and incoming $V_{\text{in}}(z=0,t)$ fields (where for convenience I am using the subscripts "in" and "out" instead of "R" and "L" to make the distinction between the input and output fields clearer). Solving for $I(t)$, the result is

$$I(t) = \frac{2V_{\text{in}}(t) - V(t)}{Z_c}.$$

Using the known relation between voltage and flux $V = \frac{d\Phi}{dt}$, our EOM for the internal field Φ is then

$$C\frac{d^2\Phi}{dt^2} + \frac{1}{Z_c}\frac{d\Phi}{dt} + \frac{\Phi}{L} = \frac{2}{Z_c}V_{\text{in}}(t) \tag{2.34}$$

The term $\frac{2}{Z_c}V_{\text{in}}(t)$ is the driving force that the incoming fields exert on the harmonic oscillator. For the case when the transmission line represents a thermal bath, V_{in} is the fluctuation or Langevin force and Eq. (2.34) can be consider just an example of a Langevin equation. Solving the EOM of the LC-resonator allows us to predict the outgoing field. In this rather simple example, the response of the oscillator is linear and can be characterized by a complex frequency dependant impedance $Z(\omega)$ (Eq. 2.16)

$$Z(\omega) = \frac{V(z=0,\omega)}{I(z=0,\omega)}.$$

From basic microwave theory using expressions (2.15) and (2.16), it can be shown that the relation between the incoming and outgoing signal is

$$V_{\text{out}}(z=0,\omega) = \Gamma(\omega)V_{\text{in}}(z=0,\omega) \tag{2.35}$$

[4] A Quantum Network theory approach to a problem usually starts by writing the Lagrangian of the system, and using the Euler-Lagrange equation, the EOM are then derived [12, 15]. However, this example is simple enough that we can skip this step.

where $\Gamma(\omega)$ is the called the reflection coefficient and is defined as

$$\Gamma(\omega) = \frac{Z(\omega) - Z_c}{Z(\omega) + Z_c}. \tag{2.36}$$

For our example, from circuit theory we know that the impedance of a parallel LC resonator is given by

$$Z(\omega) = \frac{jL\omega}{1 - (\omega/\omega_0)^2} \tag{2.37}$$

where I am using the electrical engineering sign convention of $j = -i$ and $\omega_0 = 1/\sqrt{LC}$. In the limit of low damping ($\mathcal{Q} = \omega_0 Z_c C \gg 1$), we expect the resonator to respond to inputs only near the frequency ω_0 where the impedance is large compared to Z_c, and we may approximate [3, 16]

$$Z(\omega) = \frac{jL\omega\omega_0^2}{(\omega_0 - \omega)(\omega_0 + \omega)} \approx \frac{jL\omega_0^2}{2(\omega_0 - \omega)} = \frac{1}{2Cj(\omega - \omega_0)}$$

which then yields for the reflection coefficient in the high $\mathcal{Q}$ limit

$$\Gamma(\omega) = \frac{Z(\omega) - Z_c}{Z(\omega) + Z_c} \approx \frac{\gamma - j(\omega - \omega_0)}{\gamma + j(\omega - \omega_0)} \tag{2.38}$$

where $\gamma = \frac{1}{2CZ_c}$ defines the amplitude decay rate, or half width at half maximum (HWHM).

So far, the analysis has been completely classical. We start the quantum mechanical analysis by making the input and output fields quantum mechanical signals that are represented in the fourier domain as shown in expression (2.22). In this case, the incoming field consist of the right-propagating signals at $z = 0$

$$V_{\text{in}}(t) = \sqrt{\frac{\hbar Z_c}{2}} \int_0^\infty \frac{d\omega}{2\pi} \sqrt{\omega} (a_{\text{in}}(\omega) e^{-i\omega t)} + \text{H.c.}). \tag{2.39}$$

Solving for internal fields in Eq. (2.34) in the frequency domain, the result is

$$\Phi(\omega) = \frac{1}{C}\sqrt{\frac{2\hbar\omega}{Z_c}} \frac{a_{\text{in}}(\omega)}{-\omega^2 - i2\gamma\omega + \omega_0^2}, \tag{2.40}$$

$$\Phi^\dagger(\omega) = \frac{1}{C}\sqrt{\frac{2\hbar\omega}{Z_c}} \frac{a_{\text{in}}^\dagger(\omega)}{-\omega^2 + i2\gamma\omega + \omega_0^2}. \tag{2.41}$$

From these expressions we can derive the time-dependant solution for Φ as shown below

$$\Phi(t) = \frac{1}{C}\sqrt{\frac{2\hbar}{Z_c}}\int_0^\infty \frac{d\omega}{2\pi}\sqrt{\omega}\left(\frac{a_{\rm in}(\omega)e^{-i\omega t}}{-\omega^2 - i2\gamma\omega + \omega_0^2} + \text{H.c.}\right). \tag{2.42}$$

Now consider the flux's conjugate momentum given by the charge of the capacitor $Q = CV = C(d\Phi/dt)$. Using the commutation relations (2.23 and 2.24) we can show that Q and Φ have the expected commutation relation:

$$\begin{aligned}[\Phi(t), Q(t)] &= i\frac{4\gamma\hbar}{\pi}\int_0^\infty d\omega \frac{\omega^2}{(\omega^2-\omega_0^2)^2 + (2\gamma\omega)^2}. \\ &= i\hbar.\end{aligned} \tag{2.43}$$

This is the electrical equivalent to $[x, p] = i\hbar$. Eqs. (2.34-2.42) constitute the solution for the quantum problem of an LC circuit coupled to a transmission line. We can calculate expectation values for the internal fields, and together with Eq. (2.15) we can calculate expectation values for the output fields ($V_L \to V_{\rm out}$).

2.3.2 Approximations

So far, I have not made any approximations in the analysis, and we have been able to solve this problem exactly due to its simplicity. However for more complicated systems (e.g. a non-linear harmonic oscillator), the exact solution is not possible unless some approximations are made. I introduce these approximations in this section in the same context of a SHO coupled to a transmission line from which I will derive expressions similar to those found in the quantum optics literature describing a cavity coupled a thermal bath.

Consider again the EOM for the LC-harmonic oscillator coupled to a transmission line.

$$C\frac{d^2\Phi}{dt^2} + \frac{1}{Z_c}\frac{d\Phi}{dt} + \frac{\Phi}{L} = \frac{2}{Z_c}V_{\rm in}(t).$$

We now write the expression for $\Phi(t)$ as

$$\Phi(t) = \sqrt{\frac{h\omega_0 L}{2}}[c(t)e^{-i\omega_0 t} + c^\dagger(t)e^{i\omega_0 t}] \tag{2.44}$$

where the normalization constant has been chosen according to Eq. (2.11), so that the energy in the internal field will be $E = \hbar\omega_0 c^\dagger c$. In this expression, the amplitude $c(t)$ is a slowly varying function of time.

Let's consider the incoming field $V_{\rm in}(t)$ as defined in Eq. (2.39). When the $\mathcal{Q}$ of the resonator is high, one expects it to respond to inputs only near the frequency ω_0. With this in mind, we replace $\sqrt{\omega}$ with $\sqrt{\omega_0}$:

$$\begin{aligned} V_{\rm in}(t) &= \sqrt{\frac{\hbar Z_c}{2}} \int_0^\infty \frac{d\omega}{2\pi} \sqrt{\omega} (a_{\rm in}(\omega) e^{-i\omega t} + a_{\rm in}^\dagger(\omega) e^{i\omega t}), \qquad (2.45) \\ &\approx \sqrt{\frac{\hbar Z_c \omega_0}{2}} \{ e^{-i\omega_0 t} \int_{-\omega_0}^\infty \frac{d\omega'}{2\pi} b_{\rm in}(\omega') e^{-i\omega' t} \\ &\quad + e^{i\omega_0 t} \int_{-\omega_0}^\infty \frac{d\omega'}{2\pi} b_{\rm in}^\dagger(\omega') e^{i\omega' t} \}, \qquad (2.46) \end{aligned}$$

where we have made a change of variables ($\omega \to \omega' + \omega_0$) and defined the new annihilation operator

$$b_{\rm in}(\omega) = a_{\rm in}(\omega + \omega_0)$$

which has the same commutation relations as $a_{\rm in}$ (Eqs. 2.23, 2.24). Further, because the oscillator will only respond to a driving signal whose frequency is close to ω_0, that is at frequencies $\omega' = 0$ for the new frequency variable, we can extend the integral lower limit to $-\infty$ without introducing a large error. Thus, we arrive to the following expression for the incoming field

$$V_{\rm in}(t) = \sqrt{\frac{\hbar Z_c \omega_0}{2}} [e^{-i\omega_0 t} b_{\rm in}(t) + e^{i\omega_0 t} b_{\rm in}^\dagger(t)] \qquad (2.47)$$

where

$$b_{\rm in}(t) = \frac{1}{2\pi} \int_{-\infty}^\infty d\omega b_{\rm in}(\omega) e^{-i\omega t}. \qquad (2.48)$$

We can picture $b_{\rm in}(t)$ as the slowly varying part compare to ω_0 of the input field [17]. Since $b_{\rm in}(\omega)$ satisfy the commutation relations

$$\begin{aligned} [b_{\rm in}(\omega), b_{\rm in}(\omega')] &= 0, \qquad (2.49) \\ [b_{\rm in}(\omega), b_{\rm in}^\dagger(\omega')] &= 2\pi\delta(\omega - \omega'), \qquad (2.50) \end{aligned}$$

the analysis of the temporal modes (2.48) shows that their quantum commutator obeys

$$[b_{\rm in}(t), b_{\rm in}(t')] = 0, \tag{2.51}$$

$$[b_{\rm in}(t), b^{\dagger}_{\rm in}(t')] = \delta(t-t'). \tag{2.52}$$

It can be shown that the normalization of $b_{\rm in}(t)$ results in a incoming power for a monochromatic signal at frequency ω of [3]

$$P_{\rm in} = \hbar\omega\langle b^{\dagger}_{\rm in}(t) b_{\rm in}(t)\rangle. \tag{2.53}$$

The approximations used to derive Eqs. (2.46), (2.47), (2.48) and (2.50) are referred to as the Markov approximation [3, 17, 22, 23]. A similar line of reasoning, with the appropriate changes can be applied to obtain the expression for the outgoing field and we get exactly the same equations as Eqs. (2.47-2.53) with the subscript "in" replaced by "out".

Our next set of approximations will let us write the EOMs for these coupled systems in a form similar to those found in quantum optics literature [3, 17, 22–24]. If we replace Eqs. (2.44) and (2.47) into (2.34) and separating the parts oscillating at $e^{-i\omega_0 t}$ and $e^{i\omega_0 t}$, we obtain:

$$C\frac{d^2}{dt^2}(ce^{-i\omega_0 t}) + \frac{1}{Z_c}\frac{d}{dt}(ce^{-i\omega_0 t}) + \frac{ce^{-i\omega_0 t}}{L} = \frac{2}{\sqrt{LZ_c}} b_{\rm in}(t) e^{-i\omega_0 t}. \tag{2.54}$$

The following approximations are made:

- $\frac{d^2}{dt^2}(ce^{-i\omega_0 t}) \approx -\omega_0^2 ce^{-i\omega_0 t} - i2\omega_0 \frac{dc}{dt} e^{-i\omega_0 t}$
- $|\frac{1}{c}\frac{dc}{dt}| \ll \omega_0$

These approximations constitute the "slowly varying envelope approximation" [13, 17]. It basically means that the amplitude $c(t)$ is going to be a slow varying function of time compared to the time scale of $1/\omega_0$. After substituting these equations in (2.54), we obtain

$$\frac{dc}{dt} + \gamma c = i\sqrt{2\gamma} b_{\rm in}(t). \tag{2.55}$$

The equivalent expression for the boundary conditions (2.15) in terms of the operators c, $b_{\rm in}$ and $b_{\rm out}$ is

$$b_{\rm out}(t) + b_{\rm in}(t) = -i\sqrt{2\gamma}c. \tag{2.56}$$

We can derive an expression for $Q(t)$ equivalent to (2.44) within the same set of approximations. Substituting both expressions for Q and Φ in Eq. (2.43), it can be deduced that $[c, c^\dagger] = 1$, as expected.

The previous expressions have been derived in the ω_0-rotating frame. One can transform back to the non-rotating frame through the following transformations

$$\begin{aligned} a(t) &= e^{-i\omega_0 t}c(t), \\ a_{\rm in}(t) &= e^{-i\omega_0 t}b_{\rm in}(t), \\ a_{\rm out}(t) &= e^{-i\omega_0 t}b_{\rm out}(t), \end{aligned}$$

with the same commutation relations as their counterparts in the rotating frame. The equations of motion (2.55) and (2.56) in the non-rotating frame become

$$\frac{da}{dt} + i\omega_0 a + \gamma a = i\sqrt{2\gamma}a_{\rm in}(t) \tag{2.57}$$

$$a_{\rm out}(t) + a_{\rm in}(t) = -i\sqrt{2\gamma}a. \tag{2.58}$$

We can go on to solve exactly Eqs. (2.57) and (2.58); however, I will not do that now, but in the following section. The point I wanted to make in this section was to explain the approximations that allowed us to reduce expressions (2.34) and (2.15) derived using quantum network theory to a form that is commonly encountered in quantum optics when analyzing a cavity mode (in our case the cavity's role played by the LC-resonator) coupled to an external field through a partly transparent mirror. What I will show in the next section is that Eqs. (2.57) and (2.58) can also be derived in a much more direct way when one is willing to make the approximations explained in this section since the very beginning. This method is what is more commonly described as Input-Output theory.

2.3.3 Alternative approach

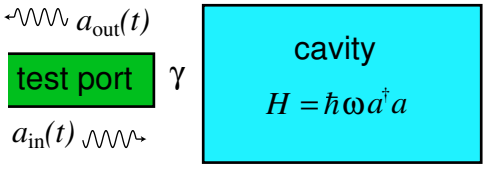

Figure 2.6: The typical example in quantum optics used to introduce Input-Output theory consists of a cavity whose Hamiltonian is that of harmonic oscillator coupled to a thermal bath via a test port. The coupling between the reservoir and the cavity is described by frequency-independent term γ.

In this section I describe a more direct way to derive the equivalent equations to (2.57) and (2.58) but for a generic system (not necessarily a SHO). The present discussion follows closely standard references on the subject [3, 17, 22–24]. In order to drive a cavity like the one shown in figure 2.6, we need to open a port which exposes the cavity to both an external drive and the noise of the thermal bath it is now coupled to. Input-Output theory allow us to formally separate the degrees of freedom into internal cavity modes and external bath modes. The Hamiltonian of a generic high-$\mathcal{Q}$ cavity coupled to a thermal bath can written in the following form

$$H = H_{\rm sys} + H_{\rm bath} + H_{\rm int}$$

where $H_{\rm sys}$ is the Hamiltonian for the system under study. In our case, $H_{\rm sys}$ is given by Eq. (2.12),

$$H_B = \sum_n \int_{-\infty}^{\infty} \frac{d\omega}{2\pi} \hbar\omega a_n^\dagger(\omega) a_n(\omega) \tag{2.59}$$

is the sum over the n thermal baths and

$$H_{\rm int} = \hbar \sum_n \int_{-\infty}^{\infty} \frac{d\omega}{2\pi} [\kappa_n^* a_n^\dagger(\omega) g + \kappa_n g^\dagger a_n(\omega)] \tag{2.60}$$

where $g = g(a, a^\dagger)$ and $g^\dagger$ are the system operators the bath couples to and κ_n is the coupling constant between the n thermal bath and the system. I have assumed that all

the baths couple to the same operator in the system under study. This Hamiltonian gives rise to linear coupling between the system variables and the bath modes. The a_n operators are the boson annihilation operators for the n-different baths the system is coupled to and they obey the usual commutation relations:

$$\begin{aligned} [a_n(\omega), a^\dagger_{n'}(\omega')] &= 2\pi\delta_{n,n'}\delta(\omega-\omega'), \\ [a_n(\omega), a_{n'}(\omega')] &= [a^\dagger_n(\omega), a^\dagger_{n'}(\omega')] = 0. \end{aligned} \tag{2.61}$$

Now there are two important points about the interaction and thermal bath Hamiltonian:

(1) The range of integration is from $-\infty$ to ∞ as opposed to from 0 to ∞: the cavity resonance only responds to frequencies within certain range. Thus, the lower integration limit has been extended from 0 to $-\infty$ as we did in the previous section under the "slowly varying envelope approximation."

(2) The coupling constants κ_n are frequency independent: we have assumed the Markov approximation by assuming κ_n is a constant over the range of frequencies that are relevant to the system.

Since the creation and annihilation operators have no explicit time dependance, we can derive their Heisenberg equations of motion from

$$i\hbar\frac{d\mathcal{O}}{dt} = [\mathcal{O}, H]$$

from which one obtains the following EOM for the bath mode operators

$$\frac{da_n(\omega)}{dt} = -i\omega a_n(\omega) - i\kappa^*_n g \tag{2.62}$$

and for the system operator f (not necessarily g), one obtains

$$\frac{df(\omega)}{dt} = -\frac{i}{\hbar}[f, H_{\rm sys}] - i\sum_n \int_{-\infty}^{\infty}\frac{d\omega}{2\pi}\{\kappa^*_n a^\dagger_n(\omega)[f,g] + \kappa_n[f,g^\dagger]a_n(\omega)\}. \tag{2.63}$$

The bath mode fields have yet to be separated into incoming and outgoing bath fields. The procedure through which this is done can be reviewed in the extensive literature [3,17,22,23]. We do not review it here since the derivation is not so intuitively appealing as in the case explained above for the transmission line coupled to a LC-resonator; we just quote the resulting EOM for the internal field in terms of the input fields:

$$\frac{df}{dt} = -\frac{i}{\hbar}[f, H_{\rm sys}] + \sum_n \left\{ \left[\frac{|\kappa_n|^2}{2} g^\dagger + i\kappa_n^* a_n^{in\dagger}(t) \right] [f, g] - [f, g^\dagger] \left[\frac{|\kappa_n|^2}{2} g - i\kappa_n a_n^{\rm in}(t) \right] \right\} \tag{2.64}$$

and the boundary condition that relates the input, output and internal fields

$$a_n^{\rm in}(t) + a_n^{\rm out}(t) = -i\kappa_n^* g(t) \tag{2.65}$$

with

$$[a_n^\alpha(t), a_{n'}^\alpha(t')] = 0 \tag{2.66}$$

$$[a_n^\alpha(t), a_{n'}^{\alpha\dagger}(t')] = \delta_{n,n'}\delta(t-t') \tag{2.67}$$

for $\alpha \to in, out$

So far, Eqs. (2.64-2.65) have been expressed for a very general case. To touch ground, let's consider the equivalent case of a harmonic oscillator coupled to a single thermal bath (Fig. 2.6). In that case we drop the index n for multiple thermal baths,

$$H_{sys} = \hbar\omega_0 a^\dagger a$$

and replace g for a in Eq. (2.60). Expressions (2.64) and (2.65) for the case of $f = a$ reduces to

$$\frac{da}{dt} = -i\omega_0 a - \frac{|\kappa|^2}{2} a + i\kappa a_{\rm in}(t) \tag{2.68}$$

and

$$a_{\rm in}(t) + a_{\rm out}(t) = -i\kappa a(t). \tag{2.69}$$

Eqs. (2.68) and (2.69) are exactly the same equations we derived in the previous section (2.57) and (2.58) with the coupling constants κ being defined as $\kappa = \sqrt{2\gamma}$. They

can be solved by Fourier transformation for both the internal field and the output field yielding

$$a(\omega) = \frac{\sqrt{2\gamma}i}{i(\omega_0 - \omega) + \gamma} a_{\text{in}}(\omega) \tag{2.70}$$

$$a_{\text{out}}(\omega) = \frac{i(\omega - \omega_0) + \gamma}{-i(\omega - \omega_0) + \gamma} a_{\text{in}}(\omega). \tag{2.71}$$

From Eq. (2.71), the ratio of the input and output field is

$$\frac{a_{\text{out}}}{a_{\text{in}}} = \frac{i(\omega - \omega_0) + \gamma}{-i(\omega - \omega_0) + \gamma}$$

which is exactly the reflection coefficient $\Gamma(\omega)$ that was derived for a parallel LC resonator coupled to a transmission line (2.38)

The reason the alternative approach is useful, is that it gives us a recipe for how to add ports, without worrying about the details of the coupling and it lets us treat more complicated systems than a SHO in a much simpler way. For these reasons, we will be doing extensive use of expressions (2.64) and (2.65) in the following chapters.

2.4 Quantum-limited amplification: Haus-Caves theorem

A comprehensive review on quantum limits of amplification can be found in Ref. [2]. This section will review the fundamental properties of amplification. The general quantum limit (Haus-Caves theorem) is first discussed for phase insensitive amplifiers, where the origin of the half a quantum of added noise is clarified. Then we will discuss the concept of a noiseless amplifier in the form of a phase sensitive amplifier. Finally we will discuss the generic example of a degenerate parametric amplifier as a phase sensitive amplifier, and its properties as a generator of quadrature-squeezed states. In this section, I will only discuss the simple case of a single-mode system. However, real signals and real amplifiers have a nonzero bandwidth, and a multimode analysis of the amplifiers is necessary. The generalization of the results derived here to the multimode case is considered in appendix A.

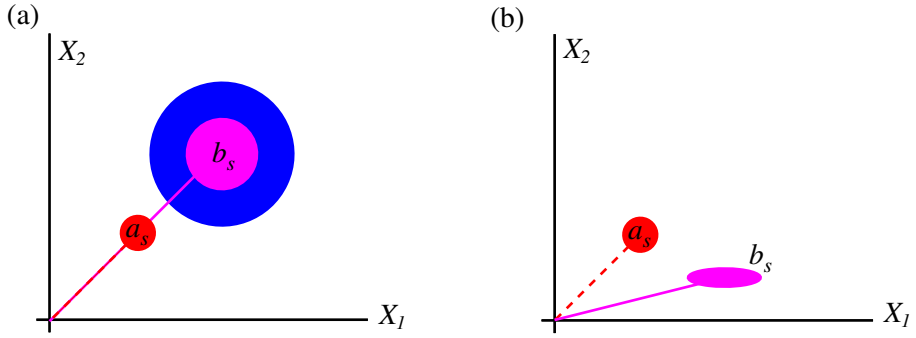

Figure 2.7: (a) Input and output signals for a linear phase insensitive amplifier. The input noise (red) is amplified (pink). However the output contains an amount on noise larger than just the amplified noise due to the added noise of the amplifier (blue). (b) For an ideal phase sensitive amplifier (such as a degenerate parametric amplifier), the output does not contain any amplifier noise. However, this comes with the restriction that only one of the quadratures (X_1) is amplified, while the other is deamplified.

2.4.1 Phase insensitive amplifier

A phase insensitive amplifier is one that for a given input, the output will not show any phase preference; that is, for a given phase shift on the input signal, the only effect is an equivalent phase shift of the output [2]. Another requirement for an amplifier to be phase insensitive is that it must add equal amount of noise to both quadratures [25]. In general, we can define a voltage signal with the time dependance explicitly included as

$$V_s = V_0 \left(a_s e^{-i\omega_o t} + a_s^\dagger e^{i\omega_o t} \right)$$

where $a_s(0) \equiv a_s$ and $a_s^\dagger(0) \equiv a_s^\dagger$. We can decompose this voltage signal into two phase or quadrature operators:

$$V_s = 2V_0 \left(X_1 \cos(\omega_o t) + X_2 \sin(\omega_o t) \right). \tag{2.72}$$

In the previous expressions, the signal V_s has been normalized so that $a_s^\dagger a_s = X_1^2 + X_2^2 - 1/2$ corresponds to the photon number operator in the signal mode [26]. The

quadrature operators are hermitian (and therefore observables) defined by

$$X_1 = \frac{1}{2}(a_s + a_s^\dagger), \tag{2.73}$$

$$X_2 = \frac{1}{2i}(a_s - a_s^\dagger). \tag{2.74}$$

From Eq. (2.72), it is evident that the quadrature operators are associated with field amplitudes oscillating 90° out of phase. Let's consider a linear amplifier with gain G_1 for the cosine quadrature component and gain G_2 for the sine quadrature component. The two quadrature components Y_1 and Y_2 of the output amplified signal are given by:

$$\begin{aligned} Y_1 &= \sqrt{G_1}X_1 + F_1, \\ Y_2 &= \sqrt{G_2}X_2 + F_2, \end{aligned} \tag{2.75}$$

where F_1 and F_2 are the fluctuation operators of the amplifier internal modes. The input and output mode operators must satisfy the boson commutation relations

$$[X_1, X_2] = [Y_1, Y_2] = \frac{i}{2}. \tag{2.76}$$

In order for Y_1 and Y_2 to satisfy the commutation relations, F_1 and F_2 cannot be zero, but they need to satisfy

$$[F_1, F_2] = \frac{i}{2}[1 - \sqrt{G_1}\sqrt{G_2}] \tag{2.77}$$

where I have assumed that the input mode is independent of the amplifier internal mode ($[X_i, F_j] = 0$).[5] Eq. (2.77) implies that the product of the fluctuations in F_1 and F_2 must satisfy the following inequality

$$\langle \Delta F_1^2 \rangle \langle \Delta F_2^2 \rangle \geq \frac{G_1 G_2}{16}(1 - \frac{1}{\sqrt{G_1}\sqrt{G_2}})^2. \tag{2.78}$$

When quoting a noise number for an amplifier, this is usually referred to the input of the amplifier; that is, the output of the amplifier is divided by its gain, and

[5] Carlton Caves mentions the possibility of systems amplifier-input field where it would be possible to have less noise added than the limit we will derive. However, this would only be possible if the input noise and the internal-mode noise of the amplifier were correlated [2].

that way we can do a fair comparison in the noise performance of different amplifiers, independent of their gains. Following the same reasoning, we can define the normalized output signals as

$$\begin{aligned} X_{1,eff} &= \frac{Y_1}{\sqrt{G_1}} = X_1 + \frac{F_1}{\sqrt{G_1}}, \\ X_{2,eff} &= \frac{Y_2}{\sqrt{G_2}} = X_2 + \frac{F_2}{\sqrt{G_2}}. \end{aligned} \tag{2.79}$$

Again, the uncertainty product for the new defined normalized output modes is given by

$$\begin{aligned} \langle \Delta X_{1,eff}^2 \rangle \langle \Delta X_{2,eff}^2 \rangle &= (\langle \Delta X_1^2 \rangle + \frac{\langle \Delta F_1^2 \rangle}{G_1})(\langle \Delta X_2^2 \rangle + \frac{\langle \Delta F_2^2 \rangle}{G_2}), \\ &\geq \frac{1}{16}(2 - \frac{1}{\sqrt{G_1}\sqrt{G_2}})^2. \end{aligned} \tag{2.80}$$

Now we can observe, in the limit of high gain, what Eq. (2.80) implies: for $G_1 = G_2 \gg 1$ the uncertainty product (2.80) will be greater or equal to $1/4$ which is to be compared with the original uncertainty product in the quadrature components of the incoming field $\langle \Delta X_1^2 \rangle \langle \Delta X_2^2 \rangle \geq 1/16$. The equality is true when two requirements are fulfilled: the input is a minimum uncertainty state and

$$\frac{\langle \Delta F_i^2 \rangle}{G_i} = \langle \Delta X_i^2 \rangle$$

where $i = 1, 2$. In such a case, it can be shown that the noise added by the amplifier to both quadratures of the signal is exactly half a quantum of noise, $A_N = \frac{1}{2}$ where A_N is the added noise number (figure 2.7a). Some authors prefer to specify the added noise as a noise temperature. In most cases, the noise temperature is defined as

$$T_N = \frac{A_N \hbar \omega}{k_B}.$$

Now the general case for a finite gain depends on whether the amplifier is phase-preserving ($\sqrt{G_1} = \sqrt{G_2} = \sqrt{G}$) or a phase conjugating ($\sqrt{G_1} = \sqrt{G} = -\sqrt{G_2}$) amplifier. The fundamental theorem is

$$A_N = \frac{\langle \Delta F_1^2 \rangle}{G_i} + \frac{\langle \Delta F_2^2 \rangle}{G_i} \geq \frac{1}{2}|1 \mp \frac{1}{G}| \tag{2.81}$$

where the upper (lower) sign holds for phase-preserving (phase-conjugating) amplifiers [2].

Haus-Caves theorem is just a consequence of a more general quantum-mechanical uncertainty relationship for the simultaneous measurement of two conjugate variables: the uncertainty product of two simultaneously measured conjugate observables is a factor of 2 larger than that dictated by the Heisenberg uncertainty principle [4, 27]. One explanation for this is that the additional noise must be introduced so that these 2 observables measured simultaneously commute; what I mean by this statement can be better described if we calculate the commutation relation of the normalized output fields in Eq. (2.79):

$$[X_{1,eff}, X_{2,eff}] = \frac{i}{2}\frac{1}{\sqrt{G1}\sqrt{G2}}$$

where we can observe that in the limit of $|\sqrt{G1}\sqrt{G2}| \gg 1$, the two normalized output signal operators will commute: after large enough amplification, the quantum signals X_1 and X_2 get to a "classical power level", where simultaneous measurements can be performed with no additional introduction of uncertainty. The quantum bounds on the simultaneous measurement of the input modes are not violated due to the noise apparently added at the amplifiers input [27].

The simplest realization of a linear phase insensitive amplifier is a nondegenerate parametric amplifier [28]. An example of such consists of three resonant modes coupled together by nonlinear elements. The three modes are called the pump, the signal and the idler. I will not discuss all the details of nondegenerate parametric amplifier but only the transformation it does on the input idler and signal modes, ignoring the fact that the pump mode is the one that does the necessary work to do the amplification.

A nondegenerate parametric amplifier performs the following transformation of

the input modes [2]:

$$\begin{pmatrix} b_s \\ b_i^\dagger \end{pmatrix} = \begin{pmatrix} \cosh r & \sinh r \\ \sinh r & \cosh r \end{pmatrix} \begin{pmatrix} a_s \\ a_i^\dagger \end{pmatrix} \tag{2.82}$$

where s stands for signal mode, i for idler mode, and r is a real constant that determines the gain of the amplifier.[6] The gain $\sqrt{G_1} = \sqrt{G_2} = \sqrt{G}$ is given by $\sqrt{G} = \cosh r$. In this case, the noise operator F_i from Eq. (2.75) is given by

$$\begin{aligned} F_1 &= \frac{\sinh r}{2}(a_i + a_i^\dagger) = X_{1,i} \sinh r, \\ F_2 &= -\frac{i \sinh r}{2}(a_i - a_i^\dagger) = X_{2,i} \sinh r. \end{aligned}$$

In this set of transformations, it is obvious that the added noise is introduced through the idler mode, and the minimum added noise will be given when this idler mode is in the vacuum state $\langle a_i^\dagger a_i \rangle = 0$. The added noise number is then given by

$$\begin{aligned} A_N &= \frac{1}{2}\frac{\sinh^2 r}{\cosh^2 r}, \\ &= \frac{1}{2}(1 - \frac{1}{G}), \end{aligned}$$

which is the Haus-Caves theorem, Eq. (2.81), for a phase preserving amplifier. In chapter 7 we will use the nondegenerate parametric amplifier to model the inefficiencies associated with any linear amplifier, including those whose added noise is larger than vacuum noise.

2.4.2 Phase sensitive amplifier

A phase sensitive amplifier is one in which the output depends in an essential way on the phase of the signal at its input. Consider Eqs. (2.75), in the special case of a phase sensitive amplifier with $G_1 G_2 = 1$. The output modes Y_1 and Y_2 will satisfy the commutation relation without the need of the operators F_1 and F_2 responsible

[6] The most generic transformation done by a nondegenerate parametric amplifier would include the possibility of complex amplitude gains in the transformation matrix of Eq. 2.82. However, this would not change any of our conclusions.

of the added amplifier noise. In this case, X_1 is amplified with no added noise and can be measured as a classical signal after the amplification process obtaining all the information stored in this quadrature. However, X_2 is deamplified, therefore losing all the information in that other quadrature. This is necessary in order not to violate the quantum limit on the simultaneous measurement of two conjugate variables [4, 27].

One example of such a noiseless amplifier is a degenerate parametric amplifier (DPA), an example that will occupy us during most of the rest of this thesis. For now I just give a taste of the transformation that a DPA imposes on the input mode, regardless of the way we are implementing it (that will be described in the next chapter). The generic scattering matrix for a lossless degenerate parametric amplifier is given by [2, 8]

$$\begin{pmatrix} b_s \\ b_s^\dagger \end{pmatrix} = \begin{pmatrix} \mathcal{G} & \mathcal{M} \\ \mathcal{M}^* & \mathcal{G}^* \end{pmatrix} \begin{pmatrix} a_s \\ a_s^\dagger \end{pmatrix} \tag{2.83}$$

where b_s is the signal output mode and a_s is the signal input mode. In order to maintain the commutation relations $[a_s, a_s^\dagger] = [b_s, b_s^\dagger] = 1$, and $[a_s, a_s] = [b_s, b_s] = 0$, we require that

$$|\mathcal{G}|^2 - |\mathcal{M}|^2 = 1.$$

For simplicity, and without loss of generality, call $\mathcal{G} = \sqrt{G}$, and therefore $\mathcal{M} = \sqrt{G-1}$. The resulting gains for both quadratures is then given by

$$\begin{aligned} Y_1 &= (\sqrt{G} + \sqrt{G-1})X_1 = \sqrt{G_1}X_1, \\ Y_2 &= (\sqrt{G} - \sqrt{G-1})X_2 = \sqrt{G_2}X_2. \end{aligned} \tag{2.84}$$

The two gains satisfy the condition $G_1 G_2 = 1$ and therefore there is no additional noise term in the output quadratures: the quadrature X_1 is amplified but X_2 is deamplified, as shown in figure 2.7b. In addition, for a gain larger than unity the fluctuations of the output quadrature Y_2 will have less fluctuations than vacuum fluctuations

$$\langle \Delta Y_2^2 \rangle < \frac{1}{4}$$

Quantum states for which this condition is fulfilled are called (quadrature) squeezed states.

2.4.3 Quadrature squeezing

For the two quadrature operator X_1 and X_2 of a system, i.e. SHO, that satisfy the commutation relation Eq. (2.76), it follows that

$$\langle \Delta X_1^2 \rangle \langle \Delta X_2^2 \rangle \geq \frac{1}{16}. \tag{2.85}$$

A state of that system is said to be squeezed if for either of the quadratures operators

$$\langle \Delta X_i^2 \rangle \leq \frac{1}{4}.$$

Obviously, because of Eq. (2.85), we cannot have both variances being squeezed. Those states for which one of the quadratures is squeezed and the equality in Eq. (2.85) holds are called ideal squeezed states. States for which one of the conditions holds will have less "noise" in one of the quadratures than for a coherent state or a vacuum state, with the requirement that the fluctuations in the other quadrature must be enhanced in order not to violate the uncertainty relation.

It is sometimes convenient to define a generic quadrature operator

$$X(\theta) = \frac{1}{2}(ae^{-i\theta} + a^\dagger e^{i\theta}) \tag{2.86}$$

where $X_1 = X(0)$ and $X_2 = X(\pi/2)$. We characterize the squeezing by introducing the parameter $\xi(\theta)$

$$\xi(\theta) = \frac{\langle \Delta X(\theta)^2 \rangle}{1/4}. \tag{2.87}$$

Squeezing exists for some θ whenever $0 \leq \xi < 1$.

Most schemes for generation of quadratures squeezed light are based on some sort of parametric process using various types of nonlinear devices. A degenerate parametric amplifier can be used for this process of squeezing. Without loss of generality, consider

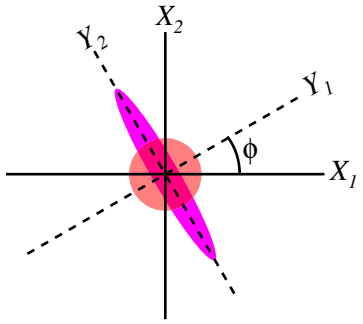

Figure 2.8: Schematic of the noise in the quadrature variable space for a vacuum state (circle) and a squeezed state (ellipse) for $r = 1$. The squeezed state is rotated by an angle ϕ according to Eqs. (2.88-2.89). The quadrature axes Y_i are defined according to Eq. (2.86), $Y_1 = X(\phi)$ and $Y_2 = X(\phi + \pi/2)$.

the DPA described in the previous section with $\mathcal{G} = \cosh r$ and $\mathcal{M} = -e^{i\phi} \sinh r$, where ϕ defines the axis where the squeezing happens. In this case, $b = a \cosh r - a^\dagger e^{i2\phi} \cosh r$ and we obtain

$$\begin{aligned} \langle \Delta X_1^2 \rangle &= \frac{1}{4}(\cosh^2 r + \sinh^2 r - 2 \sinh r \cosh r \cos 2\phi), \qquad (2.88) \\ \langle \Delta X_1^2 \rangle|_{\phi=0} &= \frac{1}{4} e^{-2r}, \\ \langle \Delta X_2^2 \rangle &= \frac{1}{4}(\cosh^2 r + \sinh^2 r + 2 \sinh r \cosh r \cos 2\phi), \qquad (2.89) \\ \langle \Delta X_2^2 \rangle|_{\phi=0} &= \frac{1}{4} e^{2r}, \end{aligned}$$

where for $\phi = 0$ evidently squeezing exists in the X_1 quadrature. For $\phi = \pi/2$, the squeezing appears in the X_2 quadrature. In general, for an arbitrary angle ϕ, the squeezing will appear along the x-axis of a frame rotated by an angle ϕ. A representation of the squeezed vacuum state where the fluctuations in one of the quadratures is reduced is shown in figure 2.8. The states generated by the parametric process of a lossless DPA are ideal squeezed states. However, in general, squeezed states do not need to equalize the uncertainty relation (2.85).

Chapter 3

Theory of Josephson parametric amplifiers

In this chapter I introduce a generic form of the Josephson parametric amplifier. I start by discussing the driven Duffing oscillator. I will then give a brief description of the nonlinear circuit element we will use to create our parametric amplifier: the Josephson junction. Finally, I will discuss the Josephson non-linear oscillator in an electric circuits language, and its behavior as an amplifier, including the necessary conditions that it must fulfill in order to be a useful parametric amplifier. In this last section I will describe how the analysis of the Josephson parametric amplifier can be discussed using IOT and discuss the equivalence of both approaches, IOT and circuit theory. I will then derive expressions for the gains of the JPA, showing how it satisfies the condition for a degenerate parametric amplifier, Eq. (2.83). I will discuss some technical aspects of the amplifier, such as bandwidth and added noise, as well as squeezing of the internal and output modes.

3.1 Non-linear driven oscillators (Duffing oscillator)

The nonlinear system we will be studying is the Duffing oscillator:

$$\ddot{x} + 2\gamma\dot{x} + \omega_0^2 x + \beta x^3 = F\cos(\omega t). \tag{3.1}$$

In mechanical terms, the left hand side (lhs) of the Duffing equation can be thought of as a damped nonlinear spring; a hard spring for $\beta > 0$ and a soft spring for $\beta < 0$.

In the next section, I will show that the Josephson non-linear oscillator is equivalent to a soft spring Duffing oscillator, consequently I will assume $\beta < 0$ in the rest of the chapter. In a typical problem of forced oscillations in a linear RLC circuit like the one studied in chapter 2 (Duffing equation with $\beta = 0$), the standard approach used to find the solution of the EOM is to assume that enough time has passed so that we can ignore the transient solution and seek the steady state periodic solution vibrating at the same frequency ω as that of the driving force. A nonlinear oscillator can respond in many additional ways that are not possible for a linear system. Nevertheless, we begin our study of forced duffing oscillator with a similar approach to that of the linear oscillator by seeking the harmonic solution which has the same frequency as the driving term.

In order to obtain the approximate analytic form for the harmonic solution, we will used the "iteration method" [29]. We write the Duffing equation in the following form:

$$\ddot{x} = -2\gamma\dot{x} - \omega_0^2 x - \beta x^3 + F\cos(\omega t) \tag{3.2}$$

and assume that to lowest (zeroth) order, the solution is given by $x_0 = A\cos(\omega t + \phi)$ and substitute it in the rhs of equation 3.2. Then we integrate the resulting equation generating a first order solution $x_1(t)$ which should represent a better approximation of $x(t)$ provided β satisfies certain conditions.[1] The iteration procedure can be then repeated until a sufficiently accurate solution for x has been achieved (after n of such iterations, the solution $x(t) \simeq x_n(t)$).

Now to keep the analysis simple, I will temporarily set the damping coefficient γ equal to zero.

$$\ddot{x} = -\omega_0^2 x - \beta x^3 + F\cos(\omega t). \tag{3.3}$$

Since there is no loss, the response is expected to be either in phase or 180°, so I can

[1] The integration constants that result from the integration of the rhs are set equal to zero in order to avoid the appearance of secular terms which would spoil the periodicity of our desired solution [29].

safely assume that $x_0 = A\cos(\omega t)$. From Eq. (3.3), we obtain

$$\ddot{x_1} = -\left(\omega_0^2 A + \frac{3}{4}\beta A^3 - F\right)\cos(\omega t) - \frac{1}{4}\beta A^3 \cos(3\omega t).$$

This equation is easily integrated twice from which we obtain

$$x_1(t) = A_1 \cos(\omega t) + \frac{1}{36}\frac{\beta A^3}{\omega^2}\cos(3\omega t) \tag{3.4}$$

where

$$A_1 \equiv \frac{1}{\omega^2}(\omega_0^2 A + \frac{3}{4}\beta A^3 - F).$$

Now, $x_2(t)$ can be derived from $x_1(t)$ and so on. I won't derive this long series, but rather argue that for small nonzero β, if $x_0(t) = A\cos(\omega t)$ is a reasonable zeroth order approximation, then the coefficient A_1 in $x_1(t)$ should differ very little from A, so we set $A = A_1$, and A now is solved from the following expression,

$$\left(\omega_0^2 - \omega^2 + \frac{3\beta}{4}A^2\right) A = F.$$

Then Eq. 3.4 reduces to

$$x_1(t) \approx A\cos(\omega t) + \frac{1}{36}\frac{\beta A^3}{\omega_0^2 + \frac{3}{4}\beta A^2 - \frac{F}{A}}\cos(3\omega t).$$

The condition that the zeroth order solution is close to the full solution is equivalent to saying that the harmonic term in Eq. 3.4 is much larger than the third harmonic term. This can be expressed as a restriction on the size of β,

$$\frac{\beta A^2}{36\omega^2} \ll 1. \tag{3.5}$$

I will return to this restriction when discussing about the requirements on the size of the non-linearity required for a good parametric amplifier.[2]

I will now relax the assumption that $\gamma = 0$. Just like in the driven damped simple harmonic oscillator, when damping is included the displacement and the driving force

[2] The actual expression for the third-harmonic correction is slightly different [30]. In order to obtain it, we just need to do the next iteration keeping both the harmonic ω term and the next 3ω term. However, for our purposes $\beta A^2/36\omega^2$ is close enough and gives us a good order of magnitude restriction on β.

will be out of phase, with an angle between 0 and 180°. The approximate series solution is similar to the lossless case, only adding the possibility of a phase shift between the response and the drive. However, in order to make the derivation simpler we fix the phase of the response and leave the phase of the driving force to be determined:

$$\begin{aligned} \ddot{x_1} &= -2\gamma\dot{x_0} - \omega_0^2 x_0 - \beta x_0^3 + F\cos(\omega t + \phi), \\ &= -2\gamma\dot{x_0} - \omega_0^2 x_0 - \beta x_0^3 + H\cos(\omega t) - G\sin(\omega t), \end{aligned}$$

with $x_0(t) = A\cos(\omega t)$. Again integrating the rhs yields

$$x_1(t) = A_1\cos(\omega t) + B_1\sin(\omega t) + \frac{1}{36}\frac{\beta A^3}{\omega^2}\cos(3\omega t)$$

with

$$\begin{aligned} A_1 &\equiv \frac{1}{\omega^2}(\omega_0^2 + \frac{3}{4}\beta A^3 - H), \\ B_1 &\equiv -\frac{1}{\omega^2}(2\gamma\omega A - G). \end{aligned}$$

If the zeroth order solution is a reasonable starting point, then $A_1 \simeq A$ and $B_1 = 0$. We can solve for H and G, and remembering that $F^2 = G^2 + H^2$, to this order, we can derive an expression that relates the amplitude A to the driving force F and the phase ϕ:

$$\tan(\phi) = \frac{G}{H} = \frac{2\gamma\omega}{(\omega_0^2 - \omega^2) + \frac{3}{4}\beta A^2}, \tag{3.6}$$

$$F^2 = \left((\omega_0^2 - \omega^2)A + \frac{3}{4}\beta A^3\right)^2 + (2\gamma\omega A)^2. \tag{3.7}$$

We plot the solution for the amplitude and phases given by Eq. (3.7) and (3.6) in figure 3.1. The nonlinear resonance curves look similar to those corresponding to linear resonance curves. For a small drive, the response curve is the familiar Lorentzian response of the simple harmonic oscillator. For large drives, the resonance curves tilt to the left; this is equivalent to saying that the nonlinearity has made the resonance of the system depend on the amplitude of the internal field A. In the high-Q limit

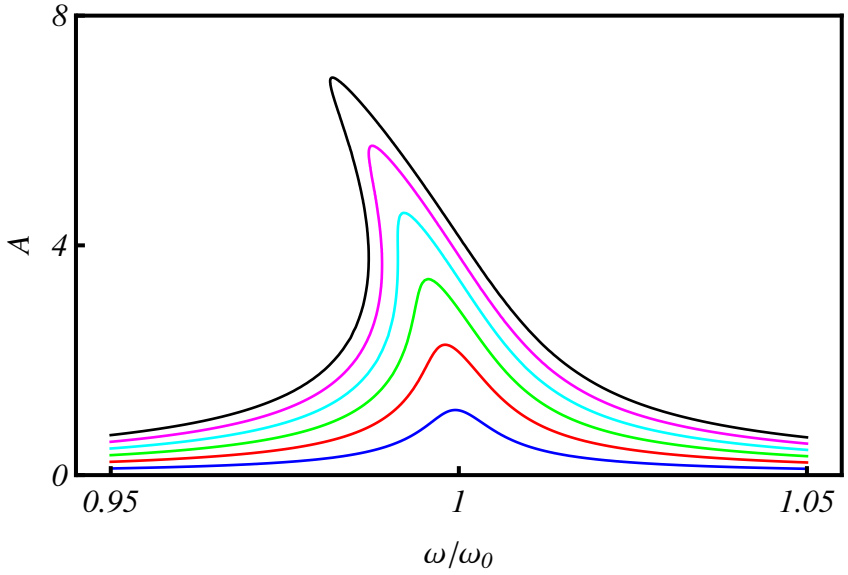

Figure 3.1: First order nonlinear response curves of a duffing oscillator with finite damping for 6 different driving forces. The nonlinear resonator variables are $Q = 100$, $\beta = -0.001$, and the driving forces are equally spaced between $0.25F_c$ and $1.5F_c$. The resonance curves bend over as the drive amplitude is increased and become multi-valued for certain drive amplitudes.

$(Q = \omega_0/2\gamma)$,[3] the following approximations can be made: $\omega_0 + \omega \approx 2\omega_0$ and $\omega/\omega_0 \approx 1$. These are equivalent to the "slowly varying envelope approximation" explained in section 2.3.2. Eqs. (3.6) and (3.7) reduce to

$$\tan(\phi) = \frac{2\gamma\omega_0}{2\omega_0(\omega_0 - \omega) + \frac{3}{4}\beta A^2}, \tag{3.8}$$

$$F^2 = \left([2\omega_0(\omega_0 - \omega) + \frac{3}{4}\beta A^2]^2 + (2\gamma\omega_0)^2 \right) A^2. \tag{3.9}$$

I can verify that the analysis of the duffing oscillator is reasonable by setting the non-linearity parameter to zero in Eq. (3.9). With $\beta = 0$, the expression obtained for A^2 is the familiar Lorentzian response of a high-Q SHO with a resonance frequency ω_0 and a linewidth (HFHM) of γ. In the case of $\beta \neq 0$, we can define the resonance frequency as

[3] In the previous chapter, the quality factor was represented by $\mathcal{Q}$, in order to avoid confusion with the charge variable Q. However, since that will not be a problem here, I will go back to the usual convention of representing the quality factor with the variable Q.

the maximum of the response curve ($dA/d\omega = 0$). This condition yields

$$\omega_0 - \omega + \frac{3\beta}{4\omega_0}\frac{A^2}{2} = 0 \tag{3.10}$$

that is, the peak of the resonance curve is shifted by an amount given by $3\beta A^2/8\omega$. Note also that for a drive above a critical force value F_c, curves shown in figure 3.1 have two points at which the slope $dA/d\omega$ is infinite. It can also been shown that the region lying between these two points is unstable while the regions outside these two points correspond to stable solution (Fig. 3.2). This behavior leads to bistability. When we operate our parametric amplifier, we will operate below the critical point[4] so I will not treat the region of bistability. References [18, 29, 31] and references therein treat the bistable region.

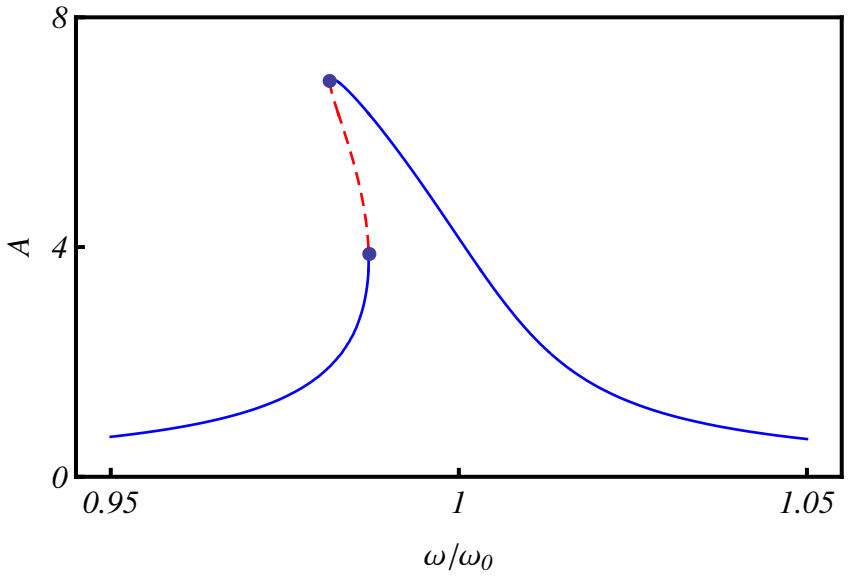

Figure 3.2: Nonlinear response for a duffing oscillator and a driving force $F = 1.5F_c$ such that for certain pump frequencies the response is multi-valued. The red-dashed section represents the unstable solution of the resonator. The dots represent the points where the slope $dA/d\omega$ is infinite.

[4] Large parametric gain is achieved close to the points where the slope $dA/d\omega = \infty$, but in order to remain stable we need to operate below the critical point with the parameters drive frequency and power chosen so the Duffing curve does not have a bistable region.

We can estimate the critical drive by looking for the points that satisfy

$$d\omega/dA = 0. \tag{3.11}$$

This would give me the two points of instability shown in figure 3.2. In addition, we need $d^2\omega/dA^2 = 0$ for the two points of instability to coincide. When these two conditions are satisfied, it is straightforward to derive the following expressions for the critical drive, critical amplitude and critical frequency detuning:

$$\omega_c = \omega_0 - \sqrt{3}\gamma, \tag{3.12}$$

$$F_c^2 = \frac{256\gamma^3}{9\sqrt{3}}\frac{\omega_0^3}{|\beta|}, \tag{3.13}$$

$$A_c^2 = \frac{16\gamma}{3\sqrt{3}}\frac{\omega_0}{|\beta|}. \tag{3.14}$$

So far I have discussed the response of a nonlinear duffing oscillator without discussing the origin of the nonlinearity. In the next section I will describe the way we create our nonlinear resonators.

3.2 General theory of Josephson junctions

As described in the previous section, in order to create a parametric amplifier we need a non-linear element embedded in an electrical resonator. This nonlinear element will provide the coupling between the two normal modes of the resonator. In this section I explain the nonlinear circuit element we will use: the Josephson junction [32].

3.2.1 Simple junction theory

The Josephson junction is made out of two superconducting electrodes separated by a thin insulating barrier (Fig. 3.3a). In a superconducting metal, the electrons bind together forming a bosonic condensate of Cooper pairs whose behavior is described by a single wave function $\Psi(r) = |\Psi(r)|e^{i\varphi(r)}$. Due to the small thickness of the insulating barrier, both wave functions of the superconducting electrodes can overlap, allowing

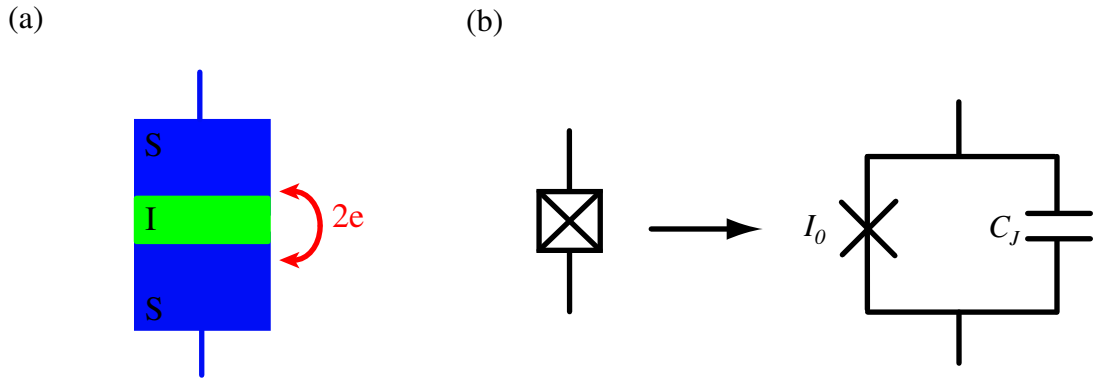

Figure 3.3: (a)A Josephson junction consists of two superconducting leads separated by an insulator layer. Cooper pairs can tunnel through the barrier, generating a dissipationless supercurrent. (b) Circuit element that represents a Josephson junction. In general, a Josephson junction is pictured as a tunneling element and a capacitor in parallel. This means that the Josephson junction has an intrinsic resonance frequency, called the plasma frequency. This plasma frequency is usually in the tens of Gigahertz, so for our purposes, this extra resonance will be neglected in the analysis.

the tunneling of Cooper pairs. The constitutive relations that describe the current of Cooper pairs across the barrier are

$$I(t) = I_0 \sin(\delta(t)), \tag{3.15}$$

$$\delta(t) = \frac{1}{\varphi_0}\int_{-\infty}^{t} dt' V(t'), \tag{3.16}$$

where I is the current, V the voltage and $\delta = \varphi_2 - \varphi_1$ the gauge-invariant phase difference[5] across the junction. In these expressions $\varphi_0 = \hbar/2e$ is the reduced flux quantum, and I_0 is the junction critical current which gives the maximum current that the junction can support in its superconducting state. At zero magnetic field, the critical current is given by the Ambegaokar-Baratoff relation

$$I_0 = \frac{\pi\Delta(T)}{2eR_n}\tanh(\frac{\Delta(T)}{2k_BT}) \tag{3.17}$$

[5] The concept of generalized flux quanta that was introduced in the previous chapter in Eq. (2.18) is closely related to the condensate phase φ at a given node of a superconducting circuit. The two quantities satisfy the relation

$$\varphi = \phi \bmod 2\pi.$$

For more details on the definition of the generalized flux and its relation to the superconducting phase φ for superconduction circuits, see Ref. [12].

where $\Delta(T)$ is the superconducting gap of the material used for the electrodes and R_n is the normal state resistance of the junction. We operate at temperatures much smaller than the superconducting critical temperature, so we use the $T = 0$ limit of Eq. (3.17), $I_0 = \pi\Delta/2eR_N$.

Now let's consider the Josephson junction effective impedance. There is some ambiguity on the definition of the Josephson junction inductance L_J. We start with $V = \varphi_0 d\delta/dt$ and $I(t) = I_0 \sin(\delta)$. Solving for I in terms of the gauge-invariant phase difference δ, the voltage can be expressed as

$$V = \frac{d}{dt}\left(\varphi_0 \arcsin(I(t)/I_0)\right). \tag{3.18}$$

Here is where the two different definitions in the usual literature appear. If we define the total Josephson inductance L_J as the ratio between the flux $\Phi_J(t) = \varphi_0\delta$ and the current $I(t)$, $L_J \equiv \Phi_J(t)/I(t)$, as done in Refs. [8, 33, 34], we obtain

$$L_J = L_{J0}\frac{\arcsin(I/I_0)}{I/I_0} \tag{3.19}$$

with

$$L_{J0} = \varphi_0/I_0. \tag{3.20}$$

On the other hand, we could perform the differentiation in Eq. (3.18), which leads us to

$$\begin{aligned} V &= \frac{\varphi_0/I_0}{\sqrt{1-(I/I_0)^2}}\frac{dI}{dt}, \\ &= \frac{L_{J0}}{\cos(\delta)}\frac{dI}{dt}, \\ &= L'_J\frac{dI}{dt}, \end{aligned}$$

where the other definition for the Josephson inductance

$$L'_J = \frac{L_{J0}}{\cos(\delta)} \tag{3.21}$$

is then the ratio of the V and dI/dt. Either definition can be used as long as the meaning is understood. In a sense, the definition of L'_J can be considered the effective differential

inductance. Depending on the context one definition or the other can be more useful. For example if I wanted to know the effective impedance of the Josephson junction when probed with a small rf tone, L'_J would be more useful. However, to calculate the flux Φ across a junction, L_J is more convenient.

I will now make a few remarks about the energy associated with the Josephson junction [35]. Consider a Josephson junction connected to a current source. The energy change due to the work done by the current generator is given by $dE = I(t)V(t)dt$, where I is the current imparted by the source and V is the voltage across the junction. Using Eq. (3.18), the total energy associated with a biased Josephson junction is given by:

$$\begin{aligned} E &= \int I(t)\frac{d}{dt}\left(\varphi_0 \arcsin(I(t)/I_0)\right) dt, \\ &= -E_J \cos(\delta(t)) + \text{constant} \end{aligned} \tag{3.22}$$

where in the second line I have used Eqs. (3.15) and (3.16), and

$$E_J = \varphi_0 I_0. \tag{3.23}$$

The constant of integration is usually ignored as it does not influence the dynamic of the junction.

3.2.2 dc-SQUID

A dc-SQUID (**S**uperconducting **Qu**antum **I**nterference **D**evice)) is created by combining two Josephson junctions in parallel, as shown in figure 3.4. When a magnetic field is applied on the SQUID, the maximum supercurrent through the SQUID shows a periodic behavior. We now explain that behavior. The total current I though the SQUID is the sum of the current though both branches, and using Eq. (3.15) this is equal to

$$I = I_{01}\sin(\delta_1) + I_{02}\sin(\delta_2). \tag{3.24}$$

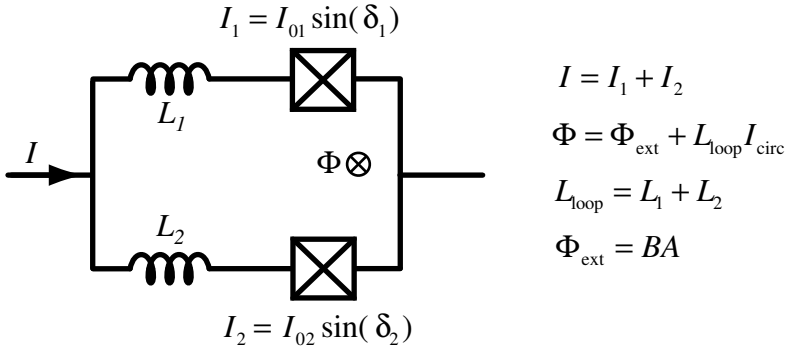

Figure 3.4: A SQUID is formed by two Josephson junctions embedded in a superconducting wire loop. This loop has an area of A and an intrinsic inductance given by $L_{\text{loop}} = L_1 + L_2$. A magnetic field perpendicular to the loop of magnitude B is applied. The total flux Φ in the SQUID loop consist of the self-induced and applied flux.

Due to the fact that the total magnetic flux though a superconducting loop must be quantized, the relation between the gauge-invariant phase differences of each junction is

$$\delta_2 - \delta_1 = 2\pi n + 2\pi\frac{\Phi}{\Phi_0}. \tag{3.25}$$

Eqs. (3.24) and (3.25) can be simplified if some assumptions are made regarding the critical currents of the Josephson junctions and the loop inductance.

Let's consider first a SQUID that has asymmetric junctions

$$I = I_{01}\sin(\delta_1) + I_{02}\sin(\delta_1 - 2\pi\frac{\Phi}{\Phi_0}). \tag{3.26}$$

The analysis is greatly simplified in the case when the loop inductance is negligible. In that case, the flux threading the SQUID loop only comes from the field Φ_{ext} applied ($\Phi = \Phi_{\text{ext}}$). At a given Φ_{ext}, the maximum current, and therefore the equivalent critical current of the SQUID I_0^S is found by maximizing Eq. (3.26) with respect to δ_1. This yields

$$I_0^S = \sqrt{I_{01}^2 + I_{02}^2 + 2I_{01}I_{02}\cos\left(\frac{2\pi\Phi_{\text{ext}}}{\Phi_0}\right)}. \tag{3.27}$$

If the two junctions have identical critical currents, $I_{01} = I_{02} = I_0$, Eq. 3.27 reduces to

$$I_0^S = 2I_0 \left|\cos\left(\frac{\pi\Phi}{\Phi_0}\right)\right|. \tag{3.28}$$

The dependance of the SQUID critical current with magnetic field is shown in figure 3.5. From expressions (3.27) and (3.28), we see that the SQUID will behave as a junction with tunable current. In the case of a SQUID with asymmetric junctions, the only difference is that the modulation of the current is not as deep as in the symmetric-junctions case. The effective SQUID inductance is just given by Eq. (3.19) with I_0 replaced by I_0^S.

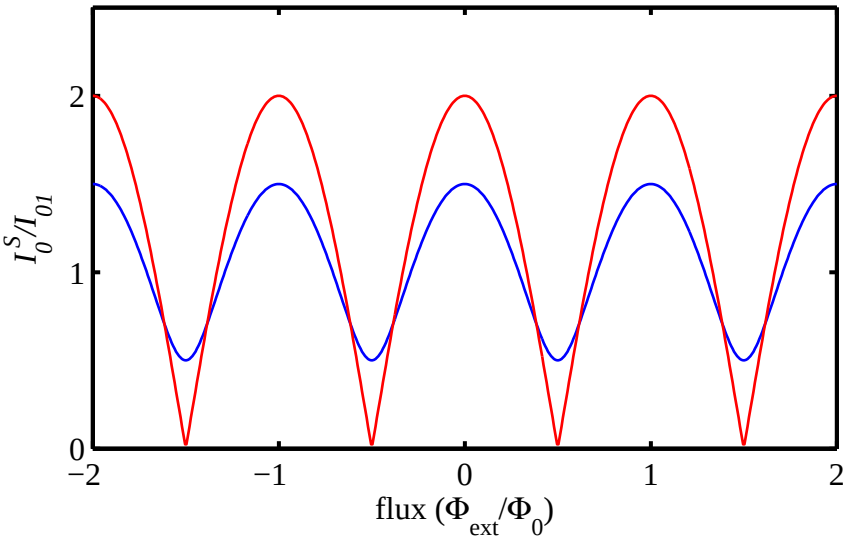

Figure 3.5: Flux dependance of the critical current of a SQUID for the case of negligible loop inductance. The two traces shown for the case of $I_{01} = I_{02}$ (red) and $I_{01} = 2I_{02}$ (blue).

When we include the loop inductance, it turns out that solving exactly for the flux dependance of the maximum current I_0^S is not possible. It must be found numerically. For simplicity, let's assume that $I_{01} = I_{02} = I_0$, and the loop inductance L_{loop} is symmetrically divided in the loop ($L_1 = L_2 = L_{\text{loop}}/2$). If the current divides equally in the loop, there is no circulating current and the fluxes created by both current will cancel. In the general case when this does not happen, $I_1 \neq I_2$, we can define a

circulating current given

$$I_{\text{circ}} = \frac{1}{2}(I_2 - I_1).$$

This current produces a flux given by $\Phi_L = L_{\text{loop}} I_{\text{circ}}$. The total flux in the loop is the sum of the applied flux and the self-induced flux:

$$\Phi = \Phi_{\text{ext}} + \frac{1}{2} L_{\text{loop}} I_0 \{\sin(\delta_2) - \sin(\delta_1)\}$$

The phase differences δ_1 and δ_2 are related by Eq. (3.25):

$$\delta_2 = \delta_1 - \frac{2\pi}{\Phi_0}[\Phi_{\text{ext}} + \frac{1}{2} L_{\text{loop}} I_0 \{\sin(\delta_2) - \sin(\delta_1)\}] \tag{3.29}$$

In order to obtain I_0^S, we need to solve Eq. (3.29) and (3.26) self-consistently, and maximizing with respect to δ_1. The flux dependance is shown in figure 3.6a. Again, the modulation of I_0^S is not complete. For small L_{loop}, the minimum critical current is approximately given by $I_{0,min}^S = \pi L_{\text{loop}} I_0 / \Phi_0$, as can be observed in figure 3.6b. When we include the loop inductance in the problem, it turns out that the nonlinear Josephson inductance is not exactly given by just Eq. 3.19 with I_0 just replaced by I_0^S, but for the parameters of our SQUIDs, it is a good approximation.

3.3 Josephson junction oscillator

Now that I have explained how a Josephson junction can be considered a nonlinear inductor, we can start analyzing the *RLC*-nonlinear resonator that includes a Josephson junction as the inductor. In this section I will first write the EOM that describes the system. I will approximate the non-linearity of the Josephson inductance to include only the first non-linear order; this approximation reduces the EOM of the *RLC*-nonlinear resonator to the duffing equation (3.1). Then I will analyze the system in a circuit theory language similar to the one used in section 2.3.1 following closely Refs. [18] and [31]. Before I calculate the gain performance of the amplifier, I will analyze the Josephson Duffing oscillator problem applying IOT (2.3.3) on a completely equivalent

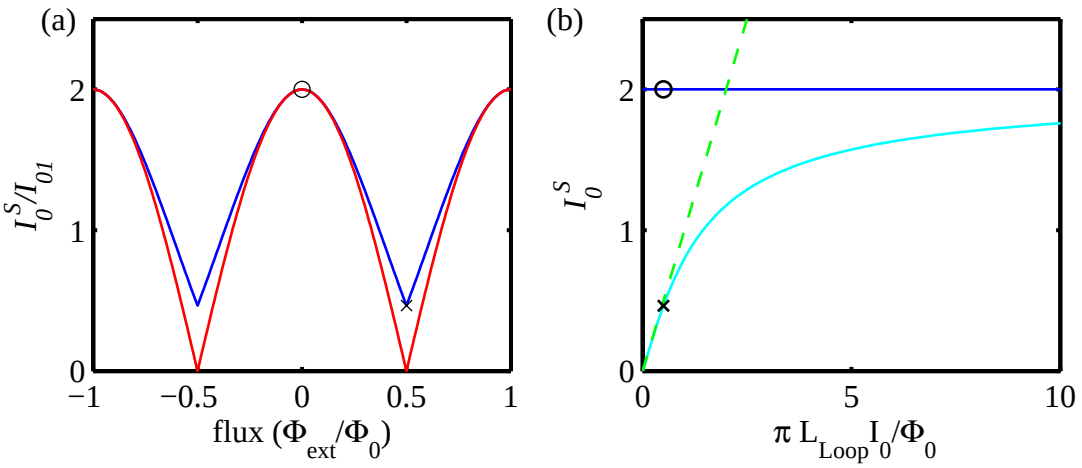

Figure 3.6: (a) Flux dependance of the critical current of a SQUID for the case of finite loop inductance ($\pi L_{\text{loop}} I_0/\Phi_0 = 0.5$) and junctions with the same critical current (blue). For comparison, the negligible loop inductance case is also plotted (red). (b) The minimum (cyan) and maximum (blue) SQUID critical currents as a function of loop inductance. The case shown in figure (a) are represented by a circle ($I^S_{0,\text{max}}$) and a cross ($I^S_{0,\text{min}}$). For small loop inductance, the minimum critical current is approximately a linear function of L_{loop} (green).

system of a cavity with a Kerr nonlinearity showing that both approaches are completely equivalent. I will then derive expressions for the gain of the amplifier, bandwidth and noise temperature. Finally I will discuss the requirements the resonator needs to fulfill in order to be a usable JPA.

3.3.1 Circuit theory of a driven Josephson junction in a RLC-resonator

The nonlinear Josephson oscillator is shown in figure 3.7a. The equation that describes its behavior is similar to Eq. (2.33) except that the current through the linear inductor is replaced by $I_J = \sin(\Phi/2\pi) = \sin(\delta)$, where I will be using $\delta = \Phi/\varphi_0$, the superconducting gauge-invariant phase across the junction as my generalized coordinate:

$$C\varphi_0 \frac{d^2\delta(t)}{dt^2} + I_0 \sin(\delta(t)) = I(z=0,t)$$

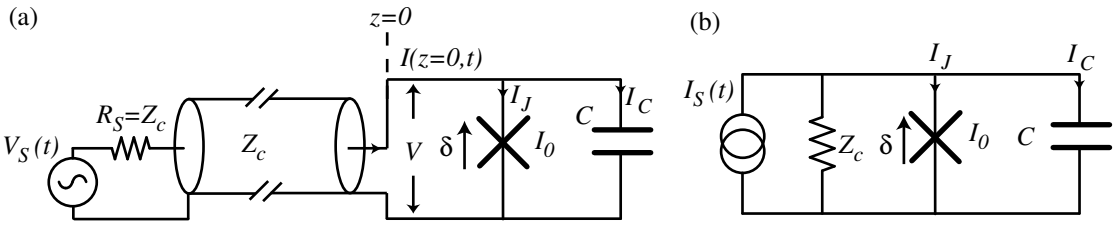

Figure 3.7: (a) Josephson junction with a critical current I_0 shunted by a capacitor C connected to a microwave source through a transmission line with an impedance Z_c. The microwave source has a source resistance $R_S = Z_c$. (b) Norton equivalent of the circuit shown in (a).

We can use the Norton equivalent of the circuit (Fig. 3.7b), which yields the following equation for a current source driving a non-linear RLC resonator:

$$C\varphi_0 \frac{d^2\delta(t)}{dt^2} + \frac{\varphi_0}{Z_c}\frac{d\delta(t)}{dt} + I_0 \sin(\delta(t)) = I_S(t). \tag{3.30}$$

where Z_c is the characteristic impedance of the transmission line, I_0 is the critical current of the junction and C is the total capacitance shunting the junction and $I_S(t)$ is the microwave power going into the resonator. It will consist of two components: a large pump and a small signal $I_S(t) = I_p(t) + i_s(t)$. We now approximate the $\sin(\delta)$ term by its first two component of the Taylor expansion.

$$\frac{d^2\delta(t)}{dt^2} + 2\gamma\frac{d\delta(t)}{dt} + \omega_0^2\left(\delta(t) - \frac{\delta^3(t)}{6}\right) - \omega_0^2\frac{I_p}{I_0}\cos(\omega_p t) = \frac{2}{C\varphi_0 Z_c}v_s^{in}(t) \tag{3.31}$$

where I have written the signal component in terms of the voltage waves coming into the resonator from the transmission line. From the point of view of microwave circuits, it is more convenient to use the incoming and outgoing modes, especially when I analyze the gain of the amplifier and quantize the noise coming in from the input port. The first task is to analyze the effect of the large pump on the circuit, so I will set $v_s = 0$. Eq. (3.31) is just the Duffing equation we studied in section 3.1, with $x \to \delta$ and $\beta \to -\omega_0^2/6$. Using the same procedure as shown in that section, we assume a zeroth order solution $\delta_p(t) = \delta_a \cos(\omega_p t - \phi)$ and solve of the amplitude δ_a for a given drive $F = \omega_0^2 I_p/I_0$.

This is shown in figure 3.8. As in the Duffing oscillator, the resonant response shifts to lower frequency as the pump amplitude is increase. Using expressions 3.12-3.14, I can write the equivalent critical expressions for the case of the Josephson resonator:

$$\omega_c = \omega_0 - \sqrt{3}\gamma, \tag{3.32}$$

$$I_{p,c}^2 = \frac{512\gamma^3}{3\sqrt{3}\omega_0^3} I_0^2 = \frac{64}{3\sqrt{3}Q^3} I_0^2, \tag{3.33}$$

$$\delta_{a,c}^2 = \frac{32\gamma}{\sqrt{3}\omega_0} = \frac{16}{\sqrt{3}Q}. \tag{3.34}$$

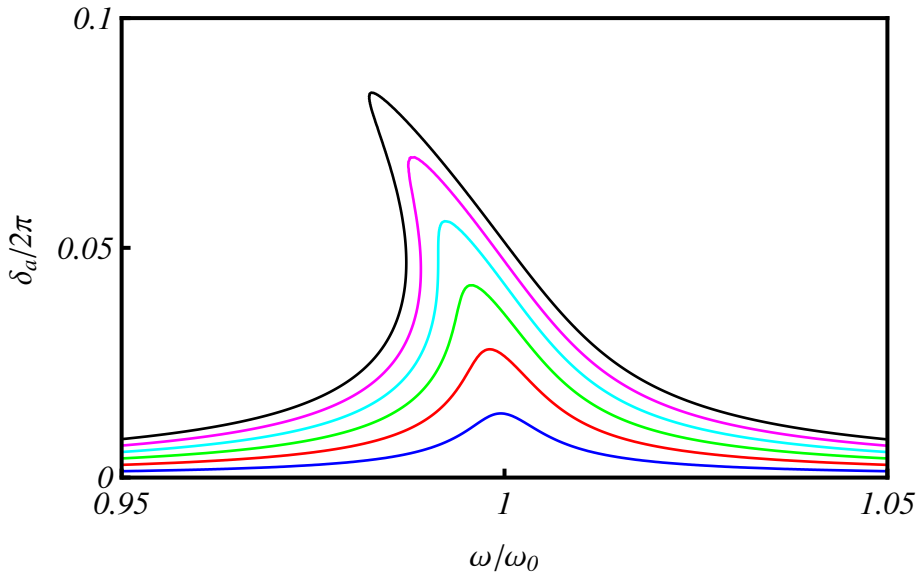

Figure 3.8: Frequency response of a driven Josephson oscillator as a function of pump detuning ω_p/ω_0 for multiple drive powers. The driving amplitudes of the incoming microwave pump are equally spaced between $0.25I_{p,c}$ and $1.5I_{p,c}$. The quality factor is $Q = 100$.

We incorporate the signal by treating it as a small perturbation around the solution of the pump (this is equivalent to making an undepleted pump approximation); that is, $\delta = \delta_p + \delta_s$, where δ_p is the internal field solution associated with the pump and is given by the zeroth order solution of the Duffing equation, and δ_s is the internal field associated with the small signal. Substituting the pump solution into Eq. (3.31) and retaining terms only to first order in δ_s, the following equation for the dynamics of δ_s

is obtained [18]:

$$\frac{d^2\delta_s(t)}{dt^2} + 2\gamma\frac{d\delta_s(t)}{dt} + \omega_1^2(\delta_a, t)\delta_s(t) = \frac{2}{C\varphi_0 Z_c}v_s^{in}(t) \tag{3.35}$$

where

$$\omega_1^2(\delta_a, t) \equiv \omega_0^2(1 - \frac{\delta_a^2}{4})\left(1 + \frac{\delta_a^2}{4(1-\delta_a^2/4)}\cos(2\omega_p - 2\phi)\right) \tag{3.36}$$

and ϕ is given by Eq. (3.6). Eq. (3.35) describes the dynamic of our small perturbation δ_s and consist of a parametrically driven oscillator [13,18,30,31,36], where the resonance frequency of the system $\omega(t) = \omega_0^2(1 + h\cos(\nu t))$ is a function of time ($h \ll 1$). It explains the origin of the parametric gain we will see in the signals coming in. For a parametric resonance to be the strongest, the frequency ν needs to be close to twice ω_0 [36]. This of course occurs naturally in our case if our pump is close to the resonance frequency of the oscillator $\omega_p \simeq \omega_0 + \delta\omega$ where the detuning $\delta\omega$ is of the order of the resonator linewidth γ.

3.3.2 Parametric processes in the Josephson junction oscillator

We are now ready to start the derivation of the expressions that describe the amplifier performance of the JPA. In the following paragraphs, we will see that when a signal is applied at a frequency ω_s, an additional tone will be created at a frequency $\omega_i = 2\omega_p - \omega_s$, called the image tone. The creation of this extra tone is a consequence of the coupling between normal modes in a parametrically driven oscillator. Because our pump is at a frequency close to our signal tone, the mode of operation of our JPA is sometimes called four-wave or four-photon mixing [8] since four photons are involved: one at ω_s, one at ω_i and two photons of the pump at ω_p. Another mode called the three-wave or three-photon mixing also exists where $\omega_s + \omega_i = \omega_p$. This requires the energy of the non-linear element to have at least some odd symmetry in the pump current. This could be achieved if we were to apply a dc-current to the Josephson junction [8,37]. As we did not operate our amplifiers in this mode, I will not discuss this case.

The solution for Eq. (3.35) is easily found in the frequency domain. We define for our internal field

$$\delta_s(t) = \int_0^\infty \frac{d\omega}{2\pi}\delta_s(\omega)e^{-i\omega t} + \text{H.c.}$$

Taking the fourier transform of Eq. (3.35) and using the convolution theorem yields:

$$(\omega_0^2(1-\epsilon) - \omega^2 - i2\gamma\omega)\delta_s(\omega) - \frac{\omega_0^2\epsilon}{2}e^{2i\phi}\delta_s^\dagger(2\omega_p - \omega) = \frac{4\gamma\sqrt{Z_c}}{\varphi_0}\sqrt{\frac{\hbar\omega}{2}}a_{\text{in}}(\omega) \qquad (3.37)$$

where I have used Eq. (2.39) for the input signal $v_s(t)$ and defined $\epsilon = \delta_a^2/4$. In deriving equation (3.37), I have used the rotating wave approximation in order to ignore terms whose frequency is close to $3\omega_0$. Before we move on, I will make the same high-Q approximation, which essentially is equivalent to the "slowly varying envelope" approximation described in section 2.3.2 ($\omega_p + \omega \approx 2\omega_p, \omega/\omega_0 \approx 1$). I will also define the internal $c(\omega')$ and incoming $c_{\text{in}}(\omega')$ mode operators in the rotation frame of the pump $\delta(\omega_p + \omega') = \sqrt{\hbar\omega_0}2E_J c(\omega')$ and $a_{\text{in}}(\omega_p + \omega') = c_{\text{in}}(\omega')$. In order to make notation simpler, I will drop the prime symbol from the ω variable, but note that from now on, ω represents a fourier frequency offset from the pump frequency ω_p. Eq. (3.37) reduces to

$$\left(\omega_0 - \omega_p - \omega - \frac{\omega_0\epsilon}{2} - i\gamma\right)c(\omega) - \frac{\omega_0\epsilon}{4}e^{-2i\phi}c^\dagger(-\omega) = \sqrt{2\gamma}c_{\text{in}}(\omega). \qquad (3.38)$$

Eq. (3.38) has a very important feature mentioned in the previous chapter: the pump of this parametric driven system will actively couple the two normal modes $c(\omega)$ and $c^\dagger(-\omega)$ [13]. We can now solve for the internal field $c(\omega)$ in terms of the input fields $c_{\text{in}}(\omega)$ and $c_{\text{in}}^\dagger(-\omega)$. However, before I do that I will describe how to derive this expression within the Input-Output theory framework.

3.3.3 Kerr-medium equivalence of a Josephson junction oscillator

So far we have analyzed the *RLC*-resonator in a simple circuit language. In section 2.3.3, I described the method of Input-Output theory that allows to analyze the same system in an equivalent way. The language used to describe such nonlinear

systems is slightly different and I discuss it here following closely Refs. [17,38,39]. I put special attention in showing the equivalence between the two methods.

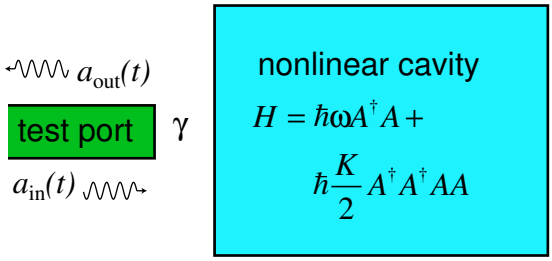

Figure 3.9: A nonlinear cavity is driven by an open port characterized by a linewidth $\gamma = \omega/(2Q)$. The incoming power is given by Eq. (2.53), $P_{\rm in} = \hbar\omega\langle b_{\rm in}^\dagger(t) b_{\rm in}(t)\rangle$, with a similar expression for the outgoing power.

Consider Eq. (3.1). Ignoring dissipation, the system can be described by the Hamiltonian

$$H = \frac{p^2}{2m} + \frac{m\omega_0^2}{2}x^2 + \frac{m\beta x^4}{4}. \tag{3.39}$$

Using the expressions for the normal modes, Eq. (2.11), this Hamiltonian may be written in the form of

$$\begin{aligned} H &= \hbar\omega_0 A^\dagger A + \hbar\frac{K}{12}(A + A^\dagger)^4, \\ &\simeq \hbar\omega A^\dagger A + \hbar\frac{K}{2} A^\dagger A^\dagger AA, \end{aligned} \tag{3.40}$$

where I have dropped the zero-point motion term since it does not affect the dynamics of the system and made the rotating wave approximation to ignore rapidly oscillating terms in the quartic term. The constant K is referred to as the Kerr constant. In this case, it is given by

$$K = \frac{3}{4}\frac{\hbar\beta}{m\omega_0^2}.$$

Now lets consider the case when we couple this nonlinear resonator to a port (Fig. 3.9). Using the IOT theory described in section 2.3.3, we can write the EOM for the cavity mode A as

$$\frac{dA}{dt} = -i\omega_0 A - iKA^\dagger AA - \gamma A + i\sqrt{2\gamma}a_{\rm in}(t). \tag{3.41}$$

In order to solve this nonlinear problem, we follow an analogue of the procedure described in the previous section. We first solve the problem of a large classical pump, and then linearize the solution for the small signal:

$$a_{\rm in} = a_{{\rm in},p} + a_{{\rm in},s}.$$

Let's first discuss the classical response to the pump in the absence of any signal. I write for the incoming and internal fields:

$$\begin{aligned} a_{{\rm in},p} &= b_{\rm in} e^{-i(\omega_p t+\psi)}, \\ A &= B e^{-i(\omega_p t+\phi)}. \end{aligned}$$

Since I am only interested in the steady state solutions, $b_{\rm in}$ and B are (real) constants. Substituting these expressions into Eq. (3.41) yields

$$(i(\omega_0-\omega_p)+\gamma)B + iKB^3 = -i\sqrt{2\gamma}b_{\rm in}e^{i(\phi-\psi)}. \tag{3.42}$$

Multiplying Eq. (3.42) by its complex conjugate, one obtains the following equation where I have defined $N = A^*A = B^2$

$$K^2N^3 + 2(\omega_0-\omega_p)KN^2 + [(\omega_0-\omega_p)^2+\gamma^2]N = 2\gamma b_{\rm in}^2 \tag{3.43}$$

and for the phase between the pump and the internal field:

$$\tan(\phi-\psi) = -\frac{\gamma}{\omega_0-\omega+KN}. \tag{3.44}$$

Expressions (3.43) and (3.44) are exactly equivalent to 3.8 and 3.9, with $F \to 2\gamma b_{\rm in}^2$, $A^2/2 \to N$ and $K \to 3\beta/4\omega_0$.[6] Therefore we expect the same behavior for the internal field of the resonator as shown in figures 3.1 and 3.8. Defining our output mode field as

$$a_{\rm out} = b_{\rm out}e^{-i(\omega t+\psi)}$$

[6] Note that these expression have already built in the high-Q approximations, since these approximations are already assumed in IOT.

where b_{out} can be complex, we can estimate our reflection coefficient $\Gamma = b_{\text{out}}/b_{\text{in}}$ using the boundary condition Eq. (2.69). Since we have only one port and no intrinsic loss in the resonator ($|\Gamma(\omega_p)| = 1$), all the information about the resonator is in the phase of $\Gamma(\omega_p)$. This is plotted in figure 3.10 for three different drives where we define $\delta\omega_p = \omega_p/\omega_0 - 1$. Equivalent expressions for the critical points are given by:

$$\omega_{p,c} = \omega_0 + \sqrt{3}\gamma\frac{K}{|K|}, \tag{3.45}$$

$$b_{in,c}^2 = \frac{4}{3\sqrt{3}}\frac{\gamma^2}{|K|}, \tag{3.46}$$

$$N_c = \frac{2\sqrt{3}\gamma}{3|K|}. \tag{3.47}$$

Using Eq. (2.53), we can then calculate the critical power that we need to apply to our resonator as $P_{\text{in},c} = \hbar\omega_p b_{\text{in},c}^2$

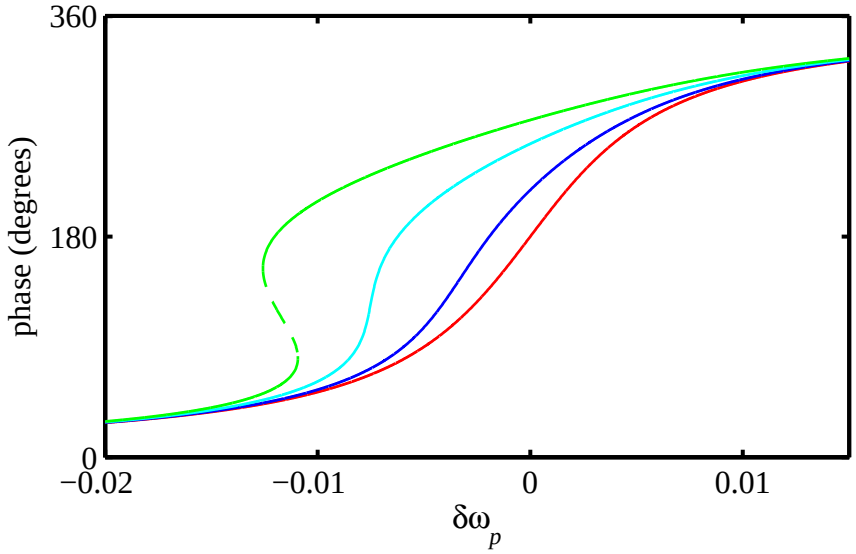

Figure 3.10: Phase of the reflection coefficient Γ as a function of the pump detuning $\delta\omega_p = (\omega_p - \omega_0)/\omega_0$ for a very low power, $0.5b_{\text{in},c}$, $0.9b_{\text{in},c}$ and $1.25b_{\text{in},c}$. For $b_{\text{in}} = 1.25b_{\text{in},c}$, the unstable solution is shown as a dashed line. The quality factor is $Q = 100$.

Now, we linearize the equation for a small incoming signal δa_{in}. We write the

incoming and internal fields as

$$\begin{aligned} a_{\rm in} &= b_{\rm in}e^{-i(\omega_p t+\psi)} + c_{\rm in}(t)e^{-i\omega_p t}, \\ a_{\rm out} &= b_{\rm out}e^{-i(\omega_p t+\psi)} + c_{\rm out}(t)e^{-i\omega_p t}, \\ A &= Be^{-i(\omega_p t+\phi)} + c(t)e^{-i\omega_p t}, \end{aligned}$$

and keep only terms linear in $c_{\rm in}$ and c. B and $b_{\rm out}$ constitute the solution to the classical pump in the absence of any signal. In this case, $c(t)$ and $c_{\rm in}(t)$ are the internal mode and incoming mode operators in the pump rotating frame and are not constants. Replacing these expressions in (3.41), we obtain the following linearized equation for c [38]:

$$\frac{dc}{dt} = [-i(\omega_0-\omega_p)+\gamma]c - 2iKNc - iKNe^{-i2\phi}c^\dagger - i\sqrt{2\gamma}c_{\rm in}. \tag{3.48}$$

Eq. (3.48) describes the dynamics of the internal field and it is equivalent to Eq. (3.35), in the Markovian and "slowly varying envelope" approximation. The equivalence of both expressions can be more easily seen if we transform Eq. (3.48) into the frequency domain:

$$[(\omega_0-\omega_p)-\omega-i\gamma+2KN]c(\omega) + KNe^{-i2\phi_B}c^\dagger(-\omega) = \sqrt{2\gamma}c_{\rm in}(\omega). \tag{3.49}$$

Eqs. (3.38) and (3.49) can be made identical by replacing KN with its circuit equivalent $-\omega_0\epsilon/4$. So far I have redone the analysis for a Duffing oscillator circuit using quantum network theory and shown that within the high-Q approximation it is exactly equivalent to treating a system with a Kerr nonlinearity using IOT. Generalizing the system to include other nonlinearities as well as loss is much easier using IOT; thus, I will follow this method. Before continuing, let's define

$$W = i(\omega_0-\omega_p)+\gamma+2iKN \tag{3.50}$$

$$V = iKNe^{-2i\phi} \tag{3.51}$$

Then Eq. (3.49) reduces

$$-i\omega c(\omega) + Wc(\omega) + Vc^\dagger(-\omega) = i\sqrt{2\gamma}c_{\rm in}(\omega).$$

We can solve for the internal field in terms of the input field:

$$c(\omega) = \frac{i\sqrt{2\gamma}\left(c_{\rm in}(\omega)(W^* - i\omega) - Vc_{\rm in}^\dagger(-\omega)\right)}{(-i\omega+\lambda_0)(-i\omega+\lambda_1)}, \tag{3.52}$$

$$= \nu(\omega)c_{\rm in}(\omega) + \mu(\omega)c_{\rm in}^\dagger(-\omega), \tag{3.53}$$

with

$$\lambda_{0/1} = \gamma \mp \sqrt{K^2N^2 - (\omega_0 - \omega_p + 2KN)^2}. \tag{3.54}$$

It is important to notice that λ_0 tends to zero as one approach a point of infinite susceptibility, Eq. (3.11). This trend represents the slowing dynamics as the parametric amplifier approaches the critical power. I will come back to this point when I discuss the bandwidth of the amplifier.

Parametric gain

Using the boundary condition Eq. (2.56), I can solve for the output field $c_{\rm out}$.

$$c_{\rm out}(\omega) = \left(-1 + \frac{2\gamma(-i\omega + W^*)}{(-i\omega+\lambda_0)(-i\omega+\lambda_1)}\right)c_{\rm in}(\omega) + \frac{2\gamma V}{(-i\omega+\lambda_0)(-i\omega+\lambda_1)}c_{\rm in}^\dagger(-\omega) \tag{3.55}$$

$$= \mathcal{G}(\omega)c_{\rm in}(\omega) + \mathcal{M}(\omega)c_{\rm in}^\dagger(-\omega) \tag{3.56}$$

where $\mathcal{G}$ and $\mathcal{M}$ are accordingly defined. It is straightforward to prove that $\mathcal{G}(\omega)$ and $\mathcal{M}(\omega)$ satisfy the expected relations for a degenerate parametric amplifier [2, 8]:

$$|\mathcal{G}(\omega)|^2 - |\mathcal{M}(\omega)|^2 = 1, \tag{3.57}$$

$$\mathcal{G}(\omega)\mathcal{M}(-\omega) = \mathcal{G}(-\omega)\mathcal{M}(\omega). \tag{3.58}$$

As explained at the beginning of this section, in a degenerate parametric amplifier, for a signal at a frequency $\omega_0 + \omega$ another tone at the image frequency $\omega_i = \omega_0 - \omega$ is also created. Signal and image gains can be defined by taking the operators $c_{\rm in}$ and $c_{\rm out}$ to represent classical c-numbers for the input and the output. Let's define for the signal

power gain:

$$G_s(\omega) = \frac{c_{\text{out}}(\omega)}{c_{\text{in}}(\omega)} = |\mathcal{G}(\omega)|^2 \tag{3.59}$$

and for the image power gain:

$$G_i(\omega) = \frac{c_{\text{out}}(\omega)}{c_{\text{in}}(-\omega)} = |\mathcal{M}(\omega)|^2. \tag{3.60}$$

We plot both signal and image gains for different pump detuning and pump magnitude in figure 3.11a and 3.11b. and signal frequency $\omega = 0$. From expressions (3.57) and (3.58), it can be shown that the the signal and image gains are symmetric in terms of the fourier frequency ω.

$$G_s(\omega) = G_s(-\omega),$$

$$G_i(\omega) = G_i(-\omega).$$

This is shown in figure 3.11c and 3.11d for both the signal and image gain, respectively. When $\omega = 0$, both gains will have in the denominator $\lambda_0^2\lambda_1^2$. As we approach the critical detuning and critical drive, both gains will diverge. It is close to the critical point where $dB/d\omega$ diverges that the amplifier achieves the highest gains. Of course, in practice the gain would never diverge; rather, amplified quantum noise would begin to saturate the amplifier.

Bandwidth

As we can observe in figure 3.11c and 3.11d, the bandwidth of the amplifier gets smaller and smaller as we increase its gain. As I mentioned at the beginning of this section, when we approach a critical point, *i.e.* for large gains, λ_0 sets the bandwidth of the amplifier. Using Eq. (3.57) in the large gain limit, the expression for $G_s \approx G_i = G$ and are approximately given by

$$\begin{aligned} G(\omega) &= \frac{4\gamma V^2}{(\omega^2 + \lambda_0^2)(\omega^2 + \lambda_1^2)}, \\ &\approx \frac{G(0)}{1 + (\frac{2\omega}{B_\omega})^2}. \end{aligned} \tag{3.61}$$

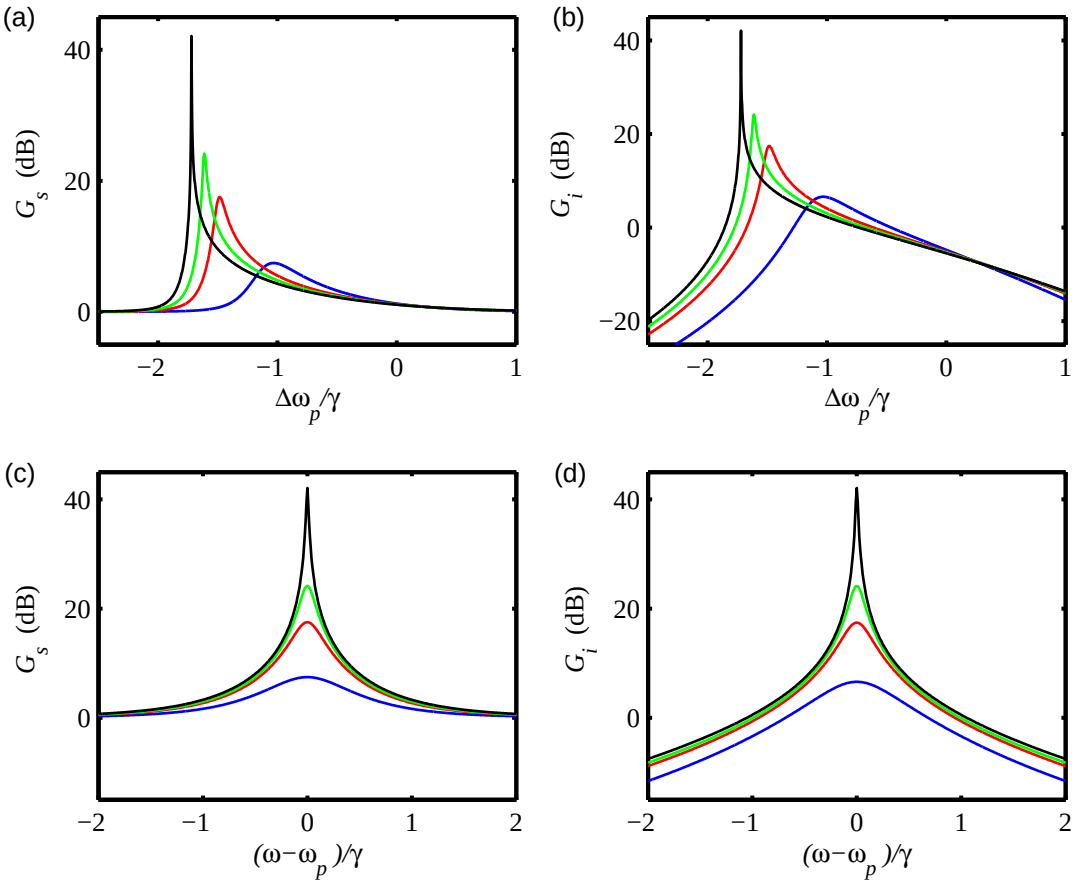

Figure 3.11: (a) and (b) Signal and image gain as a function of pump detuning $\Delta\omega_p = \omega_p - \omega_0$ for a signal frequency of $\omega = 0$ for and incoming power b_{in}^2 equal to $0.5b_{\text{in},c}$, $0.8b_{\text{in},c}$, $0.9b_{\text{in},c}$ and $0.99b_{\text{in},c}^2$. (c) and (d) Signal and image gain as function of signal frequency ω. The pump detuning was chose by finding the maximum gain from plots (a) and (b). For $b_{\text{in}}^2 \simeq b_{\text{in},c}^2$, the optimal pump detuning is given by Eq. (3.45).

The 3-dB bandwidth is $B_\omega = 2\lambda_0$. Substituting in Eq. (3.54) expressions that are correct close to a critical point, Eqs. (3.47-3.45), yields

$$B_\omega = \frac{4}{\sqrt{3}}\frac{\gamma}{\sqrt{G(0)}}. \tag{3.62}$$

This expression shows that the bandwidth of the amplifier is inversely proportional to the amplitude gain $\sqrt{G}$. This gain-bandwidth compromise is a common property of many amplifier, including parametric amplifiers both degenerate and non-degenerate. Because parametric amplifiers usually operate only in a narrow band around a center frequency,

we decided to develop parametric amplifiers with widely tunable center frequencies.

Squeezing

Squeezed state generation involves the creation of correlations between the signal $\omega_p+\omega$ and image $\omega_p-\omega$ frequency. When squeezed states are created their spectrum can go below the vacuum/thermal noise spectrum for a properly chosen phase quadrature. When describing the generation of squeezing in a cavity parametric amplifier like the one I am studying, I need to make a distinction between the internal field and the output field. Confusion regarding this distinction was the origin of the erroneous belief that cavity parametric amplifiers were bad for squeezing, as early work in the field claimed that the maximum amount of squeezing was 50% [40]. However, this limit only applies for the internal field. It was shown that for the output field the squeezing could be arbitrarily large. This large squeezing in the output field is a consequence of an interference effect between the reflected field and the squeezed field exiting the cavity [17, 24, 40, 41].

The kind of squeezing the JPA performs is quadrature squeezing, as explained in chapter 2. From Eq. (2.73), the intracavity quadrature operators are given by

$$X_1(t) = \frac{1}{2}(a(t) + a^\dagger(t))$$
$$X_2(t) = \frac{1}{2i}(a(t) - a^\dagger(t))$$

In the following calculations, I will assume that the incoming noise from the test port shown in figure 3.9 consist of only thermal or vacuum noise. This implies that in a linear cavity, the variances of both quadratures would be

$$\langle \Delta X_1^2 \rangle = \langle \Delta X_2^2 \rangle = \frac{1}{4} \coth(\frac{\hbar\omega}{k_B T}) \tag{3.63}$$

Now let's consider our degenerate parametric amplifier. The amplified quadrature is not necessarily neither X_1 or X_2 but maybe a combination of them. For that reason, it

is more convenient to define a rotated quadrature given by

$$X_\theta(t) = \frac{1}{2}(e^{-i\theta}a(t) + e^{i\theta}a^\dagger(t)) \tag{3.64}$$

Transforming Eq. (3.64) into the frequency domain and into a rotated frame around the pump frequency the quadrature operator is given by

$$X_\theta(\omega) = \frac{1}{2}(e^{-i\theta}c(\omega) + e^{i\theta}c^\dagger(-\omega)) \tag{3.65}$$

where ω represents a detuning with respect to the pump frequency ω_p (see appendix A). We can then calculate $X_\theta(\omega)$ in terms of the input noise using Eq. (3.53). In order to calculate the spectral density of the quadrature operators, we need to calculate the anticommutator of $X(\omega)$ such as in the case of the spectral density of $a_{\rm in}(\omega)$ in Eq. (2.26) [2,8]. However, within the high-Q approximation, Eq. (2.26) is approximated by

$$\begin{aligned} \langle\{a_{\rm in}(\omega_p+\omega), a_{\rm in}^\dagger(\omega_p+\omega')\}\rangle &\simeq 2\pi\coth(\frac{\hbar\omega_p}{2k_BT})\delta(\omega-\omega'), & (3.66)\\ &= 2\pi S_{a,a}\delta(\omega-\omega'). & (3.67)\end{aligned}$$

In making this approximation, we are assuming that we are dealing with a narrow band of frequencies ω in the vicinity of ω_p. Using Eqs. (3.66) and (3.67), we can then compute the spectral density of the quadrature operator

$$\begin{aligned} S_{X_\theta,X_\theta}(\omega)2\pi\delta(\omega-\omega') &= \langle\{X_\theta(\omega), X_\theta^\dagger(\omega')\}\rangle & (3.68)\\ &= \frac{1}{4}S_{a,a}\begin{pmatrix} |\nu(\omega)|^2+|\nu(-\omega)|^2+|\mu(\omega)|^2+|\mu(-\omega)|^2, \\ +2{\rm Re}[e^{-2\theta}(\nu(\omega)\mu(-\omega)+\nu(-\omega)\mu(\omega))]\end{pmatrix} & (3.69)\end{aligned}$$

For the intracavity field, in order to estimate the amount of squeezing, we need to compute $\langle\Delta X_\theta^2\rangle$. This can be computed by integrating $S_{X_\theta,X_\theta}(\omega)$ over all frequencies. I now redefine X_1 as X_θ for $\theta=\theta_1$ that maximizes the internal quadrature variance and X_2 as X_θ for $\theta=\theta_2$ that minimizes the internal quadrature variance. Defined this way, X_1 is the amplified intracavity quadrature and X_2 is the squeezed intracavity

quadrature. We then can derive the expected variances for the both quadratures which are given by:

$$\langle \Delta X_1^2 \rangle = \int_0^\infty d\omega S_{X_1,X_1} = \frac{1}{4}\coth(\frac{\hbar\omega_p}{2k_BT})\frac{|W|}{|W|-|V|}, \tag{3.70}$$

$$\langle \Delta X_2^2 \rangle = \frac{1}{4}\coth(\frac{\hbar\omega_p}{2k_BT})\frac{|W|}{|W|+|V|}, \tag{3.71}$$

where W and V are given by Eqs. (3.50) and (3.51). The limits of integration are based on the fact that our definition of the quadrature operators in the fourier domain only include positive frequencies as shown in Eqs. (A.5-A.6). We observe that the maximum amount of squeezing is given at a critical point given by Eqs. (3.45-3.47), at which $|W| = |V|$. At this configuration, $\langle \Delta X_1^2 \rangle$ diverges and $\langle \Delta X_2^2 \rangle = 1/8 S_{a,a}$. This implies that the maximum squeezing for the intracavity field is of only 50%(Fig. 3.12).

Now, let's consider the output itinerant-wave field. In this case our definition for the quadrature variables are slightly different as we are considering a traveling-wave which is intrinsically multimode (see appendix A). We define the multimode quadrature variable using the same convention as in Refs. [8] and [38] given by:

$$X_{\text{out},\theta}(\omega) = \frac{1}{2}(c_{\text{out}}(\omega)e^{i\theta} + c_{\text{out}}^\dagger(-\omega)e^{-i\theta}). \tag{3.72}$$

Again, we calculate the spectral density of the output modes by calculating the anti-commutator. The result is

$$S_{X_{\text{out},\theta},X_{\text{out},\theta}}(\omega) = \frac{1}{4}S_{a,a}\begin{pmatrix} |\mathcal{G}(\omega)|^2 + |\mathcal{G}(-\omega)|^2 + |\mathcal{M}(\omega)|^2 + |\mathcal{M}(-\omega)|^2 \\ +2\text{Re}[e^{-2\theta}(\mathcal{G}(\omega)\mathcal{M}(-\omega) + \mathcal{G}(-\omega)\mathcal{M}(\omega))] \end{pmatrix}. \tag{3.73}$$

With Eqs. (3.57) and (3.58), we can simplify Eq. (3.73):

$$S_{X_{\text{out},\theta},X_{\text{out},\theta}}(\omega) = G_\theta(\omega)\frac{1}{2}S_{a,a} \tag{3.74}$$

where $G_\theta(\omega)$ is an effective quadrature gain defined as:

$$G_\theta(\omega) = 2G_s(\omega) - 1 + 2\sqrt{G_s(\omega)(G_s(\omega)-1)}\cos(2\theta + 2\phi) \tag{3.75}$$

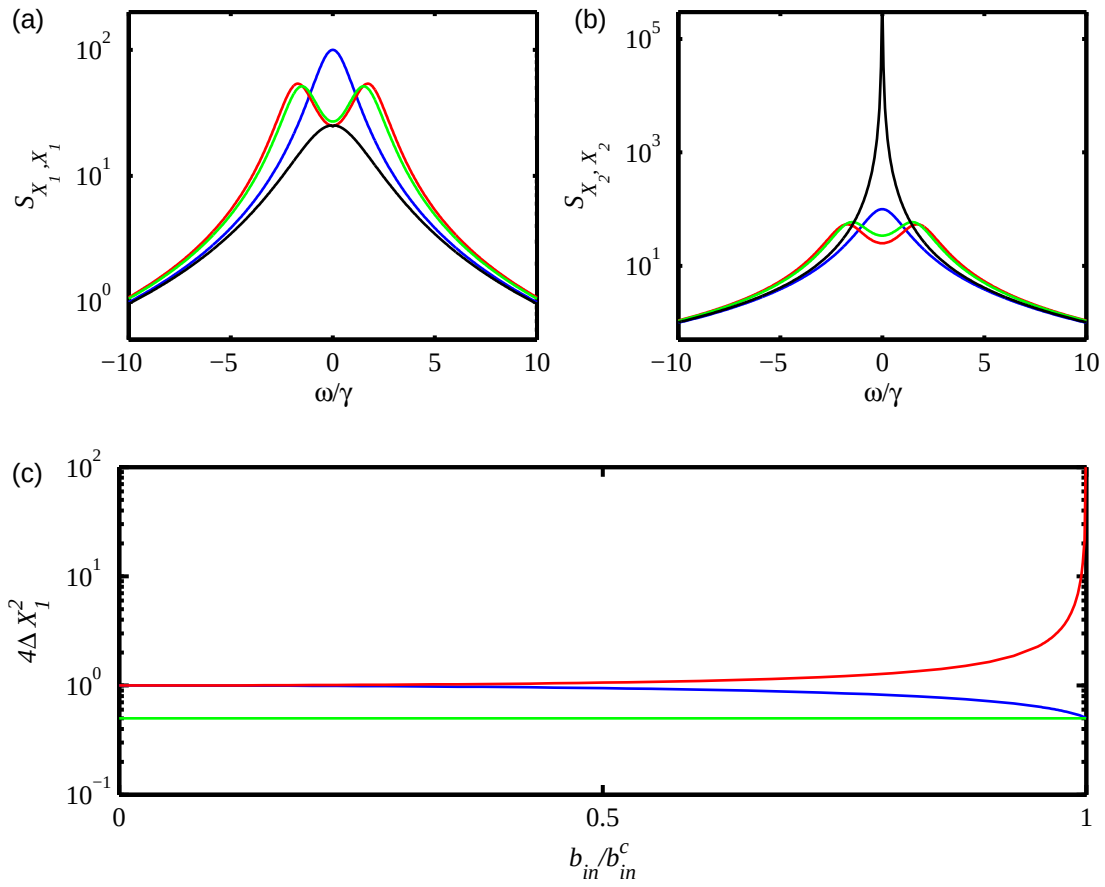

Figure 3.12: Squeezing of the internal field when the incoming thermal noise is that of a vacuum state ($S_{a,a} = 1$). Spectrum for the (a) squeezed and (b) amplified internal field quadrature for pump amplitudes $b_{\rm in}$ equal to 0, $0.5b_{{\rm in},c}$ and $b_{{\rm in},c}$. In the case of no pump power, two cases are shown, one for which the quadrature is defined around a frequency $\omega_p = \omega_0$ (blue) and for the quadrature defined around the critical detuning $\omega_p = \omega_0 - \sqrt{3}\gamma$ (red). For the other two traces, the quadrature is defined around the critical detuning. (c) Internal field quadrature as a function of incoming pump power. The pump detuning is defined as the critical detuning. Even at the critical pump amplitude, the maximum squeezing is only 50%.

where ϕ here is defined as the angle between the two complex gains $\mathcal{G}(\omega)$ and $\mathcal{M}(-\omega)$:

$$\mathcal{G}(\omega)\mathcal{M}(-\omega) = \sqrt{G_s}\sqrt{G_s - 1}e^{i2\phi}.$$

The angle for which the maximum of the gain $G_\theta(\omega)$ occurs defines the amplified quadrature, while the minimum defines the squeezed quadrature. Let's define again $X_{1,\rm out}$ as the amplified quadrature and $X_{2,\rm out}$ as the squeezed one. Squeezing as a function of the

pump power is shown in figure 3.13a. Using the expressions for the output field, Eq. (3.56), it can be shown that close to a critical point where the maximum of the gain for $X_{1,\text{out}}$ occurs ($S_{X_{1,\text{out}},X_{1,\text{out}}}(\omega = 0) = \infty$), the spectral density of the squeezed output field is given by

$$S_{X_{2,\text{out}},X_{2,\text{out}}}(\omega) = \frac{\omega^2}{4\gamma^2 + \omega^2}. \tag{3.76}$$

Note that this suggest that the output field can be arbitrarily squeezed for frequencies close to the pump frequency (Fig. 3.13b). Nonetheless, in practice, other issues would prevent us from achieving arbitrarily high squeezing such as pump depletion or gain stability issues, since while we are squeezing one quadrature, we are amplifying the other one. Noise from the losses and gain saturation will limit the maximum degree of squeezing to be below that theoretically calculated here.

For $G_s \gg 1$, Eq. 3.75 reduces to two very simple expressions for X_1 and X_2:

$$G_1 = 4G_s, \tag{3.77}$$

$$G_2 = \frac{1}{4G_s}. \tag{3.78}$$

This shows that the quadrature gain is expected to be 6 dB higher than the signal and image gains and therefore its gain-bandwidth product will be 3 dB higher as the gain is a factor of two larger but the effective bandwidth reduces to half.

Added noise

It is characteristic of parametric amplifiers that both a signal and an image mode exist. The energy in both of these modes or channels grows at the expense of the pump energy. This means that either channel can be used for amplification. The effective noise performance of the amplifier will be different depending on what kind of linear combinations of input fourier modes (modes labeled by fourier frequency ω) is inputed as a signal. Only when the input signal is a linear combinations of fourier frequencies symmetric around the pump and with the right phase the amplifier is noiseless (Fig.

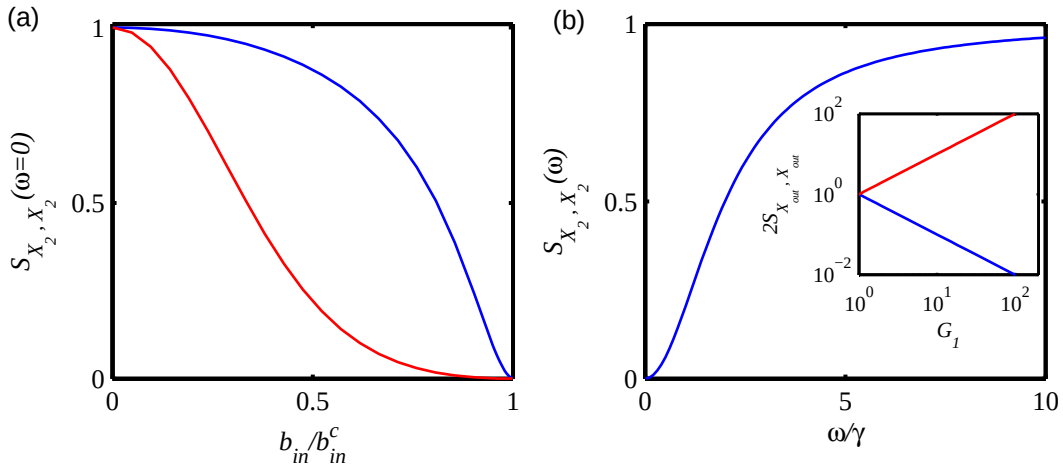

Figure 3.13: Squeezing of the external field. (a) Squeezing of the $\omega = 0$ frequency component of the noise as a function of pump amplitude $b_{\rm in}$ for a constant pump detuning equal to the critical pump detuning (blue), and for a variable pump detuning chosen to maximize the gain G_s as shown in figure 3.11a. By letting the pump detuning vary the squeezing is optimized for a pump amplitude lower than the critical amplitude. (b) Spectrum of the squeezed output field. Inset: Squeezed (blue) and amplified (red) quadrature spectrum for $\omega = 0$ as a function of the quadrature gain G_{X_1}.

3.14a). On the other hand, when the applied signal contains only 1 single frequency component (Fig. 3.14b), the amplifier behaves as a nondegenerate parametric amplifier, adding at least half a quantum of noise. In order to prove these statements in the case of an amplifier with a finite bandwidth we need to consider the fact that the quadrature of an incoming mode at a frequency ω is given by an expression similar to that of Eq. (3.72):

$$X_{{\rm in},\theta}(\omega) = \frac{1}{2}(c_{\rm in}(\omega)e^{i\theta} + c^\dagger_{\rm in}(-\omega)e^{-i\theta}) \tag{3.79}$$

where the angle θ is defined with respect to the phase of the pump. When the signal is applied to both channels (Fig. 3.14b), we are exciting a mode like the one defined by (Eq. 3.79). In this case, the gain will depend on the phase θ and the added noise of the amplifier is zero. In the case when the incoming signal is applied to only one channel (Fig. 3.14a), then the gain will not depend on phase, and in this case the amplifier does add noise. Next I will explained these claims in more detail.

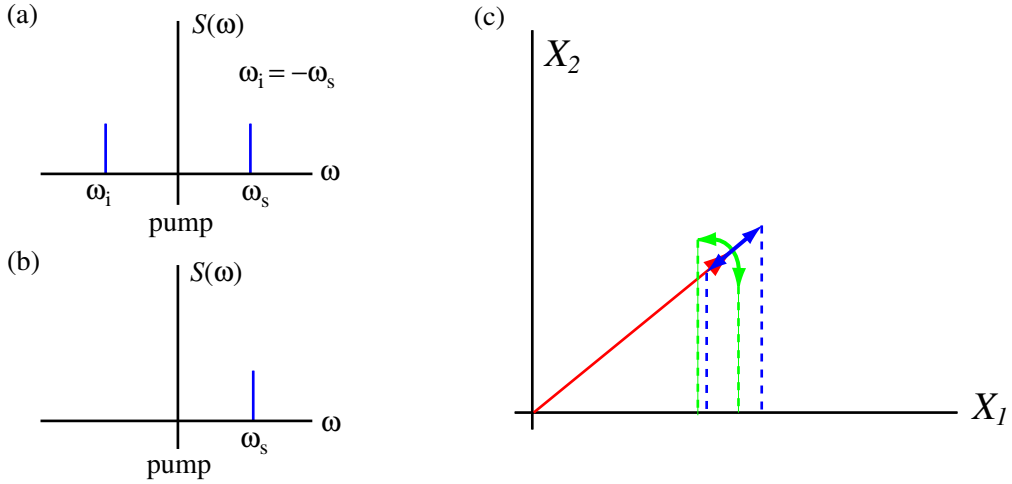

Figure 3.14: Spectrum of the two kind of signals applied to the amplifier. (a) For a linear combination of two fourier-frequency signals symmetric around the pump frequency, the amplifier will act as a degenerate parametric amplifier. (b) For a single tone detuned a frequency ω from the pump, the amplifier will add at least half a quantum of noise. This noise enters the amplifier at the image frequency $\omega_i = -\omega$. (c) When the signal is a linear combination of two fourier-frequency tones, depending on the phase between the two tones, the signal can be pictured as the slow amplitude-fluctuations (blue) or phase-fluctuations (green) of a small carrier (red). The carrier can be ignored, since all the information is in its amplitude or phase fluctuations; however, I draw it for clarity. If the JPA only amplifies the quadrature labeled as X_1, then only the projection of the signal (dashed lines) onto the quadrature X_1 is amplified. By setting the phase of the carrier properly, then the added noise of an ideal JPA can be made arbitrarily small.

In the case of a single-fourier-frequency signal, the JPA acts as a non-degenerate parametric amplifier, amplifying the signal regardless of the its phase with respect to the pump[7] and adding the half a quantum of noise Haus-Caves theorem states, Eq. (2.81). Consider the case when one is only interested in the signal that is at a frequency ω detuned from the pump. In order to compute the noise performance of the amplifier, we can calculate the output noise of the amplifier at a frequency ω for an incoming thermal field with a spectral density $S_{a_{\text{in}},a_{\text{in}}}$ given by Eq. (3.66). From Eq. (3.56), we

[7] In fact, in this case the phase between the signal and the pump is not really defined, since they are not at the same frequency, and this phase evolves constantly with time.

can calculate the noise at the output at the frequency ω, $S_{a_{\rm out},a_{\rm out}}(\omega)$ given by

$$\frac{\hbar\omega_p}{2}S_{a_{\rm out},a_{\rm out}}(\omega) = G_s(\omega)\frac{\hbar\omega_p}{2}S_{a_{\rm in},a_{\rm in}}(\omega) + G_i(\omega)\frac{\hbar\omega_p}{2}S_{a_{\rm in},a_{\rm in}}(-\omega). \tag{3.80}$$

In this expression, it becomes obvious from where the extra noise is coming. When looking at the output spectral density at a frequency ω, the parametric amplifier adds some extra noise that enters the JPA at the image frequency $(-\omega)$. Any noise at a frequency ω is part of the signal so it is not added noise. Using Eqs. (3.57) and (3.58), we can rewrite Eq. (3.80),

$$\begin{aligned}\frac{\hbar\omega_p}{2}S_{a_{\rm out},a_{\rm out}}(\omega) &= G_s(\omega)\frac{\hbar\omega_p}{2}S_{a_{\rm in},a_{\rm in}}(\omega) + (G_s(\omega)-1)\frac{\hbar\omega_p}{2}S_{a_{\rm in},a_{\rm in}}(-\omega), \\ &= G_s(\omega)\left(\frac{\hbar\omega_p}{2}S_{a_{\rm in},a_{\rm in}}(\omega) + (1-\frac{1}{G_s(\omega)})\frac{\hbar\omega_p}{2}S_{a_{\rm in},a_{\rm in}}(-\omega)\right)\end{aligned} \tag{3.81}$$

Taking $\frac{\hbar\omega_p}{2}S_{a_{\rm in},a_{\rm in}}(\omega)$ as the input noise, then Eq. (3.81) shows that the added noise in number of quanta is given by

$$A_N = \left[1-\frac{1}{G(\omega)}\right]\frac{1}{2}S_{a_{\rm in},a_{\rm in}}(-\omega). \tag{3.82}$$

We make the same approximation as in the previous section, $S_{a_{\rm in},a_{\rm in}}(\omega) = S_{a_{\rm in},a_{\rm in}}(-\omega) = \coth(\hbar\omega_p/2k_BT)$. Eq. (3.82) becomes

$$A_N = \left[1-\frac{1}{G(\omega)}\right]\frac{1}{2}\coth(\frac{\hbar\omega_p}{k_BT})$$

which for the case of $T=0$, reduces to the quantum limit of a phase preserving amplifier, Eq. (2.81). On the other hand, note that if we decide to consider the input to be $S_{a_{\rm in},a_{\rm in}}(\omega)$, but measure at the image frequency $-\omega$, the effective added noise would be

$$A_N = \left[1+\frac{1}{G(\omega)}\right]\frac{1}{2}\coth(\frac{\hbar\omega_p}{k_BT})$$

which is again the quantum limit, but for a phase conjugating amplifier.

In the case where our signal consist of two tones as shown in figure 3.14a, then the gain will depend on the effective phase between the pump and the signal. In order to quantify the added noise, we can again consider the case when the incoming signal

is thermal noise. This is exactly the case treated when analyzing squeezing, so we can use those same expressions. The only difference is that in order to study the amplified quadrature, we need to consider the case where the angle is rotated 90° compared to the squeezed quadrature. Again for the incoming signal quadrature spectral density being given by

$$S_{X_{\rm in},X_{\rm in}} = \frac{1}{2}\coth(\frac{\hbar\omega_p}{2k_BT})$$

the output amplified quadrature noise is given by

$$S_{X_{{\rm out},\theta},X_{{\rm out},\theta}}(\omega) = G_\theta(\omega)S_{X_{\rm in},X_{\rm in}}$$

where the quadrature gain $G_\theta(\omega)$ is given by 3.75, where the phase θ is chosen to maximize the gain. From this expression one thing is obvious: the lack of a term representing any added noise; thus, the amplifier will not add any noise! This last claim assumes that the desired information is contained entirely in the amplified quadrature. For example, if the desired information is encoded as amplitude or phase modulation of a tone (Fig. 3.14b), all of that information is contained in a single quadrature as the combination of two fourier frequencies, Eq. (3.79), and can therefore be amplified noislessly. Otherwise, the noise will be amplified more than the signal and then this would appear as extra added noise.

3.3.4 Necessary conditions on the amount of non-linearity to have a good parametric amplifier

After solving the equations of the parametric amplifier, it is worth discussing some details about the necessary condition to have a device that can perform appropriately. First, we need to set a limit on how small the nonlinearity can be. Following closely the line of thought in Ref. [31], consider a slightly different circuit, shown in figure 3.15. The main difference is that I have included an extra inductor in parallel to the Josephson junction to include the possibility of diluting the nonlinearity by adding extra

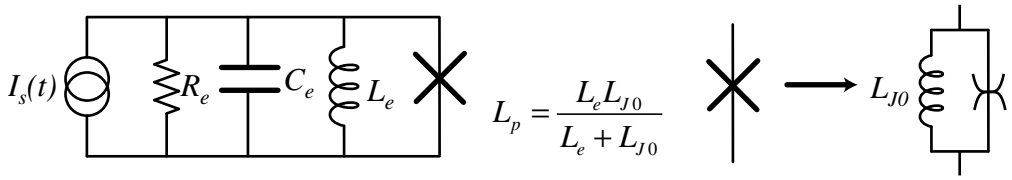

Figure 3.15: Parallel Josephson junction oscillator. An extra inductance has been added to model extra reactive elements in the circuit. By added this extra inductance, the nonlinearity is diluted. This is quantified by the participation ratio $p = L_{J0}/L_p$. For the parallel resonator, the nonlinear Josephson junction is separated in a linear term L_{J0} in parallel with a nonlinear term, following the same convention is an in Ref. [31].

linear inductance (effectively β goes from being $-\omega_0^2/6$ to being $-\omega_0^2/6 \times (L_p/L_{J0})$). We use the quantity called participation ratio as defined in [31], $p = L_p/L_{J0}$. Using equation 3.34, we can define, for a small critical amplitude δ_c, a critical current given by $I_c = I_0 \sin(\delta_c) \simeq I_0 \delta_c$. If we want the approximation of the nonlinear inductance to be accurately modeled by the Taylor expansion up to third order, we need $I_c/I_0 \ll 1$. This translates into a restriction on the quality factor and the nonlinearity given by:

$$\frac{4}{3^{1/4}} \frac{1}{\sqrt{Qp}} \ll 1 \tag{3.83}$$

A second condition we need to consider is related to Eq. 3.35. In section 3.1, I mentioned that the zeroth order solution for the duffing oscillator would be a good approximation if Eq. (3.5) was satisfied. However this only sets a limit on how accurate the zeroth order solution is. There is another concern on this non-linear systems which is the stability of the solution and the possibility for chaotic behavior. The following results are from Refs. [30, 31, 36] and are not derived in this thesis.

In solving Eq. (3.1) and (3.31) we have assumed that they have a solution with only odd multiples of the driving frequency:

$$y(t) = \sum_{k=1}^{\infty} A_{2k-1} \cos((2k-1)\omega t + \phi_{2k-1})$$

with the coefficients A_{2k-1} decreasing in magnitude with k. The first harmonic is our zeroth order solution, and its amplitude is given by Eq. (3.7). It has been observed that

in the Duffing oscillator, the transition to chaotic behavior can occur via consecutive period doubling, and period doubling is always preceded by the transition of the solution from having only odd-harmonics to one containing both odd and even harmonics. In a sense, the appearance of even-harmonics in the solution is a precursor of chaotic behavior in the case of the Duffing oscillator [30, 31]. It is usually claimed that we are in the weak nonlinear regime if our solution only has odd harmonics. The procedure is similar to the procedure of linearizing the Duffing oscillator for a small perturbation δ_s around the large pump solution δ_p. It implies analyzing the stability regions of the Mathieu equation 3.35, with $v_{\text{in}} = 0$. I will not embark myself in such an endeavor since it will takes us far from the goal of this thesis. I only quote the results from Ref. [31]. The restriction in our pump amplitude δ_a and pump detuning to avoid the instability regions that would lead us to chaos are

$$\frac{3}{2w^2}\mathbf{x}^2 < \mathcal{O}(1) \qquad \frac{1}{2} < w < 1 \tag{3.84}$$

where $w = \frac{\omega_p}{\omega_0}$ and $\mathbf{x} = \sqrt{p/6}\delta_a$. These restrictions define the boundary between the solution having only odd-harmonics and the generation of even harmonics.

The high gain region of a parametric amplifier happens close to the bifurcation point. We want to be able to access it assuming that the amplitude of the internal fields is small enough that the third order approximation of the nonlinearity is accurate enough, and that at the same time we are far from the instabilities that can cause chaotic behavior. In Ref. [31] it is shown that we can avoid these issues if we fulfill the following restrictions:

(1) Quality factor much greater than one.

(2) Large product of participation ratio and quality factor $pQ \gg 1$.

(3) Oscillation amplitude δ_a much smaller than 1.

(4) The relative detuning of the pump is of the order of the linewidth.

Other circuits

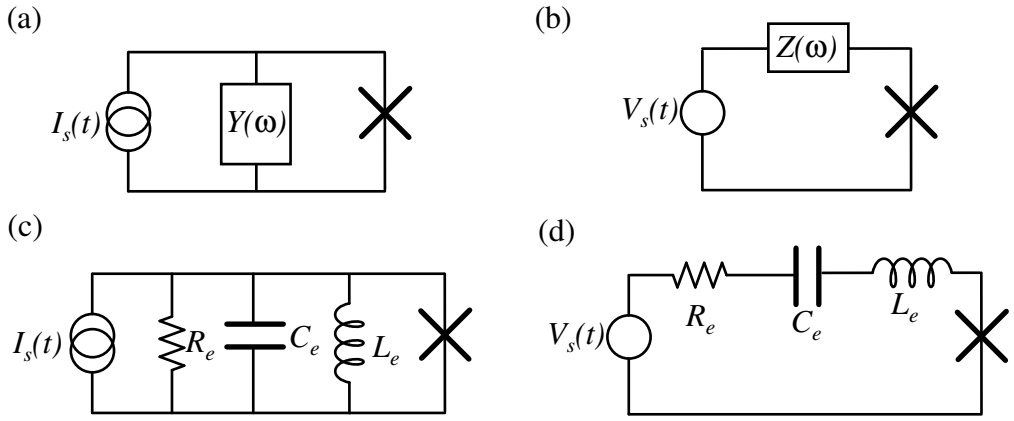

Figure 3.16: (a) and (b) Norton and Thevenin equivalents of a Josephson junction embedded in an arbitrary microwave network represented by the admittance $Y(\omega)$ or impedance $Z(\omega)$. We assume that the microwave networks have a resonance. Close to that resonance, they can be modeled by parallel or series resonators as shown in figure (c) and (d).

So far in our analysis, we have just studied the case when a junction is shunted by a capacitor, and damped via frequency independent resistance $R = Z_c$. This can be extended to the general case when the Josephson inductance is embedded in a more general electromagnetic environment with a frequency dependant impedance $Z(\omega)$ or admittance $Y(\omega)$ as shown in figure 3.16a and 3.16b. This reactive impedance allows us to tune the resonance frequency and quality factor of our resonator. For example, $Z(\omega)$ could represent a transmission line resonator in series with a coupling capacitor. Now, if $Z(\omega)$ or $Y(\omega)$ have a resonance, close to that resonance frequency they can be modeled by an effective series or parallel resonator (Fig. 3.16c and Fig. 3.16d), so a lot of insight can be gained by just analyzing these simpler cases.

The parallel case has already being analyzed in this chapter. The series resonator

can be studied using the same tools. The EOM of the circuit shown in figure 3.16d is

$$V(t) = \left[L_e + \frac{L_{J0}}{\sqrt{1-(dq(t)/dt)^2/I_0^2}} \right] \frac{d^2q(t)}{dt^2} + R_e \frac{dq(t)}{dt} + \frac{q(t)}{C} \quad (3.85)$$

$$= \left[L_e + L_{J0} + \frac{L_{J0}}{I_0^2} \left(\frac{dq(t)}{dt} \right)^2 \right] \frac{d^2q(t)}{dt^2} + R_e \frac{dq(t)}{dt} + \frac{q(t)}{C} \quad (3.86)$$

where q is the charge on the capacitor and in the second line I have made an approximation to second order in dq/dt.

Making an analogy with the mechanical harmonic oscillator, in Eq. 3.86 would be equivalent to one where the nonlinearity does not affect the restoring force but the mass of the particle. Even though it is not a Duffing oscillator, it can be shown that at low drives, large Q and the single harmonic approximation in the solution, we recover the same dynamics as in the Duffing oscillator [31]. Similar performance as parametric amplifiers is expected and equivalent restrictions can be derived regarding the conditions that the electromagnetic environments must satisfy. For more details see Ref. [31].

Chapter 4

Previous and other current work on Josephson parametric amplifiers

4.1 Noise rise

In the 1970's there was a strong effort to develop Josephson parametric amplifiers. Because of their theoretically predicted low added noise, they were expected to have promising performance for practical applications such as microwave/millimeter-wave detection in microwave astronomy and analog signal processing [42]. JPAs achieved good signal gain in 1-100 GHz band, but unfortunately these amplifiers proved impractical because of a poorly understood difficulty with their added noise [43, 44]. It was found that for moderate to high gains, the amplifiers' noise temperatures were significantly larger than the environment temperature. This noise problem is referred to in the literature as "noise rise." As the bias point was varied, the output noise of the device had a number of sharp peaks whose origin was unknown [45]. This behavior was found in most implementations. However the literature does contain examples of JPAs operated with low noise temperatures between 10 and 30 K and signal gains exceeding 20 dB [34, 46–48]. Nonetheless, good performance was only attainable if the parameters that controlled the amplifier gain such as current through the Josephson junctions or magnetic field applied to the SQUID loops were tuned to a narrow range. It was not understood why the amplifier only obtained good performance on a narrow range of

parameters.[1]

The phenomenon referred to as "noise rise" was also observed to have the feature that the noise temperature T_n was directly proportional to gain [44]. There were different theories that tried to explain the "noise rise" problem and they can be roughly divided in three different groups:[2]

(1) Amplified noise, possibly including amplified thermal radiation that saturated the amplifier.

(2) Instability caused by noise in the parameters that determine the operating point, e.g. fluctuations in the pump power.

(3) Intrinsic instabilities and chaotic behavior associated with the nonlinear dynamics of pumped Josephson junctions.

The first case seems self-explanatory, and except for some papers published in the late 1970's (see Ref. [44] and references therein), this line of thought does not seem to have been given much continuity. Regarding the second group of theories, the intuitive notion is that when an amplifier is biased for high gain, the gain itself must be very sensitive to external influences that vary the operating point. Therefore, the amplifier is more "unstable", meaning small changes in the pump power can cause large fluctuations in the operating point of the amplifier. Feldman and coworkers predicted that these large fluctuations would cause a noise temperature proportional to the gain [45].

The group of theories that seemed to have more support from the community were the ones that considered the "noise rise" problem a consequence of intrinsic nonlinear dynamics of these systems. These explanations included phase instabilities, hopping

[1] Also, some attention was given to the effect of saturation due to thermal noise from room temperature [47] which raises the question of maybe inappropriate filtering as a possible root of stability problems specially in the 3-photon mode of operation where a **stable** dc-bias needs to be applied.

[2] However, it is not entirely clear that all the excess noise found in these first experiments had this feature and more than one theory may be needed to explain all the issues regarding the poor noise performance on JPAs [44].

between coexisting attractors, deterministic chaos, and universal features of systems operated near certain types of bifurcations. Next is a brief description of all these hypothesis.

Regarding deterministic chaos, Huberman and coworkers suggested that the large broad-band noise-rise phenomenon could be understood in terms of the existence of chaotic solutions to the full nonlinear junction dynamics, associated with the appearance of a strange attractor in phase space [49]. We have seen in section 3.3.1 that in the limit of small amplitudes of phase oscillations δ, it is possible to study the stability of equation (3.30) by converting it into a Mathieu type equation, 3.35. They show that as δ increases, the first two terms of the Taylor expansion of the $\sin\delta$ term lead to a cascade of bifurcations into a chaotic regime which cannot be obtained via perturbation theory [49]. Pederson and coworkers also suggested similar arguments agreeing that the so called noise-rise observed in connection with high gains in almost all JPAs had its origin in chaos [50]. On the other hand, other people working in the field asserted that chaotic behavior could not account for noise temperature proportional to gain. Instead they argue that noise rise should occurs with no gain. In fact noise rise without any gain has been experimentally observed (see for example Ref. [51]).

The phase instability theories [44, 51], noise-induced hopping between coexisting attractors [52] and universal behavior near instabilities or bifurcations [53, 54] are somewhat similar. The essential ingredients of these theories is that the amplifier dynamics can have multiple solutions (coexisting attractors) and external noise can kick the system back and forth between stable solutions. Bryant and Yurke in Ref. [54] show qualitative agreement between their theory and experiment, and a correlation at high enough gains between the increase of noise and the increase of signal gain close to the bifurcation point. The details of each theory are outside the scope of this thesis and the reader is referred to the literature.

4.2 Previous successful implementations

In spite of the "noise-rise issue" attempts to fabricate low-noise JPAs continued with some of those attempts being somewhat successful [55]. Smith and coworkers created the lowest noise temperature microwave amplifier, other than maser based amplifiers, and published their results in 1985. They used an rf-SQUID and operated at 8 GHz reaching a noise temperature of 6 K similar to the temperature of operation (4.2 K) [42]. This opened the possibility to generate squeezed states of microwave light and operate amplifiers with quantum-limited performance.

4.2.1 Squeezing of thermal and vacuum noise

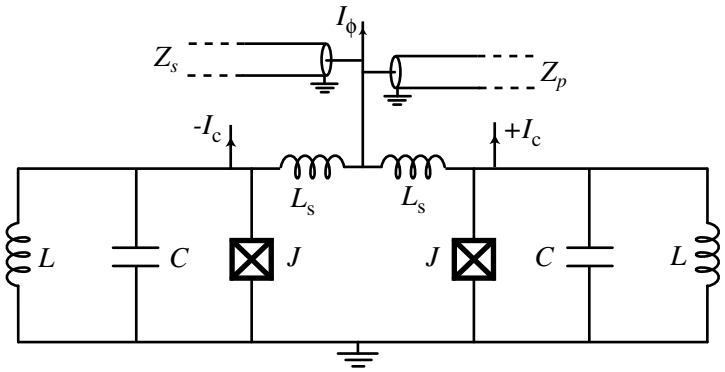

Figure 4.1: Circuit schematic of the device used in Refs. [6] and [7]. Two Josephson junctions form a dc-SQUID. Magnetic flux is coupled into this SQUID via the inductors L_s through the +Ic -Ic current bias line, adjusting the critical current of the SQUID formed by the parallel combination of the 2 junctions. The phase δ of the effective junction is controlled via the current bias line I_ϕ. Two transmission line with different impedances are used for the pump and for the signals. The JPA is operated as a reflection amplifier.

Yurke and coworkers were one of the few groups that continued their research on JPAs. The device studied consisted on a RLC-circuit as the one shown in figure 4.1. Their main goal was the generation of squeezed states of microwave fields. The JPA was operated in both modes three-photon and four-photon mode [8]. In the case

of squeezing, it was operated in the three-photon mode where the applied pump had a frequency of 38.8 GHz. In the first experiment that showed squeezing of microwave fields, 42 % squeezing of 4.2 K thermal noise was demonstrated and a noise temperature of $T_n = 0.28$ K [7]. This noise temperature implied that the JPA exhibited less internally generated noise than a linear phase insensitive amplifier. However, in this case, they reported that at 4.2 K, the highest gain achieved before the generation of excess noise due to the onset of chaos was 12 dB [8].

They also demonstrated squeezing of quantum noise at 19.16 GHz [6]. Operating in the degenerate mode (the pump frequency being twice the signal carrier frequency), they demonstrated squeezing of 47 % below the vacuum-noise floor. A noise temperature of 0.446 K is accounted by the vacuum noise emitted by the losses. In this same paper, they reported that they have operated the amplifier with gains as high as 37 dB and with a noise temperature of $T_N = 0.5$ K [6, 54]. The device used had, according to the authors, the same design as the one used earlier to do classical squeezing of thermal noise. However, they do not provide details on why this new sample shows a better performance.

4.2.2 Parametric amplifier with Josephson junction arrays

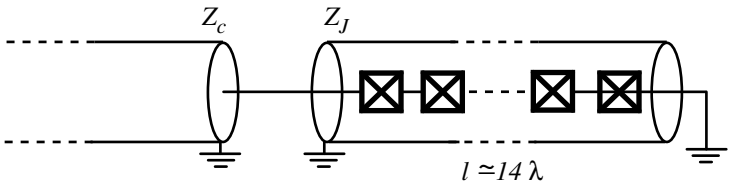

Figure 4.2: A Josephson transmission line made out of 1000 Junctions is directly coupled to a 50 Ω transmission line at one end and shorted at the other end. Due to the Josephson non-linearity, the Josephson transmission line will act as a "distributed" parametric amplifier operated in reflection.

Most of the JPA implementations consisted of resonant circuits as the one shown

in 4.1. One drawback of such implementations is their narrow bandwidth. In order to obtain large bandwidths, it is desirable to avoid the use of resonant structures to impedance match the signals from a 50 Ohm transmission line to the low impedance exhibited by a Josephson junction. It had been realized that impedance matching problems could be circumvented through the use of a series array Josephson junctions. Arrays of Josephson junctions had been used previously for JPAs, but with sizes small enough to still treat them as lumped elements [34, 46, 47]. In this new configuration suggested by Sweeny and Mahler [56], the array was significantly larger than the wavelength of the microwave field, and constituted a distributed parametric amplifier.

Yurke and coworkers implemented this idea, fabricating an array of 1000 Josephson junctions and a length of 9 mm, which greatly exceeded the wavelength of 0.65 mm for the 19 GHz signals. The amplifier was pumped at the signal carrier frequency, that is, it was operated in the four-photon mode [57]. With a critical current of $I_0 = 12$ μA per junction, the zero-current inductance per unit length was $L_l = 34.5$ μH/m. The capacitance per unit length was $C_l = 187$ pF/m which resulted in a characteristic transmission line impedance of 430 ohms and a phase velocity of $v = 1.25 \times 10^7$ m/s. [3] They then terminated one end with a short (Fig. 4.2).[4] The Josephson transmission line was operated at zero bias as a reflection parametric amplifier, where a single port was used for both pump and signal.

In this implementation, they demonstrated very low noise performance of $T_n = 0.5$ K consistent with internally generated noise from losses. Their implementation also showed a bandwidth of 125 MHz with a gain of 12 dB, or an equivalent gain-bandwidth product of 500 MHz. However, some peculiar behavior regarding the noise and gain

[3] The phase velocity and impedance given here are the same as the ones given in Ref. [57]. However, they do not agree with the critical current of the junctions the authors claim, $I_0 = 12$ μA. The inconsistency is fixed if a critical current of $I_0 = 1.2$ μA is assumed instead.

[4] I believe it is debatable calling this implementation a non-resonant parametric amplifier, as the impedance mismatch of both transmission lines is large enough to be able to create well defined resonant modes inside the Josephson transmission line. However the amplifier would be operated at an unusually large mode of the resonator.

performance were also observed. As the pump power was increased from low values, the gain of the amplifier first increased and then, after passing through a maximum, it decreased. They called this point at which the maximum gain is achieved the threshold value [57]. Good noise performance is reported only past the threshold point. Below threshold the amplified showed excess noise as large as an extra 6 K.

4.3 Current work on Josephson parametric amplifiers

After the promising results of vacuum noise squeezing and large gain with low noise performance shown in Ref. [7], research on Josephson parametric amplifiers dwindled. However, the interest in them has been growing the past few years with several groups interested in developing low-noise microwave parametric amplifiers for quantum information applications and quantum limited detection of microwave signals [9, 11]. Next I describe some of the most successful recent implementations.

4.3.1 Josephson ring modulator

The Josephson ring modulator has been developed by N. Bergeal and collaborators for quantum computing applications [58]. The four-photon mode operation of the JPA implies the presence of a large pump tone in the middle of the amplifier band which for some applications can be a problem. For some applications, it is necessary to separate the modes associated with the signal, idler[5] and pump so that all three tones are at a very different frequency. One approach is to fabricate a nondegenerate parametric amplifier where each of the modes correspond to a different resonator. The Josephson ring modulator (JRM) archives this by separating all 3 modes as observed in figure 4.3a. The JRM consists of four nominally identical Josephson junctions designed into a ring threaded by a magnetic flux Φ. The ring has only three orthogonal electrical modes that couple to the junctions: two differential ones, X and Y, and a common one,

[5] In non-degenerate parametric amplifiers the image tone is usually referred as the idler tone.

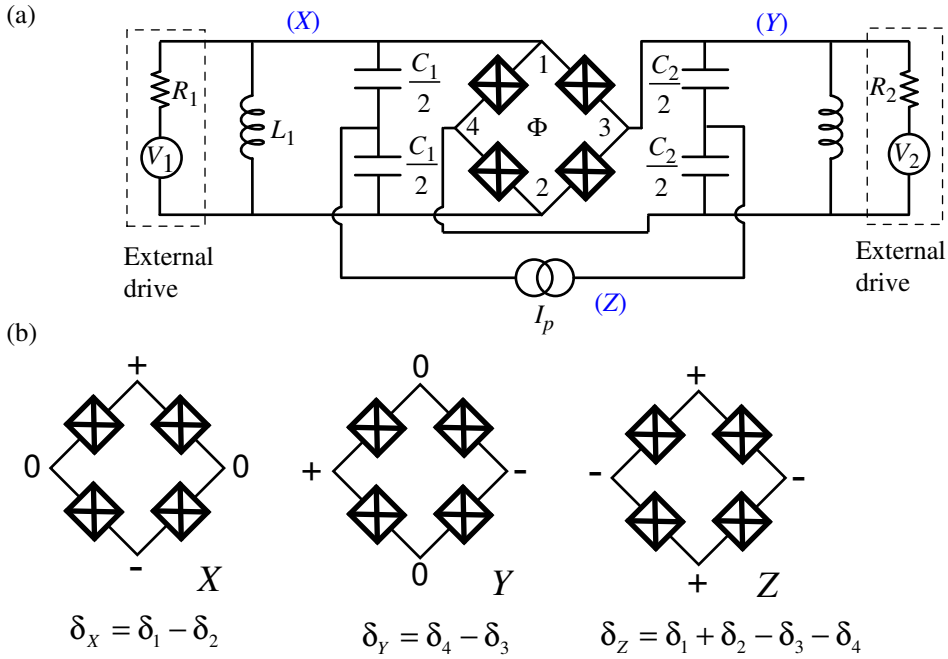

Figure 4.3: (a) Lumped element circuit schematic of the Josephson ring modulator. The ring modulator is coupled to two LC resonators and a pump drive. (b) There are four orthogonal modes, but only three of them couple to the Josephson junctions: the two differential modes X and Y used to couple to the two LC resonators, and the common Z mode is used for the pump drive.

Z (Fig. 4.3b). In the circuit schematic shown in figure 4.3a, the two resonator circuits X and Y are used as the signal and the idler modes, while the input Z for the pump drives the common mode.

The JRM amplifier is operated usually at a flux of $\Phi = \Phi_0/2$. At this flux bias, and for mode intensities δ_X, δ_Y and δ_Z much smaller than 1, the ring hamiltonian has approximately the following form:

$$H_{ring} \propto \left[\delta_X \delta_Y \delta_Z - \frac{\delta_X^2 + \delta_Y^2 + \delta_Z^2}{2}\right]$$

where terms of order higher than three have been neglected. The second term corresponds to a "contamination term" whose only effect is to renormalize the resonance frequency of the resonators. The first part is a pure nonlinearity that couples all three modes, and in the coupling each mode appears only linearly. The bridge configuration

proposed by Bergel, *et. al.* has the advantage of eliminating unwanted terms like $\delta_X^2\delta_Z$, $\delta_Y^2\delta_Z$, $\delta_X^2\delta_Y$ and $\delta_Y^2\delta_X$ which would introduce other, unwanted types of mixing. One interesting consequence is that the resonance frequency of the circuit used for the signal mode will not have the observed change in frequency as a function of amplitude of internal fields, as the one observed in the Duffing oscillator. This implementation can theoretically achieve the minimum added noise limit set by Haus-Caves theorem (2.81).

4.3.2 Flux driven Josephson parametric amplifier

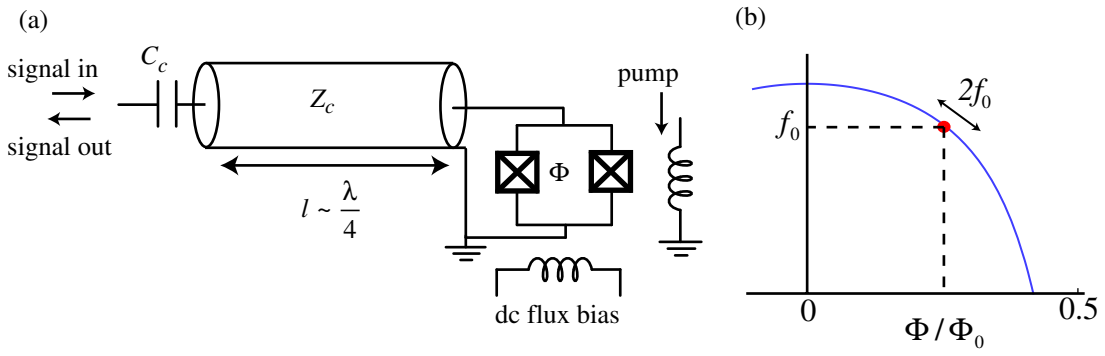

Figure 4.4: (a) The flux-driven parametric amplifier consists of a transmission line resonator terminated by dc-SQUID. By applying a dc flux bias, the boundary condition of the cavity resonator changes, modifying the resonance frequency. A microwave pump tone is inductively applied to the SQUID which modifies the resonance frequency at $f_{\text{pump}} = 2f_0$ parametrically amplifiying a signal applied at the input port through the coupling capacitor C_c. (b) In order to operate this amplifier in a three-wave mixing mode, a dc flux bias must be applied to break the even symmetry of f_0 versus flux.

This implementation of the Josephson parametric amplifier has been studied by T. Yamamoto and collaborators [59]. It consist of a superconducting transmission-line resonator terminated by a dc-SQUID (Fig. 4.4). Unlike our implementation, their pump does not modulate the current through the SQUID, but it is applied as a flux modulation. A dc-flux bias breaks the even-symmetry of the resonance frequency-versus-flux relation. Applying a microwave pump at twice the resonance frequency $f_{\text{pump}} = 2f_0 \sim 20$ GHz to the inductively coupled pump line makes the cavity's resonance to oscillate at $2f_0$.

This modulation does parametric work on a signal applied at the input port of the cavity. As the pump is applied at twice the resonance frequency of the JPA, this type of operation is a three-wave mixing or degenerate mode, as opposed to the four-wave mixing or doubly degenerate mode.

We can distinguish an important difference between our implementation and this one. As the signal and the pump are very different in frequency ($f_{\text{pump}} = 2f_{\text{signal}}$), and applied at different ports, it is simpler to separate the amplified signal from the pump. Also, the cavity resonator is a quarter-wave resonator and the next resonance mode is at a frequency $f_1 \simeq 3f_0$, so the leakage of the pump microwave power into the signal port is small due to the absence of a resonance close to the pump frequency. The performance of the amplifier has been described in Ref. [59]. They have observed a maximum gain of 17 dB. For the noise performance they have estimated an upper bound in the noise temperature of $T_N < 0.87$ or in terms of added quanta, $A_N < 1.7$ quanta.

4.3.3 dc-SQUID stripline resonator

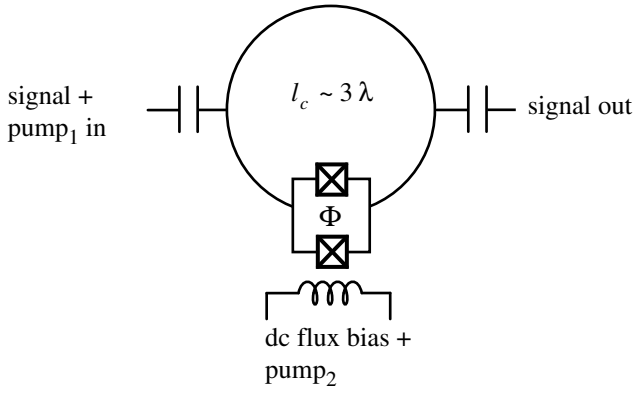

Figure 4.5: The device consist of circular microstrip resonator with a dc-SQUID located in a current antinode of the third resonance mode. The parametric amplifier is operated in two different ways. First in the double degenerate mode with the pump applied close the signal frequency and at the same port as the signal (pump_1). The second mode is the three wave mixing, where the pump is applied in the flux line (pump_2).

This implementation is in principle very similar to the previous one. The JPA consists of a stripline microwave superconducting resonator integrated with a dc-SQUID [60] (Fig. 4.5). The dc-SQUID sits at a current antinode of the third mode resonance. Abdo, *et. al.* studied the signal and image gain as a function of pump power observing gains as high as 24 dB.

They studied the noise behavior as function of pump power showing instabilities close to the critical pump power. They suggest that the reason is due to the fact that at high critical powers, the amplitude of the current inside the cavity is large compared to the critical current of the SQUID (I_0^S) [60]. This would suggest that this implementation does not satisfy all the requirements given by Ref. [31] and described previously in section 3.3.4 .

In addition, they also operate their amplifier in the three-photon mode, where the pump is applied as a microwave flux bias, similar to Ref. [59]. They show a signal gain of 38 dB but with a lot of other tones at other harmonics. They also show a signal to noise improvement of around 23 dB. Yet, without a noise temperature of the amplifier chain it is not possible to estimate the added noise of their JPA.

4.3.4 Josephson bifurcation amplifier

Developed by Siddiqi and coworkers [61, 62], the Josephson bifurcation amplifier consists of a nonlinear oscillator formed by a capacitively shunted Josephson junction (Fig. 4.6a). This is exactly the same circuit we have been analyzing so far and we know it behaves as a parametric amplifier. The name Josephson bifurcation amplifier (JBA) distinguishes the regime in which it is operated. The resonant circuit is biased with a strong microwave current to access the nonlinear regime as shown in figure 4.6b. The pump power and pump detuning are set in the parameter space to be in the bistable regime. In this regime, two possible dynamical states are accessible. A weak signal is then coupled to the amplifier junction critical current, where figure 4.6a shows just one

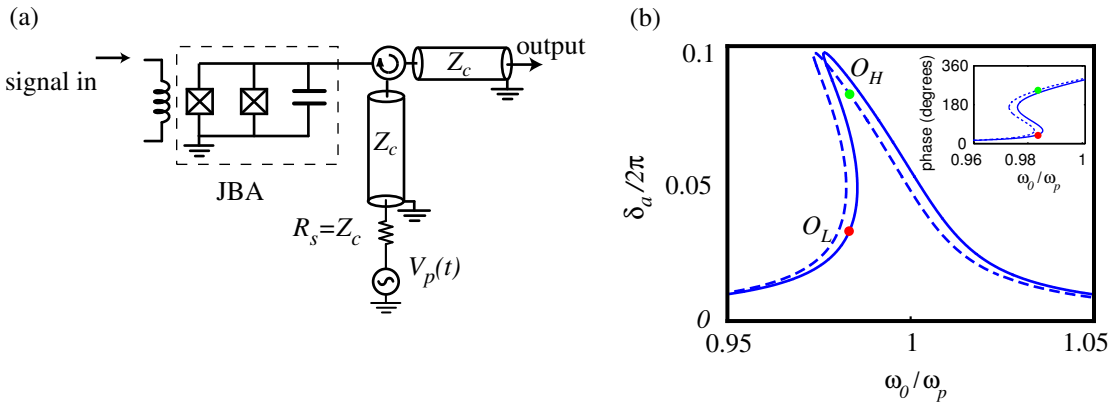

Figure 4.6: (a) Circuit schematic of a possible implementation of the Josephson bifurcation amplifier. The input line is inductively coupled to critical current of the Josephson element in the JBA. A large pump rf-bias the resonator in the nonlinear regime where two dynamical states are possible for the JBA. (b) Nonlinear resonant curve of the JBA showing a possible bias point for the JBA (solid line). A small signal coupled to the critical current will make the resonance frequency, and consequently its response, change (dashed line). If properly biased, the oscillator will change from a low amplitude state (O_L) to a high-amplitude state (O_H). Inset: Phase of the reflected pump tone for the given pump power. The two possible dynamical states are indicated (red and green dots), showing the large and detectable change in phase that allows the JBA to measure a weak signal due to small changes in the effective critical current of the junction.

example of a possible implementation of the signal-I_0 coupling. This signal coupling results in a dispersive shift of the circuit resonance frequency and consequently in the oscillator evolving from the state O_L to O_H, thus realizing a sensitive threshold detector for I_0. The dynamical state of the JBA can be measured by the large difference in phase of the reflected pump as can be observed on the inset of figure 4.6b.

However, the JBA can be operated as a Josephson parametric amplifier: instead of coupling an input signal to the critical current of the Josephson junction, we can apply a weak signal at the same port as the pump and amplify that signal as a reflection amplifier. Vijayaraghavan has operated the JBA in the parametric amplifier regime. His results have not been published, but are available in Ref. [18]. He reported a gain of over 25 dB and a gain-bandwidth product of 280 MHz. The estimated noise temperature

in the nondegenerate mode was $T_n = 0.08 - 0.15$ K, which compared to quantum-limited value of 0.072 K, it implies a performance close to the theoretical limit. They have also measured squeezing of vacuum noise.

4.3.5 Parametric amplification with superconducting resonators and weak-links

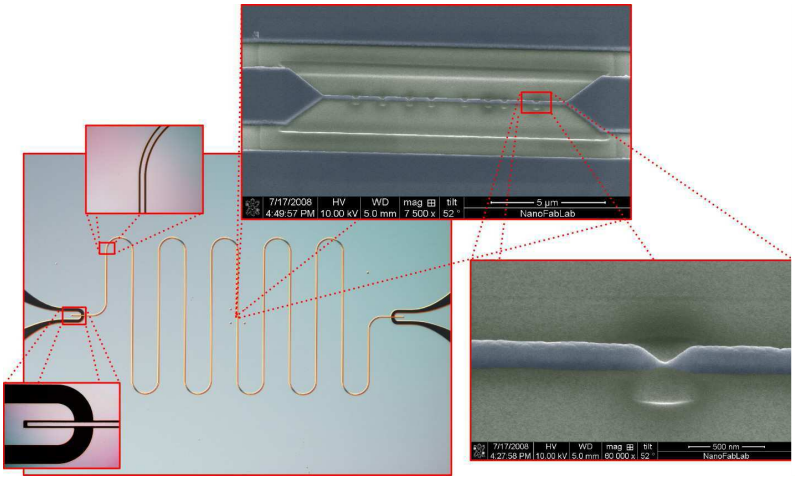

Figure 4.7: Picture of the sample used by Tholén, *et. al.* to study parametric amplification. The resonators are made of Niobium and 10 weak-links are fabricated at the center of the resonator where there is a current antinode. Reproduced with permission from Ref. [63].

It is a known phenomenon that thin superconducting films present nonlinear effects at high enough currents [64]. These nonlinear effects arise from current induced magnetic field penetration into the superconducting thin films and give rise to a nonlinear inductance. This current dependent kinetic inductance can be modeled as an effective kerr nonlinearity [38]. Tholén and collaborators have used this Kerr effect in superconducting films to fabricate nonlinear cavities that can be used for parametric amplification [65]. Using the intrinsic nonlinearity in superconducting transmission line resonators in their first implementation they achieved 22.4 dB of maximum gain (signal and image gain). Due to a lack of calibrated noise source, they were unable to estimate

the added noise of the amplification process.

In order to increase the nonlinearity of their resonators, in their second implementation they fabricated a parametric amplifier based on the nonlinear kinetic inductance of a weak link (Fig. 4.7). A weak link consists of a Josephson element where the weak electrical contact between superconducting electrodes is provided by some small metallic constriction with dimensions of the order of the superconducting coherence-length [66]. The name is used to distinguish non-tunnel from tunnel junctions Josephson elements. This type of Josephson element also behaves as a non-dissipative nonlinear inductance. However the strength of the nonlinearity is a strong function of the geometry and the current-phase relation is not necessarily a sinusoidal function as in Eq. (3.15) for a simple tunneling junction. In this second implementation of parametric amplifiers, Tholén reports an improved performance with a maximum signal and image gain of 25 dB [63].

Chapter 5

Design of JPA

In this chapter I describe the process of designing our Josephson parametric amplifier. I will begin by discussing microwave cavity resonators including the process of coupling power to them. I will also discuss some non-ideal features present in our devices such as loss. In the second part of the chapter, I discuss the integration of the Josephson junction into the microwave cavities. I will then generalize the results of chapter 3 to include both loss and the presence of additional ports. Finally, I will discuss the effect of these extra ports in the performance of the amplifier.

5.1 Microwave environment design

In chapter 3, I discussed the case of a lumped-element parallel Josephson resonator and its behavior as an amplifier. However, at microwave frequencies the wavelengths are not necessarily much bigger than the size of the circuits elements that are used. At these frequencies, the electrical response of a structure becomes highly dependent on its geometry. Thus, in order to fabricate microwave resonators, we use distributed elements in the form of transmission lines, instead of using lumped elements such as capacitor and inductors. I next discuss the two types of transmission line resonators that we use in the experiments.

5.1.1 Transmission line resonators

Consider figure 5.1a. Assume that there exists a right traveling wave with a phasor representation given by $V_R = V_0^R e^{-jkz}$. We have seen that the ratio of voltage to current for such a transmission line is the characteristic impedance Z_c. But when the line is terminated in an arbitrary load, $Z_L \neq Z_c$, the ratio of voltage to current must be Z_L. Thus a reflected wave needs to be created with the appropriate amplitude and phase to satisfy this condition. The incident and reflected waves will interfere destructively and constructively generating a standing wave pattern through the transmission line. This pattern can be found by calculating the reflection coefficient Γ for a given load (Eq. 2.37).

$$\begin{aligned} V(z) &= V_0^R e^{-jkz} + V_0^L e^{jkz}, \\ &= V_0^R (e^{-jkz} + \Gamma e^{jkz}), \qquad (5.1) \\ I(z) &= \frac{V_0^R}{Z_c} e^{-jkz} - \frac{V_0^L}{Z_c} e^{jkz}, \\ &= \frac{V_0^R}{Z_c} (e^{-jkz} - \Gamma e^{jkz}). \qquad (5.2) \end{aligned}$$

From the definition of impedance, $Z = I/V$, we can see that the observed impedance looking into the transmission line must vary with position. At a distance $z = -l$ from the load, the input impedance is given by

$$\begin{aligned} Z_{\text{in}} &= \frac{1 + \Gamma e^{-2jkl}}{1 - \Gamma e^{-2jkl}} Z_c, \qquad (5.3) \\ &= Z_c \frac{Z_L + jZ_c \tan(kl)}{Z_c + jZ_L \tan(kl)}. \qquad (5.4) \end{aligned}$$

The boundary condition imposed at both $z = -l$ and at $z = 0$ define the impedance seen and the type of resonator we have created.

Short-circuited quarter-wavelength resonator

Figure 5.1 shows a transmission line terminated at one end in a load impedance $Z_L = 0$, which is usually referred as a short circuit. The other end is left open. This

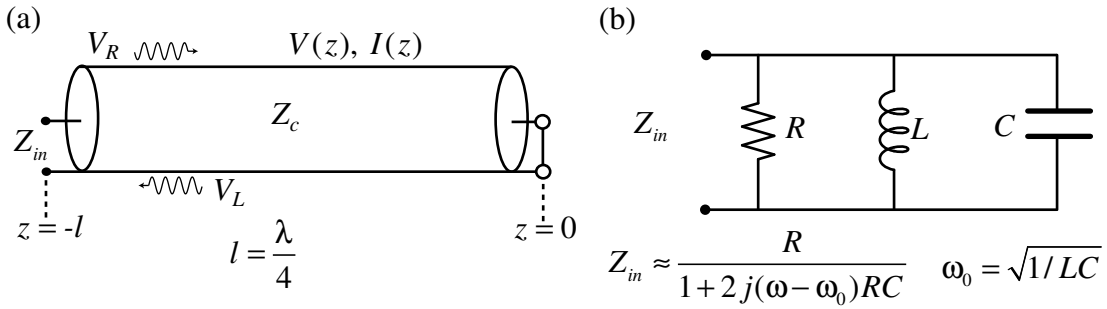

Figure 5.1: (a) A short-circuited transmission line of length $l = \lambda/4$. (b) A parallel RLC-resonator. In the high-Q limit, the impedance $Z_{\rm in}$ of the resonator will resemble the impedance $Z_{\rm in}$ of the short-circuited section of transmission line shown in (a).

configuration creates a standing wave resonance for a signal whose wavelength is $\lambda = 4l/n$ for n an odd integer. We will discuss only the case for $n = 1$, since it is the mode we will use. Therefore, $l = \lambda/4$ and this resonator is called a quarter-wavelength ($\lambda/4$) resonator. To make the analysis more accurate, I will consider a lossy transmission line. The only change in the previous expression is to replace jkl with $(\alpha + jk)l$, where α is the attenuation constant of the transmission line and whose origin can be either losses in the conductor or dielectric of the line. For a shorted end, the input impedance seen at $z = -l$ is given, from Eq. (5.4) by:

$$\begin{aligned} Z_{\rm in} &= Z_c \tanh(\alpha l + jkl), && (5.5)\\ &= Z_c \frac{1 - j\tanh(\alpha l)\cot(kl)}{\tanh(\alpha l) - j\cot(kl)}. && (5.6) \end{aligned}$$

We can then assume that $l = \lambda/4$ at $\omega = \omega_0$, and $\omega = \omega_0 + \Delta\omega$. With these assumptions

$$kl = \frac{\pi}{2} + \frac{\pi\Delta\omega}{2\omega_0}.$$

For a small amount of loss, $\tanh(\alpha l) \approx \alpha l$, and expanding to first order in $\Delta\omega/\omega_0$

$$\begin{aligned} Z_{\rm in} &= Z_c \frac{1 + j\alpha l\pi\Delta\omega/2\omega_0}{\alpha l + j\pi\Delta\omega/2\omega_0},\\ &\approx \frac{Z_c}{\alpha l + j\pi\Delta\omega/2\omega_0}. && (5.7) \end{aligned}$$

Eq. (5.7) has the same form as the impedance of a parallel RLC resonator circuit in the high-Q limit (Fig. 5.1b)

$$Z_{\rm in}^{RLC} = \frac{1}{1/R + 2j\Delta\omega C}.$$

Note that in this expression, we have included internal losses of the circuit as a resistor R. This resistor R is not related with the characteristic impedance Z_c of the transmission line coupled to our resonator. We can identify the resistance, capacitance, inductance, and quality factor of the equivalent circuit as:

$$R = Z_c/\alpha l. \tag{5.8}$$

$$C = \frac{\pi}{4\omega_0 Z_c}. \tag{5.9}$$

$$L = \frac{1}{\omega_0^2 C}. \tag{5.10}$$

$$Q_l = \omega_0 RC = \frac{\pi}{4\alpha l}, \tag{5.11}$$

showing that the quality factor Q_l decreases as the attenuation of the line α increases. Here, Q_l is the intrinsic quality factor associated with internal losses of the resonator, and not the coupling quality factor Q we used in Chapter 2. In the next section, I will describe how we couple power to these resonators.

Open-circuited half-wavelength resonator

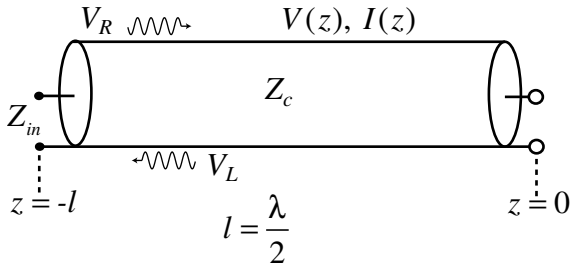

Figure 5.2: An open-circuited length of transmission line. For lengths of $l = n\lambda/2$, this transmission line will be a resonator.

Another kind of resonator we will be using is the open-circuited half-wavelength ($\lambda/2$) resonator, as shown in figure 5.2. Such a resonator will behave as well as a parallel resonant circuit, when the length is $l = \lambda/2$ or multiples of $\lambda/2$. The input impedance is given by

$$Z_{\text{in}} = Z_c \coth(\alpha l j k l).$$

In this case,

$$kl = \pi + \frac{\pi \Delta\omega}{\omega_0}.$$

Doing similar approximations to the ones done for the $\lambda/4$ resonator, the input impedance seen at $z = -l$ is

$$Z_{\text{in}} = \frac{Z_c}{\alpha l + j\Delta\omega\pi/\omega_0}. \tag{5.12}$$

Again, comparing it with the impedance of a parallel RLC resonator, the equivalent values for the resistance, capacitance, inductance and quality factor are

$$R = Z_c/\alpha l, \tag{5.13}$$

$$C = \frac{\pi}{2\omega_0 Z_c}, \tag{5.14}$$

$$L = \frac{1}{\omega_0^2 C}, \tag{5.15}$$

$$Q_l = \omega_0 RC = \frac{\pi}{2\alpha l}. \tag{5.16}$$

5.1.2 Coplanar waveguide transmission lines

So far the description of the transmission line resonator has been rather general, without describing what kind of structure we are using. In any physical implementation of a transmission line, the geometry must be chosen to best fulfill our needs. Due to several reasons, our choice was to use coplanar waveguide transmission lines (Fig. 5.3). A first advantage arises from the fact that the signal ground and conductors lie in the same plane, which makes it simple to create an electrical short on a chip. In addition the dimensions of the coplanar waveguide can be scaled while preserving the

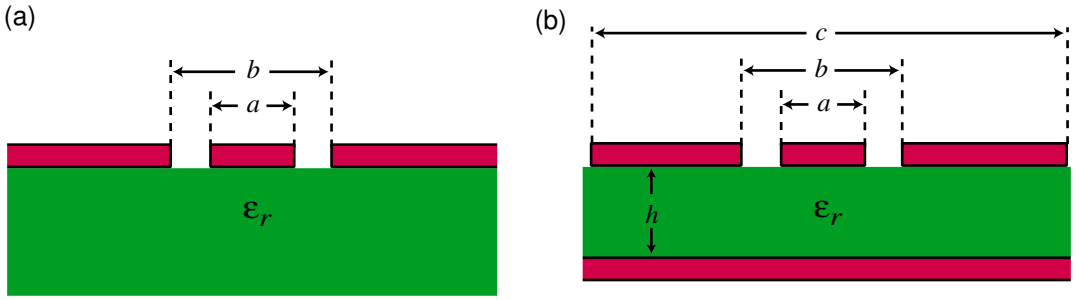

Figure 5.3: Coplanar waveguide geometry. (a) Ideal case, where the ground planes and the dielectric are assumed to extend to infinity. (b) A more realistic case of a coplanar waveguide transmission line where both the ground planes and the dielectric are finite. The dielectric is backed by a ground plane.

wave impedance. As we will see, the impedance of the transmission line depends on the ratio of the width of the center conductor to the gaps. As long as that ratio is kept the same, the geometry of the transmission line can be scaled from large structures to which we can attach macroscopic wires down to very small structures compatible with the micron size of the Josephson junctions.

The ideal coplanar waveguide (CPW) consists of two slots each of width $W = (b - a)/2$ printed on a dielectric substrate (Fig. 5.3a) . The spacing between the slots is denoted by a. The ground plates extend to infinity as well as the dielectric (infinitely thick substrate). While any physical implementation can be treated using the equations that describe a transmission line, the exact expressions for the phase velocity and impedance depend on the geometry. Approximate expressions for both the impedance and the phase velocity can be found using conformal transformations [67]. Assuming non-magnetic substrates for which $\mu = \mu_0$, for the ideal coplanar waveguide

shown in figure 5.3a the expressions are

$$\epsilon_{re} = \frac{\epsilon_r + 1}{2}, \tag{5.17}$$

$$v = \frac{c}{\sqrt{\epsilon_{re}}}, \tag{5.18}$$

$$Z_c = \frac{30\pi}{\sqrt{\epsilon_{re}}} \frac{K'(\kappa_1)}{K(\kappa_1)}, \tag{5.19}$$

with K and K' being the complete elliptic integral of the first kind and its complement, and

$$\kappa_1 = \frac{a}{b}.$$

If we introduce the necessary modifications to include the fact that our dielectric is not infinite and neither are the ground planes (Fig. 5.3b), the expressions are sligthly more complicated [67]. Defining κ_2 and κ_3 as

$$\kappa_2 = \frac{a}{b}\sqrt{\frac{1 - b^2/c^2}{1 - a^2/c^2}},$$

$$\kappa_3 = \frac{\sinh(\pi a/2h)}{\sinh(\pi b/2h)}\sqrt{\frac{1 - \sinh^2(\pi b/2h)/\sinh^2(\pi c/2h)}{1 - \sinh^2(\pi a/2h)/\sinh^2(\pi c/2h)}}.$$

The new expressions for the phase velocity and characteristic impedance are

$$\epsilon_{re} = 1 + \frac{\epsilon_r - 1}{2} \frac{K(\kappa_3)}{K'(\kappa_3)} \frac{K'(\kappa_2)}{K(\kappa_2)}, \tag{5.20}$$

$$v = \frac{c}{\sqrt{\epsilon_{re}}}, \tag{5.21}$$

$$Z_c = \frac{30\pi}{\sqrt{\epsilon_{re}}} \frac{K'(\kappa_2)}{K(\kappa_2)}. \tag{5.22}$$

For our resonators, we designed our coplanar waveguide with ground planes of reduced width, as can be seen in figure 5.4. The main reason that we used such reduced-width ground planes is to reduce the potential influence of trapped vortices of magnetic flux. To elaborate, superconductors will exhibit a characteristic referred to as Meissner effect which consists of the expulsion of a magnetic field from the superconductor [33]. In general, however, superconductors rarely exhibit a complete field expulsion; grain boundaries, normal inclusions, and other defects serve to trap magnetic flux within

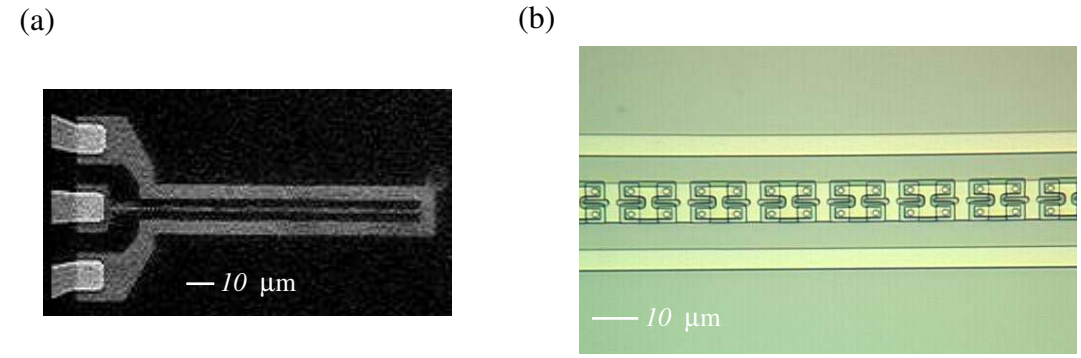

Figure 5.4: Pictures of the two kind of devices discussed in chapter 6. In both cases 5 μm-wide ground planes were used in order to avoid flux trapping close to the SQUIDs.

the superconductor. Flux expulsion can be further decreased by the geometry of the sample. Thus, for actual experiments, the Meissner effect is typically incomplete and strongly dependent on sample preparation and geometry. In our case, this concern is very important as flux trapped in the ground planes close to the SQUIDs could introduce flux noise in the SQUID loops. Although the resonators will in general be kept in a low-magnetic field environment, the situation is always critical as the superconductor is cooled though the critical temperature T_c. In Ref. [68], the authors studied flux expulsion in the case of a thin-film superconducting strip of width W when a strip is cooled through T_c. In that Letter, it is shown that such a strip exhibits a complete Meissner expulsion of vortices below a critical field B_m, independent of the details of material parameters. Furthermore, this expulsion has a universal characteristic, with $B_m = \Phi_0/W^2$. For a width of 5 μm, this maximum field for vortex expulsion is 0.8 gauss, slightly bigger than the 0.3-0.6 gauss of Earth's magnetic field. We designed the CPW so that we could cooldown through T_c with a magnetic field equal to that of the Earth's magnetic field without having trapped vortices close to the SQUIDs. In order to further protect the sample we have two levels of magnetic shielding: a cryoperm shield around the sample that sits at 15 mK and a μ-metal shield at room temperature.

5.1.3 Coupling a cavity to a transmission line

As yet I have not described the way we will excite the resonators. We could directly connect a transmission line to the resonator, as it was done in chapter 2. However, this would allow the energy stored in the cavity to leak out too quickly; that is, the resonator would be heavily loaded, and the Q would be too low. To reduce the coupling strength, we use a small capacitor to connect the resonator to the transmission line we use to launch signals as shown in figure 5.5. The impedance mismatch that the capacitor represents is analogous to a dielectric mirror that is partially transparent. Since an ideal capacitor is lossless, but transmits a small amount of power, we can inject power to the cavity or allow energy to leak out of the cavity through this "microwave mirror." Another advantage over directly connecting the resonator and the transmission line is that the coupling capacitor serves as a dc-filter for the Josephson junctions that will be inside the cavity.

In order to derive an expression for the quality factor Q, there are a variety of approaches, of which I will describe two for being the most useful. First I will consider the case of a lossy $\lambda/4$ resonator and then a lossless $\lambda/2$ resonator. The reason for this is that by comparing the final expression of the two resonators, it will become obvious that the intrinsic loss of the resonator can be modeled as just an extra port. This fictitious port allows energy to leak out of the cavity (through dissipation) as well as admits energy in the form of thermal noise.

Single port

Next we consider a $\lambda/4$ short-circuited resonator coupled to a transmission line through a capacitor C_1 (Fig. 5.5a). The normalized input impedance seen by the feedline with impedance Z_c is

$$z(\omega) = \frac{j}{Z_c}\left(Z_r \tan(kl) - \frac{1}{b_c}\right) \tag{5.23}$$

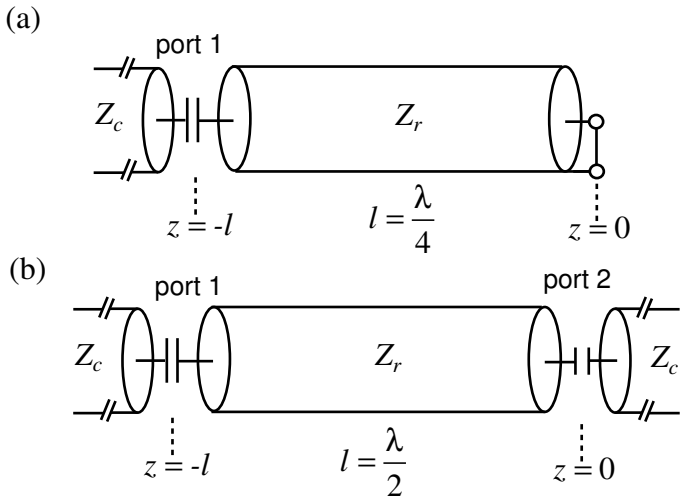

Figure 5.5: (a) $\lambda/4$-resonator coupled to a transmission line of impedance Z_c by a capacitor. (b) $\lambda/2$-resonator coupled to two transmission lines of impedance Z_c by two capacitor. Port 1 is defined as the strongly coupled port and port 2 is the weakly coupled port.

where $b_c = Z_c \omega C_1$ is the normalized susceptance of the coupling capacitor. Resonance occurs when

$$\cot(kl) - b_c = 0.$$

Solutions to this transcendental equation can only be found numerically. However, in practice $b_c \ll 1$. This is equivalent to saying that the coupling quality factor from port 1 $\sqrt{Q_1} \gg 1$. This requirement allows us to assume that the new resonance frequency will be close to the frequency for which $kl = \pi/2$ (the first resonance frequency of the unloaded resonator ω_0). By doing a Taylor expansion around the new loaded resonance frequency ω_r, it can be shown that the normalized impedance is given by

$$z(\omega) = j \frac{\pi}{2\omega_r Z_c Z_r (\omega_r C_1)^2} (\omega - \omega_r).$$

So far we have not included losses. For high-Q cavities, loss can be easily included following the common recipe of replacing the resonant frequency ω_r with the complex resonance frequency $\omega_r(1 + j/2Q_l)$ [13,16]. In this substitution, Q_l is the quality factor

associated with the intrinsic loss of the resonator, Eq. (5.11). Then, the normalized impedance of the lossy $\lambda/4$ resonator is

$$z(\omega) = \frac{Q_1}{Q_l}\left(1 + 2jQ_l\frac{(\omega - \omega_r)}{\omega_r}\right) \tag{5.24}$$

where the quality factor associated with the coupling port Q_1 is given by

$$Q_1 = \frac{\pi}{4}\frac{1}{Z_c Z_r(\omega_r C_1)^2} \tag{5.25}$$

I can then calculate the reflection coefficient using Eq. (5.24),

$$\Gamma = \frac{\Gamma_0 + 2jQ\delta\omega}{1 + 2jQ\delta\omega} \tag{5.26}$$

where $\delta\omega = (\omega_r - \omega)/\omega_r$, Q is the total quality factor

$$\frac{1}{Q} = \frac{1}{Q_1} + \frac{1}{Q_l} \tag{5.27}$$

and Γ_0 is the reflection coefficient at the resonance frequency, and it is given by

$$\Gamma_0 = \frac{Q_1 - Q_l}{Q_1 + Q_l}. \tag{5.28}$$

Note also that in this case, there are two types of quality factors we are interested in: the internal quality factor, Q_i and the coupling quality factor, Q_1. Defining the coupling coefficient g as

$$g = \frac{Q_l}{Q_1} \tag{5.29}$$

we find there are three different cases.

(1) $g < 1$ The resonator is undercoupled to the feedline.

(2) $g = 1$ The resonator is critically coupled to the feedline.

(3) $g > 1$ The resonator is overcoupled to the feedline.

The reflection coefficient will be very different depending on the value of g as can be seen in figure 5.6.

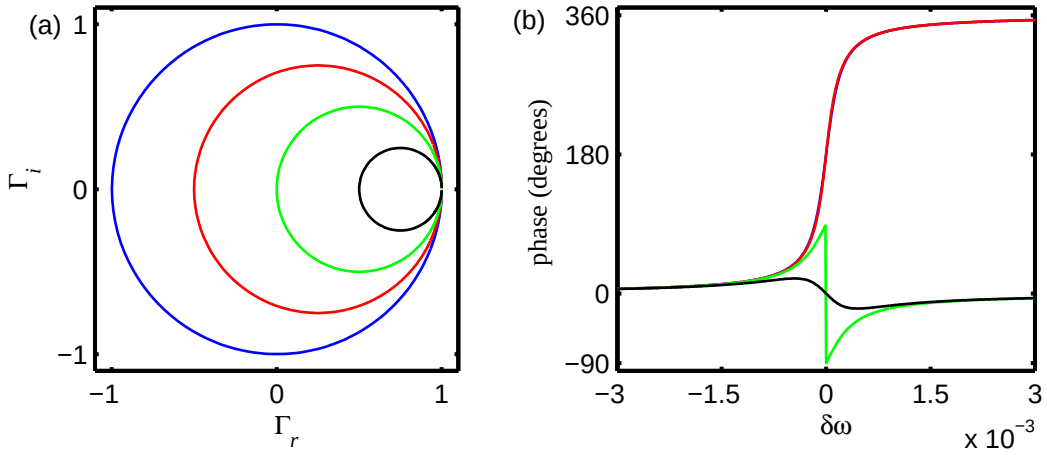

Figure 5.6: (a) Parametric plot of the real and imaginary part of the reflection coefficient Γ as a function of frequency for different values of coupling coefficient: $g = \infty$ (blue), $g = 3$ (red), $g = 1$ (green) and $g = 1/3$ (black). (b) Phase of Γ as of function of the detuning $\delta\omega = (\omega - \omega_r)/(\omega_r)$ for the same coupling coefficients as in (a). Regardless of the exact value, for $g > 1$ the phase evolves a full 360° as we sweep the frequency. This is not the case for $g \leq 1$, in which the phase only evolves 180° or less as we sweep the frequency through resonance.

Double port

We could use a similar method to the one described above for the single port to calculate the coupling quality factors associated with the two ports connected via coupling capacitors to a $\lambda/2$-resonator as shown in figure 5.5b. However, I will use energy consideration so that the meaning of quality factor becomes obvious [69]. For now, let's assume a lossless transmission line. This loading (or coupling) calculation yields the coupling quality factors, Q_j, where $j = 1, 2$ denotes the port.

Let's assume that the resonator has been initially excited, and some energy is stored. Due to the coupling, this energy is going to leak out through the capacitors. In a $\lambda/2$-resonator we have seen that the voltage antinodes are located at the end of the resonator, where the capacitors are located, and using the shape of the voltage standing

wave we can estimate the electric energy stored inside.

$$E_c = \frac{1}{2} C_l \int_{-l}^{0} dz \langle V^2(z,t) \rangle$$

where the averaging $\langle V^2(z,t) \rangle$ is done over one cycle of oscillation. Assuming that the coupling is weak enough that the normal modes of the resonator are close to the unperturbed one, the shape is just one half of a sinusoidal wave, so we can perform the integration. Furthermore, on resonance, the electric and magnetic energy stored in the transmission line are the same, so the total energy is given by

$$E = \frac{1}{2} C_l l \langle V^2(t) \rangle$$

where the extra factor of 2 is from the space integration. In order to calculate the power dissipated through the coupled ports, we calculate the current flowing in the transmission line, $P = \langle (I_1^2 + I_2^2) \rangle Z_c$, where I_j indicates the current flowing out of port j. Assuming that the coupling capacitors are the dominant impedance (basically that $Z_c \ll 1/\omega C_j$), $I_j \approx V \omega C_j$, and the power dissipated is then

$$P = \langle (C_1 V(t)^2 + C_2 V(t)^2) \rangle \omega Z_c.$$

The total quality factor Q of the resonator is defined as [16]

$$\begin{aligned} Q &= \omega \frac{\text{average energy stored}}{\text{energy loss/second}} \\ &= \omega_0 \frac{1/2 C_l l \langle V^2(t) \rangle}{\langle (C_1 V(t)^2 + C_2 V(t)^2) \rangle \omega Z_c} \end{aligned}$$

This expression reduces to

$$\frac{1}{Q} = \frac{1}{Q_1} + \frac{1}{Q_2} \tag{5.30}$$

with the coupling Q_j given by

$$Q_j = \frac{C_l l}{2 Z_c C_j^2 \omega_0} \tag{5.31}$$

$$= \frac{\pi}{2 Z_r Z_c (C_j \omega_0)^2}. \tag{5.32}$$

Comparing Eqs. (5.30) and (5.27), we can see that in terms of the total quality factor, port 2 just looks like extra loss. This is even more obvious when we calculate the reflection coefficient S_{11}.[1] S_{11} can be calculated by doing a similar procedure to estimate the impedance of the $\lambda/2$ resonator close to the new loaded resonance frequency ω_r as it was discussed for the $\lambda/4$ resonator. The result is

$$S_{11} = \frac{\Gamma_0 + 2jQ\delta\omega}{1 + 2jQ\delta\omega} \tag{5.33}$$

where Γ_0 is given by

$$\Gamma_0 = \frac{Q_1 - Q_2}{Q_1 + Q_2}.$$

The fact that loss can be modeled as an extra port will simplify the analysis of the nonlinear resonator in the next section.

Intrinsic Resonator Losses

The measured Q of a resonator is expected to depend on the total energy loss per cycle of the resonator. We expect energy to leak out through several paths. Some paths, like one through the coupling capacitor, are designed by us, while others, like the loss of energy to electromagnetic radiation, are governed by geometry and material parameters. The quality factors loss terms add as follows:[2]

$$\frac{1}{Q} = \frac{1}{Q_1} + \sum_{\text{all other paths}} \frac{1}{Q_j}.$$

Ideally the quality factor of a resonator would be something that we would completely control by adjusting the coupling capacitors. However, this is not necessarily the case. There are three primary mechanisms of loss in superconducting microwave resonators:

[1] For the $\lambda/2$-resonator, I will use S_{11} to refer to the reflection coefficient as opposed to Γ as in the $\lambda/4$-resonator. This is done to distinguish the fact that in the $\lambda/2$-resonator, there is actually two possible scattering parameters we will measure, S_{11} and S_{12}.

[2] The equivalent expression for the linewidths is simpler as they just add:

$$\gamma = \gamma_1 + \sum_{\text{all other paths}} \gamma_j.$$

resistive, dielectric and radiative losses. In principle, resistive losses should be negligible as we are dealing with superconducting devices. It has been shown that radiative losses would limit the quality factor of a resonator like the ones studied in this thesis to 10^6 [69], so we do not consider them as limiting factors as they are several orders of magnitude larger than our designed coupling Qs.

Dielectric loss can also affect the Q of the resonator. Microwave materials are usually characterized by specifying the real permittivity and the loss tangent all as a complex number

$$\epsilon = \epsilon' - j\epsilon'' = \epsilon'(1 - j\tan\delta)$$

where $\tan\delta$ is referred to as the loss tangent. In order to reduce these losses, we use high-resistivity silicon for our resonators, which have been shown to achieve Qs as high as 100,000 [70]. However, due to the trilayer process used to fabricate the second generation of devices (see appendix C), we need a layer of deposited SiO_2 as an insulating layer. This layer is known to be extremely lossy (see for example, Ref. [59]) and could be a limiting factor for our internal quality factor.

5.2 Cavity JPA

If we were to put a Josephson junction inside a microwave cavity resonator, the analysis of the JPA could be done in terms of the quantum network theory described in sections 2.3.1 and 3.3.1. Close to the resonance frequency the full circuit could be mapped into one of the two circuits shown in figure 3.16. Such an implementation has been used in the bifurcation limit as the JBA explained in section 4.3.4 [71]. However, one of the problems with such amplifiers is that they will have a very narrow bandwidth. In order to partially circumvent this problem, a SQUID (or maybe even a few SQUIDS) instead of a Josephson junction can be used. This modification provides some tunability to the resonance frequency, and thus in the amplified band of the JPA [72,73].

Nevertheless, in such implementations, the Josephson inductance is heavily diluted by the geometrical inductance of the microwave cavity (small participation ratio p). Thus, for low magnetic flux (Φ close to zero), the resonance frequency is rather insensitive to flux and it is only when the applied flux is close to $\Phi_0/2$ that large changes of resonance frequency can be achieved. Yet, for such fluxes, the critical current of the SQUID is very small, and therefore the critical power of the resonator is very small as well. Very small critical power has the effect of making the amplifier saturation power too small to be useful as an amplifier. In addition, in those implementations, it has also been observed that close to $\Phi_0/2$, the intrinsic losses of the resonator increase. This additional loss would hurt the performance of the amplifier [72, 73]. When we were designing our parametric amplifier, we were trying to fabricate a JPA that could be used over a wide range of frequencies without a large degradation of the amplifier performance. I next describe our approach.

5.2.1 Widely tunable resonator

In order to create an amplifier with a tunable band, we decided to create a transmission line whose phase velocity across the whole resonator could be tuned by an external knob that we had control over. Then for a fixed length of a transmission line resonator, by adjusting the phase velocity we could adjust the resonance frequency. Therefore, instead of embedding 1 or a few SQUIDs inside a cavity, our approach was to take a CPW transmission line and replace the center conductor with a long series array of SQUIDs (Fig. 5.7a). We have seen in section 3.2 that the small signal inductance of a Josephson junction is given by $L_{J0} = \phi_0/I_0$. I also showed that the critical current of a SQUID I_0^S can be tuned by applying a magnetic field. Therefore, a resonator made out of a transmission line like the one shown in figure 5.7a would allow us to adjust the phase velocity and the resonator resonance frequency [74]. By adjusting the resonance frequency, we adjust the amplified band of the JPA. This feature will allow us to use

the amplifier over the whole tunable band.

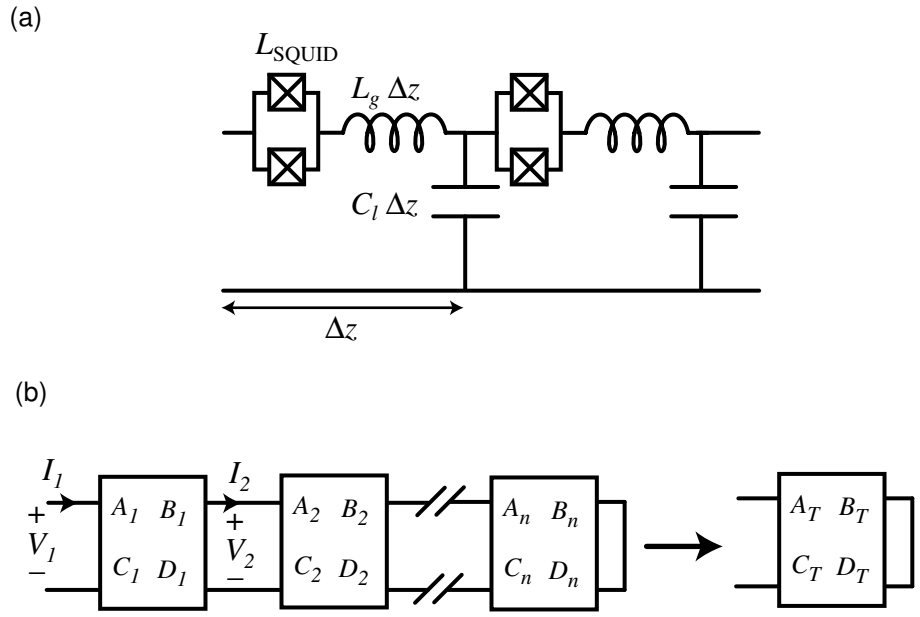

Figure 5.7: (a) Lumped element model of the series array of SQUIDs used to fabricate a JPA. In each cell, the capacitance to ground of the center conductor is modeled by the geometrical capacitance $C_l\Delta z$ of the CPW. The inductance of the cell is modeled by the Josephson inductance of the SQUID and the small geometrical inductance $L_l\Delta z$ of the CPW. (b) The behavior of such periodic structure can be easily described by calculating the ABCD-matrix of each cell and calculating the total ABCD-matrix of the whole array.

At microwave frequencies the SQUIDs are spaced much less than a wavelength apart, so we treat the array as a continuous medium with flux tunable and intensity dependent phase velocity (c.f. an optical Kerr medium). We call this nonlinear effective medium a Josephson metamaterial. The resonance frequency (f_{res}) of this cavity is proportional to the phase velocity. As the inductance per unit length L_l and therefore the phase velocity are nonlinear functions of the currents due to the SQUIDs in the center conductor, f_{res} is a function of the intensity of the microwave field stored in the cavity. When a large tone (the pump) is applied through the coupled port close to the resonance frequency of the cavity, it makes the resonance frequency oscillate at twice the pump frequency just as in the case of a lumped-element resonator (Eq. 3.35). This

process creates parametric gain [13].

Josephson parametric amplifiers using series arrays have been suggested in the literature [56] and even implemented [48, 57]. However, in Ref. [48], the array was treated as a lumped element rather than as a medium. In Refs. [56, 57], the array is treated as a nonlinear medium, as in our case. Nonetheless, in their implementation Josephson junctions instead of SQUIDs were used. In Ref. [57], it is argued that by using a distributed parametric amplifier with a nonlinear medium, the problem of a small bandwidth is eliminated. However, distributed parametric amplifiers still have a limited gain-bandwidth product [57] and other concerns such as matching the Josephson metamaterial to the feedline transmission line arise.[3] In addition a distributed parametric amplifier requires at least one junction per wavelength, and length of several wavelengths. From a fabrication point of view, it is hard to do at microwave frequencies on a chip.

In order to estimate the magnetic field dependance of the resonator and justify treating the array as a continuous medium, we model the cells as shown in figure 5.7a, where we have included the small geometrical inductance that the cells have (for this analysis only the linear part of the SQUID inductance is used). The arrays are made out of hundreds of such cells, with the last of these cells loaded by a boundary condition that will depend on the type of resonator we are building. As an example we will model a shorted $\lambda/4$ resonator. Such periodic structures as the one shown in figure 5.7a, can be easily analyzed using the method of ABCD matrix [16]. (Fig. 5.7b). The ABCD matrix consist of a 2×2 transmission matrix defined only for a two-port network. For a microwave network that consists of a cascade connection of multiple two-port networks as the one shown in figure 5.7, the analysis is simplified by using this approach. The

[3] If the characteristic impedance of the transmission line used to send and recover the signals from the distributed JPA and the characteristic impedance of the Josephson metamaterial are too different, well defined standing waves modes appear and the Josephson metamaterial would just be a very strongly coupled microwave cavity JPA.

ABCD matrix of the whole network is found by multiplying the ABCD matrices of its components. The components of the ABCD matrix are defined using the convention shown in figure 5.7b

$$V_1 = A_1 V_2 + B_1 I_2,$$

$$I_1 = C_1 V_2 + D_1 I_2.$$

The full network is then given by

$$\begin{pmatrix} A_T & B_T \\ C_T & D_T \end{pmatrix} = \begin{pmatrix} A_1 & B_1 \\ C_1 & D_1 \end{pmatrix} \begin{pmatrix} A_2 & B_2 \\ C_2 & D_2 \end{pmatrix} ... \begin{pmatrix} A_N & B_N \\ C_N & D_N \end{pmatrix}. \tag{5.34}$$

For a simple cell as shown in figure 5.8a, the ABDC matrix can be easily calculated:

$$\begin{pmatrix} A & B \\ C & D \end{pmatrix} = \begin{pmatrix} 1 + Z_1/Z_2 & Z_1 \\ 1/Z_2 & 1 \end{pmatrix} \tag{5.35}$$

where Z_1 consists of the total inductance of the cell, the small geometrical inductance $L_l \Delta_z$ and the linear part of the SQUID inductance L^S_{J0}; and Z_2 is the small capacitance to ground of the transmission line $C_l \Delta_z$. For the simple case where all the cells are exactly the same, it is possible to show that a large enough array can be treated as a continuous medium with an effective phase velocity approximately given by

$$v_p = \frac{\Delta z}{\sqrt{(L^S_{J0} + L_l \Delta_z)(C_l \Delta_z)}} \tag{5.36}$$

where I have assumed that the wavelength of microwave modes we are interested in is much bigger than the cell spacing Δz.[4] In this case, a simple expression can be found for the resonance frequency

$$f_{\rm res}(\Phi) = f^0_{\rm res} \sqrt{\frac{L_{T,0}}{L_l \Delta z + L^S_{J0}(\Phi)}}, \tag{5.37}$$

$$= f^0_{\rm res} \sqrt{\frac{L^0_T}{L_l \Delta z + L^{S,0}_{J0} / |\cos(\pi \Phi / \Phi_0)|}}, \tag{5.38}$$

[4] We can make an analogy with a similar system such as a one-dimensional array of masses connected with springs as the one studied in the context of phonons. In that case, for very large wavelength phonons or frequencies much smaller than the Debye frequency of the system, it can be shown that the dispersion relation reduces to a linear expression between the frequency and the wavelength. Eq. 5.36 is completely equivalent to this limit in the phonon case.

where $L_{T,0} = L_l \Delta z + L_{J0}^S(\Phi = 0)$, $L_{J0}^{S,0} = L_{J0}^S(\Phi = 0)$ and in the second line I have assumed the most ideal case, which implies identical junctions and negligible loop inductance. In order to take into account loop inductance or different junctions in the SQUID, we only need to substitute the appropriate flux-dependant value $L_{J0}^S(\Phi)$ in Eq. (5.37). Examples for the ideal case, Eq. (5.38), and the case of finite loop inductance are plotted in figure 5.9.

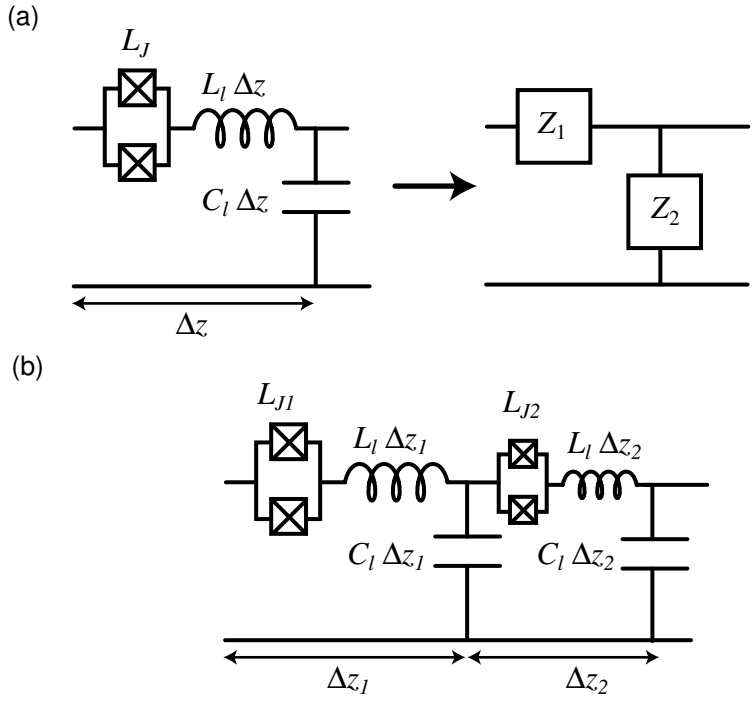

Figure 5.8: (a) The unit cell of the microwave network used for the ABCD matrix analysis in the ideal case of completely uniform cells. (b) A more complicated case consist of a network with two different kind of cells (both the length of the cell and the SQUIDs are different). The primitive cell consists of two of such smaller cells grouped together.

Asymmetries in the junctions, or finite loop inductance only prevent a complete suppression of the critical current of the SQUIDs (and therefore, put a limit on the lowest achievable resonance frequency). However, other more serious problems can arise in such large arrays. One in particular that we have observed is the case of non-

identical SQUID areas. For example, one of the devices discussed in chapter 6 exhibited this problem. The analysis with ABCD matrices can be done similarly as in the previous case, as long as in the matrix-multiplication we consider the fact that there are going to be two different ABCD matrices, one for each cell. It is also possible to consider a larger cell of size $\Delta z_T = \Delta z_1 + \Delta z_2$ that encompasses both cells (Fig. 5.8b). Again, in the case where the wavelength is much larger than the cell size, the array will behave as a continuous medium with a phase velocity approximately given by

$$v_p = \frac{\Delta z_T}{\sqrt{(L_{J2} + L_{J1} + L_l \Delta z_T)(C_l \Delta z_T)}},$$

from which the resonance frequency can be easily obtained.

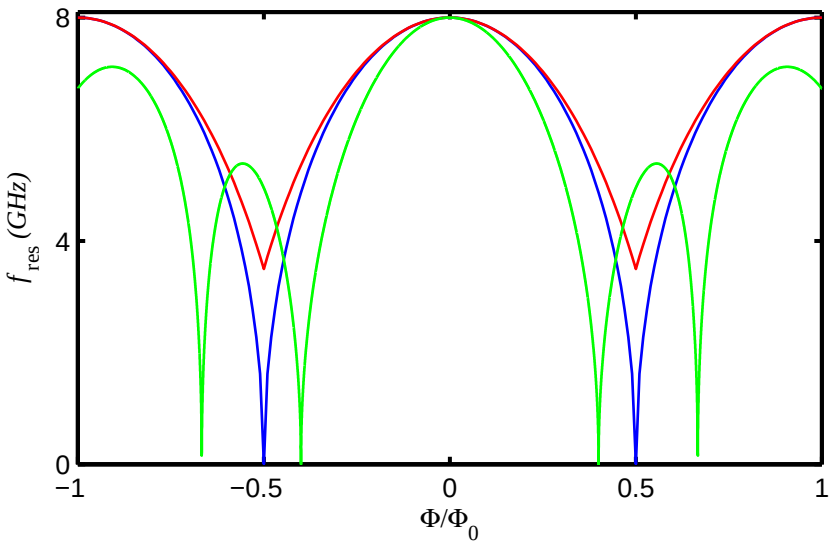

Figure 5.9: Resonance frequency f_{res} as function of flux for there different networks: an uniform array with identical junctions and negligible loop inductance (blue), an uniform array with identical junctions and $L_{\text{loop}} I_0/\Phi_0 = 0.1$ (red), and an array that presents two size of cells, $\Delta z_1 = 1.67 \Delta z_2$ (green).

5.2.2 SQUID arrays: a metamaterial with a Kerr-nonlinearity

So far we have only considered the linear limit of the Josephson junction array resonator. In order to consider the nonlinear limit, microwave circuit theory becomes

extremely cumbersome if we want to analyze the 400 degrees of freedom that describe the 400 SQUIDs. Instead, we use the formalism of IOT. In order to do that, we model the Josephson metamaterial as a Kerr-medium. We will estimate the effective Kerr constant following closely Ref. [38] where they use the methods of quantum network theory (Ref. [15]) to analyze a nonlinear transmission line.

The Lagrangian of a lossless transmission line with a length l is given by Eq. (2.19)

$$\begin{aligned}\mathcal{L} &= \int_{-l}^{0} dz \frac{C_l}{2}\left(\frac{\partial\phi(z,t)}{\partial t}\right)^2 - \frac{1}{2L_l'}\left(\frac{\partial\phi(z,t)}{\partial z}\right)^2, \\ &= \frac{1}{2}\int_{-l}^{0} dz C_l V^2 - L_l' I^2, \end{aligned} \tag{5.39}$$

where C_l and L_l' are the capacitance and inductance per unit length. However, in this case L_l' is a nonlinear function of the current in the transmission line given by

$$L_l' = L_{l0} + \Delta L_l \left(\frac{I}{I_0}\right)^2 \tag{5.40}$$

where I is the current in the transmission line, and I_0 is the critical current of the medium.[5] The quantization of Eq. (5.39) is described in [38] and is not reproduced here, but only briefly described. As in the linear resonators, the imposed boundary conditions set the resonance frequency as well as the basis used for expanding $I(z,t)$:

$$I(z,t) = \sum_n v_n(t) u_n(z).$$

The normal modes in the z-coordinate are the solutions of

$$\frac{d}{dz}\left(\frac{1}{C_l}\frac{du_n}{dz}\right) = -\omega_n^2 L_{l0} u_n \tag{5.41}$$

with the following orthonormalization condition:

$$\int_{-l}^{0} L_{l0} u_n u_m = \delta_{n,m}.$$

[5] Reference [38] was meant to study the parametric gain observed in resonators made out of thin-film superconductors which exhibit a nonlinearity described by Eq. (5.40). In that case I_0 is just a parameter that describes the nonlinearity of the film and it is a function of geometry and current distribution in the superconducting film [64]. In our case, the nonlinearity of the medium comes primarily from the nonlinear Josephson inductance of the SQUIDs and therefore, I_0 will be given by the critical current of the SQUIDs I_0^S.

In Eq. (5.41), C_l and L_{l0} can be space-dependant. Nonuniform transmission lines can be used to to avoid strong intermode coupling when the resonators are driven non-linear, as the different n-modes would not be equally spaced. However, the resonators that we studied had uniform transmission lines. Ignoring the intermode coupling and all the other modes of the resonator except for the first mode, the Hamiltonian is approximately given by an expression similar to Eq. (3.40)

$$H = \hbar\omega_0 A^\dagger A + \frac{\hbar}{2} K A^\dagger A^\dagger A A$$

where K is the effective Kerr constant. K is given by [38]

$$K = -\frac{\hbar\omega_0^2}{I_0^2}\int_0^l dz u_0(z)^4 \Delta L_l. \tag{5.42}$$

For the the half-wavelength resonator, the boundary conditions used are

$$u_0(0) = u_0(-l) = 0,$$

and for the quarter-wavelength resonator

$$u_0(-l) = \frac{du_0(0)}{dz} = 0.$$

However, the final result for the Kerr constant K is equal for both cases, assuming an uniform transmission line, and it is given by

$$K = -\frac{3}{2}\frac{\hbar\omega_0^2}{I_0^2}\frac{\Delta L_l}{L_{l0}^2 l} \tag{5.43}$$

In order to determine the Kerr constant for a series array of SQUIDs (Fig. 5.7a), let's first consider the Lagrangian per cell of an array of Josephson junctions:

$$C_l \Delta_z \frac{V^2}{2} - L_l \Delta_z \frac{I^2}{2} + E_J \cos(\delta).$$

In the previous expression, I used Eq. (3.22) for the energy of the Josephson junction and L_l is the geometrical linear inductance per unit length of the transmission line. Again, doing a Taylor expansion and ignoring the constant terms that do not affect

the dynamics of the system, we obtain that the Lagrangian for a cell of size Δz with a Josephson junction is

$$C_l \Delta_z \frac{V^2}{2} - \frac{I^2}{2}\left[L_l \Delta_z + L_{J0} + \frac{L_{J0}}{4}\left(\frac{I}{I_0}\right)^2\right]. \tag{5.44}$$

Comparing Eq. (5.44) with Eq. (5.40), we deduce that in our case in the continuum-medium limit

$$L_{l0} \approx L_l + \frac{L_{J0}}{\Delta z}, \tag{5.45}$$

$$\Delta L_l \approx \frac{L_{J0}}{4\Delta z}. \tag{5.46}$$

In the case of a SQUID, the Kerr constant will be a function of the magnetic flux through its dependance of the SQUID critical current (Eq. 3.23). In the case that the self inductance of the SQUID loop is negligible compared to the Josephson inductances of the SQUID junctions, the SQUID can be described as a single junction with effective flux-dependent Josephson energy [75]:

$$E_J^S = \sqrt{E_{J,1}^2 + E_{J,2}^2 + 2E_{J,1}E_{J,2}\cos\left(\frac{2\pi\Phi_{\text{ext}}}{\Phi_0}\right)},$$

where $E_{J,i}$ is the Josephson energy of the $i = 1, 2$ junction. We then would obtain similar expressions to Eqs. (5.44-5.46), with $I_0 \to I_0^S(\Phi)$ and $L_{J0} \to L_{J0}^S(\Phi)$.

Once we have estimated the effective nonlinearity of our Josephson metamaterial, we can derive equivalent conditions to those explained in section 3.3.4. The main restriction comes form the need of having the current through the SQUIDs be much smaller than their critical currents when the amplifier is operated close to the bifurcation point. Assuming a current standing wave with an amplitude I_a, the total energy inside the resonator can be calculated by integrating over the standing wave shape. This yields:

$$E = \frac{1}{4}(lL_l)I_a^2$$

where I have assumed $I(z) = I_a \cos(\pi z/2l)$ and averaged over a cycle of oscillation. This energy is also equal to the number of photons inside the resonator times the energy per

photon, $E = \hbar\omega_0 N$. Using Eq. (3.47) for the critical number of photons, N_c, as well as Eq. (5.43) for the Kerr constant, I can then derive a condition similar to Eq. (3.83) so that $I_a/I_0 \ll 1$. This restriction is:

$$\frac{I_a}{I_0} = \sqrt{\frac{16}{3\sqrt{3}}\frac{\gamma}{\omega_0}\frac{L_{l0}}{\Delta L_l}} \ll 1 \tag{5.47}$$

Defining an effective participation ratio[6]

$$p = \frac{L_{J0}}{L_l \Delta z + L_{J0}},$$

then the restriction on the product of participation ratio and quality factor of the resonator is

$$\sqrt{\frac{32}{3\sqrt{3}}\frac{1}{Qp}} \ll 1.$$

Note that this expression is, except for a factor of the order of unity, equal to Eq. (3.83). The extra numerical factor is related to the averaging over the mode shape.

5.2.3 Loss and other ports

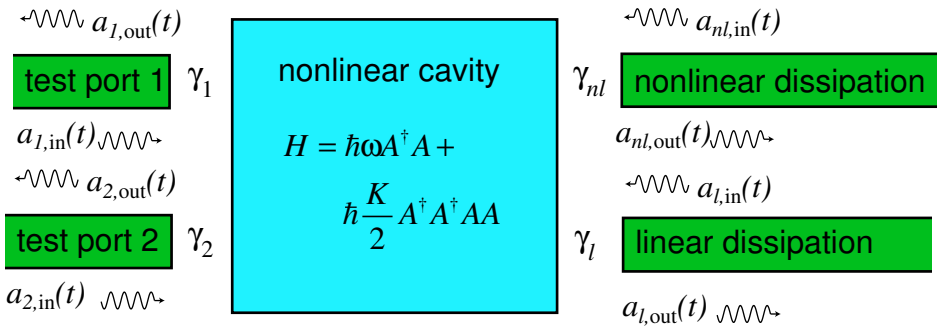

Figure 5.10: Nonlinear cavity coupled to two ports plus two additional loss ports: a linear loss port characterized by a coupling γ_l and a nonlinear loss port characterized by a coupling γ_{nl}.

The inclusion of loss in the theory is easily done with the methods of IOT. As it was shown in section 5.1.1 when we compared the results of the $\lambda/4$ and $\lambda/2$ resonator,

[6] The participation ratio defined here is similar to the one expected for a series RLC-resonator as the one shown in figure 3.16d (see Ref. [31]).

the loss behaves as an extra port (one whose only input is noise). Therefore, we model a resonator with loss by adding an extra port as shown in figure 5.10. The analysis is very similar to the one port case, with the only difference being that the sum in Eqs. (2.59) and (2.60) is done over all the n-ports (including the loss-ports). The analysis of the critical points gives similar results to Eqs. (3.45-3.47)

$$\omega_{p,c} = \omega_0 + \sqrt{3}\gamma\frac{K}{|K|}, \tag{5.48}$$

$$(b^c_{i,\mathrm{in}})^2 = \frac{4}{3\sqrt{3}}\frac{\gamma^3}{\gamma_i|K|}, \tag{5.49}$$

$$N_c = \frac{2\sqrt{3}\gamma}{3|K|}, \tag{5.50}$$

where i denotes the index port ($i = 1, 2$), and $\gamma = \gamma_1 + \gamma_2 + \gamma_l$.

For simplicity, I will consider the case where there is one driving port and one loss-port. In that case, it can be shown that the equivalent equation to Eq. (3.56) is given by

$$\begin{aligned} c_{1,\mathrm{out}}(\omega) &= \left(-1 + \frac{2\gamma_1(-i\omega + W^*)}{(-i\omega+\lambda_0)(-i\omega+\lambda_1)}\right)c_{1,\mathrm{in}}(\omega) + \\ &\quad \frac{2\gamma_1 V}{(-i\omega+\lambda_0)(-i\omega+\lambda_1)}c^\dagger_{1,\mathrm{in}}(-\omega) + \left(\frac{2\sqrt{\gamma_1\gamma_l}(-i\omega + W^*)}{(-i\omega+\lambda_0)(-i\omega+\lambda_1)}\right)c_{l,\mathrm{in}}(\omega) + \\ &\quad \frac{2\sqrt{\gamma_1\gamma_l}V}{(-i\omega+\lambda_0)(-i\omega+\lambda_1)}c^\dagger_{l,\mathrm{in}}(-\omega) \qquad (5.51) \\ &= \mathcal{G}_1 c_{1,\mathrm{in}}(\omega) + \mathcal{M}_1 c^\dagger_{1,\mathrm{in}}(-\omega) + \mathcal{G}_l c_{l,\mathrm{in}}(\omega) + \mathcal{M}_l c^\dagger_{l,\mathrm{in}}(-\omega). \qquad (5.52) \end{aligned}$$

The signal and image gain are still defined the same way as in Eqs. (3.59) and (3.60). From the amplifier's point of view, the effect of linear loss (or even extra ports such as in a lossless $\lambda/2$ resonator) is to generate extra-added noise as well as to reduce the amount of squeezing. Calculating the spectral density of the output quadrature operator (Eq. 3.72), I obtain

$$\begin{aligned} S_{X_{\mathrm{out},\theta},X_{\mathrm{out},\theta}}(\omega) = &\frac{1}{4}S_{a_{1,\mathrm{in}},a_{1,\mathrm{in}}}\left(|e^{i\theta}\mathcal{G}_1(-\omega) + e^{-i\theta}\mathcal{M}_1^*(\omega)|^2 + |e^{i\theta}\mathcal{G}_1(\omega) + e^{-i\theta}\mathcal{M}_1^*(-\omega)|^2\right) \\ &\frac{1}{4}S_{a_{l,\mathrm{in}},a_{l,\mathrm{in}}}\left(|e^{i\theta}\mathcal{G}_l(-\omega) + e^{-i\theta}\mathcal{M}_l^*(\omega)|^2 + |e^{i\theta}\mathcal{G}_l(\omega) + e^{-i\theta}\mathcal{M}_l^*(-\omega)|^2\right) \end{aligned} \tag{5.53}$$

where $S_{a_{1,\text{in}},a_{1,\text{in}}}$ is the spectrum of the incoming field of port 1 and $S_{a_{l,\text{in}},a_{l,\text{in}}}$ is the spectrum for the incoming field of the port representing the intrinsic resonator loss. These spectrums are given by Eq. (3.67). Eq. (5.53) allow us to compute the noise-power spectrum at any quadrature X_θ for any set of device parameters. It is important to point out that due to the inclusion of loss, the signal gain $\mathcal{G}_1$ and image gain $\mathcal{M}_1$ will not fulfill anymore the relations (3.57) and (3.58). Eq. (5.53) can be further simplified in the case of $\omega = 0$:

$$\begin{aligned} S_{X_{\text{out},\theta},X_{\text{out},\theta}}(0) &= \frac{1}{2}S_{a_{1,\text{in}},a_{1,\text{in}}}|e^{i\theta}\mathcal{G}_1 + e^{-i\theta}\mathcal{M}_1^*|^2 \\ &\quad + \frac{1}{2}S_{a_{l,\text{in}},a_{l,\text{in}}}|e^{i\theta}\mathcal{G}_l + e^{-i\theta}\mathcal{M}_l^*|^2, \qquad (5.54) \\ &= \frac{1}{2}S_{a_{1,\text{in}},a_{1,\text{in}}}G_\theta + \frac{1}{2}S_{a_{l,\text{in}},a_{l,\text{in}}}G_{l,\theta}. \qquad (5.55) \end{aligned}$$

Eq. (5.55) will allow us to calculate the added noise of the amplifier as well as the maximum amount of squeezing. In general, the added noise and squeezing will not only depend on the gain of the maximum amplified quadrature $G_1 = G_{\theta=\theta_1}$ as in the case of the lossless JPA, but it will also depend on the pump-detuning and pump powers; that is, for the same gain G_1, there is more than one possible value of squeezing and added noise. This is shown in figure 5.12. However, the maximum squeezing and added noise become single-valued in the limit of high gain. For the amplified quadrature, in the high-gain limit, the added noise is given by:[7]

$$A_N = \frac{1}{2}\left(\frac{\gamma_l}{\gamma_1}\coth(\frac{\hbar\omega_p}{2k_BT_l})\right). \qquad (5.56)$$

For the case of multiple ports, Eq. (5.56) is easy generalized to

$$A_N = \frac{1}{2\gamma_1}\left(\sum_{j\neq 1}\gamma_j\coth(\frac{\hbar\omega_p}{2k_BT_j}) + \gamma_l\coth(\frac{\hbar\omega_p}{2k_BT_l})\right). \qquad (5.57)$$

From Eq. (5.57) we can conclude that increasing the number of ports will just hurt the noise-performance of the amplifier. It can be tempting to add a second port so that we

[7] Note that we are using a single-sided spectral density and A_N is really the added noise per unit-bandwidth as defined in appendix A. In this convention, the added noise **per quadrature** per unit-bandwidth of a quantum-limited phase-insensitive amplifier is 1/2.

have a port dedicated for the pump (port 2) and another for only the signals (port 1). However, if such a thing is necessary or desired, care must be taken to make the ports highly asymmetric so that $\gamma_2/\gamma_1 \ll 1$.

In the case of squeezing, again for large gains and $\omega = 0$, Eq. 5.55 simplifies to

$$S_{X_{\mathrm{out},2},X_{\mathrm{out},2}}(0) = \frac{\gamma_l}{\gamma}\left(\frac{1}{2}\coth(\frac{\hbar\omega_p}{2k_BT_l})\right) \tag{5.58}$$

where the output is specified in number of quanta. Eq. (5.58) shows the effect of loss in the squeezing. In the case of $S_{a_{1,\mathrm{in}},a_{1,\mathrm{in}}} = S_{a_{l,\mathrm{in}},a_{l,\mathrm{in}}}$, the maximum squeezing is given by $\xi = \gamma_l/\gamma$ (Eq. 2.87). The generalization to multiple ports is easily done by adding to Eq. (5.58) the noise at the input of each extra ports multiplied by γ_i/γ. An interesting thing, however, is that regardless of the number of ports, the maximum squeezing of the internal field is always 50%, just as in the case of a single-port lossless parametric amplifier.

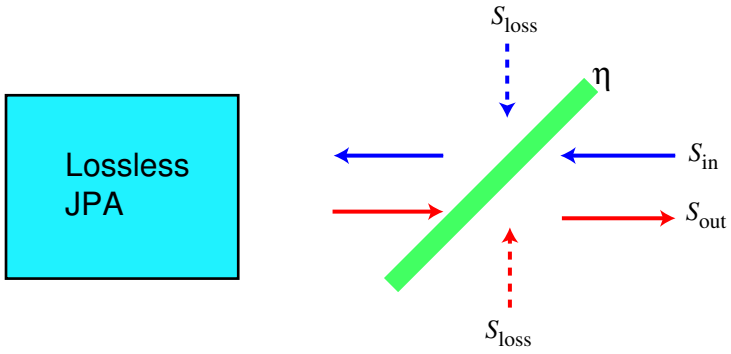

Figure 5.11: Loss model for a JPA where the loss is included as a beam splitter at the input of a lossless amplifier (see Ref. [8]).

The inclusion of loss has complicated the expressions for the squeezing and added noise, specially since they do not have a simple closed form unless we are in the large-gain limit. There is another way to include loss that is somewhat simpler. Following the model used by Yurke, *et. al.*, in Ref. [8], the losses of an amplifier could be modeled by placing a beam splitter at the input of the amplifier. In chapter 7, I will discuss

more details of how inefficiencies of an amplifier can be modeled with a beam splitter. For now, let's just assume it is possible to model it this way. The effect of a beam splitter is described by the relation between the input and output ports of the beam splitter [26, 28, 76, 77].

$$\begin{pmatrix} a' \\ b' \end{pmatrix} = \begin{pmatrix} \sqrt{\eta} & -\sqrt{1-\eta} \\ \sqrt{1-\eta} & \sqrt{\eta} \end{pmatrix} \begin{pmatrix} a \\ b \end{pmatrix} \tag{5.59}$$

where a represents the operator of the modes we want to amplify, and b the operator of the noise that always accompanies dissipation. The effect of an amplifier with losses on an input signal is then modeled as an ideal lossless JPA with a beam splitter at its input, as shown in figure 5.11. One port is the signal port and the other port is just a noise-port (this can also be considered a model for an attenuator). Assuming that both noise-ports have the same spectrum (same temperature T_l), the output power at the quadrature $X_\theta(\omega)$ is given by

$$S_{X_{\text{out},\theta},X_{\text{out},\theta}}(\omega) = \eta^2 G_\theta(\omega)\frac{1}{2}S_{a_{1,\text{in}},a_{1,\text{in}}} + (1-\eta)(\eta G_\theta(\omega)+1)\frac{1}{2}S_{a_{l,\text{in}},a_{l,\text{in}}} \tag{5.60}$$

where G_θ is given by the lossless case of a JPA, Eq. (3.75). For the amplified quadrature, X_1, and large gains, the added noise is given by

$$\begin{aligned} A_N &= \frac{S_{X_{\text{out},\theta},X_{\text{out},\theta}}}{\eta^2 G_1} \\ &\simeq \frac{1-\eta}{\eta} S_{a_{l,\text{in}},a_{l,\text{in}}} \end{aligned} \tag{5.61}$$

where the second line has been expanded to the leading order in G_1. For the squeezed quadrature X_2, again in the case of large gain, the output quadrature noise is

$$S_{X_{\text{out},\theta},X_{\text{out},\theta}} \simeq (1-\eta) S_{a_{l,\text{in}},a_{l,\text{in}}}. \tag{5.62}$$

Both equations, Eqs. (5.61) and (5.62) can model Eqs. (5.56) and (5.58) by setting the value of the beam splitting transmission to

$$\eta = \frac{\gamma_1}{\gamma}.$$

Note, however, that this is only valid at high gains. The functional form of the output power spectrum evaluated from Eqs. (5.54) and (5.60) will in general not be identical. The exact form depends on where the losses are embedded in the microwave network [8]. However, the beam splitter model has the advantage of having closed forms that can be used to understand semi-quantitatively the effect of losses in the detection of a signal and the squeezing of noise.

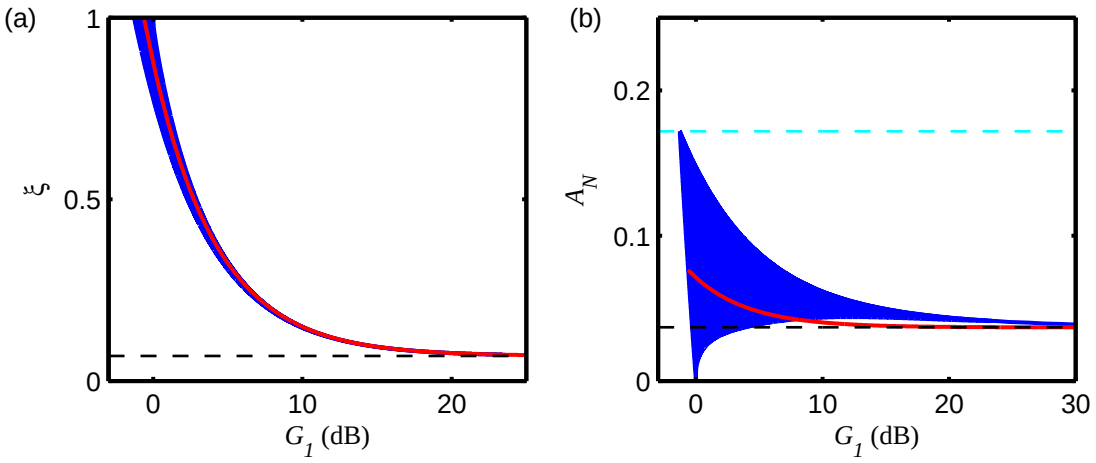

Figure 5.12: (a) Squeezing ξ as a function quadrature gain G_1 for the case of cavity with loss $\gamma_1 = 13.6\gamma_l$. The blue-shaded area represents all the possible values that ξ can take for a given gain. The dashed-black line represent the theoretical high-gain limit given by Eq. (5.58) and the red line represents the squeezing ξ according to the loss model of a beam-splitter. η is given by γ_1/γ. (b) Added noise A_N as a function of G_1 for the same case as in (b). The dashed-black line represents the theoretical high-gain limit according to Eq. (5.56). The dashed-cyan line represents the effective added noise a linear cavity would have just due to its attenuation on resonance $|\Gamma_0|^2$, where Γ_0 is given by Eq. (5.28). The value of $\gamma_1 = 13.6\gamma_l$ was chosen based on the fact that most of the data shown in chapter 6 for the $\lambda/2$-resonator was for a frequency at which the resonator linewidths had these particular values.

Finally, one phenomenon that has been observed in these microwave cavities is power-dependant loss. Power-dependant loss has been observed in superconducting resonators [69,70,78] where the loss decreases as the power of the probing tone is increased. However, the effect observed in our resonators has the opposite power-dependance: as we increase the probing microwave tone power, the loss of the resonator seems to in-

crease. We do not have an explanation of this phenomenon. Although we do not know the specific process that causes this nonlinear loss, we can still model it as it is done in Ref. [38]. The most obvious effect of this nonlinear loss is a deviation from the expected behavior of the resonance frequency (Fig. 5.13). In a nonlinear resonator with only linear loss, as we increase the pump power, the Kerr nonlinearity makes the resonance frequency decrease according to the equation $\omega_0 - \omega_m + KN = 0$, where ω_m is the frequency at which Γ is minimum, K is the Kerr constant, and N is the energy stored in the resonator in number of quanta [38]. In the case of zero non-linear loss, the pump-amplitude dependance of the resonance frequency would be purely quadratic:

$$\omega_m - \omega_0 = -\frac{8\gamma}{3\sqrt{3}} \left(\frac{b_{1,\text{in}}}{b^c_{1,\text{in}}} \right)^2$$

where $b^c_{1,\text{in}}$ is the critical amplitude of the pump given by (5.49). Nonlinear loss is modeled by defining a nonlinear loss coefficient γ_{nl} such that the total loss is given by

$$\gamma = \gamma_1 + \gamma_l + \gamma_{nl} N.$$

In this case the simple quadratic dependance of the resonance frequency ω_m is no longer valid, and it then becomes a slightly more complicated expression:

$$\omega_m - \omega_0 = -\frac{\gamma}{3\varepsilon}[g(x) - 2] \tag{5.63}$$

where $\varepsilon = \gamma_{nl}/|K|$ (See Ref. [38]). The function $g(x)$ is given by:

$$g(x) = \frac{1 + (|x| - \sqrt{x^2 - 1})^{2/3}}{(|x| - \sqrt{x^2 - 1})^{1/3}}$$

and x is given by

$$x = -\frac{36}{\sqrt{3}} \varepsilon \frac{1 + \varepsilon^2}{(1 - \sqrt{3}\varepsilon)^3} \left(\frac{b_{1,\text{in}}}{b^c_{1,\text{in}}} \right)^2 - 1.$$

The observed effect due to nonlinear loss in the first experiments using aluminum resonator was not small, thus a nonlinear term was included in their analysis. However, for the second generation of devices (niobium resonators) the nonlinear loss was small so I will not include it in their analysis.

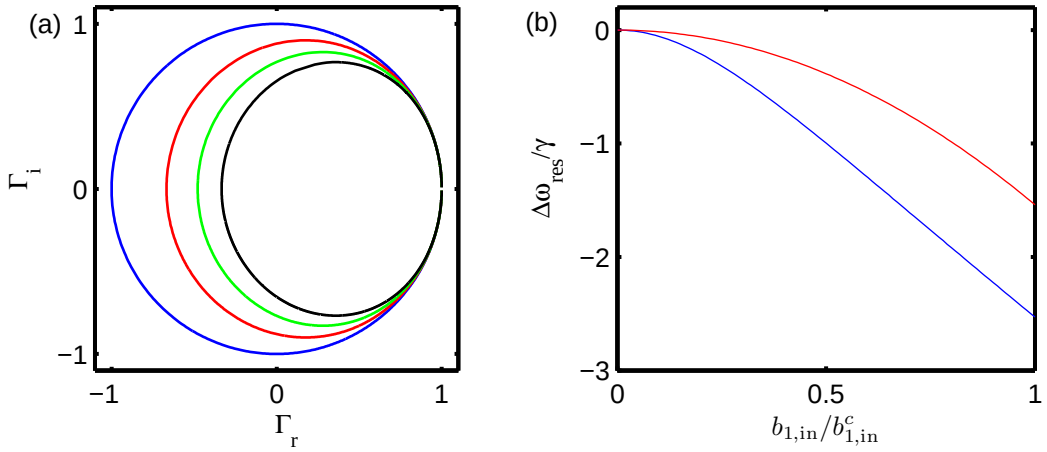

Figure 5.13: (a) Parametric plot of the real and imaginary part of the reflection coefficient Γ as a function of frequency for 4 different values of pump amplitude $b_{1,\mathrm{in}}$: $b_{1,\mathrm{in}}/b^c_{1,\mathrm{in}} \simeq 0$ (blue), $b_{1,\mathrm{in}}/b^c_{1,\mathrm{in}} = 0.5$ (red), $b_{1,\mathrm{in}}/b^c_{1,\mathrm{in}} = 0.75$ (green), and $b_{1,\mathrm{in}}/b^c_{1,\mathrm{in}} = 1$ (black). The resonator does not have any linear loss, $\gamma_l = 0$, and the nonlinear loss is $\varepsilon = 0.2$. As the the pump power is increased, the circle that represents the reflection coefficient shows an increase of the losses represented by the reduction in size of the circle. (b) Change of resonance frequency ω_m as function of normalized pump amplitude $b_{1,\mathrm{in}}/b^c_{1,\mathrm{in}}$ for $\varepsilon = 0$ (red) and $\varepsilon = 0.2$ (blue).

Chapter 6

Experimental results of JPAs

In previous chapters I have laid the necessary background to understand the experiments that I will now describe. But before I describe the experiment, it is necessary to discuss the different experimental techniques used to characterize the amplifier.

The experiments I now discuss are, in a sense, very similar to quantum optic experiments, with the very important difference of the frequency of light used. Maxwell's equations do not show a preference for a particular frequency, but practical issues do matter when it comes to doing the experiments. The frequency band where we operate is between 4 to 8 GHz. Higher microwave frequencies imply a more challenging design, as parasitic reactances are harder to prevent and parasitic resonance modes can affect the measurement of the Josephson parametric amplifiers. Lower microwave frequencies could be used. However at much lower frequencies, even at the temperatures of a dilution refrigerator ($T_{\text{fridge}} = 10$ mK) it would not be possible to achieve a true vacuum state of the electromagnetic environment ($k_B T_{\text{fridge}}/\hbar \simeq 2\pi \times 200$ MHz).

In this chapter I will first discuss the requirements to make our measurements at cryogenic temperatures and the apparatus used to analyze the measurements at room temperature. Then I will discuss, in general terms, all the measurements used to characterize the Josephson parametric amplifier, and then discuss individually the different samples that we have tested.

6.1 Instrumentation and measurement techniques

Performing quantum optics experiments at GHz frequency demands careful filtering and attenuation of microwave signals generated a room temperature. First the thermal energy at room temperatures $k_B T_{\text{room}}$ is much greater than photon energy $\hbar\omega$ at microwave frequencies (300 GHz$> \omega >$300 MHz). In addition, Josephson junctions, which provide the crucial dissipationless nonlinearity at microwave frequencies, only work at low enough temperatures for the metal used in the fabrication to become a superconductor. These facts imply that the experiments discussed here are all performed at cryogenic temperatures, with temperatures as low as 10 mK. Thus, there are strict filtering requirements in order to ensure that the electromagnetic environment that the sample sees is mostly devoid of thermal photons.

6.1.1 Microwave measurement at ultra-low temperatures

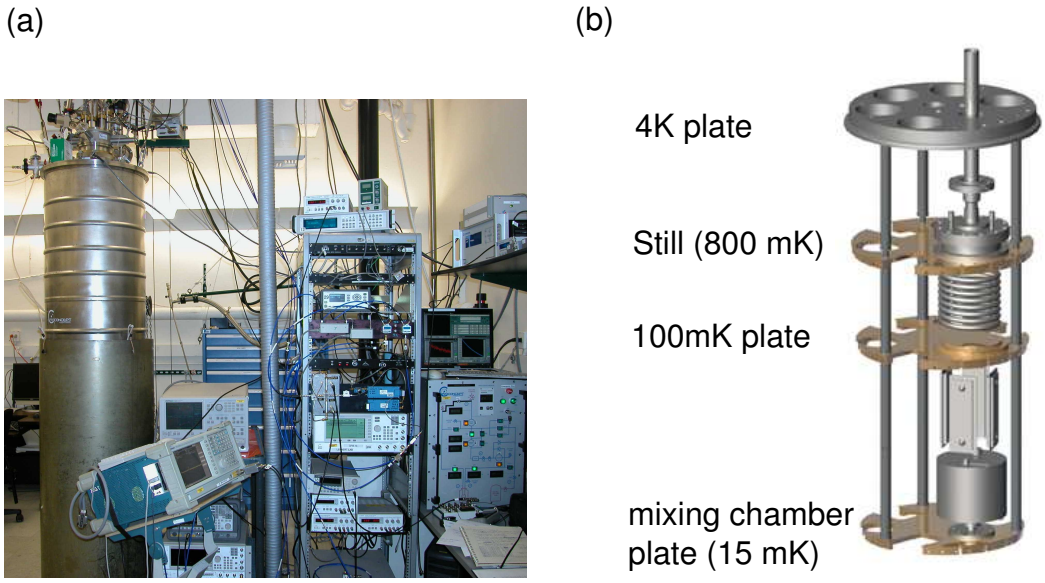

Figure 6.1: The dilution cryostat is a Cryoconcept system. (a) The full cryostat is shown with a typical measurement setup. The metallic cylinder around the dewar is a μ-metal magnetic shield. (b) The main part of the fridge sits inside a vacuum can (not shown). The sample is located at the coldest stage, the mixing-chamber plate.

All the experiments I describe in this thesis were performed in a Cryoconcept 200 μW dilution cryostat with a base temperature of 10 mK (Fig. 6.1). The cryostat contained a Nb-Ti magnet capable of generating magnetic fields as high as 9 T. But it was only used to apply small fields (a few gauss) to tune the critical current of the SQUIDs inside the resonator. However, for the most recent experiments, the 9-tesla magnet was removed and replaced by a much smaller magnet manually built using superconducting wire with a copper core (Fig. 7.8). Due to certain problems with the cryostat, its performance is somewhat degraded and the base temperature is only 15 mK.

Launching and sample box

The sample was placed at the mixing chamber stage (Fig. 6.1b). The chip which contained the device was located inside a light-tight sample box where a printed circuit board (PCB) with the appropriate traces was located (see Fig. 6.2a). The sample box is a gold-plated OFHC (oxygen-free-high-conductivity) copper enclosure that provides a shielded environment to the chip as well as to the circuit board to which the chip is wirebonded (Fig. 6.2b).

The main purpose of the PCB is to implement the transition of the signals from the semirigid coaxial cables that transport them, via connectors, to the circuit board. The transition from the cables to the circuit board is accomplished using a right angle surface mount SMP connector from Rosenberger. These connectors have good performance up to 20 GHz. In order to suppress parasitic modes between the ground planes, the top ground plane is shunted periodically to the bottom plate using vias as shown in figure 6.2b. However, this does not prevent possible microwave sample-box modes. Initially, we had not been concerned about this possibility, but measurements performed by other members of our group [79] found that the sample box initially used for the measurements did contain 3 resonant modes in the 4-9 GHz range (Fig. 6.2c). Another

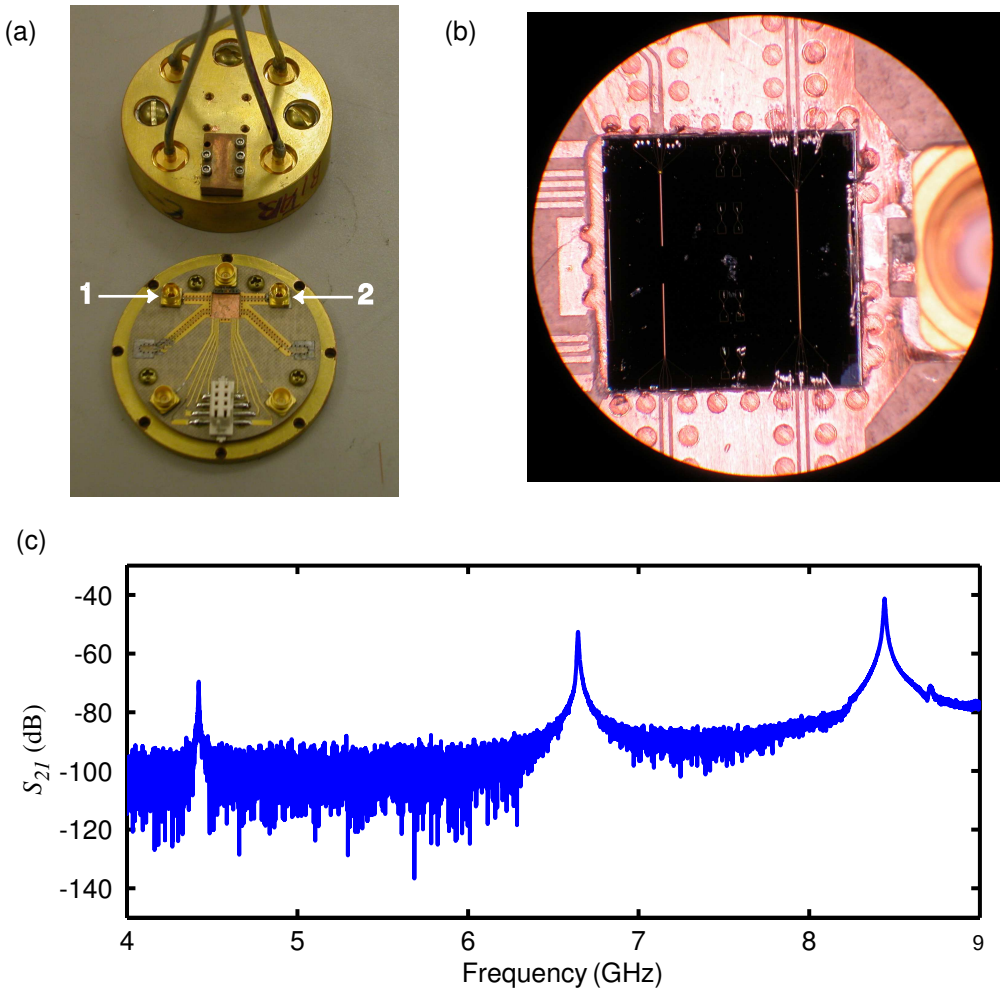

Figure 6.2: The sample box is a light-tight enclosure. It was built out of high-conductivity-oxygen-free copper and gold-plated for maximal thermal conductivity. The circuit board has 4 coplanar waveguide lines, 3 lines for coaxial dc-lines, and 8 lines for dc-wires. This last lines have not been used yet, so a copper plate is screwed on the lid of the sample box to keep it light-tight. (b) A chip is glued down to the sample box with GE-varnish or rubber cement. It is electrically connected to the PCB with aluminum wirebonds. The chip is placed in a cut-out in the circuit board to align the traces on the PCB and on the chip as closely as possible. (c) The sample box was cooled down to 77 K with no PCB or chip inside. Using ports (1) and (2) shown in (a) the transmission parameter S_{21} was measured showing three well defined resonant modes of the sample box.

concern is the impedance mismatches when coupling to the chip using wirebonds. The inductance of these wirebonds is approximately proportional to their length. Their inductance per unit length is of the order of the free space value, $\mu_0 = 4\pi \times 10^{-7}$ H/m. In order to minimize the length of the bonds as much as possible as well as match the modes of the chip and circuit board as closely as possible, the CPW traces of the chip are aligned to the CPW traces in the PCB (Fig. 6.2b). Also, the chip is located in a hole cut out in the circuit board that closely matches the size of the chip (Fig. 6.2a). The circuit board is connected to the chip using as many wirebonds as we can fit around in the center connector (2-3 wirebonds depending on the graduate student wirebonding skills) and the skinny ground-planes (5-8 wirebonds in each skinny-ground-plane), to lower the inductance as much as possible.

Filtering and attenuation

As I mentioned at the beginning of the chapter, filtering is an integral part of any cryogenic experiment. In our experiments, all the signals (both dc and rf signals) are carried using semi-rigid coaxial cable. Even though the sample box provides a shielded environment, the cables provide a path for the noise to couple to the JPA. In general, we only have rf-lines. However, for some diagnostic measurements, we use dc-lines.

The rf-lines are divided into input and output lines. The filtering and attenuation of input rf-lines is related to the removal thermal noise from room temperature. At frequencies of interest (4-8 GHz), the power has an exponential dependance with temperature. Hence the filtering requirements become very important. At a frequency of 8 GHz and temperatures above 400 mK, thermal Johnson noise will be significant. Since the signal and noise are in the same band, in the case of the rf-lines rather than filtering we attenuate the noise coming from room temperature. The amount of attenuation implies a compromise, as the more attenuation one puts, the more power one has to be able to generate at room temperature to send down the heavily attenuated

input lines. Also, if too much attenuation is used, that means there will be a significant amount of power dissipated at the different cold stages of the cryostat. This dissipated power may be so large, that the temperature of the cryostat may increase substantially. Ideally, the necessary attenuation is the ratio of the black body spectra at the two temperatures [80] of interest, 10 mK and 290 K

$$A(f) = -10 \log \left(\frac{e^{hf/k_B T_1} - 1}{e^{hf/k_B T_2} - 1} \right).$$

A frequency of $f = 8$ Ghz implies a total of 140 dB of attenuation, which is from a practical point of view, impossible. The attenuation that we use is much less than that. Nevertheless, the estimated quanta of noise per unit bandwidth.$S_{X,X} = 1/2 \coth(hf/k_B T)$ is still close to the 1/2 of vacuum noise[1] In order to go from room temperature (290 K) to liquid helium temperature (4 K), a 20 dB attenuator is placed at the 4 K plate. To go from 4 K to 15 mK another 20-40 dB of attenuation was used, depending on the experiment. The attenuators were placed at the mixing-chamber plate. The cables provide an additional 10 dB of attenuation, for a total of 50-70 dB. In spite of the large amount of attenuation, the power of the tones sent to probe the JPA was low enough that heating of the mixing chamber stage was not observed. When only 40 dB of attenuation was used, the estimated incident noise in the device was $S_{\text{in}} = 0.65 - 0.7$ quanta. When 60 dB was used, the thermal noise due to the attenuated noise coming from room temperature was insignificant, with $S_{\text{in}} = 0.502$ quanta.[2]

The attenuation of the rf-input lines is required to remove classical noise from microwave tones. In our case, we use an Agilent E8257D microwave analog signal generator. However, the signals at the output of these microwave generators are not coherent states, having large amount of phase and amplitude noise, as can be observed in

[1] In the rest of chapter 6, 7 and appendix B, I will change the convention to name the single-sided spectral densities of a quadrature $S_{X,X}$. The main reason is that I will use the subscript index to refer to the different possible locations in the experiment setup.

[2] As we will see in this chapter, depending on the attenuation used for the noise-calibration line, the main source of thermal noise can be the losses of the microwave switch used to estimate the added noise of the amplifier.

their data sheet [81]. In order to obtain a coherent state at the sample inside the dilution refrigerator, we must attenuate the output of the microwave generator to remove this extra phase and amplitude noise. The amplitude and phase noise are defined relative to the carrier, in units of dBc/Hz. Thus, they are approximately independent of the carrier power. Nonetheless, the voltage fluctuations associated with the AM or PM noise do depend on carrier power. It is the critical power of the parametric amplifier that determines the amount of attenuation required to reduce the amplitude and phase noise of the generator below the level of vacuum fluctuations. In the case of the Niobium resonators, the critical power using the strongly coupled port in the case of the half-wavelength resonator, or using the only port in the quarter-wavelength resonator, is about -90 dBm or less. From the data sheet of the signal generator, for an 8 GHz carrier tone the manufacturer's estimate of phase noise is -120 dBc/Hz at 100 kHz offset from the carrier. The phase noise decreases at larger offset frequencies; *i.e.* it is -140 dBc/Hz at a 500 kHz offset. The amplitude noise is always smaller than the phase noise. The question is how does the amplitude and phase noise of a -90 dBm carrier tone compare to the noise of vacuum flucuations at 8 GHz, $\hbar\omega/2 = 2.65 \times 10^{-24}$ W/Hz? At 100 kHz, -210 dBm/Hz is 1×10^{-24} W/Hz, or slightly more than 1/3 of vacuum noise. However, at 500 kHz, the extra phase noise is 2 orders of magnitude smaller, which for our purpose is rather insignificant.[3]

Filtering of the dc-lines is very different. The only kind of dc-measurement we performed was current versus voltage (I-V) curves. These measurements do not require high bandwidth, but they employ much higher voltages. We use low pass filters with very low attenuation at dc, but very large attenuation at microwave frequencies where most of the thermal noise power is located. There are many different types of low pass

[3] Note however that when performing a homodyne measurement with a mixer, if both the LO and pump of the JPA come from the same signal generator, we become immune to the phase noise in the detection, but when two different signal generators are used, we will filter the low frequency phase noise at the output of the detector.

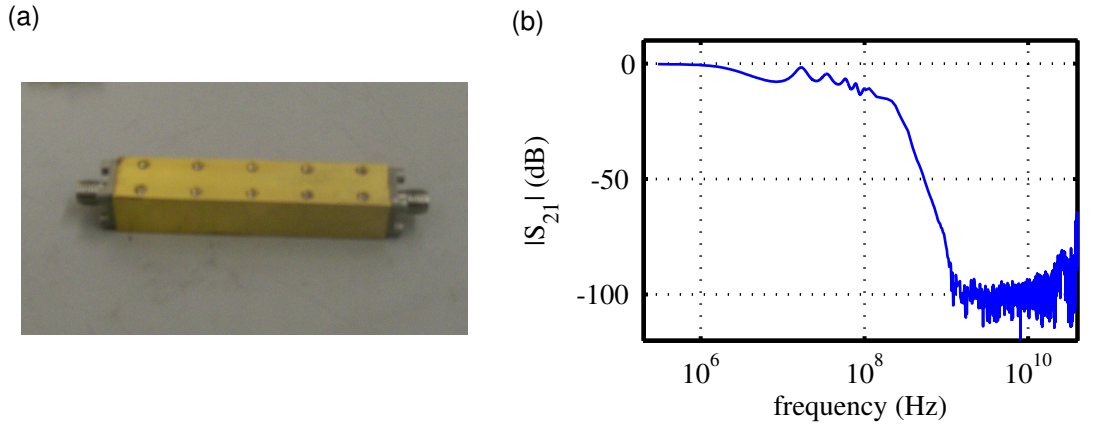

Figure 6.3: (a) Picture of one of the low pass powder filters (PF) used for the dc-measurements in our cryostat. (b) $|S_{21}|$ as a function of frequency for the filter shown in (a). Transmission data from 100 MHz to 40 GHz was taken with the Anritsu 37269B network analyzer. Data below 100 MHz was taken with a Hewlett Packard 8712B network analyzer. While this data was taken at room temperature, there is only a small change in when used at cryogenic temperatures.

filters available but for this experiment we use copper powder filters (Fig. 6.3a) [82]. These filters consist of a long (1 m) copper wire that is coiled and immersed in epoxy (*Emmons and Cummins* 2150) and copper mesh powder (spherical APS 10 microns) mixture. This structure is housed in a copper box with SMA connectors at both ends. The high frequency loss comes from the powder itself, and the filters achieve attenuation greater than 80 dB at frequencies greater than 1 GHz (Fig. 6.3b). These filters have a cutoff at around 5-10MHz.

Separation of input and output signals

The Josephson parametric amplifier is operated as a reflection amplifier, and in order to characterize it, we need to be able to separate the incoming and outgoing signals in the same cable. This is accomplished using directional couplers and microwave circulator. Directional couplers are passive microwave components used for power division or power combining (Fig. 6.4a). A directional coupler is a four port network with

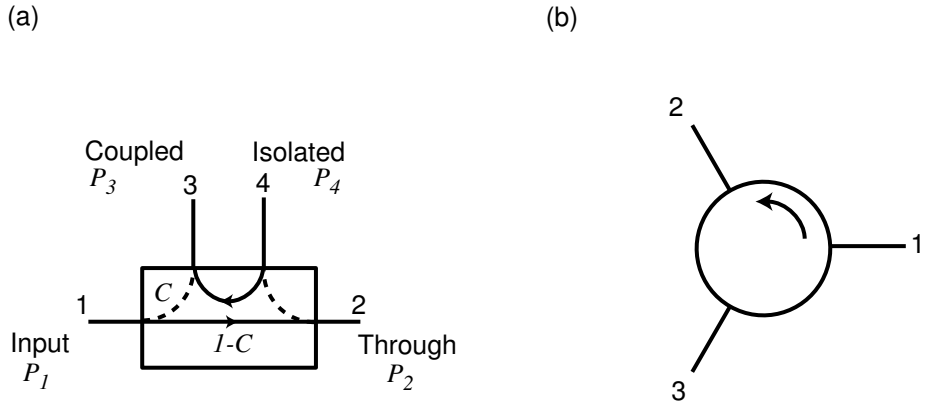

Figure 6.4: For the separation of the input and output signals, two microwave devices are used. (a) The directional coupler is characterized by the coupling C, the directivity D and the isolation Is. The coupling indicates the fraction of the input power P_1 that is coupled to port 3 (P_3). The isolation is a measure of the directional coupler's ability to avoid power-leakage from port 1 into port 4 (P_1/P_4) as is the directivity (P_3/P_4). The ideal directional coupler would have infinite directivity and isolation, so it would be completely characterized by the coupling factor C. (b) A circulator is a passive non-reciprocal three-port device. Power entering any port is ideally only transmitted to the next port in rotation. In reality, some power leaks to the other port. The amount of leakage power is determined by the isolation Is of the circulator.

one of the ports usually terminated with a 50 Ω resistor; it is the microwave analog of a beam splitter. The basic operation of an ideal directional coupler is the following. Power supplied to port 1 is coupled to port 3 with the coupling factor of C, while the remainder $(1-C)$ is delivered to port 2. In an ideal directional coupler, no power is delivered to port 4. The directional coupler used in our experiment was a MAC C2056-20, with $C = 0.01 = -20$ dB of coupling.

A circulator is a three-port non-reciprocal device (Fig. 6.4b). In an ideal circulator, all the power entering port 1 will exit port 2, powering entering port 2 will exit port 3 and powering entering port 3 will exit port 1. And assuming all ports are matched, no power flows in the reverse direction. The nonreciprocal nature of the circulator requires a magnetized material to break time reversal symmetry; therefore, they emit large stray magnetic fields.[4] For that reason, we place them outside the magnetic shield far from

[4] Shielded circulators can be purchased, but the shielding is big and bulky. This bulk can be a

the sample. The circulator used at low temperatures is a Pamtech CTH-1394K. It is specified to work at low temperatures. It provides 18-30 dB (a specified minimum of 18 dB) of isolation and has a bandwidth of one octave (4-8 GHz).

Low temperature amplification

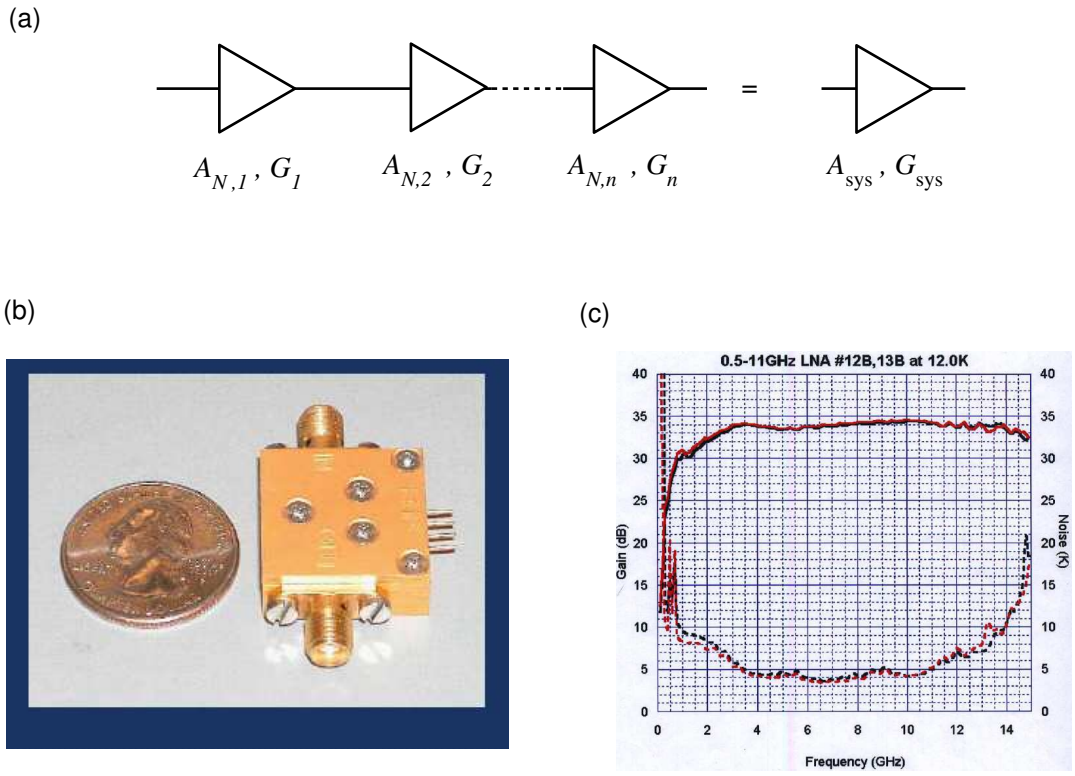

Figure 6.5: (a) The effective noise temperature of the whole chain of amplifiers is calculated by referring each amplifier's noise to the input of the entire chain. Ideally, the first amplifier has enough gain that it sets the noise-floor. (b) Picture of the HEMT amplifier. It was purchased from Sandy Weinreb's group in Caltech. (c) Gain and noise temperature measured by the manufacturer at 12 K of both HEMTs our group owns. The used amplifier performance is shown as the red-trace.

As I mentioned in chapter 2, any phase-preserving amplification must necessarily result in an increase in the noise of the measurement. If there are several amplifiers in series, the first stage of amplification is the most important in determining the noise

nuisance in the small space inside a dilution refrigerator.

of the measurement. Ignoring possible losses between different amplifiers, the added noise of the amplifier chain with n amplifiers can be calculated by referring the total output noise at the output of the chain to the input of the first amplifier (Fig. 6.5a). By dividing the total output noise by the total gain, then it is easy to see that the effective added noise $A_{\rm sys}$ is given by

$$A_{\rm sys} = A_{N,1} + \frac{A_{N,2}}{G_1} + ... + \frac{A_{N,n}}{G_1 G_2 ... G_{n-1}}.$$

Ideally, the first amplifier is operated with high enough gain such that it sets the noise floor of the detector, $A_{\rm sys} \simeq A_{N,1}$.

Our first amplifier (ignoring the JPA) is a high-electron-mobility-transistor (HEMT) amplifier with a noise temperature of $T_N = 5 - 10$ K, depending on the frequency (Fig. 6.5b). We did the appropriate tests to ensure that less than three percent of the system noise was contributed by the amplifiers and components that follow the HEMT amplifier. It is thermally anchored to the 4 K plate, the lowest temperature at which it is possible to dissipate the 20 mW of amplifier bias power without raising the temperature. In order to prevent the noise emitted by the input of the HEMT amplifier from exciting the JPA, a circulator with the third port terminated with a 50 Ω resistor is placed at base temperature (in this configuration, the circulators are called isolators). Thus, the noise seen by the device would ideally be the Johnson noise of the 50 Ω resistor.

Thermal anchoring

One final situation that deserves some discussion is the thermal anchoring of the cables. At low temperatures, thermal conductivity, especially due to phonons, is substantially reduced. This means that care must be taken to ensure that cables and components are properly heat sunk. The outside of the cables is easily heat-sunk to the different stages[5] by using brackets that are attached to the plates of the cryostat

[5] The outer conductor is anchored to the all the plates 4 K, still, 100mK as well as the mixing chamber in order to minimize the total heat load.

as shown in figure 6.6a. However, a constant problem is how to heat-sink the center conductor of the cables. The attenuators provide a resistive connection through which heat can be dissipated from the center pin to the cable shield (and cryostat). Both the outside shield and center pin of the circulators are heat-sunk as well. The outside is heat-sunk using copper braid and copper brackets, and the center pin is heat-sunk when they are used as isolators as the third port is terminated with a 50 Ω resistor to ground. This termination is anchored to the base temperature. In the case of the dc-lines, the heat-sinking is accomplished via the filtering elements. The copper powder filters allow the center pin to come to thermal equilibrium.

In some instances, we need to thermalize the center conductor of a coaxial cable without using an attenuator. In those cases, we use a microwave component called bias tee. Bias tees consist of an inductor and a capacitor connected as shown in figure 6.6b and are usually used to supply dc currents or voltages to rf-devices. However, we use it to heat-sink the center conductors by shorting the dc-port to the fridge ground. The rf-signals are injected though the rf-port and come out of the rf+dc port with very low attenuation. The insertion loss of the the bias tee used for this purpose (Anritsu K250) is about 0.5 dB at room temperature at the frequencies we used.

In order to thermally isolate the different stages of the fridge the choice of semi-rigid cable is also important. For this purpose, we can divide the cryostat in 4 sections. For the cables from room temperature to the liquid-helium bath, we use stainless steel outer, silver-plated-copper-weld (SPCW) inner conductor. In the helium bath, we used cable with copper outer and copper, or SPCW, inner conductor. The cables chosen to go between the 4 K plate to the mixing chamber must be of a low thermal conductance material for both the center pin and the outer conductor. Stainless steel inner and outer conductor (ss-ss) cables were used for the input lines. Unfortunately, its high thermal resistance comes with a large electrical resistance making them quite lossy, and

attenuating a signal around 2 dB/ft at 8 GHz.[6] This extra attenuation is not a concern for the input lines, but in the output lines it would increase the noise temperature of the amplifying chain. For the output lines, superconductor cables, niobium, or niobium-titanium (NbTi) alloy, were used to avoid the attenuation of the stainless steel cables.

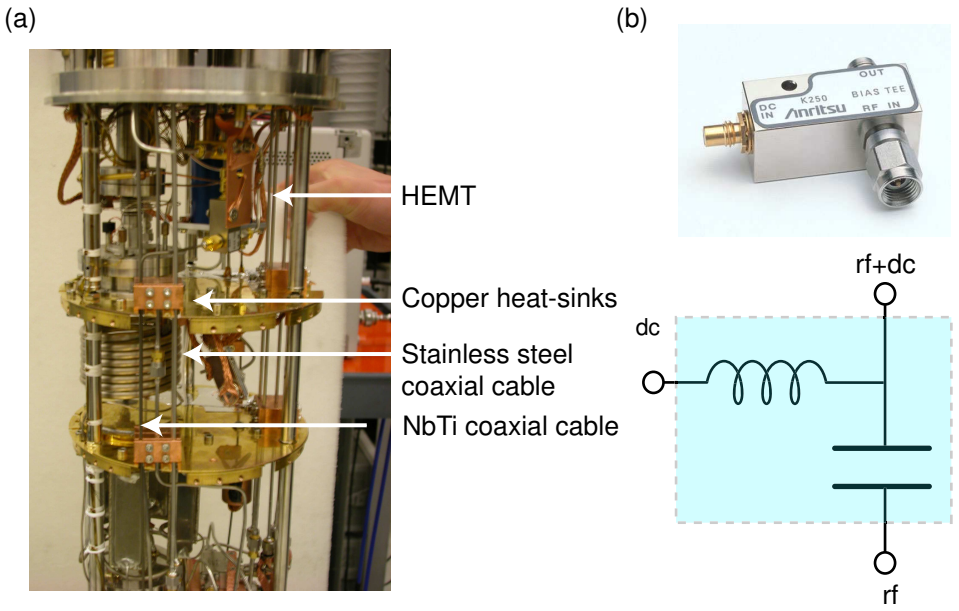

Figure 6.6: (b) Heatsinking of the semi-rigid cables is done using copper-brackets machined from OHFC copper. The HEMT is heatsunk with a copper bracket for the outer shell. The center pin is thermalized to 4-K using a bias-tee with the dc-lines short-circuited. (a) Picture and schematic of a bias tee used for thermal sinking. The model used is an Anritsu K250.

6.1.2 Microwave measurements at room temperature

The generation of microwave tones, in order to probe the behavior of the JPAs, is accomplished either using the microwave signal generators I described in the previous section, or using a vector network analyzer (Anrtisu 37269B). The vector network analyzer is a two-channel microwave receiver, which is used to measure the scattering parameters of a microwave network. It is designed to provide phase and magnitude

[6] This value was estimated based on a ss-ss cable cooled down to 77 K.

information by generating a signal at one of its ports and analyzing the power transmitted to a second port and the power reflected back to the first port. However, for most of our measurements, the microwave tones are created by signal generators. To create multiple copies of the same tone, we split the generators output using 3-dB power splitters and we attenuate and phase-shift the tones for their different purposes: the pump, the mixer LO, the small gain-calibration tone and the carrier-cancelation tone. For the carrier cancelation tones used in experiments described in chapter 7, variable attenuators Arra 5814-20A-1A and variable phase shifter Arra 9425A are used to set the appropriate amplitude and phase.

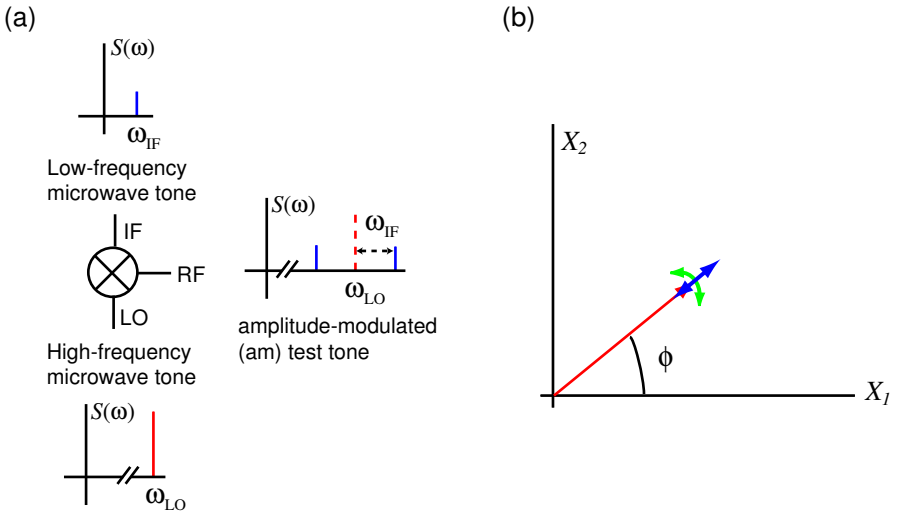

Figure 6.7: (a) Up-conversion using a mixer. A low frequency tone enters the IF-port and is multiplied by a the local oscillator (LO). The output of the mixer is an amplitude modulated signal with power in its spectrum at frequencies $\omega_{LO} \pm \omega_{IF}$. (b) In principle, two different kind of modulated signals can be used to probe the phase-dependent gain of the JPA: amplitude-modulated (blue) and phase-modulated (red) tones. For our experiments, we only used AM-tones. However, in chapter 8, the signal I will amplify using a JPA consists of phase-modulated information on top of a large carrier (red). The only difference is a 90° phase shift in the phase dependance of the JPA gain.

For the detection of the signals at room temperature, we use commercial spectrum and network analyzers. A spectrum analyzer gives a frequency-domain representation of an input signal and displays the average power spectral density as a function of

frequency. The spectrum analyzer we used was Hewlett Packard E4407B spectrum analyzer. We also implement our own analyzer using a mixer and digitalization cards. A mixer is a device used to provide frequency conversion between an input signal and an output signal. We use mixers for both up-conversion and down-conversion. Up-conversion refers to the process of taking a low-frequency signal and transforming it into a higher frequency one (Fig. 6.7a). There are two options to do this, using amplitude modulated or phase modulated signals (Fig. 6.7b). We chose amplitude modulated signals for the test-tone to measure the phase-dependant gain (the only difference in using a phase modulated signal is that the maximum gain would occur with a 90° phase-shift in the LO). The output of the mixer is an AM microwave tone with the carrier strongly suppressed. It is basically the same as the AM-tone shown in figure 6.7b, with the exception that the modulation amplitude is large compared to the average value of the carrier (indicated by the red phasor). The up-conversion in the case of an AM-tone is equivalent to multiplying the LO tone by the input of the IF-port. The output port in the up-conversion is the RF-port. The microwave tone at the RF-port $A(t)\cos(\omega_{\rm LO}+\phi)$ is given by

$$\begin{aligned} A(t)\cos(\omega_{\rm LO}+\phi) &= \cos(\omega_{\rm IF})\times\cos(\omega_{\rm LO}+\phi) && (6.1)\\ &= \frac{1}{2}\left[\cos(\omega_{\rm LO}-\omega_{\rm IF}+\phi)+\cos(\omega_{\rm LO}+\omega_{\rm IF}+\phi)\right]. && (6.2)\end{aligned}$$

In Eq. (6.1), it is clear that even though the signal consists of two tones at different frequencies $\omega_{LO}\pm\omega_{\rm IF}$, the phase of the signal is given by the LO phase ϕ, and the amplitude of the signal is $A(t)=\cos(\omega_{\rm IF})$, a slow function of time ($\omega_{\rm IF}\ll\omega_{\rm LO}$). The AM-tone generated allows us to apply a signal with the appropriate linear combination of input fourier modes (Eq. 3.79) in order to measure the phase-dependance of the JPA gain G_θ. The mixer used for the up-conversion is a Mini-Circuits ZMX-10G.

For the detection of microwave fields, the mixer is used for down-conversion. In the down-conversion process, the input is the RF port and the output is the IF port.

Next a brief and qualitative description of the down-conversion operation of a mixer is discussed; for a full explanation of the operation of a mixer, the reader is referred to Ref. [16]. For a given RF and LO microwave tone frequencies, two nominally equal-amplitude output signals are produced at the sum and at the difference of the RF and LO frequencies. This is effectively the same as saying that the mixer output consists of the result of multiplying the input signal $A\cos(\omega_s t+\phi)$ by the LO

$$A\cos(\omega_s t+\phi)\times\cos(\omega_{\rm LO}t)=\frac{1}{2}A\left[\cos([\omega_s-\omega_{\rm LO}]t+\phi)+\cos([\omega_s+\omega_{\rm LO}]t+\phi)\right].$$

In the down conversion process, the second term is removed by a low pass filter. In most of our cases $\omega_{\rm LO}=\omega_s$. This case is usually referred in the literature as homodyne detection, and the case where $\omega_{\rm LO}\neq\omega_s$ is called heterodyne detection. We use a pair of mixers configured in a particular way to form a so-called IQ-mixer. In this configuratoin, the LO is split in two tones and one of them is phase-shifted by 90°. Then, the input signal at the RF-port is also split in two and each multiplied by the two LO-tones. The two output ports are given by

$$I(t)=B(A(t)\cos(\phi)) \tag{6.3}$$

$$Q(t)=B(A(t)\sin(\phi)) \tag{6.4}$$

where B is just the mixer gain.[7] From Eqs. (6.3) and (6.4), we can then deduce that the I-port just gives the X_1 quadrature and the Q-port the X_2 quadrature relative to the LO (Fig. 6.8). With this down-conversion process, the amplitude and phase of the original signal have been mapped onto two lower frequency signals. Both, the amplitude

[7] In reality, the IQ-mixers are not ideal and contain both phase and amplitude unbalance. That is that the real outputs of the I and Q port are given by

$$\begin{aligned} I &= I_0+B_I A(t)\cos(\phi)\\ Q &= Q_0+B_Q A(t)\sin(\phi+\vartheta)\end{aligned}$$

where I_0 and Q_0 are dc-offsets, $B_I\neq B_Q$ and $\vartheta\neq 0$. In the cases that it is necessary, such as when implementing a network analyzer with the mixer, this imperfections are corrected in the computer by calibrating the mixer before taking the data. The calibration is similar to the one explained in appendix F of Ref. [83].

A (AM-tone) and the phase ϕ (PM-tone) of the signal can be a slow (compared to ω_s) function of time (Fig. 6.8b). In this case, the spectral content associated with the slow variations in $A(t)$ and $\phi(t)$ appear with a frequency offset ω as the spectral content at the I and Q ports of the mixer (Fig. 6.8b). The mixers used for the down-conversion are Marki Microwave IQ0307LXP and IQ4509LXP.

The output of the I and Q ports are first amplified (to compensate for the 6 dB conversion-loss of the mixer), low-passed filtered by an anti-alising filter that sets the bandwidth of the measurement, and then digitized using a digitizer card (DAC). For all the experiments in this chapter, a NI-6122 and an Acquiris DP-240 card were used. The NI-6122 had a maximum sampling rate of 500 kHz and a 16-bit resolution. This card was used for the aluminium resonators, which had much smaller bandwidth. The Acquiris DP-240 was used for the niobium resonators since it had a maximum sampling rate of 1 GHz, but it was an 8-bit resolution card. For the experiments of chapter 7, an Alazar ATS460 card with 14-bit resolution was used in order to improve the linearity and accuracy of the measurements.

6.2 Characterization of the resonator

In order to characterize the resonators, we need to perform multiple kinds of measurements. The first ones I will describe are dc-measurements of test junctions. I will then describe the measurements done on the JPA that test only its linear and non linear resonator behavior. Finally I will describe all the tests made to characterize the amplifier performance.

6.2.1 dc-Characterization of Josephson junctions

In order to estimate the resonance frequency of the resonator, I need to know the total inductance of the Josephson junctions. For that, we placed a few test junctions in the chip. Once fabrication is completed, whether it is done by me or our colleagues at

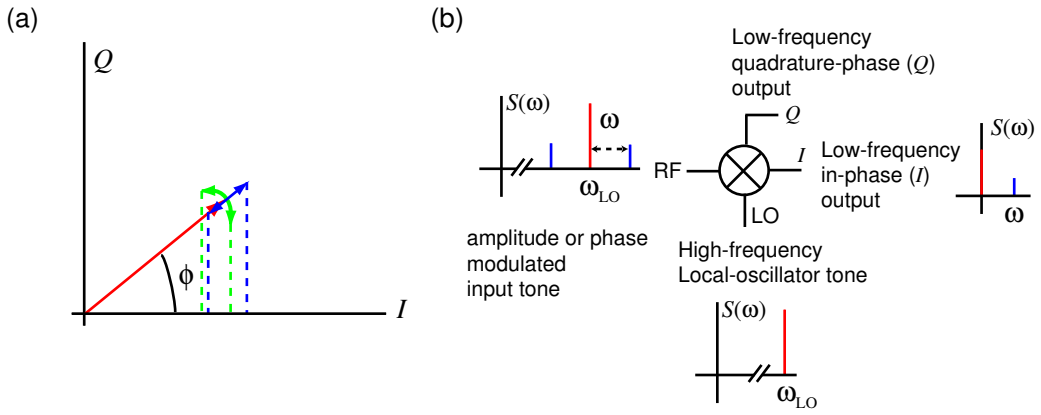

Figure 6.8: (a) Signal entering the RF-port of the mixer. Besides the carrier (red phasor), the signal contains information in the form of amplitude modulation (blue) and phase modulation (red). The projections of those modulations onto the I-axis are shown. (b) Down-conversion process. A tone is applied to the RF-port of the mixer. Regardless of whether it is phase or amplitude modulated, its spectrum has two tones equally spaced from the main carrier. After going through the mixer the information contained in those tones are shifted down in frequency. The main carrier (red) will appear at dc ($\omega = 0$), while the side-tones will appear at a frequency ω. The magnitude of the power at ω will be proportional to the projection of the modulation onto the I or Q channel.

NIST, these test junctions are probed at room temperature to ensure that the resistances are as designed. This is done with a probe station connected to the same equipment used for the dc-measurements in the cryogenic experiments (Fig. 6.9a). Two kind of test structures were probed: single SQUIDs and series arrays of SQUIDs. Particular care must be taken not to damage the devices with electrostatic discharge during handling and dc measurement. Single SQUID test structures are the most susceptible to damage. The arrays are more robust.

The dc measurements setup is shown in figure 6.9a. All measurements were single-ended using coaxial cables (either BNC when probing the junctions at room temperature, or semi-rigid cable with SMA or SMP connectors when tested in the cryostat). The devices are wirebonded to the cryostat ground through the PBC ground. The I-V curves are taken by measuring the voltage drop across a series bias resistor at room temperature. In order to have a very stable dc-bias, a Yokogawa 7651 dc-voltage source is used. Using low noise instrumentation amplifiers, the voltage across the bias resistor and across the device are measured with Agilent 34401A digital multimeters. When their I-V curves are measured at 15 mK, we can observe the characteristic features of Superconducting-Insulator-Superconducting junctions (Fig. 6.9b).

There are essentially three distinct regimes. The first region is the dissipationless supercurrent at $V = 0$. In the second region, the subgap region $0 < |V| < 2\Delta/e$, the current drops many orders of magnitude. As the voltage bias reaches $2\Delta/e$, there is a sudden increase of quasiparticle tunneling current. At higher voltages, the dynamic resistance asymptotically approaches the normal state resistance R_n of the junction above the transition temperature T_c [33]. Our dc-measurement measures all three regions, providing a direct measurement of the two main parameters for characterizing a junction, R_n and I_0. Yet, there is a few caveats I should mention. The two sharp features of the I-V curves, the gap-rise current at $V = 2\Delta/e$ and the supercurrent at $V = 0$ are very susceptible to noise. Specifically, the supercurrent itself is an extremely

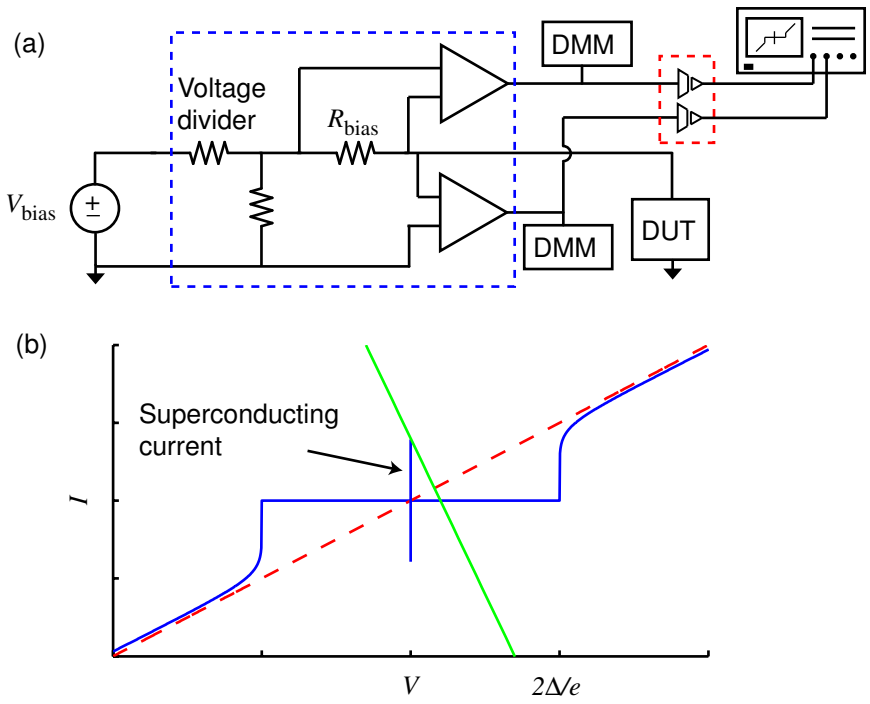

Figure 6.9: (a) Setup for the dc-measurements of the test SQUIDs. The output of a floating voltage source (Yokogawa 7651 dc-voltage source) is sent to a "bias-box", shown as the blue dashed-line box in the figure. In the bias-box, the voltage is attenuated with a voltage resistive-divider. The attenuated voltage is then connected to the device under test (DUT) via a bias resistor R_{bias}. The voltages across the bias resistor and the device are amplified for simultaneous measurement of the current and voltage and measured with two digital multimeters (DMM) Agilent 34401A. The output of the bias-box is also splitted and sent to two unity-gain-isolation amplifiers, referred to as the iso-box (and shown as the red dashed-line box in the figure). The iso-box is used to prevent a ground-loop between the oscilloscope and the cryostat. (b) Characteristic I-V curve of Superconducting-Insulator-Superconducting junction with a normal resistance of R_n, (blue) and the expected linear response of a resistor with the same value. The measurement of the I-V curve using the setup just described would use a load-line (green) with a slope of $1/R_{\text{bias}}$.

sensitive threshold detector and spurious noise can make the junction to switch from the supercurrent state to a dissipative state prematurely, that is before the current reaches the theoretical maximum of I_0. Likewise, the gap-rise also represents a sharp feature that can easily be rounded. In some cases, due to self-heating, the gap-rise shows a "backbend" caused by an excess of quasiparticles, locally reducing the gap.[8] There-

[8] This is particularly true in the SQUID arrays.

fore, it is important to distinguish the measured maximum supercurrent and the one that we would theoretically expect from the junction resistance and Eq. (3.17). Also, there will be features that I will miss in the measured I-V curve, as the load line of the measurement will determine exactly how close to the supercurrent one can stably bias (Fig. 6.9b). In order to estimate the Josephson inductance, the resistance of the junction and Eq. (3.20) is used.

6.2.2 Linear measurements of the resonators

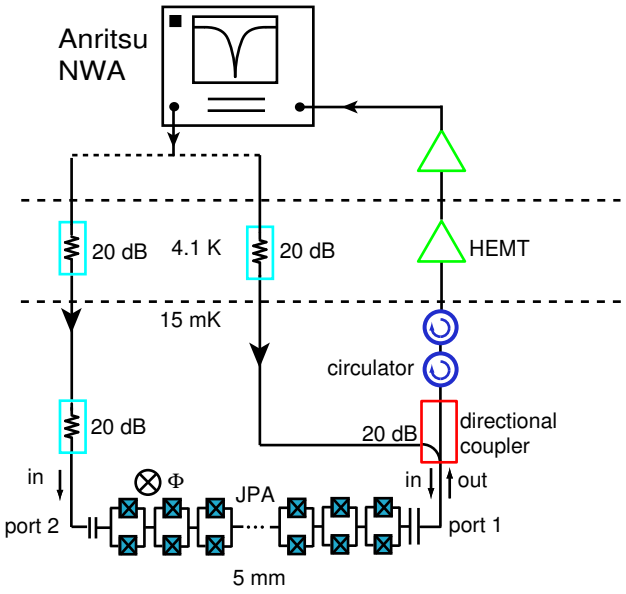

Figure 6.10: Simplified schematic used to measure the S-parameters and nonlinear behavior of the resonator with a Network analyzer. The JPA is measured in a cryostat held at 15 mK. We can send the testing signal to port 1 or 2 of the resonator to measure S_{11} or S_{12}. In the case of a quarter-wave resonator, it only has one port. Hence only S_{11} is measured.

The linear parameters of the resonators are measured using a vector network analyzer using a probing signal with very low power (compared to the critical power of the resonator). By measuring the reflection and transmission coefficient of the resonators, we can estimate the linear coupling parameters γ_i and the loss γ_l. Depending on the

kind of resonator ($\lambda/4$ or $\lambda/2$), only the reflection coefficient S_{11}, or both the reflection and transmission S_{12} coefficient can be measured. A simplified schematic of the measuring setup is shown in figure 6.10.

Extraction of linewidths, or equivalently the quality factors $Q = \omega_0/2\gamma$, based on the S-parameters is done by fitting the S-parameters to the expected transmission and reflection expression. For transmission, we expect a Lorentzian response

$$S_{12} = \frac{T_0}{1 + 2jQ(\omega - \omega_0)/\omega_0} \tag{6.5}$$

where Q is the total quality factor given by

$$\frac{1}{Q} = \frac{1}{Q_1} + \frac{1}{Q_2} + \frac{1}{Q_l}$$

and T_0 is given by

$$T_0 = \frac{2Q_cQ_l}{\sqrt{Q_1Q_2}(Q_c + Q_l)}.$$

Q_i, $i = 1, 2$, is the quality factor associated with the ports 1 and 2, Q_l represents the internal losses of the resonator, and Q_c is the coupling quality factor associated with both ports

$$Q_c = \frac{Q_1Q_2}{Q_1 + Q_2}.$$

As it was describe in chapter 5, the expected reflection response, is given by

$$S_{11} = \frac{\Gamma_0 + 2jQ(\omega - \omega_0)/\omega_0}{1 + 2jQ(\omega - \omega_0)/\omega_0} \tag{6.6}$$

where Γ_0 is given by

$$\Gamma_0 = \frac{1/Q_2 + 1/Q_l - 1/Q_1}{1/Q_2 + 1/Q_l + 1/Q_1}.$$

In the case of a single ended cavity, there is not transmission coefficient S_{21} to measure. But S_{11} has the same response, with $Q_2 \to \infty$. In order to more accurately estimate the reflection coefficient S_{11} and remove delay effects due to the finite length of the signal path, we first calibrate the latter by tuning the resonator out of the measurement frequency range. This is done by applying a current to the magnetic coil that tunes

the resonance frequency of the resonator. By applying a large enough current, we move the resonance frequency several linewidths from the frequency range of interest. Then, the resonator behaves as a mirror, reflecting all the signal and allowing us to calibrate the signal path. Then the resonance frequency is tuned back to the expected frequency. Finally the two traces are divided.

6.2.3 Non-linear characterization

The final feature of our resonators to probe are its nonlinear characteristics: Kerr constant and the nonlinear loss [38]. Both of these characteristics are estimated based on the power dependence of the resonance frequency. The measuring setup is exactly the same as the one to measure the S-parameters, the only difference being that we vary the power of the probing signal. As we increase the pump power, the Kerr nonlinearity makes the resonance frequency decrease according to the equation $\omega_0 - \omega_m + KN = 0$, where ω_m is the frequency at which Γ is minimum, K is the Kerr constant, and N is the energy stored in the resonator in number of quanta [38]. Defining, $K' = K/\hbar\omega_0$, then the change in resonance frequency is given by

$$\omega_0 - \omega_m + K'E = 0,$$

where E is the energy of the resonator in energy units and $\hbar K'$ is a unit-less number. Above the critical power P_c, S_{11} and S_{12} are discontinuous, and the resonators response is bistable. From the onset of this bi-stability we can estimate the critical power, and hence the Kerr constant using Eq. (5.49).

$$\begin{aligned} P^c_{i,\mathrm{in}} &= \hbar\omega (b^c_{i,\mathrm{in}})^2, \\ &= \frac{4\hbar\omega}{3\sqrt{3}} \frac{\gamma^3}{\gamma_i |K|}, \\ &= \frac{4}{3\sqrt{3}} \frac{\gamma^3}{\gamma_i |K'|}. \end{aligned} \tag{6.7}$$

Then nonlinear loss is estimated based on Eq. (5.63): when the loss is only linear,

the pump-amplitude dependance of the resonance frequency would be purely quadratic:

$$\omega_m - \omega_0 = -\frac{8\gamma}{3\sqrt{3}} \left(\frac{b_{1,\text{in}}}{b^c_{1,\text{in}}} \right)^2$$

where $b^c_{1,\text{in}}$ is the critical amplitude of the pump given by (5.49). However, when there exist non-linear loss, this simple quadratic dependance is no longer valid. From that deviation, we can estimate $\varepsilon = \gamma_{nl}/|K|$ (See Ref. [38]).

6.3 Characterizing the amplifier

The analysis of the parametric amplifier closely follows the theory developed by Yurke and Buks for parametric amplification in superconducting resonators [38]. In their model, the Kerr nonlinearity is provided by the intrinsic kinetic inductance of a superconducting film, while in our case it arises from the nonlinear Josephson inductance of the SQUIDs. The full characterization of the amplifier implies measuring the signal G_s and image G_i gain, measuring the correlation between these two gains by observing the phase-dependance of the quadrature gain G_θ, measuring the added noise of the amplifier, the squeezing of noise on one of the quadratures and finally the saturation of the amplifier. Next is a brief description of each measurement.

6.3.1 Signal and image gain

Once the critical power has been found by finding the bifurcation point, then we can set the pump power as close to it as we want in order to generate the appropriate gain. Then, it is a matter of sending a small test signal to measure the amplifier gain. The setup used is shown in figure 6.11. The schematic is drawn assuming a $\lambda/2$-resonator and pumping the resonator through the weakly coupled port. However, the pump could also be applied though the signal port. This is the way the $\lambda/4$-resonator is pumped. The only change in the setup is the requirement to use a power-splitter to add the two tones, the test signal and the pump, outside the cryostat. Two signal generators create

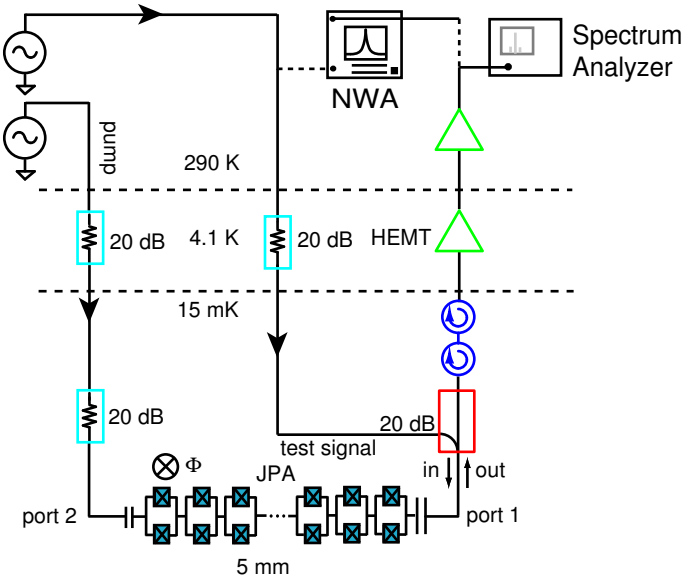

Figure 6.11: Schematic of the setup used to measure the signal and image gain. Two microwave generators are used to study the JPA. One generator creates the pump, while the second creates a gain-test tone. The pump tone is injected through port 2 of the JPA, while the calibration tone is incident on port 1 of the JPA through a 20 dB direction coupler. Signals emerging from port 1 pass through a circulator and are then amplified by a HEMT amplifier and a room temperature amplifier before entering input of a spectrum analyzer. Another setup to measure the gain only uses one signal generator and a network analyzer. The generation of the probing tone and its detection is done by the network analyzer.

two tones, a pump at frequency f_p and a signal at f_s. The two tones are injected into the dilution refrigerator. The pump is attenuated by 20 dB at 4 K and at 15 mK. The signal is attenuated by 20 dB at 4 K and a directional coupler at 15 mK provides an additional 20 dB of attenuation and separates the incident tones from the reflected tones.

The image gain G_i and signal gain G_s can be predicted from the resonator's parameters measured using the S-parameters. We define G_s as the ratio between the reflected signal power with the pump on and the incident signal power; G_i is the ratio between the image tone and the incident signal. Initially, I used a spectrum analyzer to do the measurement. This way I could measure both the direct and image gain. Yet,

since both give us the same information, we found it was simpler and faster to use the network analyzer to measure G_s only. Our network analyzer is not capable of measuring the tone at the image frequency $2\omega_s - \omega_p$, making it unable to measure G_i. In order to calibrate the gain, we do a similar procedure as the one to measure the reflection coefficient. Once the amplified signal is measured, the resonance frequency is tuned out of the frequency range of interest by applying a different current to the coil, therefore, changing the flux in SQUID loops. Then, we measure the signal reflected from the resonator to calibrate the signal path.

We generally do two kind of signals and image gain measurements: a bandwidth vs gain where we observe the expected behavior of limited gain-bandwidth product (Eq. 3.62); and a measurement of gain versus pump-detuning, which it is only used to compare it with the theory from Ref. [38] described in the previous chapters.

6.3.2 Phase dependence gain

The phase dependance gain is a consequence of the correlation between the signal and image gain. This correlation is measured using the setup shown in figure 6.12a. The correlation between G_i and G_s can be measured by applying a single tone slightly detuned from the pump and measuring the output in either the I-channel or Q-channel. The power gain in the I-channel is then given by

$$G_{\text{mixer}} \propto (G_s + G_i + 2\sqrt{G_s}\sqrt{G_i}\cos(2\theta + 2\psi)) \tag{6.8}$$

where θ is the LO-phase [8]. The proportionality constant consist of the the gain of the whole amplifier chain after the JPA and the term between parenthesis is the phase-dependant quadrature gain of the JPA (G_θ). ψ is a phase offset that depends on the signal-path length and the difference in phase between the signal and image amplitude-gain. Without loss of generality and for simplicity, in the rest of the chapter I will assume $\psi = 0$. Another way to measure these correlations is to apply the appropriate linear

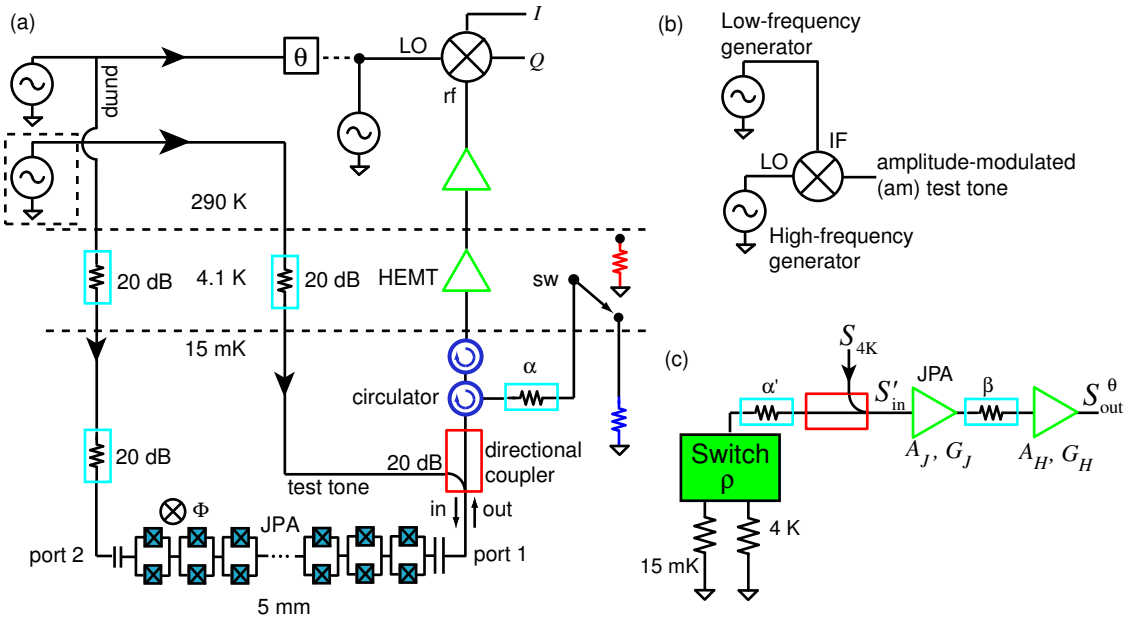

Figure 6.12: (a) The schematic used to measure the phase dependant gain, the added noise of the amplifier and squeezing is very similar to the one used to measure the signal and image gain. The main change is the incorporation of a mixer to perform homodyne detection of the output of the JPA. The pump tone is injected through port 2 of the JPA, while the calibration tone is incident on port 1 of the JPA through a 20 dB direction coupler. Signals emerging from port 1 pass through a circulator and are then amplified by a cryogenic high-electron-mobility transistor amplifier (HEMT) and a room temperature amplifier before entering the radio-frequency (rf) port of a mixer. The noise incident on port 1 of the JPA which comes primarily from the isolated port of the circulator can be switched (sw) to come from two different resistors held at different temperatures. The mixer LO comes from either the same signal generator as the pump, in which case the phase is tuned by a manual phase-shifter or from another phase-locked signal generator. In the latter case, the phase is changed by using the phase-knob of the apparatus. (b) The calibration tone can be a single frequency tone or a linear combination of two fourier frequencies around the carrier frequency f_{pump}. The latter is realized by using a mixer as an up-converter. By using a two-fourier-frequency signal, we can measure the phase-dependant gain of the JPA. (c) The noise model for the input noise-power of the JPA consist of two calibrated noise generators in the form of two resistor connected to a switch. The switch located at 4 K has a loss ρ that adds $(1-\rho)1/2\coth(\hbar\omega/k_B T_{4\text{K}})$ of thermal noise. The output of the switch is attenuated by an attenuator and the loss of the circulator and goes into the port 1 of a directional coupler. At the output of the directional coupler and the input of the JPA, the noise is formed by 99% of the input noise plus 1% of the noise coming from the 4 K plate. This noise, plus the added noise of the JPA is amplified by the JPA and the amplifier chain, down-converted by the mixer and appears at the output I and Q channels. Considering only one of the channels (say I), the noise spectral density measured S^{θ}_{out} is chosen by the angle θ of the LO. To measure the amplified quadrature, $\theta = 0$, while to measure the squeezed quadrature, $\theta = \pi/2$.

combination of input fourier modes (Eq. 3.79). As I mentioned in section 6.1.2, there are two options to do this: using amplitude modulated or phase modulated signals. We chose amplitude modulated signals with suppressed carrier to test the phase-dependance gain. The setup to generate this AM-tone is shown in figure 6.12b. The LO of the mixer used to generate the test-am-tone is assumed to have the same frequency as the JPA pump; in fact, both tones come from the same signal generator. In Eq. (6.1), it was shown that even though the signal consists of two tones at different frequencies $\omega_p \pm \omega_{\rm IF}$, the phase of the signal is given by the LO phase ϕ, and the effective amplitude of the signal, $A(t)$ is just a slow function of time (in our case $\omega_{\rm IF} = 10 - 200$ kHz). Note that, even though the two ways of measuring the correlations of the signal and image gain are completely equivalent, it is only for signal modes that correspond to particular linear combinations of frequencies above and below the pump (Eq. 6.2), that the JPA will not be quantum limited; that is, it will be able to amplify those signal with less added noise than a quantum-limited amplifier.

6.3.3 Noise measurements

The correlations measured in the phase-dependant gain can also manifest themselves in the form of noise squeezing and amplification, depending of what quadrature of the JPA we measured. So far the analysis of the mixer as done in section 6.1.2 was rather classical. Now, I use a quantum-language (where the physics variables are now considered operators) to explain the effect of an ideal homodyne detector. Imagine we could have an ideal mixer right at the output of a JPA operated in the homodyne mode in which $\omega_{LO} = \omega_p$ are equal and in which the input at both the signal frequency $\omega_p + \omega$ and image frequency signal frequency $\omega_p - \omega$ are both regarded as the signal. The output of the I port in the frequency domain is given by

$$I(\omega) = B[b(\omega)e^{i\theta} + b^\dagger(-\omega)e^{-i\theta}]$$

where B is just a normalization factor [8, 84, 85]. If we chose the normalization factor so that the expected value of the anticommutator of I of a vacuum state is (assuming a single-sided spectral density convention)

$$\langle 0|\{I^\dagger(\omega), I(\omega)\}|0\rangle = \frac{\hbar\omega}{2},$$

then I gives the quadrature X_θ of the field at the input of the mixer (Fig. 6.13).

$$I(\omega) = X_1(\omega)\cos\theta - X_2(\omega)\sin\theta.$$

where $X_j(\omega)$ are defined as in appendix A. However, at microwave frequencies, there is not such a thing as an ideal mixer, and homodyne detections are far from quantum-limited. Besides, the mixer is not at all located right at the output of the JPA. Instead, at the output of the I and Q-port of the mixer, what we really have is

$$I(\omega) = \sqrt{G_T}(\hat{X}_1(\omega)\cos\theta - \hat{X}_2(\omega)\sin\theta + \chi_I)$$

and

$$Q(\omega) = \sqrt{G_T}(\hat{X}_1(\omega)\sin\theta + \hat{X}_2(\omega)\cos\theta + \chi_Q),$$

where G_T is the total power gain of the commercial amplifiers and mixer, θ is the phase between the pump and the LO, and χ_I and χ_Q are random variables whose variance are the spectral density of the noise of the amplifier chain. Both will have a variance with an average value of A_T, where A_T is the noise number [2] of the commercial amplifier chain expressed as noise added at the output of the JPA.

Let's consider first the amplified quadrature, and study the JPA's added noise and the total noise of the amplifier chain as a function of the JPA gain. In these measurements, the LO and pump come from the same signal generator, and a manual phase shifter is used to send all the amplified quadrature into the I channel of the mixer. By switching between two calibrated noise sources (Fig. 6.12a and c), we can change the incident noise on the JPA. This method to estimate the added noise of an amplifier is

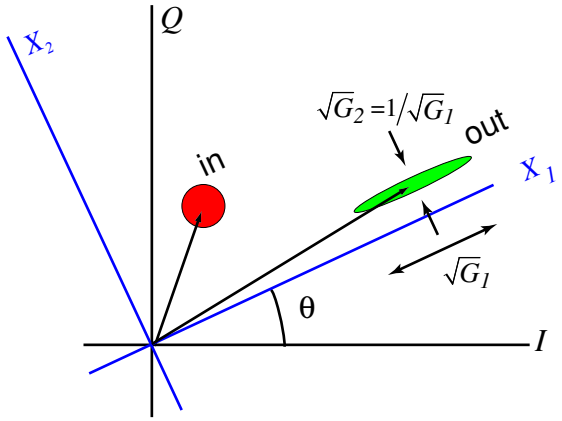

Figure 6.13: (a) This diagram represents the operation of an ideal degenerate parametric amplifier which transforms an input state (red circle) into an output state (green ellipse) by amplifying the X_1 component by $\sqrt{G_1}$ and squeezing the X_2 component by $\sqrt{G_2} = 1/\sqrt{G_1}$. The mixer projects the output state into axes rotated by θ.

called Y-factor measurement. The microwave switch used for our Y-factor measurement is a Radiall R573423600. The change in noise power at the output of the mixer allows us to estimate the noise A_J just added by the JPA, the JPA gain[9] $G_J \equiv G_1$, the total added noise of both the JPA and the commercial amplifier chain A_{sys} (i.e., the total noise referred to the input of the JPA), and the total gain $G_J \times G_H \times \beta = G_J \times G_T$, where $G_T = \beta G_H$ is the effective gain taking into account the loss between the JPA and the HEMT. The calibrated noise sources are derived from two resistors held at different temperatures. The resistances are matched to the wave impedance of the cables that carry signals to the JPA input. The noise emitted by both resistors is attenuated by an attenuator held at a temperature $T_\alpha = 15$ mK and then passed to the JPA through a microwave circulator which separates the incident and reflected signals from the JPA. Ideally, the power spectral density in units of noise quanta incident on the JPA through

[9] During the rest of this chapter, I define G_J as the maximum quadrature gain of the JPA G_1.

the circulator is

$$\begin{aligned} S_{\rm in}(T_{\rm load}) &= \frac{1}{2}(\alpha \coth \frac{\hbar\omega}{2k_BT_\alpha} + (1-\alpha)\coth\frac{\hbar\omega}{2k_BT_{\rm load}}) \\ &= \frac{1}{2} + \alpha\frac{1}{e^{\frac{\hbar\omega}{k_BT_\alpha}}-1} + (1-\alpha)\frac{1}{e^{\frac{\hbar\omega}{k_BT_{\rm load}}}-1}, \end{aligned} \tag{6.9}$$

where $T_{\rm load} = T_c = 15$ mK or $T_{\rm load} = T_h = 4.1$ K depending on the position of the switch shown in Fig. 6.12a and c, and α is the attenuation that we have intentionally placed in the mixing chamber to prevent saturation of the JPA with thermal noise when the Y-factor measurement is done at high gains.

The attenuation α also reduces the thermal noise originated in the loss of the switch. This loss can actually be a problem since even in the case of the switch being positioned in the cold load, the finite (unknown) loss of the switch can be large enough to generate significant thermal noise. The first term in equation (6.9) is the quantum noise, while the second and third terms are the thermal noise which is small compared to the quantum noise at $T_{\rm load} = T_c$. Yet, due to loss of the circulator, the attenuation α of Eq. (6.9) needs to be replaced by an $\alpha' > \alpha$ that takes into account this extra sources of loss. Also, a small amount of noise that comes from the coupled port of the directional coupler as shown in figure 6.12c needs to be added.[10] Hence, the complete expression for the noise incident on the JPA when the non-ideal behavior of the all the microwave components is taken into account includes contributions from: thermal noise introduced with the calibration tone via the directional coupled port, the insertion loss from the circulator, directional coupler and the switch. Expression (6.9) then becomes

$$\begin{aligned} S'_{\rm in}(T_{\rm load}) &= \frac{1}{2}[\left((\rho\coth\frac{\hbar\omega}{2k_BT_{\rm load}} + (1-\rho)\coth\frac{\hbar\omega}{2k_B4.1})\alpha' + (1-\alpha')\coth\frac{\hbar\omega}{2k_BT_{\rm cry}}\right)\times \\ &\quad (1-C) + C\coth\frac{\hbar\omega}{2k_BT_{\rm 4K}}] \end{aligned} \tag{6.10}$$

The unknown insertion loss at cryogenic temperatures of the circulator and of the microwave switch are the dominant uncertainties in the added noise and squeezing mea-

[10] When an extra 20 dB are placed between the attenuator at the 4 K plate and the directional coupler, the noise coming through the 20 dB-coupled port is negligible, as it is possible to model it as extra attenuation at 15 mK whose added noise is just vacuum noise.

surements. In the data shown in the following sections, the extreme values represented by the error bars are derived by assuming: first, that there in no insertion loss, and then, that the insertion loss has not changed between room temperature and the operating temperature. In the case of the circulator, the data-sheet specifies the maximum loss at 77 K.

By selecting $\theta = 0$, the amplified quadrature appears at the I port of the mixer (Fig. 6.12a). We measure the ratio Y of the noise power at the output I with the hot load incident on the JPA divided by the noise power with the cold load incident on the JPA. This Y-factor measurement allows us to extract

$$A_{\rm sys} = (S'_{\rm in}(T_h) - Y S'_{\rm in}(T_c))/(Y-1) \tag{6.11}$$

and the total gain $G_J G_T$. We then adjust the cavity's resonance frequency about 10 linewidths away from the LO frequency and turn off the pump. Because the JPA now acts as a passive mirror, we can perform a Y-factor measurement on our commercial amplifier chain, finding A_T and G_T. From both measurements, we extract the JPA gain G_J and A_J (Fig. 6.12c). To avoid unknown loss and noise in the cables carrying the calibrate noise signals, superconducting Niobium coaxial cables were used to carry these signals between the 15 mK region of the refrigerator and 4 K region. A calibrated ruthenium oxide thermometer measured the refrigerators base temperature and the temperature of the helium bath (4.1 K), to which the 4 K resistor and microwave switch were thermally anchored. A calibration tone, (Fig. 6.12a) is used to verify the gain inferred from the Y-factor measurements.

6.3.4 Squeezing

We now turn our attention to the squeezed quadrature X_2 when the incident noise is mostly quantum noise ($T_{\rm load} = T_c$). When $\theta = 0$, X_2 appears at the Q port (Fig. 6.13). The noise at the Q port referred to the input of the HEMT is composed

of the effective added noise of the commercial amplifiers ($A_H/\beta = A_T \approx 26$) and noise in the rotated quadrature $X_{\theta+\pi/2}$ coming from the JPA, $\Delta X^2_{\theta+\pi/2} = \Delta X_1^2 \sin^2\theta + \Delta X_2^2 \cos^2\theta$ (Fig. 6.13). In order to illustrate the JPA's unequal effect on the noise of both quadratures, we re-define the quantity $\xi(\theta) = (\Delta X^2_{\theta+\pi/2})_{\text{pump on}}/(\Delta X^2_{\theta+\pi/2})_{\text{pump off}}$. In order to measure $(\Delta X^2_{\theta+\pi/2})_{\text{pump off}}$, I turn the JPA pump off and adjust its resonance frequency so that the resonator behaves as a mirror. When $\theta = 0$, we will observe that $\xi < 1$ which means that the noise at the output of the JPA has been squeezed. If instead $\theta = \pi/2$ radians, we will find $\xi \approx G_J > 1$. For an ideal JPA $\xi(\pi/2) = G_J$ [8]. (Because a small fraction of the incident noise on port 2 is either lost through port 1 or absorbed in the cavity, for our device there is a small difference between $\xi(\pi/2)$ and G_J.) We also measured the squeezing ξ as a function of gain G_J and compare it with theory (Ref. [38]).

In this measurement, we tested both setups shown in figure 6.12a, using the same signal generator for the pump and the LO, and a manual phase shifter to change the phase in the LO . We also used a different signal generators (with their internal clocks locked) and change the phase with the built-in phase option of the generators. In both cases we got the same answer, but in the second option the measurement could be automated so we chose the second option. Another advantage is that all manual phase shifters have some phase-dependance insertion loss as high as 0.2 dB, which could affect the "observed squeezing" unless care was taken in adding another signal to monitored the conversion-loss of the mixer as the phase (and hence the LO power) was changed. We do not have this problem if we use two different signal generators as the output power does not depend on its output phase. One caveat, though, is that when two signal generators are used, the phase-noise of the signal generators is observed at the output of the mixer. This phase noise looks like a phase-dependance noise on top of the noise at the input of the mixer. This would not look like squeezing in the sense that it would not make the noise to go below the vacuum noise level. However, if it is large

enough, it could prevent us from measuring squeezing. In our case, for frequencies larger than 100 kHz, the phase noise of the signal generators is not an issue. A calibration tone was added to the measurement chain to measure the gain of the squeezer and to ensure that the noise reduction arises from genuine squeezing and not saturation of the amplifiers.

6.3.5 Amplifier saturation

The amplifier saturation was measured using the same setup used to measure the amplifier's gain with a network analyzer as shown in figure 6.11. We measure the direct gain as a function of the signal power as we increase it. We cannot compare it with theory as the theory used to analyze the amplifier assumes an undepleted-pump approximation. The effect of saturation on parametric amplifiers has not been extensively treated in the literature, with only a few exceptions for very particular implementations [47, 86].

6.4 Aluminum resonators

This sample was fabricated in March, 2006, with the original idea of testing phase transition physics in arrays of Josephson junctions. We cooled it down first on April, 2006 and then again in January 2007. This device was fabricated out of aluminum, and the SQUIDs were made from aluminum-aluminum oxide-aluminum junctions. They were fabricated using traditional electron beam lithography techniques using a double-angle evaporation (Dolan bridge technique [87]). A picture of a similar device to the one measured is shown in figure 6.14a. The details of the fabrication are described in appendix C. Next I discuss all the measurements done on this particular sample. It consists of a quarter-wave CPW resonator whose center conductor is an array of 400 SQUIDs in series (Fig. 6.14). Typically, the resistance of the device tends to increase over time. This was definitely observed in this sample as the critical current per SQUID dropped from 1.9 to 1.5 μA. In the first cooldown, only its linear properties

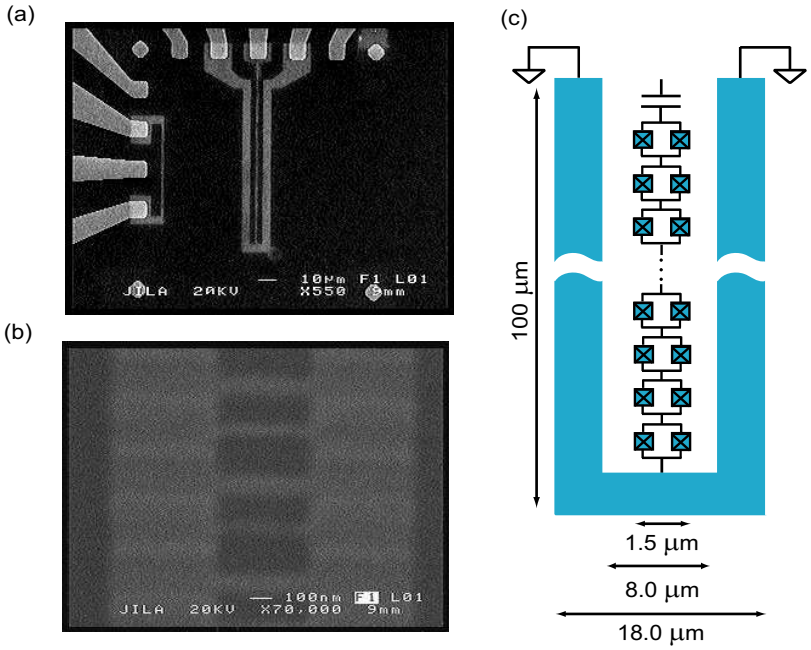

Figure 6.14: (a) Image of a test sample. An array is also shown on the left of the device. However, the I-V curves at 15 mK were taken from an array exactly as the one used for the rf-measurements (including the ground planes) with the only difference being that the capacitance was replaced by a short circuit. (b) Zoom-in of the array, where the two periodicity of the SQUID loop size is shown. This imperfection in the fabrication is responsible for the "beating" manifested in the magnetic-field dependance of the resonance frequency. (c) The tested device is a CPW transmission line resonator where the center conductor is a series array of 400 SQUIDs. The associated dimensions of the CPW are shown in the figure. The resonator's ground plane is made out of aluminum, and the SQUIDs are made from Al/AlOx/Al junctions. They are fabricated using e-beam lithography and double angle evaporation on an oxidized silicon substrate.

were tested while in the second cooldown, we measured its performance as a parametric amplifier. All the data shown is from the second cooldown where the device was used as an amplifier, unless it is specifically stated that it is from the first cooldown. The resonance frequency can be adjusted over an octave in frequency, between 4 and 7.8 GHz by applying a magnetic field (4.5 and 8.8 GHz before the junctions aged).

6.4.1 dc-measurements

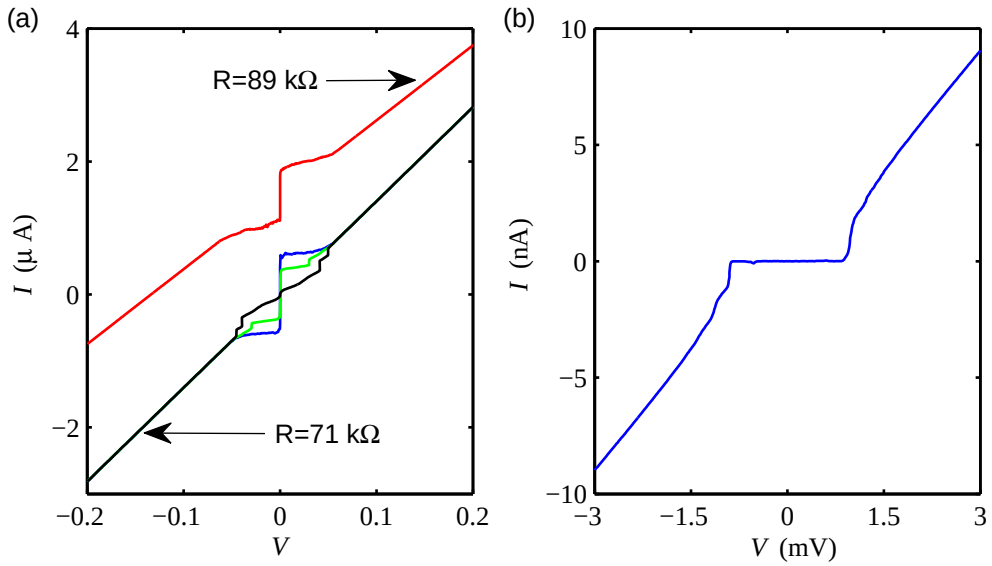

Figure 6.15: (a) IV characteristic of an array of 400 SQUIDs measured in the superconducting state at 15 mK. Data from both cooldowns is plotted in order to show the observed aging of the junctions. Three I-V curves for three different applied magnetic fields is shown for the case of $R = 71$ kΩ to show the modulation of the critical current of the SQUIDs. An offset has been added to the I-V curve of the $R = 89$ kΩ case for clarity. (b) IV curve of a co-processed SET (2 junctions in series) at 15 mK. From this IV curve, the size of the superconducting gap was estimated to be $\Delta = 215$ μeV.

We performed dc-measurements as described in section 6.2.1. We measured arrays of SQUIDs to find the average resistance of the junctions. There were two type of arrays, some small ones like the ones shown on the left of the resonator in figure 6.14a, and other arrays that were identical to the resonators, but with the capacitor replaced with a

short-circuit. Only the latter were measured at 15 mK. The IV-curves for both cooldown are shown in figure 6.15. The estimated total resistance per SQUID is that of the array divided by the 400 SQUIDs per array. The size of the superconducting gap is measured using the I-V curves of a co-fabricated single-electron-transistor (SET), in a different chip (Fig. 6.15b), from which we estimate $\Delta = 215$ μeV. Using Eq. (3.17), we estimate the critical current I_c^0 for one SQUID to be 1.5 μA (1.9 μA for the SQUIDs in the first cooldown). When one measures a single SQUID or an series array of SQUIDs, the maximum measured current at $V = 0$, that is, the current at which the junctions switch from the supercurrent branch to a resisitive state is not a way to estimate I_c since it dependes on how well isolated the junction is. Instead, I will use the resistance of the SQUID and the Ambegaokar-Baratoff expression for the critical current, Eq. (3.17).

From the dc measurements, we estimate that the resulting metamaterial has a zero-flux inductance per unit length of $L_l = 0.9$ mH/m $\approx 700\mu_0$. The CPW was designed to have a capacitance per unit length of $C_l = 0.11$ nF/m, yielding a zero-flux phase velocity of $v_{ph} = 1/\sqrt{L_l C_l} = 0.01c$ and a zero-flux characteristic impedance of $Z_c = 2.9$ kΩ. The reason for the rather large characteristic impedance of this sample is that it was originally designed to study phase transitions in Josephson junction arrays [72, 74].

6.4.2 Linear measurements of the resonator

Since this device was a quarter-wave resonator, we only measure its reflection coefficient Γ using the setup shown in figure 6.10. We apply a low enough incident power P, in order to assure that the resonator response is linear (by low enough power I mean that I only use $P < P_c/1000$). From the imaginary and real part of Γ, the quality factors associated with losses Q_l and capacitively coupled port Q_1 are calculated. In this device, both turn out to be very similar (the resonator is slightly overcoupled). Hence, the resonance frequency $f_{\rm res}$ is easily identified by a dip in $|\Gamma|$. Figure 6.16(a) shows how

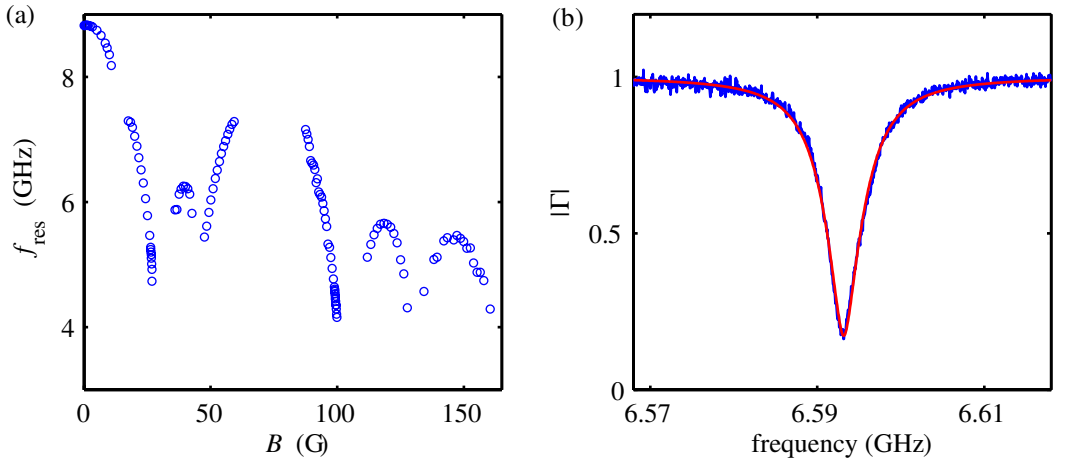

Figure 6.16: Linear measurements for the aluminum resonator made on April, 2006. (a) Resonance frequency as a function of flux. (b) Magnitude of the reflection coefficient showing the expected Lorentzian behavior. Data shown in blue and fitting in red. From the fitting, the quality factors are calculated: $Q_1 = 1530$ and $Q_l = 2170$.

the resonance frequency behaved as a function of the applied magnetic field B in the first cooldown of this device. A few things are worth mentioning. In figure 6.14b is easy to see that the SQUIDs loops are not uniform but have two different sizes, consequence of a small difference in the two angles of evaporation during the fabrication. This creates a bimodal distribution in the SQUID-loop area that manifests as a two-periodicity in the magnetic field dependance of the critical currents of the SQUID array and the resonance frequency of the resonator. This is observed in the figure 6.16a. In this plot, it is also obvious that there are certain frequency ranges (7.3-8.2 GHz) where the plot does not show measured resonance frequencies. The reason for that is that we were unable to see a resonance frequency in that region,[11] which we refer to as the "desert." For frequencies close to them, the resonators losses rise significantly. We do not understand this behavior. However, away from these regions, the resonator behaved normally. The

[11] There were other regions where a resonance frequency was not observed only at certain higher magnetic fields. For example, in the second (small) lobe around $B = 40$ G, no resonance frequency was observed below 5.8 Ghz, even though they could be observed in the first and third large lobes. This, however, is thought to be related with a large increase in internal losses when the magnetic field was close to half a flux quantum for some of the SQUIDs.

reflection coefficient Γ for a particular field is plotted in figure 6.16b. Based on the measured reflection coefficient and Eq. (6.6), we extract the quality factors Q_1 and Q_l. For this case, the values of quality factor are $Q_1 = 1530$ and $Q_l = 2170$. In general, the internal quality factors were over 2000, except for regions close to the desert and at magnetic fields close to half a flux quantum for both types of SQUIDs (basically for $f_{\rm res} < 5.2$ Ghz). The origin of the desert is not yet understood.

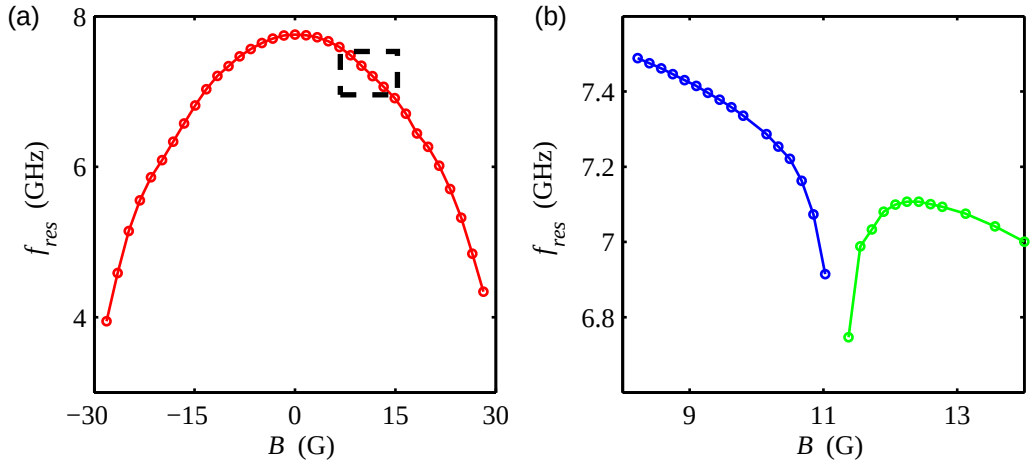

Figure 6.17: (a) Resonance frequency as a function of flux for the second cooldown of the device. Due to aging, the zero-flux resonance frequency decreased from 8.8 to 7.8 GHz. At first sight, the "desert" seemed to have disappeared. However, if we looked more carefully in the regions enclosed by the square, we find that at $B = 11$ G a strange feature appears (b). We believe this feature is the same as the one that we called the "desert" in the previous cooldown, but that it has changed due to the aging of the junctions.

As mentioned at the beginning of this section, we cooled down this same device 10 months later and it showed signs of aging. However, the increase of the resistance was not the only change. The desert itself changed also as it is shown in figure 6.17, assuming the feature called previously as the desert and this one are the same. Again, we do not understand it, but it seems to be something intrinsic to the resonator, as it changes with the aging of the junctions. We did not look into this feature as we were more interested in studying it as a parametric amplifier. Therefore, we stayed away

from this feature at $B = 11$ G. We estimated the quality factors and the linewidths (HWHM) $\gamma = \omega_0/2Q$. For example, for a flux of $\Phi = 0.2\Phi_0$, we find the resonator's linear parameters $f_{\rm res} = 6.952$ GHz, $Q_1 = 1830$, and $Q_l = 3160$ (Fig. 6.18a). To demonstrate the tunability of the JPA, we also test the performance of the amplifier at lower frequencies. For example, for $\Phi = 0.35\Phi_0$, the resonance frequency is $\omega_0/2\pi = 5.203$ GHz. A similar analysis as the one described for $\Phi = 0.2\Phi_0$ gives the following parameters: $Q_1 = 2740$, $Q_l = 3060$ (Fig. 6.18b). The quality factors did not change dramatically from the previous cooldown, except in the regions close to the desert, where now the high-loss is only reduced to a small range of only ~ 100 MHz (Fig. 6.17b). Nonetheless, we still do not have an explanation for the losses in this resonator.

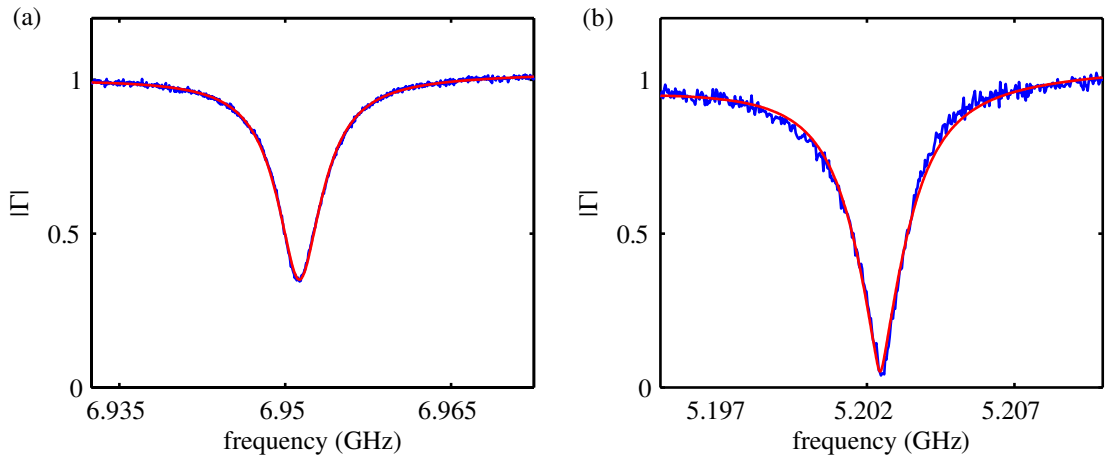

Figure 6.18: Linear measurements for the aluminum resonator made on January, 2007 (second cooldown). Magnitude of the reflection coefficient showing the expected Lorentzian behavior for 2 different resonance frequencies. Data shown in blue and fitting in red. From the fitting, the quality factors are calculated. (a) At $f_{\rm res} = 6.951$ GHz, $Q_1 = 1650$ and $Q_l = 3170$. (b) At $f_{\rm res} = 5.202$ GHz, $Q_1 = 3160$ and $Q_l = 3200$.

6.4.3 Non-linear characterization

From the frequency and power dependence of Γ, we estimate the critical power and (modified) Kerr constant K' as defined by Eq. (6.7). We performed this test at

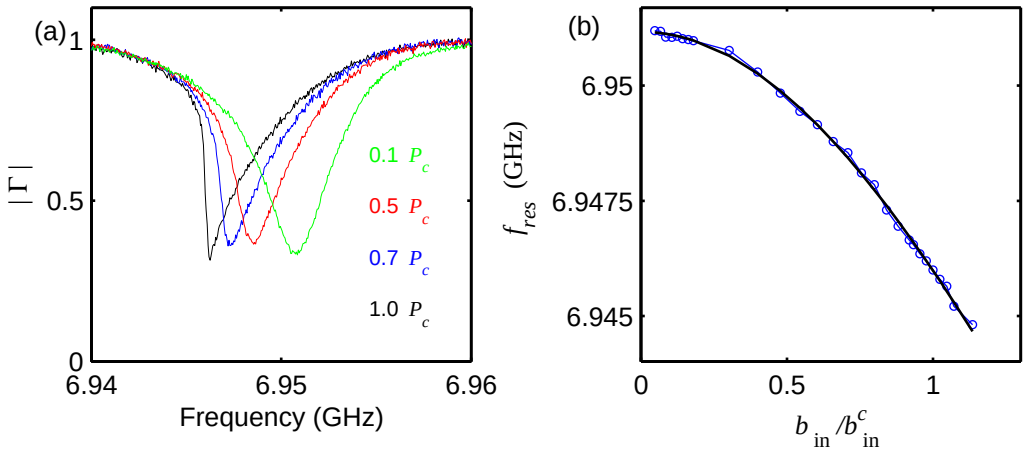

Figure 6.19: Power dependance of the resonance circuit. (a) Reflection coefficient magnitude as a function of frequency at different pump powers for $B = 14.4$ G. (b) By doing a fitting to the expected power dependance of the resonance frequency, Eq. (5.63), the ratio of nonlinear loss and kerr constant $\gamma_{nl}/|K|$ is estimated. For this case, from the fitting we estimate that $\gamma_{nl}/|K| = 0.03$

three different frequencies. At $\Phi = 0.2\Phi_0$ and $f_{\rm res} = 6.952$ GHz, the critical power and Kerr constant were $P_c = 3 \pm 1.3$ fW and $\hbar K' = -1.6 \pm 0.7 \times 10^{-5}$, respectively. The large uncertainty comes from the 4 dB uncertainty of the incident power on the resonator. From appendix A in Ref. [38], we can calculate our estimate for the Kerr constant using Eqs. (5.44-5.46). The expected value for the Kerr constant is $\hbar K' = -1 \times 10^{-5}$, in agreement with our measurement. To model more completely the behavior of the resonator, we also include a nonlinear dissipation term $\gamma_{nl} = 0.03\,|K|$.

A similar analysis as the one described for $\Phi = 0.2\Phi_0$ gives the following parameters for $\Phi = 0.05\Phi_0$: $f_{\rm res} = 7.756$ GHz, the critical power was $P_c = 3.5 \pm 1.5$ fW, the Kerr constant was $\hbar K' = -1.9 \pm 0.8 \times 10^{-5}$ and the nonlinear loss was $\gamma_{nl} = 0.02\,|K|$. For $\Phi = 0.35\Phi_0$, the resonance frequency is $\omega_0/2\pi = 5.203$ GHz and the nonlinear parameters are: $P_c = 0.5 \pm 0.2$ fW, $\hbar K' = -9 \pm 4 \times 10^{-5}$ and $\gamma_3 = 0.145\,|K|$. For frequencies of 5.5 GHz and below, we have observed an increase of the nonlinear loss, which starts affecting the performance of the amplifier.

Since this device has very small critical powers, the phase noise of the generator is not an issue, as can be easily proved by seeing that at 10 kHz, the phase noise is the same as at 100 kHz [81], which compared to the vacuum noise is of the order of 0.1%.

6.4.4 Gain measurements

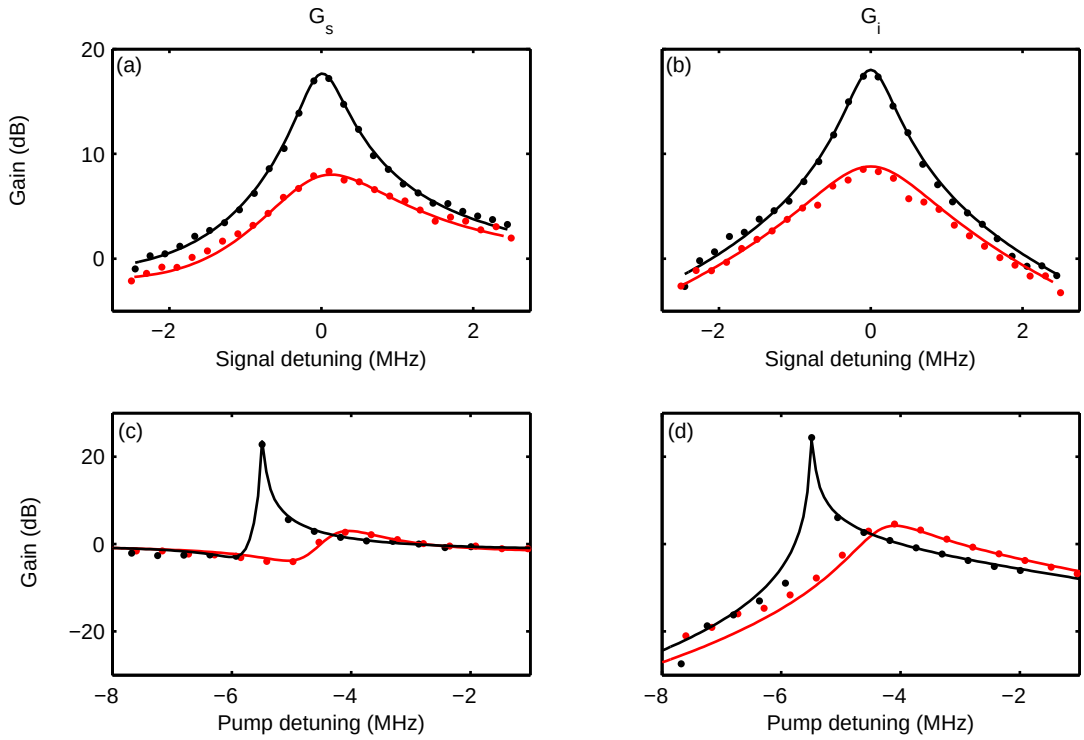

Figure 6.20: Performance of the amplifier. (a) and (b) G_s and G_i as functions of signal detuning (points) and predictions of Ref. [38] (lines) for two different pump powers. G_s and G_i for $P = 0.9\ P_c$ (black) and for $P = 0.75\ P_c$ (red). (c) and (d) G_s and G_i as functions of pump detuning (points) for $P = 0.95\ P_c$ (blue) and $P = 0.5\ P_c$ (red) and prediction (lines) of Ref. [38].

The parametric amplifier is operated in reflection mode, as shown in Fig. 6.11(a). We operate it first by applying a calibrating tone slightly detuned from the pump and measure the frequency dependence of both gains in two different ways. In the first case, the signal and the pump frequencies are different. In the first test, we apply the pump at a frequency close to ω_m and analyze G_s and G_i as we detune the signal frequency

from the pump by an amount Δf. In Figs. 6.20(a) and 6.20(b), we plot both G_s and G_i as a function $\Delta f = f_{\text{signal}} - f_{\text{pump}}$ for two different pump powers. We also plot the predictions from the theory in Ref. [38] where the parameters in the theory are extracted from the measurements of Γ. From this plot, we estimate the 3 dB bandwidth to be about 300 kHz when G_s and G_i are 18 dB. Next, we measure G_i and G_s as a function of pump detuning, *i.e.*, the difference in frequency between the applied pump and f_{res}. In this test, the signal and the pump frequency differ by a fixed amount, $\Delta f = 10$ kHz, (Figs. 6.20(c) and 6.20(d)). The agreement seen in Fig. 6.20 between the data and theory explained in chapter 3 and 5, suggests that Ref. [38] provides an appropriate model for our device.

In the second test, for $f_{\text{res}} = 6.95$ GHz we measured the phase dependance of the gain of the degenerate parametric amplifier. In this case the the pump and the signal frequencies are the same (Fig. 6.12a and b). The gain of the parametric amplifier is sensitive to the phase between the pump and the signal. To measure this phase dependence, we amplitude modulate the signal at 20 kHz and adjust the phase of the pump relative to the signal. We define the gain as the ratio of the am-modulation sideband power with the pump on and pump off. From Eq. (6.8), for $G_s \sim G_i \gg 1$, the quadrature gain G_J is 6 dB larger $G_J \equiv G_{X_1} \approx 4G_s$, (see Eq. 3.77), if the phase between the pump and signal is tuned for maximum gain. The phase dependence of the gain for a pump power close to P_c is shown in Fig. 6.21(a); there, it is evident that we see deamplification, a hallmark of degenerate parametric amplifiers.

To demonstrate the tunability of the JPA, we also test the performance of the amplifier at lower frequencies. However, as mentioned above, the performance is greatly affected for resonance frequencies $f_{\text{res}} < 5.2$ GHz due to the onset of large nonlinear loss. This increase of nonlinear loss made the measured gains smaller than the ones at 6.95 GHz. The highest G_i and G_s observed at this frequency are both 12 dB.

6.4.5 Estimate of the added noise of the amplifier

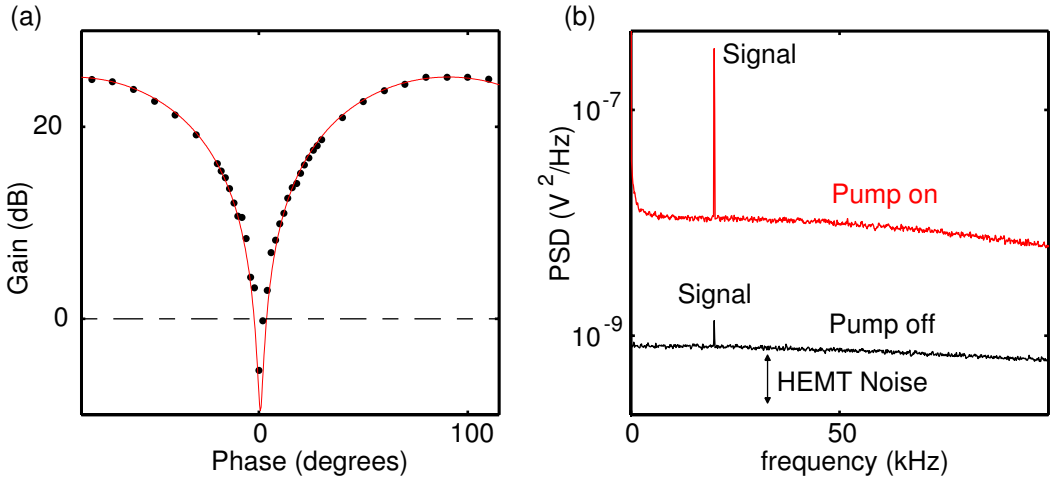

Figure 6.21: (a) Gain as a function of the phase between the pump and the signal (points) and prediction (line) from Ref. [38] showing the expected behavior for degenerate parametric amplifiers ($P = 0.9P_c$). (b) Power spectral density of the demodulator output for the cases when the pump is on ($P = 0.95P_c$) and off. The gain in this case is 630 (28 dB). The applied signal power is $1.6 \pm 0.7 \times 10^{-20}$ watts.

In Fig. 6.21(b), we plot the power spectral density (PSD) of the demodulated signal with the pump off and pump on for $P = 0.95P_c$, where the signal-pump phase has been adjusted for maximum gain (28 dB). At this gain, the HEMT amplifier's input noise is overwhelmed by the noise at the output of the parametric amplifier, effectively improving the signal-to-noise ratio (S/N) by 16 dB. A definitive measurement of the noise added by our parametric amplifier requires a calibrated noise source. In this cooldown, we did not have such calibrated noise source. However, by measuring the S/N with the pump off, we find that the noise referred to the input of the HEMT is $T_N = 12 \pm 5$ K. From the S/N improvement with the pump on, we estimate the total noise referred to the input of the JPA as 300 ± 130 mK. This value suggests that the parametric amplifier adds an amount of noise comparable to the vacuum noise ($hf_{\rm res}/2k_B = 166$ mK), which must be present at the input of the JPA. The error bars were estimated based on the losses of the semi-rigid cables. We measure their loss at

room temperature and then at 77 K.

6.4.6 Final comments

With this aluminum sample, we demonstrated a widely tunable parametric amplifier based on a coplanar waveguide resonator whose inner conductor is made from a SQUID array. We observed good gains and performance that was understood within the theory frame of Ref. [38]. Although some features were not understood, such as the origin of the loss in this superconducting devices, or the region called the "desert," it still performed well enough to act as a low noise preamplifier for the quietest commercial amplifier available. For the next generation of devices, we increased the critical power of the resonators by increasing the critical current of the junctions and we increased the bandwidth by using a much larger coupling capacitor. Also, the devices were made out of niobium, which has a larger critical temperature than aluminum. We do not have the capability of making niobium Josephson junctions at JILA so for this new generation of resonators we collaborated with Kent Irwin's group from NIST.

6.5 Niobium resonators

In this case, two different realization of a JPA were measured, a quarter-wavelength and a half-wavelength cavity. The inductance per unit length of this transmission line comes mostly from the nonlinear Josephson inductance of the SQUIDs, but unlike the aluminum device, at zero-flux the geometrical inductance does provide a non-negligible amount of inductance (30% at zero flux). Unless, explicitly said, the data shown is from the half-wavelength resonator. We create the half-wavelength microwave cavity from this metamaterial by interrupting the center conductor with two capacitors, one much bigger than the other, thus creating a strongly coupled port and a weakly coupled port (Fig. 6.22).

6.5.1 Description of the device

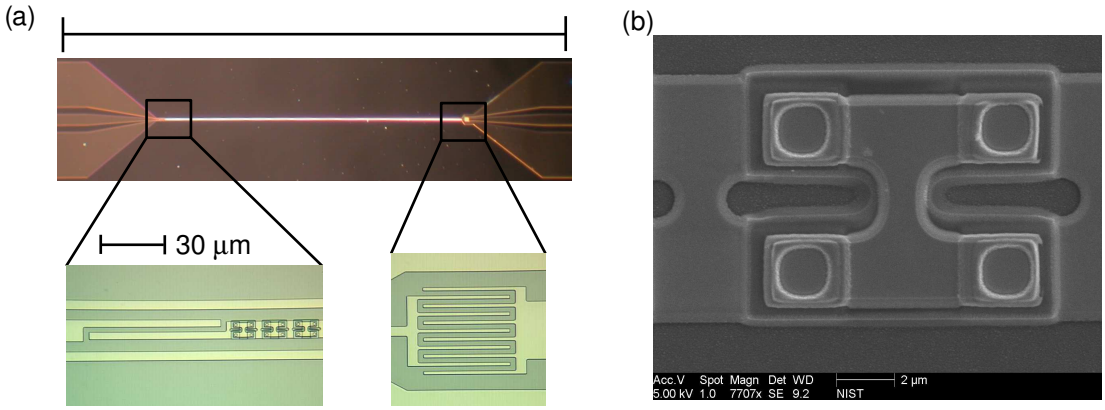

Figure 6.22: Images of the device. (a) The images are a picture of the full device, and a magnified image of the weakly coupled port, a few SQUIDS and the strongly coupled port. (b) SEM picture of a pair of SQUIDs (picture courtesy of Leila Vale).

Devices were fabricated at NIST Boulder on a high purity uncompensated silicon wafer with resistivity > 17 kΩcm. Standard Nb/AlOx/Nb trilayer process [88] was used, modified by eliminating the shunt resistor layer and minimizing deposited oxides [89] (see appendix C). The device studied here was coprocessed with 10 other devices used for dc characterization. Initially, only a μ-metal shield was used. Recently, a cryoperm metal shield from the company Amuneal has been added at the mixing chamber in order to increase the supression of external magnetic noise. The center conductor is a series array of 480 SQUIDs (in the case of the quarter-wave resonator, the array contains 250 SQUIDs). Next is a summary of the multiple tests performed on these devices.

6.5.2 dc-Characterization of Josephson Junctions

A total of 92 chips were fabricated with three different values of overlap (junction) size. The reason for the three "flavors" of SQUIDs was that the fabrication process for this junctions was somewhat different from the usual process used at NIST. Since we were trying to get $I_c = 30$ μA per SQUID, the three different junction sizes gave us a

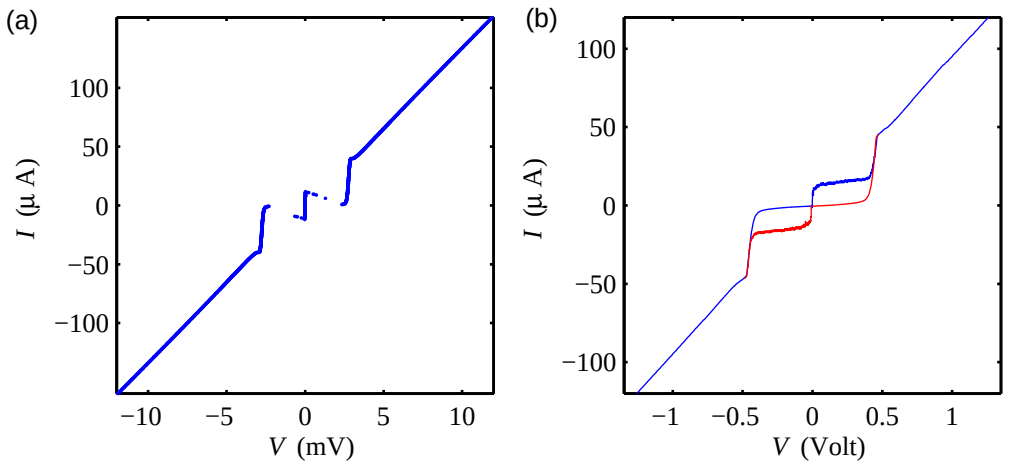

Figure 6.23: I-V curves of test niobium devices. (a) I-V curve of a single SQUID for $B = 0$. From this measurement we estimate the resistance per SQUID to be $R_n \simeq 73\ \Omega$. The measured superconducting gap was $2\Delta = 2.9$ mV. (b) I-V curve of an array. The blue curve was sweep increasingly in voltage and the red curve the opposite direction, showing hysteresis. The measured resistance and superconducting gap were not consistent with the expected number of SQUIDs (250) but with a significantly smaller number. We suspect some of the Josephson junctions turned into short-circuits. The reason why some of the SQUIDs are dying to short circuits is not understood.

larger target to shoot at. The junction with the closest value had a size of $2 \times 2\ \mu\text{m}^2$. The dc-measurements on single SQUIDs indicate an average resistance 73 Ω and a superconducting gap of $2\Delta = 2.9$ mV. This implies an average critical current I_c per SQUID in the JPA of 31 μA (Fig. 6.23a). The transmission lines from which the cavities were built were designed to have a capacitance per unit length of $C_l = 0.15$ nF/m and a geometrical inductance per unit length of $L_l = 0.49\ \mu$H/m. For $I_c = 31\ \mu$A, the Josephson inductance per SQUID is $L_J = 10.6$ pH and each cell had a length of 7 μm. These values imply a zero-flux impedance of $Z_c = 117\ \Omega$. In the case of the half-wavelength resonator, these values predicts a first-mode resonance frequency of 8.23 GHz when the loading the capacitors is included, and when no flux is applied. This value is within 3% of the observed value. A slightly smaller resonance frequency is expected for the quarter-wavelength as it is more strongly loaded by the large capacitor.

While this particular device worked well, the device yield from the wafer was poor. Of the 92 chips, one half had the right value of junction size. However, only 3 chips were found to have working resonators. We have also observed problems with the test devices fabricated for dc-measurement. We measured arrays of 250 SQUIDs, as shown in figure 6.23b. These measurements show that if we assume that there are 250 SQUIDs, the resistance per SQUID is less than the expected value. In the case of the array shown in figure 6.23b with a total resistance of 10.3 kΩ, a resistance per SQUID of 41 Ω would be then estimated if we assumed that the array had 250 working SQUIDs. But if we measure the superconducting gap, then this would also suggest a much smaller gap, $2\Delta = 1.6$ mV. This reduction of the superconducting gap seems much bigger than what could be explained by an increase in the temperature on the central junctions by bias heating. A possible explanation for such a small measured superconducting gap, which would also explain the fact that only 3 out of 46 chips had working devices, could be that some of the junctions are dying and turning into short-circuits. Whether this happens during fabrication or handling of the chips is still under investigation.[12] Our colleagues at NIST that do the fabrication are studying this problem.

6.5.3 Linear measurements of the resonators

Before operating the device as a parametric amplifier, we first characterize its linear behavior using the same setup as in figure 6.10. In figures 6.24a and b, we measure the cavity's response both by measuring the reflectance of a signal on port 2 (S_{22}) and the transmittance from port 1 to port 2 (S_{21}) as functions of frequency, for two different magnetic fields. The powers used are low enough so that the cavity's response is still linear. From this measurement we can extract the cavity's resonance frequency $f_{\rm res}$, the quality factors Q_1 and Q_2 that describe the cavity power loses through both ports as

[12] Although the devices also die during handling due to electrostatic discharge, in previous devices we have found that arrays are extremely hard to kill. Also, resonators are isolated from us, specially the half-wavelength resonators, since they do not have a dc-connection to the outside world.

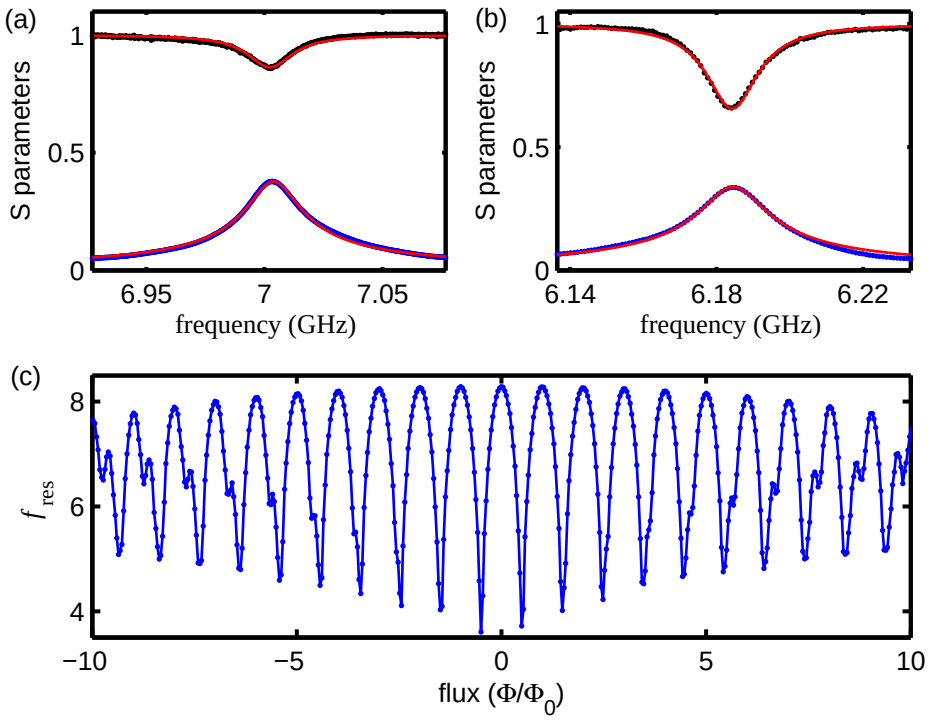

Figure 6.24: We plot the fraction of microwave amplitude transmitted from port 2 to port 1 $|S_{12}|$ (blue) and the fraction reflected from port 2 $|S_{11}|$ (black) as functions of frequency at two particular values of applied magnetic flux: (a) $\Phi = 0.29\Phi_0$ and (b) $\Phi = 0.37\Phi_0$. (a) By fitting this data to a model of a two port cavity (red lines), we extract $f_{\rm res} = 7.0038$ GHz, $Q_2 = 8010$, $Q_1 = 330$ and $Q_l = 10,300$. (b) From the fittings, we extract $f_{\rm res} = 6.184$ GHz, $Q_2 = 9570$, $Q_1 = 396$, and $Q_l = 2420$. (c) Measured value of $f_{\rm res}$ as a function of applied magnetic flux Φ in units of the magnetic flux quantum Φ_0. We use the obvious periodicity (in the first few periods) in this data to infer the magnetic flux enclosed by the SQUIDs. The inevitable imperfections in fabrication start to manifest after 6 flux-quanta, where interference between the different SQUID sizes start to affect the magnetic field dependance.

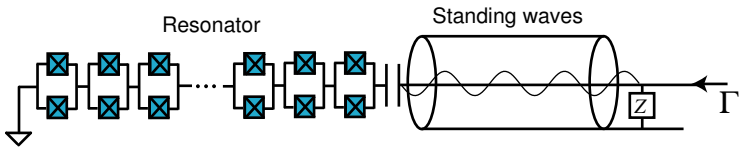

Figure 6.25: As the experiment has become more involved (see for example, the schematic of the next two chapters), imperfections in the microwave components start adding up causing standing waves in the measured reflection coefficient. In order to do a better job in the fitting, the slightly more complicated model shown here is used.

well as through internal loss processes Q_l. When operating as a parametric amplifier, the center of the amplified band will be close to $f_{\rm res}$, and the unity gain signal bandwidth will be limited by the total linewidth $\gamma_1 + \gamma_2 + \gamma_l = \omega_{\rm res}(1/2Q_1 + 1/2Q_2 + 1/2Q_l)$. By applying magnetic flux we can move the center of the amplified band over a large range of frequencies (Fig. 6.24c).

The flux dependence shown in figure 6.24c is also a demonstration of the uniformity in the junctions and in the SQUIDs areas. Unlike the aluminum device where the two different sizes of SQUIDs areas were so different that a "beating" of the two periods was obvious at very small magnetic fluxes, in this devices it is necessary to go to fluxes larger than $5\Phi_0$ to observe an obvious "beating" between the different periods in the flux dependance of the multiple SQUIDs in the array. The lowest resonance frequency in the resonators is consistent with the critical current of the SQUIDs being limited by the finite loop inductance of the SQUID loop $L_{\rm Loop} = 13$ pH. This value of loop inductance is consistent with simulations using Fast Henry, a software capable of computing the frequency-dependant self and mutual inductances of superconducting structures. Finally, another important difference is that we avoided having large characteristic impedances in the coplanar waveguide that formed the resonator even at the lowest resonance frequency ($Z_c < 0.3$ kΩ). Finally, in these devices we do not observe any "desert" region, rather a clear cavity resonance is visible at all values of applied flux.

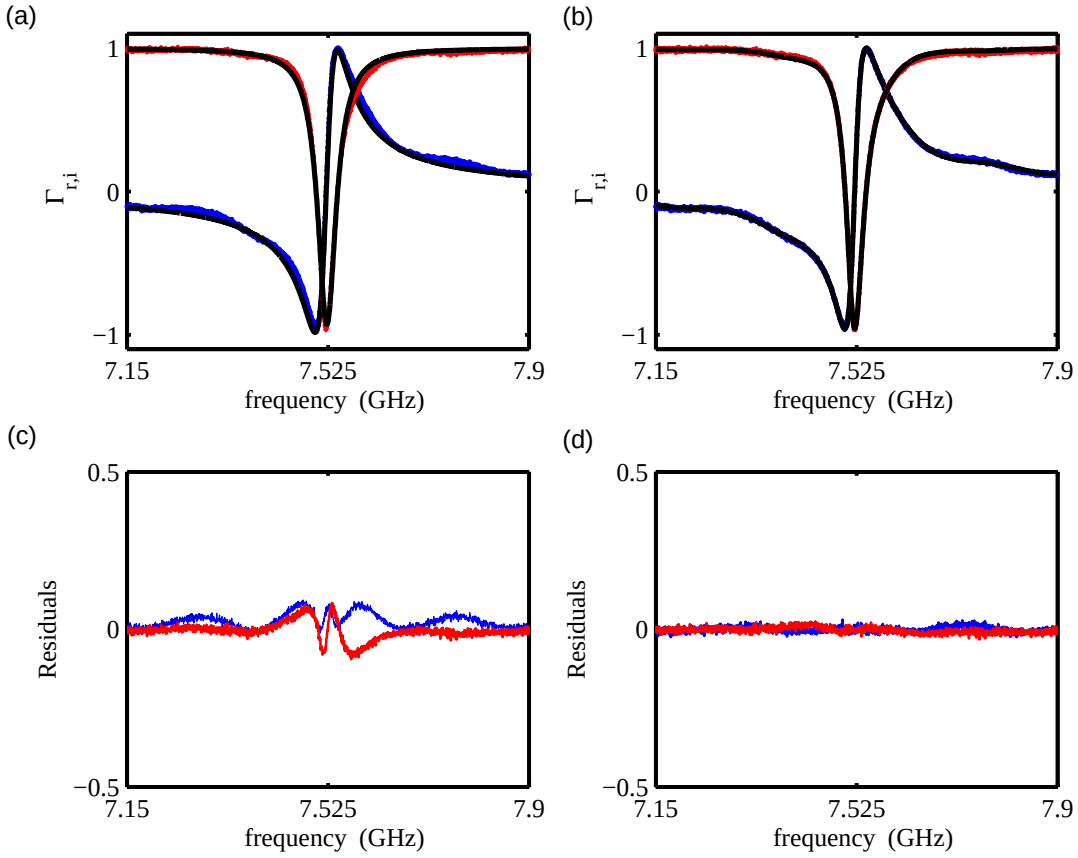

Figure 6.26: Fits to the resonance frequency of a quarter-wave resonator using the model of figure 6.25. (a) Fits to the imaginary Γ_i and real part Γ_r of Γ using only Eq. (6.6). Data in red for Γ_r and blue for Γ_i. Fits are plotted in black. The standing waves on top of the plots are easily observed especially in the residual of the plots shown in (c). (b) Fits to the data using the model of figure 6.25 and (d) residuals showing that the new model used for the fits now does a much better job.

The coupling capacitances were estimated to be 4.6 fF and 22.6 fF using microwave simulations in Microwave Office. Based on measurements of the S-parameters for low powers these values are very close to the observed ones. For recent experiments where the setup has increasingly become more complex and more microwave connectors are used, the measured reflection coefficients are not as clean as those shown in figure 6.24, presenting a standing wave structure on top of the expected Lorentzian response. This can interfere with our attempts to do an appropriate fitting to obtain the liner

parameters of the resonator. In order to solve this problem we use a somewhat more complicated model shown in figure 6.25. In this model we assume that an impedance mismatch a length ℓ away from the input port of the resonator shunts the center conductor of the transmission line connected to the resonator, generating the standing waves observed in the data. This model allows us to do a better fitting as can be observed in figure 6.26.

In general, the quality factors associated with the intrinsic losses of the resonator are over $Q_l > 2000$ and at some frequencies we have measured $Q_l > 10000$ as shown in figure 6.24. A possible reason for the loss observed is the lossy dielectric used in the fabrication process (see appendix C). However, we do not completely understand the large variation of loss over the whole 4-GHz band of the resonator. On possible explanation is the existence of other resonant modes, for example those observed in the sample-box (Fig. 6.2c).

6.5.4 Nonlinear characterization

We measured the nonlinear behavior of the resonator as well. Based on the critical powers measured and the linear S-parameters, we estimated the values of the Kerr constant for different frequencies. Next, I show examples of the measured Kerr constant for six different frequencies using Eqs. (5.44-5.46). The results of this measurement are shown in the following table.

f_{res}	Measured $\hbar K'$	Expected $\hbar K'$
8.3 GHz	$-2.8 \pm 0.3 \times 10^{-7}$	-2.4×10^{-7}
8.0 GHz	$-3.4 \pm 0.4 \times 10^{-7}$	-2.7×10^{-7}
7.0 GHz	$-4.4 \pm 0.5 \times 10^{-7}$	-3.7×10^{-7}
6.2 GHz	$-5.8 \pm 0.8 \times 10^{-7}$	-4.9×10^{-7}
5.1 GHz	$-12.5 \pm 2 \times 10^{-7}$	-6.8×10^{-7}
4.1 GHz	$-57 \pm 7 \times 10^{-7}$	-10×10^{-7}

We observe that there is some quantitative agreement with the expected Kerr constant at low magnetic fluxes. However, as we increase the flux through the SQUID loops to

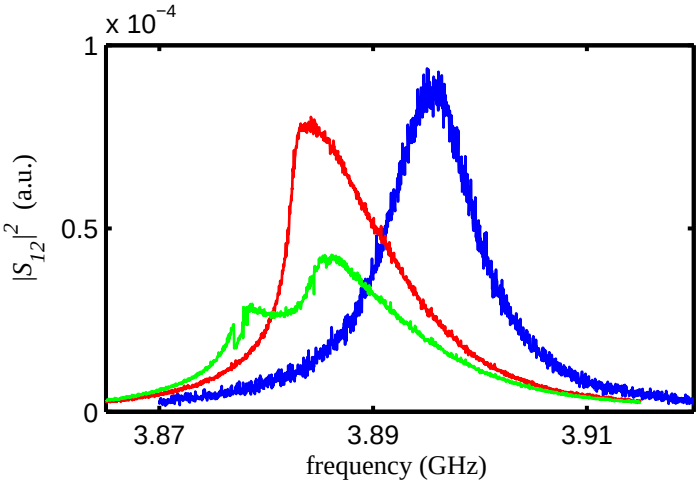

Figure 6.27: Magnitude squared of the transmission $|S_{21}^2|$for the $\lambda/2$ resonator for $\Phi = 0.48\Phi_0$. At low powers ($P \approx -125$ dBm) the response has the expected lorentzian shape (blue). For 27 dB higher power (red), the response has the expected Duffing-like response of a resonator about to reach the bifurcation state. However, before the bifurcation happens, the response becomes unpredictable.

suppress the critical current I_0^S of the SQUIDs to tune down the resonance frequency, the disagreement grows. For example, at 4.1 GHz the difference between the estimated Kerr constant K' and the expected Kerr constant is a factor of close to 6. This is not the only unexpected behavior at fluxes close to $\Phi = \Phi_0/2$. Close to this values of flux, the nonlinear behavior of the resonator becomes somewhat unpredictable as can be observed in figure 6.27. However, this behavior is only observed at frequencies $f_{\text{res}} < 4$ GHz.

Unlike the aluminum devices, in this device we do not observe a large increase of nonlinear loss for the lower resonance frequencies (between 5 and 4 GHz). This is observed in figure 6.28, where even at $f_{\text{res}} = 4.5$ GHz, close to the lowest frequencies observed, the nonlinear loss is only $\gamma_{nl}/|K| = 0.007$. However, it is hard to measure the nonlinear dependance of the resonance at frequencies below 4 GHz due to the behavior observed at those frequencies. Thus, we cannot estimate whether the nonlinear loss increases at those frequencies.

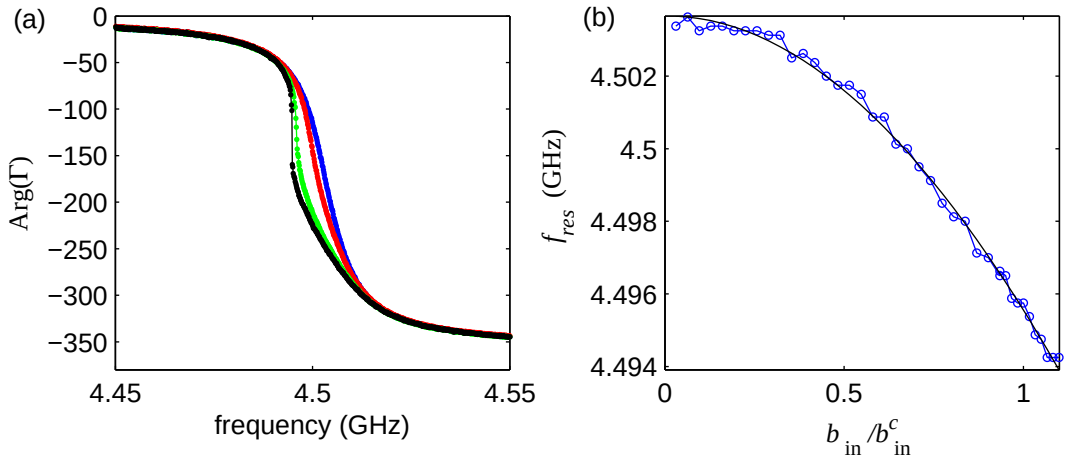

Figure 6.28: Power dependance of the resonator. (a) Phase of the reflection coefficient as a function of frequency at different pump powers for $\Phi/\Phi_0 = 0.46$. (b) By fitting to the expected power dependance of the resonance frequency, Eq. (5.63), the ratio of nonlinear loss and kerr constant $\gamma_{nl}/|K|$ is estimated. From the fit, we estimate that $\gamma_{nl}/|K| < 0.01$

6.5.5 Gain measurements

We study the amplifier's properties using the apparatus shown in Fig. 6.11 using the spectrum analyzer [90]. As described in Ref. [91], we determine the critical pump power at which the JPA gain diverges. We then characterize the image gain (G_i) and signal gain (G_s) for pump powers less than this critical power. To characterize the bandwidth of the parametric amplifier, we measure the frequency dependance of both gains. For sufficiently large gains, these are Lorentzian functions of the signal-pump detuning $\Delta f = f_{\text{signal}} - f_{\text{pump}}$ between the signal and pump frequencies. For each pump power we determine the 3 dB bandwidth $\Delta f_{1/2}$ and gain at $\Delta f = 0$. We observed that with increasing gain, $\Delta f_{1/2}$ is reduced. We find that the expression

$$\sqrt{G_s}\Delta f_{1/2} = \alpha\gamma \tag{6.12}$$

is correct for a factor α of the order of two [38]. The exact expression is not given by $\sqrt{G_s}\Delta f_{1/2} = 4/\sqrt{3}\gamma$, Eq. (3.62), since we derived that expression for the case of no losses

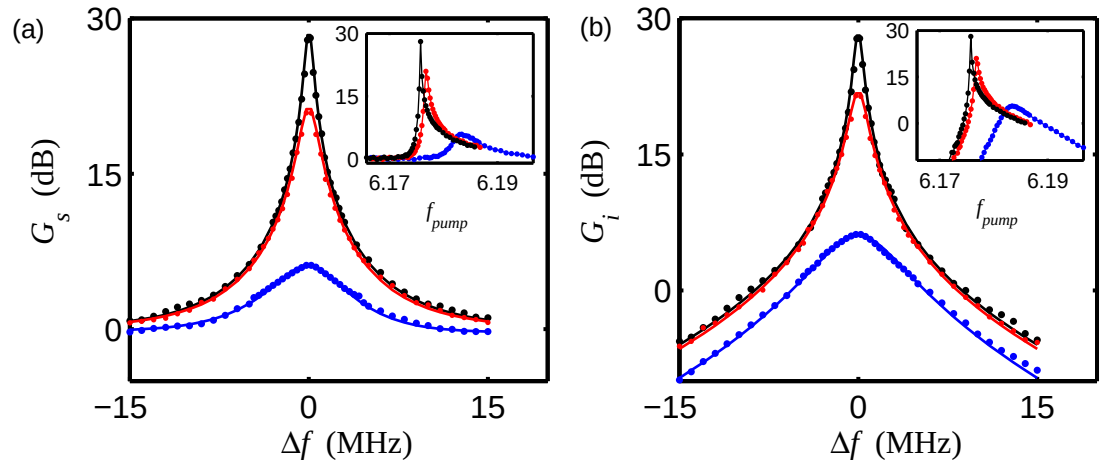

Figure 6.29: Gain measurements. (a) and (b) G_s and G_i as functions of signal detuning (points) and predictions of [38] (lines) for three different pump powers. G_s and G_i for $P = 0.95\ P_c$ (black), $P = 0.9\ P_c$ (red) and for $P = 0.6\ P_c$ (green). For each pump power, we find an optimum pump frequency which decreases as a function of pump power due to the Duffing-like behavior of the resonator [38]. Insets: G_s and G_i as a function of pump detuning for the same pump powers as in the main plot. The device shows the expected behavior described by [38]. The test signal was detuned from the pump by 100 kHz in all the measurements. The data shown in this figure was taken using the setup shown in figure 6.11 with the spectrum analyzer.

inside the resonator. Eq. (6.12) is also correct for G_i if $\sqrt{G_i} > 2$. These results are shown in Figs. 6.29(a) and 6.29(b), where we plot both G_i and G_s as a function Δf for three different pump powers for $f_{\rm res} = 6.184$ GHz ($\Phi = 0.37\Phi_0$). Qualitatively, this behavior is expected for parametric amplifiers, and we find quantitative agreement with the theory of [38]. From this plot, we estimate the 3 dB bandwidth to be about 1.38 MHz when G_s and G_i are 22 dB, or a showing a gain-bandwidth product of $\sqrt{G_s}B_\omega = 17.5$ MHz [90].

The setup of Fig. 6.11 with the network analyzer only allow us to measure the direct gain of the amplifier. However, the image gain does not provide any extra information. Additionally, this setup is much faster. Therefore, for the last experiments this is the only way we have characterized the bandwidth of the amplifier. An example for the quarter-wave resonator of this measurement is shown in figure 6.30. This resonator is expected to have a bandwidth at least a factor of two larger, which is observed in the

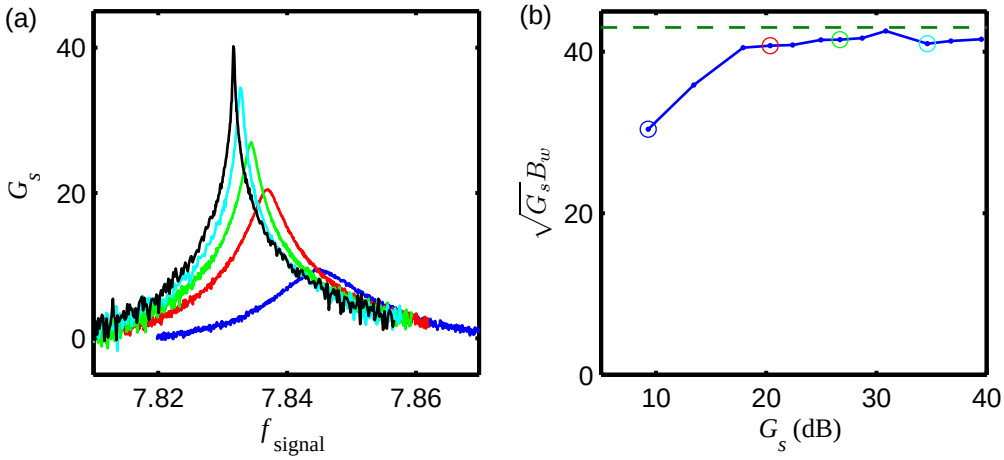

Figure 6.30: (a) Signal gain for different pump powers for the quarter-wave resonator. The data shown in this figure was taken using the setup shown in figure 6.11 with the network analyzer. (b) Signal amplitude-gain-bandwidth product as a function of power gain. The dashed line represents the theoretical limit of the gain-bandwidth product for a lossless parametric amplifier (Eq. 3.62). For this resonator, the internal loss quality factor of the resonator is significantly larger than the coupling quality factor, so we expect to get close to this limit, as observed in the graph. The total quality factor was measured to be $Q = 210$, so the theoretical limit is $\sqrt{G_s}B_\omega = 4/\sqrt{3}f_{\rm res}/(2Q) = 43$ MHz.

measurements, showing a gain-bandwidth product of $\sqrt{G_s}B_\omega = 42$ MHz.

6.5.6 Measurement of the added noise of the amplifier

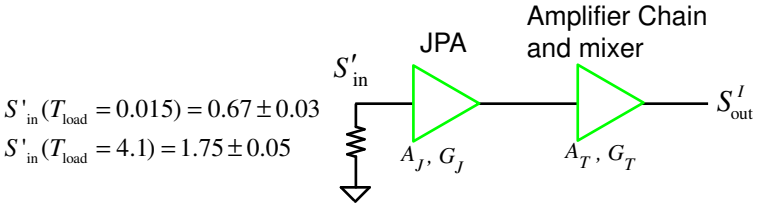

Figure 6.31: Simplified diagram of the setup shown in figure 6.12a and c. The input noise is modeled as the noise coming from a resistor with an effective temperature T_r whose noise is found using equation 6.10. The JPA adds A_J to the noise power $S'_{\rm in}$ at its input. Both noises are multiplied by the JPA power gain G_J before entering the input of the commercial amplifier chain. The cascaded commercial amplifiers and mixer can be modeled as a single amplifier with added noise A_T and gain G_T

Using the setup shown in figure 6.12, and switching between two calibrated noise

sources we can change the incident noise on the JPA and measure the added of the amplifier [92]. The change in noise power at the output of the mixer allows us to estimate the noise A_J just added by the JPA, the JPA gain $\sqrt{G_J}$, the total added noise of both the JPA and the commercial amplifier chain $A_{\rm sys}$ (i.e., the total noise referred to the input of the JPA), and the total gain $\sqrt{G_J \times G_T}$. The effective temperature of the incident noise is calculated using Eq. (6.10). In this case, the attenuation α place in the calibration line was 10 dB. The circulator maximum insertion loss was -0.4 dB and the switch's room-temperature maximum insertion loss is -0.3 dB. Using these values, we can estimate the incident noise quanta $S'_{\rm in}(T_{\rm load})$, where $T_{\rm load} = T_c = 15$ mK or $T_{\rm load} = T_h = 4.1$ K depending on the position of the switch shown in Fig. 6.22a.

By selecting $\theta = 0$, the amplified quadrature appears at the I port of the mixer (Fig. 6.31). The spectral densities of the noise at the output if the I-channel of the mixer is shown in figure 6.32. We measure the ratio Y as defined by Eq. (6.11) to extract $A_{\rm sys}$ and the total gain $\sqrt{G_J \times G_T}$. We then then perform a Y-factor measurement on our commercial amplifier chain, finding A_T and G_T (Fig. 6.32b). From both measurements, we extract the JPA gain $\sqrt{G_J}$ (Fig. 6.32c) and A_J (Fig. 6.32d). As observed in figure 6.32d, our JPA adds less than 1/2 a quantum of noise for fourier frequencies above 100 kHz. We did this measurement for various gains, finding only a very weak gain dependance. However, the added noise is significantly higher than the theoretical minimum, $A_J = 0.04$ quanta.

In addition, the amplifier can can be operated at large enough gain to amplify the quantum noise above the commercial amplifier's noise (Fig. 6.33a). We performed similar Y-factor measurements over the whole $4 - 8$ GHz band where the amplifier operates. The results of this measurements are shown in figure 6.33b. Over the whole band, the estimated added noise was less that half a quantum of noise [92]. However, the added noise was always bigger than expected from the theory of Ref. [38] (see Eq. 5.57). The origin of this noise is not yet understood and is under investigation. Another

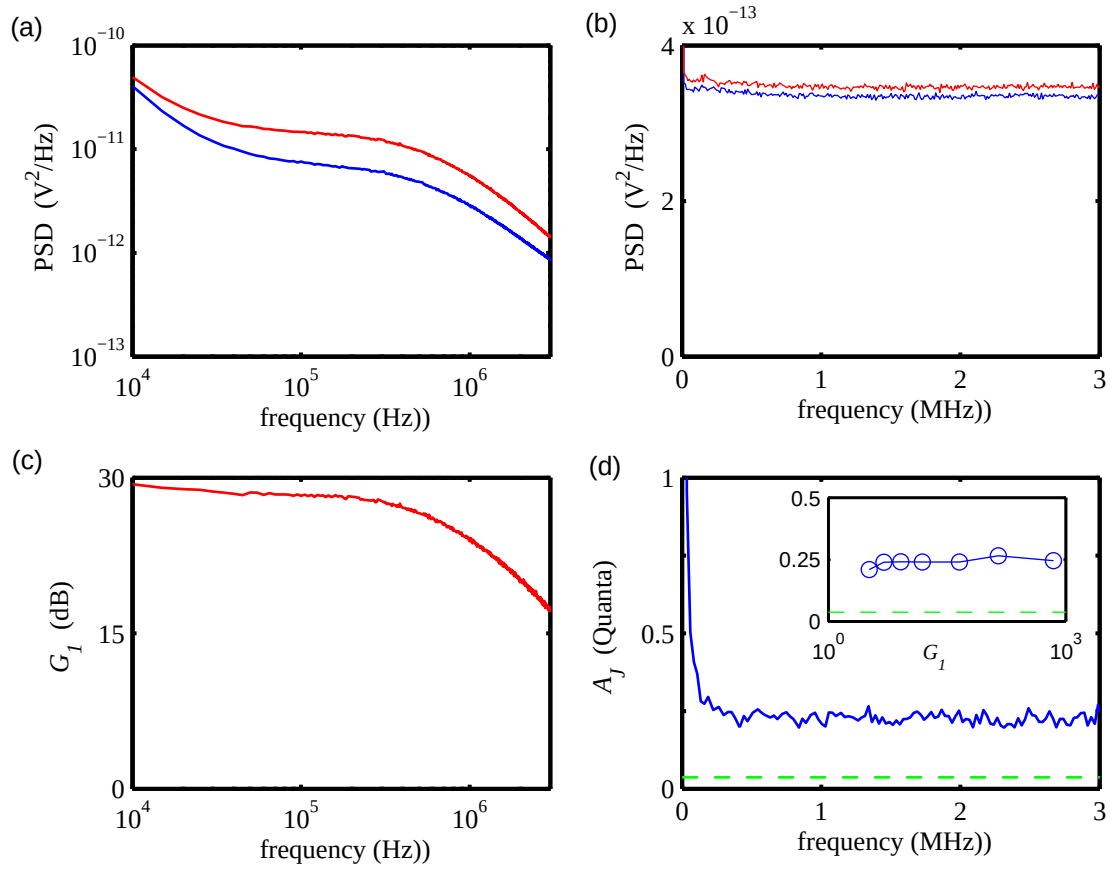

Figure 6.32: Y-factor measurement done at 7 GHz. Power spectral density of the demodulator output for the cases when the pump is on (a) and off (b), and the switch is turned to the cold resistor (blue) and the hot resistor (red). For the case of the pump off, the resonanance has been moved to avoid the reduction of the hot-load noise due to losses in the resonator. (c) Using the difference in noise between the pump off and pump on spectral density, the gain of the amplifier can be measured. In this case the gain is 28 dB. (d) Using Eq. (6.11), we estimate the added noise of the JPA as a function of fourier frequency (x-axis). Below 100 kHz $1/f^n$ noise is observed, whose origin is not known. But for fourier-frequencies larger than 100 kHz, the estimated added noise is $A_J \simeq 0.23$. This added noise is larger than the expected added noise according to Eq. (5.57), (green-dashed line). Inset: added noise for different JPA gains.

point of concern is the low frequency noise that is easily observed in figure 6.32d below 100kHz. A thermal sweep was used to see its temperature dependance. This is shown in figure 6.33c where it is shown that this noise presents a linear temperature dependance. One hypothesis is that it consist of current noise present in any closed-loop of metal

(like for example the circular walls of the sample box) which inductively couples noise to the SQUID loop. But this still needs to be studied.

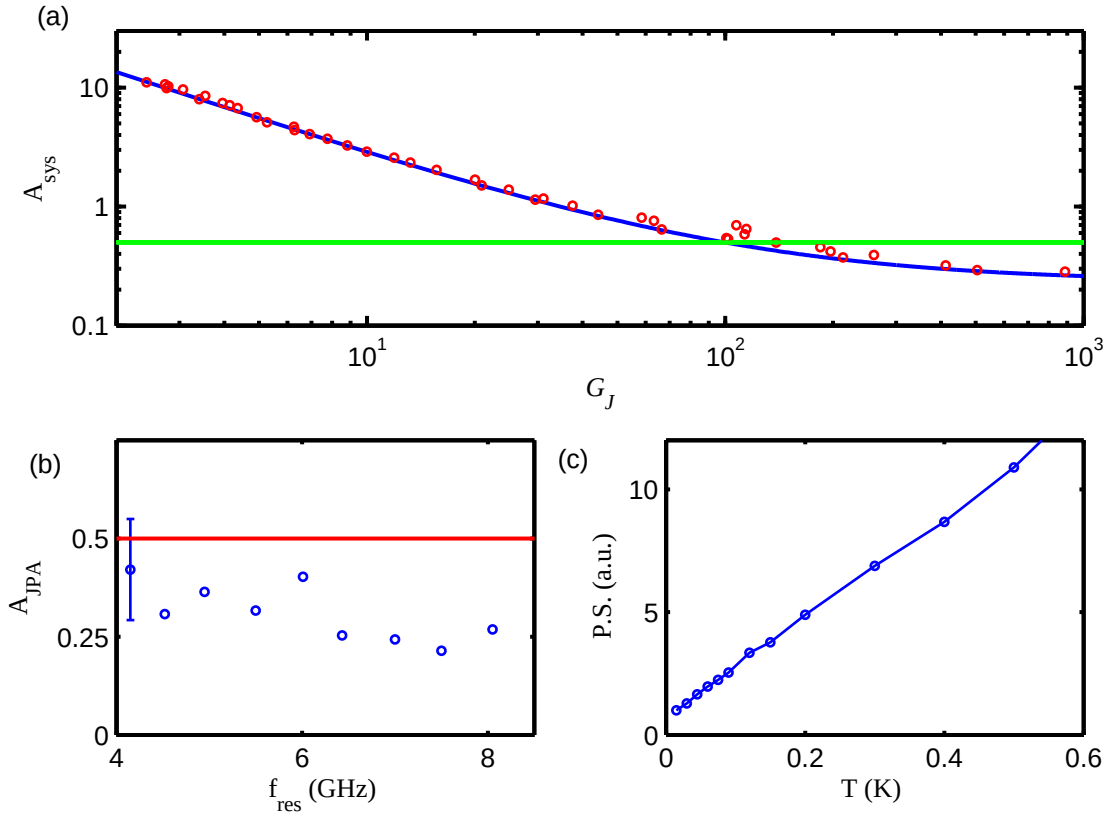

Figure 6.33: (a) We plot $A_{\rm sys}$ when $f_{\rm res} = 7.00$ GHz versus G_J (points). At this frequency $A_T = 26$ and is dominated by the HEMT. With increasing G, this noise becomes negligible compared to $A_J = 0.23$, where we expect $A_{\rm sys} = A_J + A_T/G_J$ (blue line). At the largest gains $A_{\rm sys} < 0.5$ (green line) and $A_T/G = 0.04$. (b) We measure A_J at nine different values of $f_{\rm res}$ between 4 and 8 GHz and observe that the added noise is less than half a quantum (green line). The error bar applies to all points; it represents the systematic uncertainty introduced primarily by the unknown loss of the microwave components when operated cryogenically. (c) We performed a thermal sweep in order to study the low frequency noise that appears in figure 6.34a and d . If I integrate the spectral density noise below 100 kHz, we observe a linear dependance with respect to temperature.

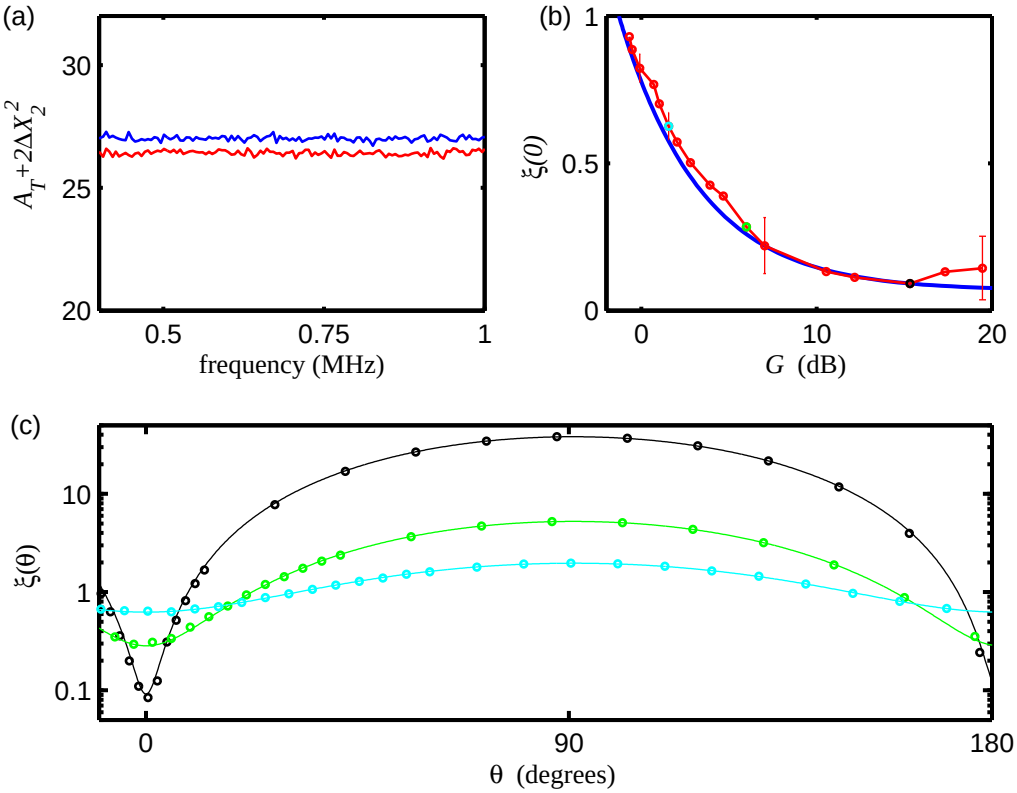

Figure 6.34: Demonstration of squeezing. (a) Power spectral density versus frequency at the Q output of the mixer referred to the input of the commercial amplifier chain in units of quanta, measured with the pump on (red) and the pump off (blue) for $\theta = 0$, $f_{\rm res} = 7$ GHz and $G_J = 15.3$ dB. (b) The squeezing ξ as a function of G_J (points) and the maximum predicted squeezing from Ref. [38] (line). The error bars represent the same systematic error as in Fig. 6.31b. This uncertainty varies smoothly between the error bars shown in selected data points. (c) $\xi(\theta)$ as a function of θ for three different gains (points) and $G_J = 34$ (black), $G_J = 4$ (green), $G_J = 1.4$ (cyan) and the expected θ dependance (lines) [8, 38].

6.5.7 Inferred squeezing

We now turn our attention to the squeezed quadrature X_2. The squeezing data is shown in figure 6.34. The spectral density at the output of the Q port when the LO phase is set to $\theta = 0$ is shown in figure 6.34a. There it is obvious a small reduction of close to 2% of the noise. Based on the Y-factor measurements done on the HEMT (Fig. 6.32b), we convert it into a squeezed-noised quanta $\xi(\theta = 90°)$ at the output of the

JPA. As we increase the JPA gain, we observe an increase in the noise squeezing up to $G = 16$ dB (Fig. 6.34b) where we observe an squeezing of about 90% [92]. For $G < 16$ dB the squeezing we observe is consistent with the expected behaviour from a model of parametric amplification that includes loss in the JPA but no other imperfections [38]. However, for $G > 16$ dB we observe less than the predicted squeezing probably due to instability in the phase acquired by the pump as it passes through the cryostat in the time required to complete one measurement. In Fig. 6.34c, we show $\xi(\theta)$ as a function of the LO phase θ demonstrating that the fluctuations at the output of the JPA are indeed squeezed along the axis defined by the pump (Fig. 6.13).

6.5.8 Amplifier saturation

We have also estimated the dynamic range and saturation power of this amplifier at 2 different frequencies: 6.184 and 8.012 GHz. We determine the saturation power as the input power for which the gain is reduced by 1 dB (6.35b). In Fig. 6.35b we plot G_s as function of input signal power for two different cavity's resonance frequency. At 8.012 GHz and $G_s = 27$ dB, the 1 dB compression point is -130 dBm. From the noise measurements previously described, the minimum detectable signal for this amplifier in 1 Hz band is $0.77\hbar\omega$. From these two measurements, we estimate the dynamic range to be 74 dB/Hz. At 6.18 GHz and $G_s = 26$ dB, the 1 dB compression point was -137 dBm and the dynamic range is 67 dB/Hz. The reduction in dynamic range is expected: when we tune down the resonance frequency by applying a magnetic field, we are reducing the critical currents of the SQUIDs and the critical power of the resonator.

As a rule of thumb, we have observed that the saturation powers for large gains can be found as $P_{\text{sat}} \approx (\gamma_2/\gamma_1)P_c/(20G_D)$, where P_c is the critical pump power. The factor γ_{c1}/γ_{c2} arises because we applied the pump to the weakly coupled port, but applied the signal to the strongly coupled port. In the case of applying the pump in the strongly coupled port (as it is necessary in the $\lambda/4$-resonator), this rule of thumb

simplifies to $P_c/(20G_s)$, where P_c is the critical pump power associated to the signal (strongly coupled) port. This expression is reasonable as we expect to observe saturation behavior when the amplified signal power becomes a significant fraction of the pump power. For the case of the quarter-wave resonator, since its critical power is 3 dB higher and have similar noise performance, its dynamic range is about 3 dB higher.

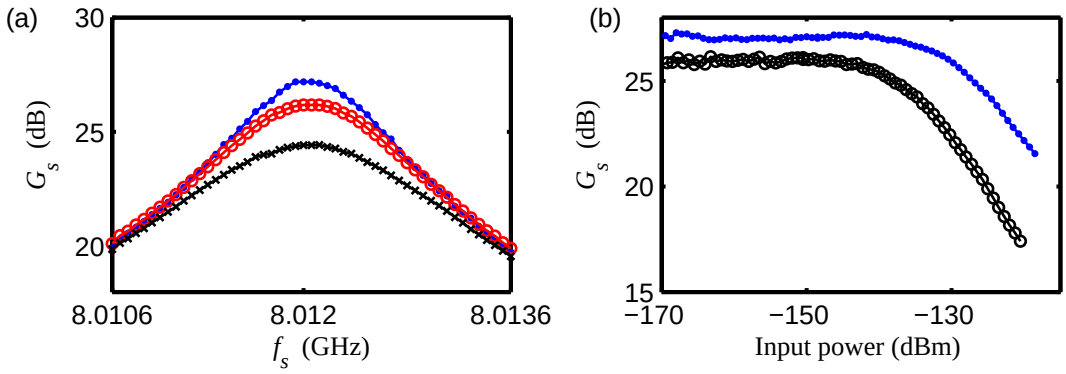

Figure 6.35: (a) Direct gain as a function of signal-pump detuning for $\Phi = 0.15\Phi_0$ for three different signal powers, showing the expected saturation behavior at large enough signal powers. Signal powers shown are -145 dBm (dots), -130 dBm (circles) and -125 dBm (crosses).(b) Direct gain as a function of input signal powers for $f_{\rm res} = 6.184$ GHz (circles) and $f_{\rm res} = 8.040$ GHz (dots).

6.5.9 Final comments

Once we have characterized the behavior of the JPA and found that it has a good noise performance we can now use it for doing other interesting experiments. For example, the measurement of the squeezed state would have proceeded much more rapidly if we had used a subquantum limited amplifier, such as a second JPA, instead of a HEMT amplifier. This experiment will be the main subject of our next chapter. In addition to characterizing states of microwave fields as I will show in chapter 7, the JPA is also well suited to amplifying the signal generated by a nanomechanical beam moving in a microwave cavity [11], enabling a quantum-limited measurement of position. This application will be the subject of chapter 8.

Chapter 7

Applications I. Microwave homodyne tomography of squeezed states

In the previous chapter I showed how it is possible to generate microwave squeezed states with Josephson parametric amplifiers. However, we have only characterized the squeezed states by measuring the variance or spectral density of the itinerant squeezed mode. These measurements do not fully characterize the states; to fully characterize the state of a light field, we need to determine the density matrix which will account for noise that is both quantum and classical in origin. In this chapter, I will describe how we approach this problem of fully characterizing a squeezed state. Rather than measuring the density matrix in a photon number basis, we measure the Wigner function using our own implementation of "microwave homodyne tomography." The Wigner function is a particular representation of density matrix

In the first part of this chapter I describe the Wigner function as well as some of its more important properties. I will also discuss other possible representations of the density matrix in the form of the P, Q and s-parameterized distribution functions. The experimental estimation of Wigner functions for quantum states of light based on real physical measurements is called quantum tomography and will be the subject of the second part of this chapter. It consists of measuring complementary features (position and momentum, for example) in identically prepared quantum objects in a series of distinct experiments. I will explain how quantum tomography allows us to use a complete set of observations to reconstruct the Wigner function. I will also describe how

imperfections in the measurement can affect our reconstruction of the Wigner function. Finally, I will explain our experimental implementation of quantum tomography using a Josephson parametric amplifier as the one described in the previous chapter.

7.1 Quasiprobability distributions

In the standard formulation of quantum mechanics, (for a pure state) the probability density $\rho(x)$ in position space x is given by the square of the magnitude of the wave function $\rho(x) = |\psi(x)|^2$. Thus, knowing $\psi(x)$ it is easy to visualize the distribution $\rho(x)$. We can easily obtain the distribution in the momentum p space by performing the Fourier transform on $\psi(x) \rightarrow \varphi(p)$. Although straightforward, knowing $\psi(x)$ does not make it easy to visualize $\varphi(p)$. It would be desirable to have a function that displays the probability distribution simultaneously of x and p. The Wigner function allows us to do that. It could be described as an attempt to describe the quantum mechanical state of a system in almost a classical language. In classical optics as well as in classical mechanics we can characterize the statistics of a system by introducing a phase-space distribution $W(q, p)$. The distribution $W(q, p)$ quantifies the probability of finding a particular value of q and p in a simultaneous measurement. This means that the phase-space distribution describes the state in classical physics. However, this is more subtle in quantum mechanics. Due to the Heisenberg's uncertainty principle, two conjugate variables values cannot be simultaneously known precisely. This means that defining a quantum phase-space distribution is more difficult and, as we will see, it may be ill-defined in the sense that $W(p, q)$ could become negative. For this reason, we will call it a quasiprobability distribution. We can still try to use $W(q, p)$ to make statistical predictions as if it were a classical distribution; however, these predictions will only coincide with the classical prediction in special cases. Furthermore, there are infinitely many ways of defining quasiprobability distributions (simply because there is no way to define them uniquely) [76]. However, we will mainly discuss one option, the

Wigner function and mention very briefly other possible definitions of quasiprobability distributions.

7.1.1 Wigner function

The Wigner function was introduced by Wigner in 1932 with the original goal of finding quantum corrections to classical statistical mechanics where the Boltzmann factors contain energies which are expressed as functions of both x and p [93]. As it is well known from the Heisenberg uncertainty principle, there must be constraints on this distribution and thus on the Wigner function. One way to define a quantum quasiprobability distribution $W(p,q)$ is by postulating its properties. For the Wigner function, just one postulate turns out to be enough [76, 94]: let's assume that $W(q,p)$ behaves like a joint probability distribution of both quadratures. In that case, the marginal distributions defined as $\int W(x_1,x_2)dx_1$ or $\int W(x_1,x_2)dx_2$ must yield the probability distributions for x_2 and x_1 respectively. In addition, we can perform a phase shift θ for all complex amplitudes and accordingly the phase-space distribution will be expected to rotate in the two-dimensional phase space of x_1 and x_2. Hence, the way to define the Wigner function is by postulating the existence of the following probability distribution [76]:

$$\begin{aligned} \mathrm{pr}(x_1,\theta) &\equiv \langle x_1|\hat{U}(\theta)\hat{\rho}\hat{U}^{\dagger}(\theta)|x_1\rangle && (7.1)\\ & && (7.2)\\ &= \int_{-\infty}^{\infty} W(x_1\cos\theta - x_2\sin\theta, x_1\sin\theta + x_2\cos\theta)dx_2. && (7.3) \end{aligned}$$

where $\hat{\rho}$ is the density operator defining the quantum state of the system and $U(\theta) = \exp(-i\theta\hat{a}^{\dagger}\hat{a})$ is the phase-shifting operator [76]. These equations also define how the Wigner function is related to a quantum mechanics description of a state. I will not give a detailed explanation of how Eqs.(7.1) and (7.3) are sufficient to postulate the existence of the Wigner function or that it has a one-to-one correspondence with the

density operator. For that, I refer the reader to Ref. [76]. I will only mention some of its more important properties. Eqs.(7.1) and (7.3) tie $W(x_1, x_2)$ to physical observations. For example, consider the special cases of $\theta = 0$

$$\int_{-\infty}^{\infty} W(x_1, x_2) dx_2 = \langle x_1|\hat{\rho}|x_1\rangle$$

and $\theta = \pi/2$

$$\int_{-\infty}^{\infty} W(-x_2, x_1) dx_2 = \langle x_2|\hat{\rho}|x_2\rangle.$$

Both integrals show how to derive the probability distribution for both quadratures. The previous integral transformations are called Radon transformations and they are studied in the context of tomographic imaging. The inversion of the Radon transformation is what we need to reconstruct the Wigner function from physical observations. This will be explained in the next section.

It can be shown that the relation between the Wigner function and the density operator of a system is given by

$$W(x_1, x_2) = \frac{1}{\pi} \int_{-\infty}^{\infty} dy e^{2iyx_2} \langle x_1 - \frac{y}{2}|\hat{\rho}|x_1 + \frac{y}{2}\rangle \tag{7.4}$$

where this expression is sometimes referred to as the Weyl-transform of the density operator $\hat{\rho}$ [95]. First, we note that the Wigner function is real for hermitian operators $\hat{\rho}$ and normalized

$$\int_{-\infty}^{\infty} \int_{-\infty}^{\infty} W(x_1, x_2) dx_1 dx_2 = 1$$

because the density operator $\hat{\rho}$ is by definition normalized: $\mathrm{tr}\{\hat{\rho}\} = 1$. Another interesting property is the overlap formula for two arbitrary operators $\hat{F}_1$ and $\hat{F}_2$:

$$\mathrm{tr}\{\hat{F}_1 \hat{F}_2\} = \pi \int_{-\infty}^{\infty} \int_{-\infty}^{\infty} W_{F_1}(x_1, x_2) W_{F_2}(x_1, x_2) dx_1 dx_2 \tag{7.5}$$

for the Wigner function of the operators $\hat{F}_1$ and $\hat{F}_2$.[1] The usefulness of the overlap

[1] The Wigner function of an arbitrary operator $\hat{O}$ is defined using equation 7.4 with $\hat{\rho}$ replaced by $\hat{O}$. However, unless we make the distinction, we use the term Wigner function only to refer to the special case when the operator $\hat{O}$ is the density operator.

formula is that it can be used to calculate expectation values

$$\mathrm{tr}\{\hat{\rho}\hat{F}\} = \pi \int_{-\infty}^{\infty}\int_{-\infty}^{\infty} W(x_1, x_2) W_F(x_1, x_2) dx_1 dx_2. \tag{7.6}$$

This equation shows that the Wigner function plays the role of a classical phase-space density with $W_F(x_1, x_2)$ being the physical quantity that is averaged with respect to $W(x_1, x_2)$ in a "classical-like" fashion. A special case happens when the operator $\hat{F}$ is Weyl, or symmetrically, ordered in terms of the operators $\hat{x}_1$ and $\hat{x}_2$. For example, for the operator $\hat{F} = \hat{x}_1\hat{x}_2 + \hat{x}_2\hat{x}_1$, Eq. (7.6) becomes

$$\langle \hat{x}_1\hat{x}_2 + \hat{x}_2\hat{x}_1 \rangle = \int_{-\infty}^{\infty}\int_{-\infty}^{\infty} 2x_1x_2 W(x_1, x_2) dx_1 dx_2.$$

which then resembles closely the averaging of a physical quantity with a classical distribution. Another simple consequence of Eq. (7.5) is the expression

$$|\langle \psi_1 | \psi_2 \rangle|^2 = \pi \int_{-\infty}^{\infty}\int_{-\infty}^{\infty} W_{\psi_1}(x_1, x_2) W_{\psi_2}(x_1, x_2) dx_1 dx_2$$

However, this quantity must be zero when both states $|\psi_1\rangle$ and $|\psi_2\rangle$ are orthogonal. Because the overlap Eq. (7.5) cannot be zero for two positive functions W_{ψ_1} and W_{ψ_2}, this means that the Wigner function cannot be in general always positive for all values of x_1 and x_2.[2] This case shows why the Wigner function cannot be regarded as a probability distribution function since we would expect it to have only positive values in all its domain in x_1 and x_2. Negative regions in the Wigner function of a given state can be seen as signatures of nonclassical behavior.

The overlap formula can also be used to estimate the purity of state

$$\mathrm{tr}\{\hat{\rho}^2\} = \pi \int_{-\infty}^{\infty}\int_{-\infty}^{\infty} W(x_1, x_2)^2 dx_1 dx_2.$$

The purity $\mathrm{tr}\{\hat{\rho}^2\}$ ranges between zero and one, and equals unity only if the state is pure ($\hat{\rho} = |\psi\rangle\langle\psi|$). One more characteristic of the Wigner function is that their values

[2] In fact, for pure states, only those having Gaussian wave functions have nonnegative Wigner functions [76].

are constrained, that is

$$|W(x_1, x_2)| \leq \frac{2}{\pi}$$

This constraint shows that the Wigner functions cannot be highly peaked meaning it cannot approach delta functions or other problematic functions.

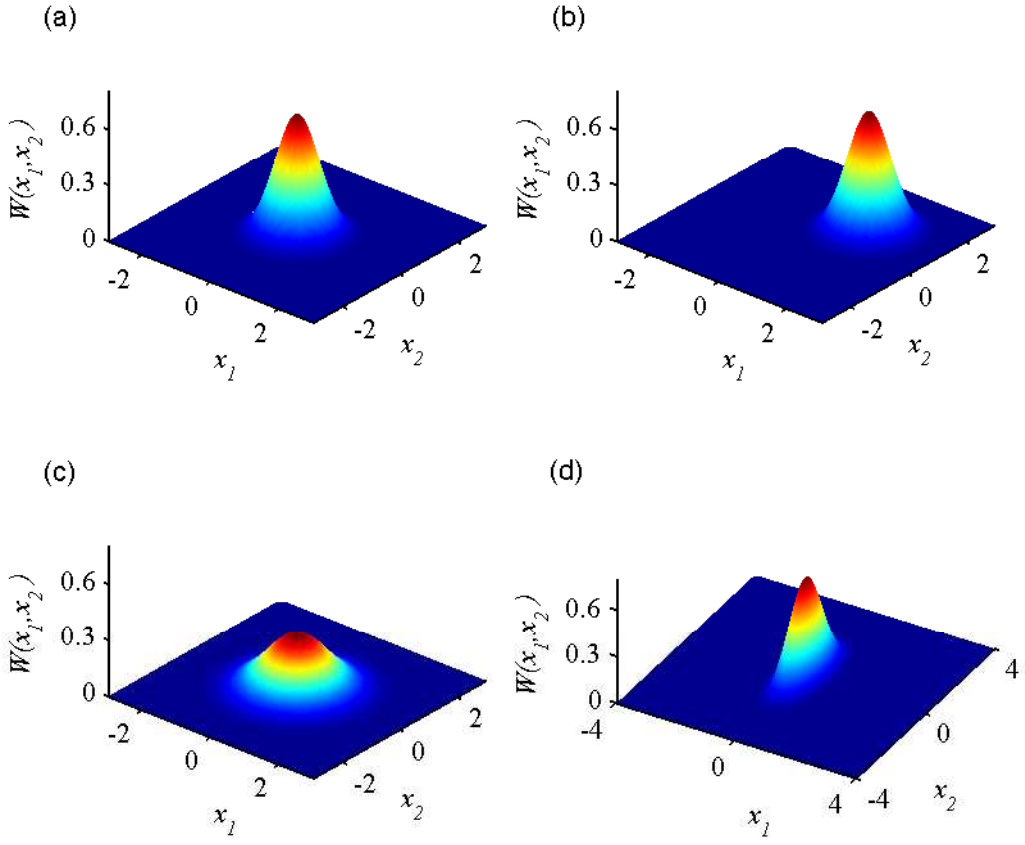

Figure 7.1: Wigner functions of a vacuum state (a), a coherent state with $\alpha = 1+i$ (b), thermal state with $\hbar\omega/k_BT = 1$ (c), and an ideal squeezed state with Δx_1^2=1/10(d). All four states have Gaussian Wigner functions.

Now that I have defined what the Wigner function is, I will describe the Wigner function of a few important examples: vacuum and thermal states, coherent states and squeezed states. One interesting thing about all these states is that their Wigner function consist of two-dimensional Gaussian functions. For a vacuum state, the Wigner

function is given by

$$W_0(x_1, x_2) = \frac{2}{\pi} \exp(-2x_1^2 - 2x_2^2). \tag{7.7}$$

In this case, the variance of each variable x_1 and x_2 is given by $\Delta x_j^2 = 1/4$ as expected (Fig. 7.1a). For a coherent state $|\alpha\rangle$, the Wigner function is given by

$$W_c(x_1, x_2) = \frac{2}{\pi} \exp\left[-2(x_1 - \mathrm{Re}(\alpha))^2 - 2(x_2 - \mathrm{Im}(\alpha))^2\right]. \tag{7.8}$$

As expected, the Wigner function of the coherent state consists of the Wigner function of vacuum displaced by an amount α from the origin (Fig. 7.1b). For a thermal state with a density operator in the number basis given by

$$\hat{\rho} = \left(1 - \exp(-\frac{\hbar\omega}{k_B T})\right) \sum_{n=0}^{\infty} |n\rangle\langle n| \exp(\frac{-n\hbar\omega}{k_B T})$$

the Wigner function is given by

$$W_{\mathrm{thermal}}(x_1, x_2) = \frac{2}{\pi \coth(\frac{\hbar\omega}{2k_B T})} \exp\left[-\frac{2}{\coth(\frac{\hbar\omega}{2k_B T})}(x_1^2 + x_2^2)\right] \tag{7.9}$$

with both quadrature variances being larger than vacuum's, $\Delta x_j^2 = 1/4 \coth(\hbar\omega/2k_B T)$. Finally, for the case of an ideal squeezed state (one for which the equality holds in Eq. (2.85)), the Wigner function is given by

$$W_s(x_1, x_2) = \frac{2}{\pi} \exp(-2e^{2r}x_1^2 - 2e^{-2r}x_2^2). \tag{7.10}$$

The Wigner function is a Gaussian distribution, but with unequal variances, $\Delta x_1^2 = 1/4e^{-2r}$ and $\Delta x_2^2 = 1/4e^{2r}$, indicating the effect of quadrature squeezing. Using Eq. (7.3) it is easy to estimate the marginal distribution for the rotated quadrature x_θ:

$$\mathrm{pr}(x, \theta) = \frac{1}{\sqrt{2\pi\Delta x_\theta^2}} \exp(-\frac{x^2}{2\Delta x_\theta^2})$$

where the phase-dependent variance of the Gaussian probability distribution is

$$\Delta x_\theta^2 = \frac{1}{4}(e^{2r}\sin^2\theta + e^{-2r}\cos^2\theta) \tag{7.11}$$

$$= \frac{1}{4}[\cosh(r) + \sinh(r)\cos(2\theta)] \tag{7.12}$$

7.1.2 Other distribution functions

From a practical point of view, the Wigner function can be considered as the best compromise between a classical phase-space density and the correct quantum-mechanical behavior: it generates the right marginal distributions and it can be easily used to estimate expectation values using the overlap formula Eq. (7.5). However, there are other definitions of quasiprobability distributions, the more important being the P, Q and s-parametrized distribution. I will describe them very briefly, mainly regarding their relation with the Wigner function.

Q function

The Q function can be obtained from the Wigner function by convolving it with a Gaussian distribution with the same width as vacuum

$$Q(x_1, x_2) = \frac{2}{\pi} \int_{-\infty}^{\infty} \int_{-\infty}^{\infty} W(z_1, z_2) \exp(-2(z_1 - x_1)^2 - 2(z_1 - x_1)^2) dz_1 dz_2. \qquad (7.13)$$

Comparing the second part of Eq. (7.13) with Eq. (7.8), we see that the Q function gives simply the overlap of the density operator ρ and the projection operator for the coherent state $|\alpha\rangle$, where $\alpha = x_1 + ix_2$:

$$\begin{aligned} Q &= \frac{1}{\pi} \mathrm{tr}\{\rho|\alpha\rangle\langle\alpha|\} \\ &= \frac{1}{\pi} \langle\alpha|\rho|\alpha\rangle \end{aligned}$$

Clearly the Q function will not be negative and since the coherent states $|\alpha\rangle$ form an over-complete basis [26], it can be shown that the Q function is normalized. This smoothing with the Wigner function of a vacuum state effectively averages the values of $W(z_1, z_2)$ in a circular area around (x_1, x_2) with a radius given by the vacuum fluctuations. Because any negativity disappears after this procedure, the negative values of a Wigner function must be concentrated in an area smaller than vacuum fluctuations.[3]

[3] Note that this point puts a restriction in the kind of function that can be considered to represent the Wigner function of a state. It means that the negative values of a valid Wigner function cannot be

Looking from an experimentalist point of view, this means that resolving these negative values of the Wigner function requires an accuracy on the order of vacuum fluctuations.

The smoothing of the Wigner function is also clearly seen in the Fourier domain. Performing the Fourier transform on the Q function

$$\begin{aligned}\tilde{Q}(u,v) &= \int_{-\infty}^{\infty}\int_{-\infty}^{\infty} Q(x_1,x_2)\exp(-iux_1 - ivx_2)dx_1dx_2 \\ &= \tilde{W}(u,v)\exp\left[-\frac{1}{8}(u^2+v^2)\right].\end{aligned}$$

This shows that the details in the Wigner function that correspond to high "frequencies" of u and v are suppressed in the Q representation.

P function

The P function has a very important role in the context of calculating expectation values of normally ordered operators in quantum optics [26, 76]. I will not discuss its properties other than its relation to the Wigner function. In the Fourier domain, it can be shown that

$$\tilde{W}(u,v) = \tilde{P}(u,v)\exp\left[-\frac{1}{8}(u^2+v^2)\right] \tag{7.14}$$

One feature of the P function is that it can be very ill-behaved. For example, from Eq. (7.14), we see that the Wigner function is a smoothed version of the P function. But if the Wigner function can be negative for nonclassical states, the P function may not only be negative, but it may be more singular than a delta function [26, 76]; that is, it will not be possible to express it in terms of ordinary functions. For this reason, there is no practical way to reconstruct it from experimental data.

s-parameterized quasiprobability distributions

I have shown how the relation between the P, the Wigner, and the Q functions is just a smoothing process with a Gaussian that represents the Wigner function of

extended over areas significantly wider than 1/4 measured in quadrature units; otherwise the Q function could be negative.

vacuum. However, I could also convolve the Wigner function with a Gaussian having a different width. I then obtain a family of distributions called the s-parameterized distributions $W(x_1, x_2, s)$. In the Fourier domain this family of distributions is defined as:

$$\tilde{W}(u, v, s) \equiv \tilde{W}(u, v) \exp\left[\frac{s}{8}(u^2 + v^2)\right] \tag{7.15}$$

where $s < 0$ for smoothing of the Wigner function. All previous examples correspond to the parameters

(1) s=1: P function,

(2) s=0: Wigner function,

(3) s=-1: Q function.

In this new family of distributions the s parameter is defined over the whole range of the real numbers. However, for our purposes in this thesis I will only consider the cases of $s \leq 0$. In this case, consider the definition for the s-parameterized distribution

$$W(x_1, x_2, s) = -\frac{2}{\pi s} \int_{-\infty}^{\infty} \int_{-\infty}^{\infty} W(z_1, z_2) \exp\left(\frac{2(z_1 - x_1)^2 + 2(z_1 - x_1)^2}{s}\right) dz_1 dz_2 \tag{7.16}$$

provided $s \leq 0$ so that the integral converges. We can then define the marginal distribution of the smoothed Wigner function as

$$\begin{aligned} \mathrm{pr}(x_1, \theta; s) &\equiv \int_{-\infty}^{\infty} W(x_1 \cos\theta - x_2 \sin\theta, x_1 \sin\theta + x_2 \cos\theta; s) dx_2 \\ &= \frac{1}{\pi}\sqrt{\frac{2}{|s|}} \int_{-\infty}^{\infty} \mathrm{pr}(x, \theta) \exp\left[-\frac{2}{|s|}(x_1 - x)^2\right] dx. \end{aligned} \tag{7.17}$$

The main reason we are interested in the s-parameterized distributions is that, as I will show in the next section, inefficiencies in the process of measuring the Wigner function can be mapped into an effective smoothing. The smoothing parameters s is a function of such inefficiencies. These inefficiencies will have two main culprits: losses at the input

of the detector and added noise of the amplifiers used to measure the (microwave) light field.

7.2 Quantum tomography: using a homodyne detector to measure the Wigner function

As a fundamental feature of quantum mechanics, we cannot know all the information about a system simultaneously. If we observe its position, then we cannot gain momentum information at the same time, or at least not with arbitrary precision. However, there is no principle that prevents us from seing all complementary aspects of a system in a series of distinct experiments on identically prepared objects. The question is then, can we infer the quantum state from such a set of observation? The answer is yes. In the same way medical tomographic imaging can reconstruct the shape of a hidden object inside a patient's body by gathering projection data from multiple directions, in quantum optics, tomography has been experimentally applied to reconstruct the quantum state of light from a complete set of measured quantities. Quantum tomography explains how quantum states can be tomographically reconstructed from experimental data. The first theoretical suggestion about how to reconstruct the Wigner function using homodyne detection was done by Vogel and Risken [96] and the experimental demonstration that proved this method was published in 1993 by Smithey, *et.al.* [97, 98]. Yet, these experiments have always been done in the optical frequencies, where highly efficient detectors exist. In the next section I describe the basics of quantum tomography and demonstrate that it is now possible to perform quantum state tomography at microwave frequencies.

7.2.1 Histograms and radon transformation

In order to understand the concept of tomography in this context, we need to remember Eq. (7.1) that explains how to obtain the distribution function for the values

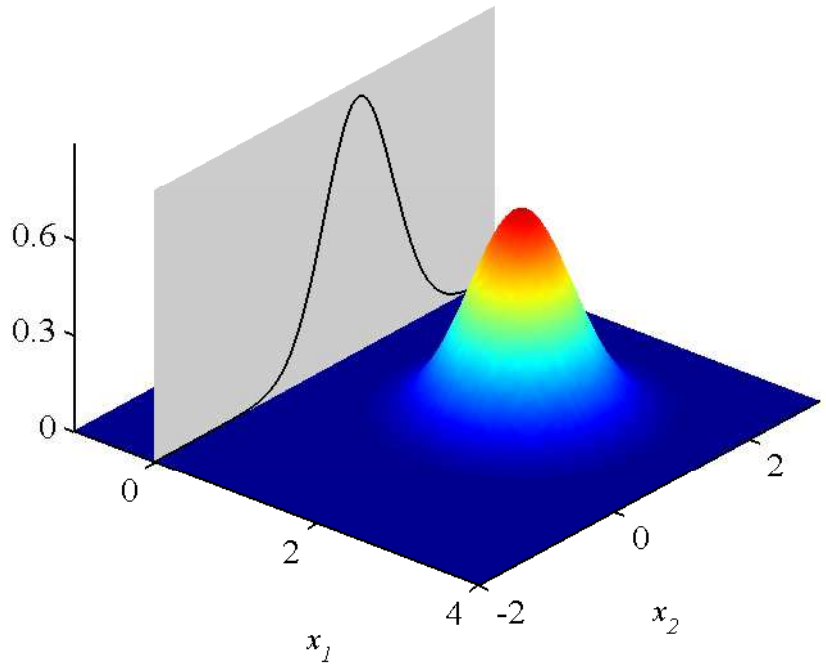

Figure 7.2: Tomographic projection of the Wigner function of a coherent state for $\theta = 0$. Tomography is a method that allows us to infer the "shape" of an object by taking multiple cross-sectional images or projections of that object. In quantum-state tomography, the Wigner function of the state plays the role of the "shape" of the object, and its projections are the quadrature probability distributions.

of a quadrature in terms of the Wigner function. In this case, we imagine the "shape" of the quantum object to be the Wigner function and the transmission profiles are the marginal distributions

$$\mathrm{pr}(x_1, \theta) = \int_{-\infty}^{\infty} W(x_1 \cos\theta - x_2 \sin\theta, x_1 \sin\theta + x_2 \cos\theta) dx_2$$

which in a sense are the projections of $W(x_1, x_2)$ onto a line of the quantum space (Fig. 7.2) [76]. As mentioned previously, integrals as the one described in this equation are called Radon transformations and are the basis for the mathematical theory of tomographic imaging. Although we cannot observe the Wigner function directly, we can measure the marginal distributions as quadrature histograms by performing homodyne

(quadrature) measurements (Fig. 7.3). By varying the phase θ, we can observe the quantum object under different angles and measure the quadrature histograms at all these different angles. Given the distributions $\mathrm{pr}(x_1, \theta)$, the mathematics of computerized tomography can be used to estimate the Wigner function (basically, by performing the inverse radon transformation on the multiple histograms).

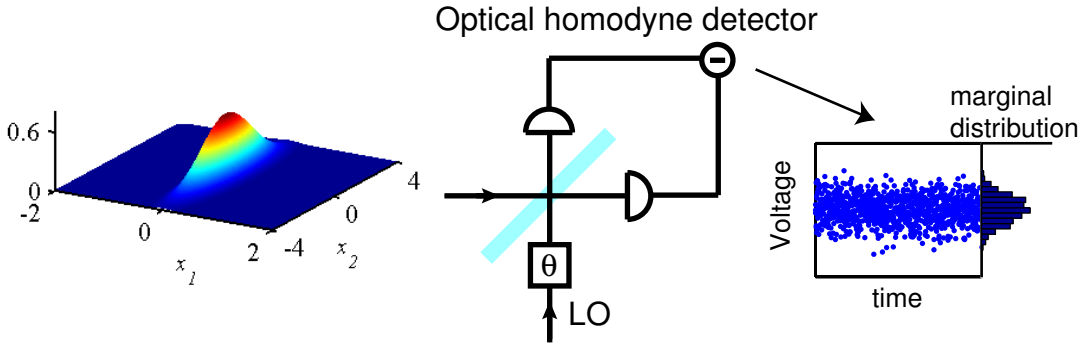

Figure 7.3: Schematic diagram for Wigner function reconstruction. A light signal from the prepared state enters a balanced homodyne detector where the projection of the Wigner function is set by the phase of the local oscillator (LO). The voltage output of the homodyne detector is measured and its histogram is created. This histogram is an estimate of the quadrature distributions for that particular phase.

In optics experiments, the quadrature of a light field can be measured using the balanced homodyne detection [99]. In the microwave world, this is done by using the microwave mixer that we described in section 6.1.2[4] However, a microwave mixer has a very poor efficiency, so in order to measure the nonclassicality of quantum states in microwave fields, we need to add a few elements to the measurement scheme as we will describe in the next section. Just like a microwave mixer (only better), an optical homodyne detector measures a quadrature component x_θ of the incoming field. The reference phase θ is provided by the local oscillator (LO) and it can be adjusted by changing its phase. To measure the quadrature distribution, we can either fix the angle

[4] It is interesting to notice that even though it can be said that balanced homodyne detection is intrinsically more efficient in the quantum optics world, the idea of balanced homodyne detection was actually born in the context of microwave technology development during World War II [100].

of the LO or sweep it as a function of time, and perform a series of homodyne measurements at all the required different phases. From these measurements, we then build up a histogram that in the limit of a large number of measurements will approximate $\mathrm{pr}(x_1, \theta)$ (Fig. 7.3). The homodyne measurement must be repeated many times to gain sufficient statistical information about the quadrature values and at sufficient number of phases in order to accurately reconstruct the Wigner function. These last details will be discussed in a later section.

7.2.2 Inverse radon transformation

The general idea of quantum tomography has already been explained by defining the probability distribution for a quadrature measurement as the Radon transform of the Wigner function, Eq. (7.1). Fourier transforming the marginal distribution results in

$$\begin{aligned} \tilde{\mathrm{pr}}(\xi, \theta) &= \int_{-\infty}^{\infty} \mathrm{pr}(x, \theta) e^{-i\xi x} dx \\ &= \tilde{W}(\xi \cos\theta, \xi \sin\theta). \end{aligned} \tag{7.18}$$

In order to obtain the Wigner function we need to perform the inverse Fourier transform in polar coordinates of the measured marginal distribution

$$\begin{aligned} W(x_1, x_2) &= \frac{1}{(2\pi)^2} \int_0^{\infty} \int_0^{2\pi} \tilde{W}(\xi \cos\theta, \xi \sin\theta) e^{i\xi(x_1 \cos\theta + x_2 \sin\theta)} \xi d\xi d\theta \\ &= \frac{1}{(2\pi)^2} \int_{-\infty}^{\infty} \int_0^{\pi} \tilde{W}(\xi \cos\theta, \xi \sin\theta) e^{i\xi(x_1 \cos\theta + x_2 \sin\theta)} |\xi| d\xi d\theta \\ &= \int_0^{\pi} \left[\frac{1}{(2\pi)^2} \int_{-\infty}^{\infty} \tilde{\mathrm{pr}}(\xi, \theta) e^{i\xi(x_1 \cos\theta + x_2 \sin\theta)} |\xi| d\xi \right] d\theta \end{aligned} \tag{7.19}$$

where in the second line we have used the property that $\tilde{W}(\xi, \theta + 180^\circ) = \tilde{W}(-\xi, \theta)$. The integral of Eq. 7.19 may be expressed as

$$W(x_1, x_2) = \int_0^{\pi} H_\theta(x_1 \cos\theta + x_2 \sin\theta) d\theta \tag{7.20}$$

where

$$H_\theta(t) = \frac{1}{(2\pi)^2} \int_{-\infty}^{\infty} \tilde{\mathrm{pr}}(\xi, \theta) e^{i\xi t} |\xi| d\xi \tag{7.21}$$

This estimate of the Wigner function $W(x_1, x_2)$ based on the Fourier transform of the measured histograms $\mathrm{pr}(x, \theta)$ has a simple interpretation. It represents a filtering operation where the frequency response of the filter is given by $|\xi|$. The term H_θ is usually referred as the "filtered projection." The phase integration is approximated by a sum over the measured phases θ to generate the estimate of $W(x_1, x_2)$.

Expression (7.21) presents certain mathematical difficulties. From the convolution theorem it can be expressed as

$$H_\theta(t) = \int_{-\infty}^{\infty} \mathrm{pr}(x, \theta) K(t - x) dx$$

where $K(t)$ is nominally the inverse Fourier transform of $|\xi|$. However, this kernel $K(t)$ exists only in the sense of a generalized function. I will not get into this detail or the regularization of the generalized function $K(t)$. I refer the interested reader to the appropriate literature [76, 101]. Numerical recipes for the proper implementation of Eq. 7.20 are easy to find in the literature and will not be reviewed here. In our case, we did not write our own implementation, but used the filter back-projection algorithm already programmed as the function *iradon* in MATLAB 7.7.0. This particular implementation is explained in Ref. [101].

7.2.3 Inefficiencies and measurement issues

In our experiment where we try to detect microwave squeezed states there are two main sources of inefficiencies in detection: losses between the amplifiers and the JPA that generates the squeezed states, and added noise of our amplifiers. Losses between the squeezer and amplifiers can be easily modeled in the same way losses are modeled in optical systems: by incorporating a fictitious beam splitter (the microwave equivalent being a directional coupler) in front of the detector. This beam splitter accounts for the losses by letting only a fraction η of the incoming intensity pass and diverting the fraction $(1 - \eta)$ of lost intensity to an unobserved port of a beam splitter (Fig. 7.4).

From the fluctuation-dissipation theorem, the loss must be accompanied by fluctuations, which are modeled as noise introduced at the fourth port of the beam splitter. These fluctuations are described as the vacuum noise that enters the detector via the other port of the beam splitter or directional coupler.[5]

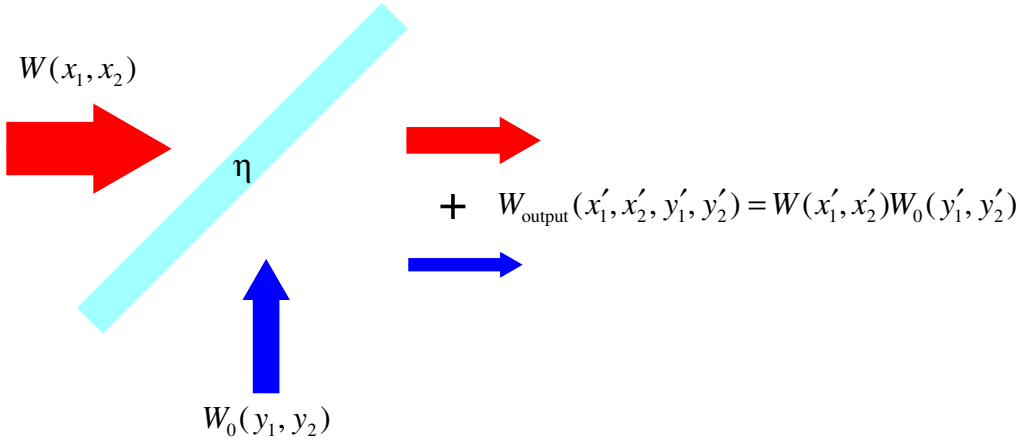

Figure 7.4: Effect of a beam splitter on a Wigner function $W(x_1, x_2)$. The second port is assumed unused and therefore only vacuum fluctuations enter this port represented by the Wigner function of vacuum $W_0(y_1, y_2)$. The effect of the beam-splitter losses (η) manifests in the transformation $\{x_1, x_2, y_1, y_2\} \rightarrow \{x_1', x_2', y_1', y_2'\}$, Eq. (7.22)

The effect of a beam splitter on the Wigner function is easily found by using the relation between the input and output ports of the beam splitter [26, 28, 76, 77].

$$\begin{pmatrix} a' \\ b' \end{pmatrix} = \begin{pmatrix} \sqrt{\eta} & -\sqrt{1-\eta} \\ \sqrt{1-\eta} & \sqrt{\eta} \end{pmatrix} \begin{pmatrix} a \\ b \end{pmatrix} \tag{7.22}$$

We are only interested in one of the outputs of the beam splitter $a' = \sqrt{\eta}a - \sqrt{1-\eta}b$, the other output representing the absorbed power. The Wigner function for the joint system of the input modes is given by $W_{\text{input}}(x_1, x_2, y_1, y_2) = W(x_1, x_2)W_0(y_1, y_2)$, where $W_0(y_1, y_2)$ is the vacuum Wigner function given by Eq. (7.7). We express the Wigner function in terms of the total Wigner function for both output fields of the beam

[5] The loss we are modeling sits inside the dilution refrigerator at 15 mK. Therefore, it is accurate to model the noise introduced by the loss as vacuum noise given that $\hbar\omega \gg k_B T$ for the frequencies we are interested.

splitter. The output Wigner function consists of

$$W_{\text{output}}(x_1', x_2', y_1', y_2') = W(\sqrt{\eta}x_1' - \sqrt{1-\eta}y_1', \sqrt{\eta}x_2' - \sqrt{1-\eta}y_2') \times W_0(\sqrt{1-\eta}x_1' + \sqrt{\eta}y_1', \sqrt{1-\eta}x_2' + \sqrt{\eta}y_2').$$

Because we only measure one of the outputs of the fictitious beam splitter, the measured distribution $W_{\text{meas}}(x_1, x_2)$ is

$$W_{\text{meas}}(x_1, x_2) = \int_{-\infty}^{\infty}\int_{-\infty}^{\infty} W(\sqrt{\eta}x_1 - \sqrt{1-\eta}y_1, \sqrt{\eta}x_2 - \sqrt{1-\eta}y_2) \times W_0(\sqrt{1-\eta}x_1 + \sqrt{\eta}y_1, \sqrt{1-\eta}x_2 + \sqrt{\eta}y_2)dy_1dy_2. \quad (7.23)$$

We see that the measured Wigner function is really a smoothed version of the ideal distribution $W(x_1, x_2)$. By making a change of variables and comparing Eq. (7.23) with the definition of the s-parameterized distribution, Eq. (7.16), it is possible to show that after including losses, the measured distribution is not the Wigner function but a s-parameterized distribution given by

$$W_{\text{meas}}(x_1, x_2) = \frac{1}{\eta}W(\frac{x_1}{\sqrt{\eta}}, \frac{x_2}{\sqrt{\eta}}, s = 1 - \frac{1}{\eta}). \quad (7.24)$$

How losses affect the Wigner function has a simple interpretation: the rescaling corresponds to the linear loss in the intensity, whereas the s-parameter smoothing ($s < 0$) corresponds to the introduction of fluctuations that averages the details in the Wigner function. Losses and inefficiencies smooth the Wigner function of the considered quantum state and lead ultimately to a supression of nonclassical behavior. It is interesting to note that for 50% detection efficiency, the distribution obtained is a scaled Q function. This means that for $\eta = 0.5$, the amount of noise introduced in the measurement is enough to wash out all the nonclassicality of the Wigner function (recall that the Q-function is everywhere positive).

So far I have only discussed efficiency problems due to losses. In order to do our measurements outside the dilution fridge, we amplify our signals before going into

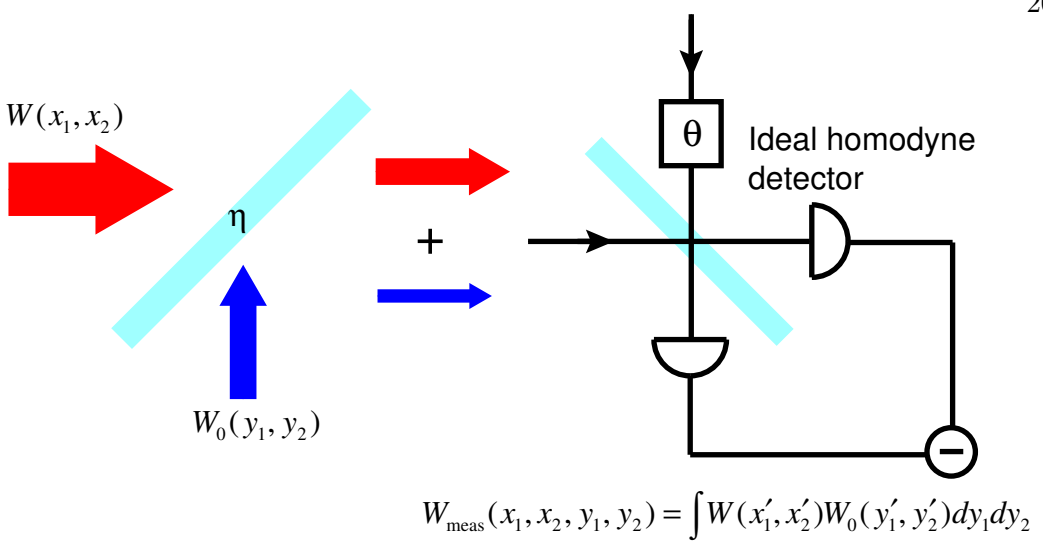

Figure 7.5: Effective model for losses in the detector. The signal is attenuated and contaminated by vacuum fluctuations entering the unused port (y_1, y_2) of the fictitious beam splitter. The transmittance of the beam splitter represents the homodyne detector efficiency.

the mixer that will allow us to measure the quadrature of the microwave fields. What sets the noise floor of our measurement is the first amplifier in the measuring chain (assuming it has enough gain to overcome the noise of the next amplifies). This noise floor represents the added noise of the amplifier A_N and unless $A_N = 0$, this added noise can be modeled as an effective loss. In order to explain this claim, we will model the noisy amplifier (in this case our HEMT amplifier) as a nondegenerate parametric amplifier.[6] In chapter 2, I described the transformation that a parametric amplifier does to the incoming fields (Eq. 2.82):

$$\begin{pmatrix} a' \\ b'^{\dagger} \end{pmatrix} = \begin{pmatrix} \cosh(r) & \sinh(r) \\ \sinh(r) & \cosh(r) \end{pmatrix} \begin{pmatrix} a \\ b^{\dagger} \end{pmatrix} \tag{7.25}$$

where a represents the mode we are interested in. Although the origin of the noise may be a very large amount of degrees of freedom, we can model it as a single fictitious bosonic mode b, the idler mode of this nondegenerate parametric amplifier. This linear

[6] Nondegenerate parametric amplifiers can be used to modeled any linear amplification process caused by Gaussian reservoirs [28, 102].

amplification transformation is very similar to the transformation performed by a beam splitter, Eq. (7.22). Thus, following a similar approach to the one for the beam splitter, the Wigner function of the amplified signal field is given by integrating over the idler mode variables [28]

$$W_{\rm ampl}(x_1', x_2') = \frac{1}{\pi A_N}\int_{-\infty}^{\infty}\int_{-\infty}^{\infty} W(x_1, x_2)\exp(-\frac{(y_1^2+y_2^2)}{A_N})dy_1'dy_2' \tag{7.26}$$

where x_i' and y_i' are the modes transformed by Eq. (7.25), and the added noise is given by the noise in the idler mode

$$A_N = \frac{1}{2}\langle\{\hat{b}, \hat{b}^\dagger\}\rangle = \frac{1}{2}\coth(\frac{\hbar\omega}{k_B T_{\rm idler}}).$$

This integral can be mapped into a scaled s-parameterized distribution,

$$W_{\rm ampl}(x_1, x_2) = \frac{1}{\cosh^2(r)} W(\frac{x_1}{\cosh(r)}, \frac{x_2}{\cosh(r)}, -\frac{\sinh^2(r)}{\cosh^2(r)}\frac{A_N}{1/2}) \tag{7.27}$$

with the smoothing s-parameter given by

$$s = -\frac{\sinh^2(r)}{\cosh^2(r)}\frac{A_N}{1/2}.$$

For large gain, $\cosh(r) \simeq \sinh(r)$, so the effective efficiency for the amplification process becomes

$$\eta = \frac{1}{1+2A_N}. \tag{7.28}$$

For a linear phase preserving amplifier, the smallest possible added noise (standard quantum limit) is $A_N = 1/2$, consequently $\eta = 0.5$. We then see that even for a quantum-limited amplifier, amplifying a signal removes all the nonclassicality of the Wigner function, because the resulting quasiprobability distribution is the everywhere-positive Q function. In our case, when we use the HEMT amplifier to measure squeezed states our efficiency is less than 2%, assuming an added noise of $A_N = 26$ quanta. In order to estimate the total efficiency of a measurement, we only need to estimate the efficiency of the separate components, $\eta_{\rm loss}$ and $\eta_{\rm amp\ noise}$. The total efficiency is then

given by

$$\eta = \eta_{\text{loss}} \times \eta_{\text{amp noise}}. \tag{7.29}$$

Next, I will explain how we improve this efficiency in our measurements.

7.2.4 Implementing an ideal homodyne tomography detector with a JPA

So far it has not been possible to do much with the microwave squeezed states that we have generated since the detectors at microwave frequencies are highly inefficient. Unlike optics, where the large energy per photon can be used to create highly efficient detectors (efficiencies as high as $\eta = 0.97$ [103]), the energy of one microwave photon is so small that a plausible scheme for a single-photon detector has yet to be developed. The way small signals at microwave frequencies are measured is by measuring voltages after the signals have been amplified. Yet, the amplification process is rather noisy; state-of-the-art commercial microwave amplifiers have an estimated added noise number of 10-20 quanta at 5-10 GHz. To provide a sense of the problem, 20 quanta of added noise is equivalent to only 2.5% efficiency, Eq. (7.28). However, the same type of JPA that was used to generates squeezed states can also be used to improve the efficiency of the detection.

In homodyne detections, only one quadrature is measured. We have seen that, in principle, it is possible to noiselessly amplify one of the quadratures of a signal and squeeze the other one. Therefore, a way to circumvent issues of efficiency in the homodyne detection is to noiselessly amplify the measured quadrature by a large enough factor so that the smoothing due to inefficiencies in the detector is negligible. The transformation on the signal mode a and $a^\dagger$ described for an ideal generic parametric amplifier was discussed in chapter 2 (Eq. 2.83) and it can be re-expressed as in section

2.4.3 in the following way

$$\begin{pmatrix} a' \\ a'^{\dagger} \end{pmatrix} = \begin{pmatrix} \cosh(r) & \sinh(r) \\ \sinh(r) & \cosh(r) \end{pmatrix} \begin{pmatrix} a \\ a^{\dagger} \end{pmatrix} \tag{7.30}$$

where r is just a parameter that determines the gain of the amplifier. Based on this transformation, the quadrature modes are then transformed in the following way

$$x_1' = e^r x_1,\ x_2' = e^{-r} x_2, \tag{7.31}$$

showing that x_1 is amplified and x_2 is squeezed. Defining $\sqrt{G_1} = e^r$ as the quadrature gain, the transformed Wigner function at the output of the squeezer is given by

$$W'(x_1', x_2') = W(\frac{x_1'}{\sqrt{G_1}}, \sqrt{G_1} x_2'). \tag{7.32}$$

The proposed set-up shown in figure 7.6 would use a JPA as pre-amplifier for the inefficient homodyne detector (here modeled as a black box that represents the amplification chain and mixer combined and a beam splitter that models the inefficiencies of the detector). The phase of both the JPA pump and the LO of the homodyne detector must be properly adjusted so that the measured quadrature corresponds to the amplified quadrature and not to the squeezed one. The effect of both the noiseless amplification $\sqrt{G_1}$ and absorbtion of the loss η on the Wigner function $W(x_1, x_2)$ resulting in a squeezed-smoothed Wigner function W_{meas} can be easily computed. However, we are more interested on the final histogram $\text{pr}_{\text{meas}}(x_1', \theta)$ measured:

$$\begin{aligned} \text{pr}_{\text{meas}}(x, \theta) &= \int_{-\infty}^{\infty} W_{\text{meas}}(x, y) dy \\ &= \sqrt{\frac{2}{\pi(1-\eta)}} \int_{-\infty}^{\infty} \text{pr}(x', \theta) \exp\left(-\frac{2\eta G_1}{1-\eta} [x' - \frac{x}{\sqrt{\eta G_1}}]^2 \right) dx' \end{aligned} \tag{7.33}$$

where $\text{pr}(x', \theta)$ is the original marginal distribution of $W(x_1, x_2)$. From Eq. (7.33), it can be observed that the smoothing is reduced by increasing the gain G_1. In the limit of high gain, the exponential approaches a delta function resulting in measuring a scaled ideal distribution

$$\text{pr}_{\text{meas}}(x, \theta) = \frac{1}{\sqrt{\eta G_1}} \text{pr}(\frac{x}{\sqrt{\eta G_1}}, \theta).$$

This means that using an ideal degenerate parametric amplifier as a pre-amplifier would allow us to measured the marginal distributions of the original Wigner function, with the appropriate rescaling.

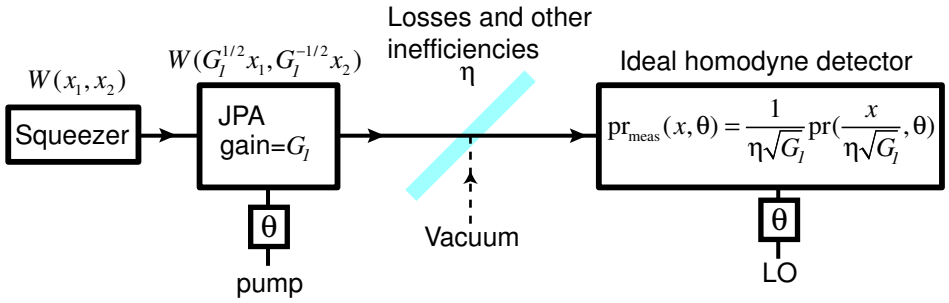

Figure 7.6: Schematic diagram with a JPA used as a preamplifier for an inefficient homodyne detector. For large enough JPA gain G_1, the measured histograms approach the quadrature probability distribution of the ideal Wigner function $W(x_1, x_2)$, hence allowing for its tomographical reconstruction.

Comparing Eq. (7.33) and Eq. (7.17) we can see that if we were to use the histograms from Eq. (7.33) measured with this set-up, we would be able to reconstruct the following s-parameterized distribution

$$W'(x_1, x_2') = \frac{1}{\eta G} W(\frac{x_1}{\sqrt{\eta G}}, \frac{x_2}{\sqrt{\eta G}}; -\frac{1-\eta}{\eta G}). \tag{7.34}$$

We observe that in the limit of high gain, the smoothing factor s approaches zero and the reconstructed Wigner function is the original, but scaled, Wigner function $W(x_1, x_2)$.[7]

7.3 Results

Using a parametric amplifier as a preamplifier to increase the efficiency of the detectors has already been suggested in quantum optics [28], but it has never been implemented at microwave frequencies. Next, I will show our implementation of this idea using Josephson parametric amplifiers to increase efficiency of the measurement of microwave squeezed states as well as the reconstruction of their Wigner function.

[7] Note, however, that this tomographically reconstructed Wigner function is not the Wigner function W_{meas} at the input of the homodyne detector.

7.3.1 Details of the experiment

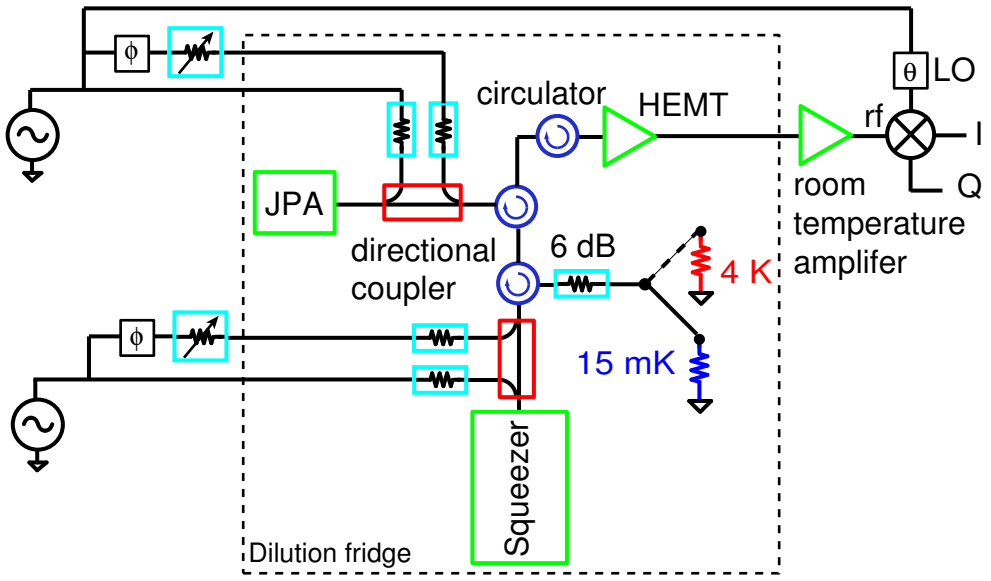

Figure 7.7: Schematic of the experimental setup for our implementation of quantum-state tomography of squeezed states with a high-efficiency microwave homodyne detector. Two signal generators are used in the experiment: one as the pump of the squeezer and the other one as the pump of the JPA (anti-squeezer) and the LO of the microwave mixer. A pair of noise sources (resistors) are used to estimate the added noise of the different amplifiers that determine our detector efficiency. All four ports of the directional couplers are used since we need to perform carrier-cancelation of both JPA and squeezer pumps. This is accomplished by splitting the pumps and sending a copy of the pumps to the fourth port of the directional coupler. The appropriate phase and magnitude of this cancelation tones are adjusted with manual variable attenuators and phase shifters. The incoming and outgoing tones are separated in the same way it was explained in chapter 6 using microwave circulators. Due to losses in the different microwave components and cables and added noise of the JPA, our detector inefficiency cannot be made arbitrarily small even at the highest JPA gain (see appendix B)

The full schematic of the measurement is shown in figure 7.7. It is similar to the one shown in chapter 6 (fig. 6.12). However, we have added an extra JPA in order to amplify the squeezed state generated by the first JPA (from now on referred only as squeezer). The resonance frequencies of both the squeezer and the JPA meet at two points for low currents: $f_{\text{res}} \simeq 7.45$ GHz and $f_{\text{res}} \simeq 8.15$ GHz, as shown in figure 7.8. Since the performance of the circulators was better at 7.45 GHz, we operated at this

frequency. For this reason the performance of the HEMT, JPA and squeezer was tested close to this particular frequency as explained in appendix B. We are operating the JPA and squeezer in the four-photon mode ($\omega_p \simeq \omega_{\text{resonance}}$), thus in order to prevent saturation of the JPA with the squeezer pump we need to suppress it by sending an interfering or cancelation tone using a directional coupler (Fig. 7.7). However, the microwave circulators are not ideal, having only 20 to 30 dB of isolation. This means there is some leakage of the JPA pump into the squeezer. Although small, it could affect the magnitude of the squeezer pump as we switch the phase of one with respect to another due to interference modifying the amount of squeezing. Hence we also send a carrier cancelation tone for the JPA pump. Nonetheless, the most important cancelation is the squeezer pump cancelation.

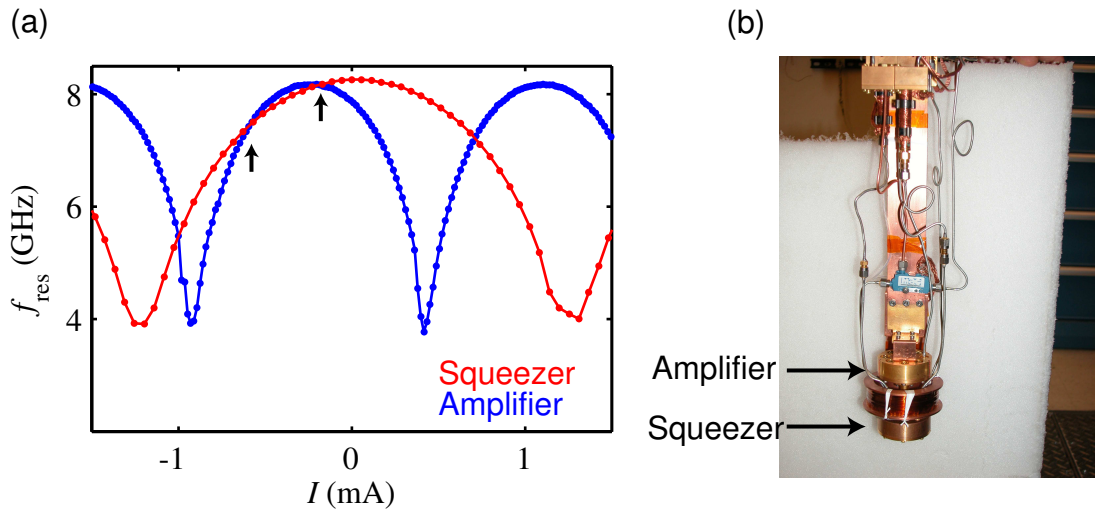

Figure 7.8: (a) Resonance frequency for the JPA and the squeezer as a function of the current though a coil installed in the mixing chamber. Both resonance meet at multiple currents, but only for two values if we restrict the current to be smaller than the needed to create a flux quanta at the resonators. These two values are shown by arrows. (b) The difference in the current dependance for both resonators was achieved by placing the samples at different locations relative to the magnetic field coil.

We use two signal generators for the measurement setup. In principle the JPA pump, the squeezer pump, and the LO of the mixer could all come from the same

microwave generator. Yet, the carrier cancelations and calibration measurements were significantly simplified by using two signal generators. One provides both the LO and the pump of the JPA. The other provides the squeezer pump. The cancelation tone for each pump came from the same signal generator as the respective pump (Fig. 7.7). The appropriate amplitude and phase to suppress the pumps are chosen with variable attenuators and variable phase shifters. The cancelation could be as good as 60 dB, but it was only stable for a few seconds (long enough to do our measurements). Still, a stable cancelation of 40 dB was achieved for several minutes.

Based on the discussion of the previous section, it can be concluded that knowing the losses as well as other inefficiencies such as amplifier noise in the path of your signal is very important. We performed some tests including thermal sweeps and Y-factor measurements as the ones described in the previous chapter. These tests are summarized in appendix B. From that analysis, I will model our setup as shown in figure 7.9. For the analysis I will assume the following values of attenuation (obtained from the thermal sweep data): $\alpha + \beta \simeq 3 \pm 0.2$ dB, $\alpha \simeq 1.7 \pm 0.1$ dB, $\beta = 1.3 \pm 0.3$ dB. Note that due to imperfections in the JPA ($A_J \neq 0$) and losses between the squeezer and JPA, the equivalent model (Fig. 7.6) of the microwave homodyne detector will have an additional beam-splitter at the input the JPA. This means that even with the largest gain possible of the JPA, it will not be possible to reconstruct the ideal Wigner function coming from the squeezer.

Another important point that needs to be addressed is to avoid saturation of the JPA with the squeezer amplified noise. Even though one of the quadratures of a squeezed state may have fluctuations below those of a vacuum state, the photon distribution of a squeezed state can be rather large (Fig. 7.12). In order to calculate the power at the input of the JPA, we can calculate the power in the amplified quadrature noise at the output of the squeezer. At the input of the squeezer there is a total of around 1 quanta of noise (the 0.5-0.8 quanta of incoming noise plus the 0.2 quanta of added noise). If

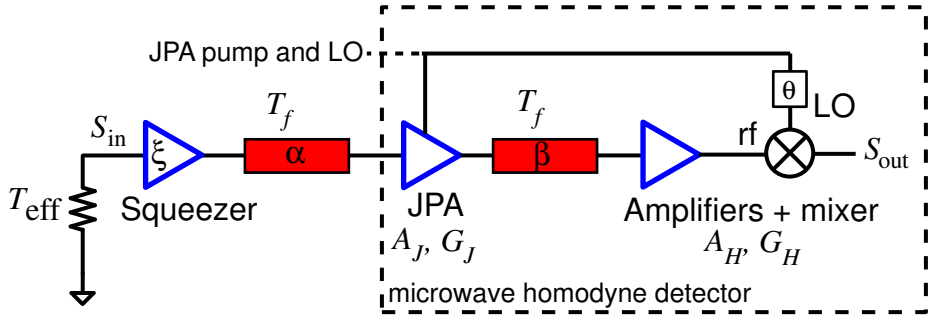

Figure 7.9: Schematic of our implementation for a high efficiency microwave homodyne detector. The microwave homodyne detector consist of the Josephson parametric amplifier operating as the JPA plus the commercial microwave amplifiers and the mixer. The phase of the mixer needs to appropriately chosen to measure the amplified quadrature of the JPA. The noise at the input of the squeezer is modeled as noise coming from a resistor with an effective temperature $T_{\rm eff}$. The main reason $T_{\rm eff} \neq T_c$ is due to the unknown insertion losses at 4.1 K.

the squeezer has a gain G_{SQ}, the noise power per unit bandwidth at the input of the JPA is then $G\hbar\omega$ (for simplicity, I am ignoring the loss α between the squeezer and JPA and the Lorentzian frequency dependance of the squeezer gain, as the squeezer is operated at a small gain, so its bandwidth is bigger than the JPA amplifier bandwidth). Assuming this noise at the input of the JPA, this means that if the total (fullwidth) amplifier bandwidth of the JPA is $\gamma_{\rm Gain}$, the total amplified power at the output of the JPA is $G_J(G_{\rm SQ}\hbar\omega)\pi\gamma_{\rm Gain}/2$. Here we have again used the convention of defining the quadrature gain G_1 of the JPA as G_J as in chapter 6. The JPA has a saturation power at the output of about -95 dBm. For a JPA quadrature gain of around 23 dB (direct gain of 17 dB) and a half-width of around 3.5 MHz, this means that we may be saturating the amplifier with a squeezer gain of 15 dB or a squeezer power gain of $G_{\rm SQ} = 30$. However, from appendix B, I know that the a maximum squeezing of about 80% is achieved at a gain of about 10 dB (see appendix B), so we should be able to operate at this gain with only small saturation problems.

We can now estimate the expected observed squeezing. For a given frequency we did a Y-factor measurement (sect. 6.3.3) and estimate the HEMTs noise. We did

as well a Y-factor on the JPA.[8] From figure 7.9, the output power of our microwave homodyne detector is

$$\begin{aligned} S_{\text{out}} &= G_H\{(S_{\text{in}}\xi\alpha + (1-\alpha)P_f + A_J)G_J\beta + (1-\beta)P_f + A_H\} && (7.35)\\ &= G_H G_J \alpha\beta\{S_{\text{in}}\xi + \frac{(1-\alpha)}{\alpha}P_f + \frac{A_J}{\alpha} + \frac{(1-\beta)}{G_J\beta\alpha}P_f + \frac{A_H}{G_J\beta\alpha}\} && (7.36)\\ &= G_{\text{eff}}\{S_{\text{in}}\xi + A_{\text{eff}}\} && (7.37)\end{aligned}$$

where $\xi = S_{\text{out}}^{squeezer}/S_{\text{in}}$, $S_{\text{in}} = \frac{1}{2}\coth(\frac{hf}{k_B T_{\text{eff}}})$, and $S_c = \frac{1}{2}\coth(\frac{hf}{k_B T_c}) \simeq \frac{1}{2}$ with T_c being the temperature of the cryostat (15 mK). A_{eff} is the effective added noise of the homodyne detector. In the limit of high JPA gain, A_{eff} can be approximated as:

$$A_{\text{eff}} \simeq \frac{(1-\alpha)}{\alpha}S_c + \frac{A_J}{\alpha} + \frac{A_H}{G_J\beta\alpha}. \qquad (7.38)$$

The effective added noise of the detector has three components: the HEMT noise divided by the effective gain of the JPA ($G_J\alpha\beta$), the added noise of the JPA scaled by the loss α and the noise coming from this loss $S_c(1-\alpha)/\alpha$. The effective efficiency of the homodyne detector is then given, according to Eq. (7.28), by

$$\begin{aligned}\eta &= \frac{1}{1+2A_{\text{eff}}}\\ &= \frac{\alpha}{1+2(A_J + A_H/G_J\beta)}.\end{aligned}$$

Note that the effective efficiency has the form of Eq. (7.29) for two main sources of noise: an amplifier with an added noise of $A_J + A_H/G_J\beta$ and loss α at its input.[9] Using values for all the attenuation and noises of amplifiers, with a JPA gain of 180, $\alpha = 1.7$ dB, $\beta = 1.3$ dB, $A_{J=}0.25$ quanta and $A_{HEMT} = 17.3$ quanta, the expected efficiency is 38%. Operating at higher gains would have increased the efficiency up to

[8] We also compared these values with the ones obtained from the thermal sweeps making sure they agreed within the error of the measurements.

[9] In Eq. (7.28), it is obvious that the origin of the numerical factor of 2 is the fact that there is half a quantum of noise in the vacuum state. Thus, there can be some ambiguity about whether to use $2A_{\text{eff}}$ or $4A_{\text{eff}}$ in Eq. (7.28), as that equation was obtained for a phase-insensitive amplifier, which adds $A_N/2$ to each quadrature (compared to the 1/4 quanta of noise in the quadrature of a vacuum state), and our quoted noise is the noise added to a single quadrature. However, since we are using a single-sided spectrum convention, the total quanta per unit bandwidth in one quadrature for a vacuum state is 1/2 (see appendix A) so $\eta = 1/(1+2A_{\text{eff}})$ is the right expression to use in our case.

45% but at a much reduced bandwidth and the difficulty of achieving perfect cancelation of the JPA pump, so the highest gain we used was $G_J = 180$.

To measure the quadrature histograms there are two possible approaches. We can fix the phase between the squeezer and the homodyne detector and perform a series of homodyne measurements at this particular phase to build up a quadrature histogram $\mathrm{pr}(x, \theta)$. Then, the LO and JPA pump phase should be changed and repeat this procedure as many times as the required numbers of phases. Another possibility is to sweep the phase in a known way while measuring the output of the homodyne detector, each sample representing a different phase. We used both approaches, but all of the data shown below comes from the second option where the phase was swept at a known rate.[10] The squeezer and JPA pumps were detuned by 100 kHz. This means that when we take a time trace, each point corresponds to a different phase between the squeezer and JPA pumps (basically a different phase between the squeezed noise and the homodyne detector). The time traces were 0.2 seconds long and digitized at a 10 MHz sample rate with a data acquisition Alazar card (ATS460) with 14 bit resolution and a 200 mV voltage range. The bandwidth was set by our 5 MHz anti-alias filter. With a detuning of 100 kHz, we have a full 360 degrees of rotation between the pumps every 100 samples, which means that in 1 time trace there are 20000 realizations for each phase.[11]

7.3.2 Histograms of the traces

The analysis of the time traces include some digital filtering in order to remove the low frequency noise observed in the amplification and squeezing process explained in the previous chapter. Besides, it helps remove the remaining squeezer pump that was not possible to suppress, which appears as small tone at $\Delta f = 100$ kHz. We also

[10] We chose the second option since the cancelation of both pumps was better accomplished.

[11] Actually, since the histograms $\mathrm{pr}(x, \theta)$ and $\mathrm{pr}(x, \theta + \pi)$ are not independent the only phases that matter for the Wigner function reconstruction are $0 - 180^\circ$ and we then have 50 independent phases with 40000 realizations

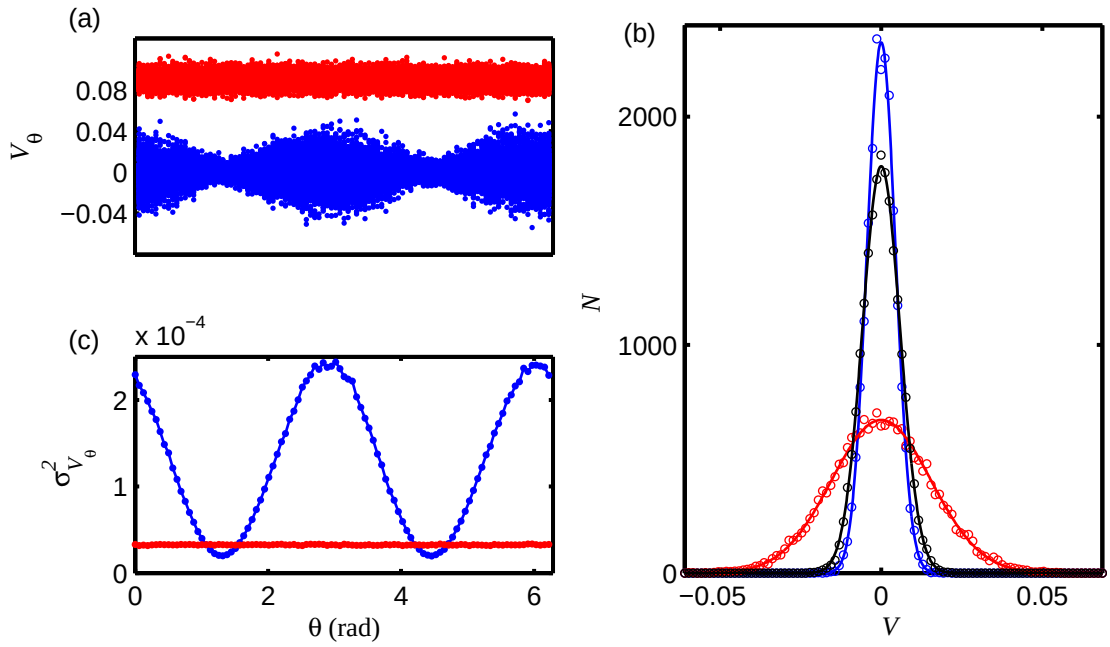

Figure 7.10: Noise at the output of our microwave homodyne detector as a function of the JPA-pump and LO phase. Blue points are the measured noise when the squeezer pump is applied and the red points are measured when the squeezer pump is turned off. The detection bandwidth is 5 MHz. (b) Histograms of the voltage fluctuations. Circles (o) are data and lines represent Gaussian fittings. The red circles are taken when measuring the amplified quadrature of the squeezer and the blue circles represent the squeezed quadrature. The black circles represent the calibration noise measured when the squeezer pump is turned off. (c) Variance of the Gaussian fittings as a function of phase. Both figures (a) and (c) share the same x-axis.

need to do a calibration of the noise level. Traditionally, in the optical experiments this is done by blocking the input of the homodyne detector and measure the "shot noise" level, which represents the vacuum noise level. A similar approach is done in our case. However, we can not go and block the signal path since it sits at 15 mK inside the dilution refrigerator. What we do is we turn off the squeezer pump and measure the noise level at the output of the microwave homodyne detector with the JPA pump on. Unfortunately, due to issues[12] in the calibration (Y-factor) line, we estimate that the input noise is not a vacuum state, but a low occupancy thermal state

[12] These issues are mainly the losses at 4.1 K due to the microwave switch and the bias tee used to heatsink the center conductor of the coaxial lines.

($\langle n\rangle + 1/2 = 0.65 - \pm 0.15$) quanta of noise. For the rest of this chapter I will assume that $\langle n\rangle + 1/2 = 0.65$. Assuming an efficiency of 38 %, that means that the noise level we measure of our calibration represents 0.56 quanta. The data was taken with 2 different JPA quadrature power gains, $G_J = 50$ and $G_J = 180$. Most of the shown data, however, is from the highest gain since it has a better effective efficiency. For each JPA gain, 6 different squeezer power gains were taken between $G_{\rm SQ} = 1.1$ and $G_{\rm SQ} = 14$. The gain of the squeezer was modified by adjusting the pump power, but keeping the same frequency of the pump.

A characteristic time trace for both the squeezer pump on and off is shown in figure 7.10a. For the case when the squeezer pump is turned on, the time trace reveals the characteristic phase-dependance noise of a squeezed state. A Gaussian fitting to the points representing a phase is used to estimate the variance of the histograms (Fig. 7.10b). The variance of the Gaussian fitting as a function of phase is shown in figure 7.10c where it is clear the squeezing of noise below our calibration noise.

We can now estimate the amount of squeezing we expect to see. We first start with the low JPA gain ($G = 50$). In this case, the efficiency of the detector is $\eta = 0.28$. The input power is $S_{\rm in} = 0.65$ quanta. The ratio between the variance of the signal at the output of the homodyne detector ($\sigma_V \propto \int_{B_\omega} S_{\rm out}(\omega) d\omega$) with the squeezer on and off is defined using Eq. 7.37 as

$$\zeta = \frac{\sigma_V(\xi, \theta)}{\sigma_V(\xi = 1)}. \tag{7.39}$$

In this case, the maximum observed squeezing should be $26 \pm 4\%$. The observed maximum squeezing as a function of gain is shown in figure 7.11a for the low JPA gain, and the phase dependance of ζ is shown for two different squeezer gains in figure 7.11b. In the case of large JPA gain ($G = 180$), we already estimated the efficiency, which is $\eta = 0.38$. The expected squeezing ζ is $36 \pm 5\%$. The observed squeezing ζ as a function of squeezer gain is shown in figure 7.11c, and its phase dependance for two different

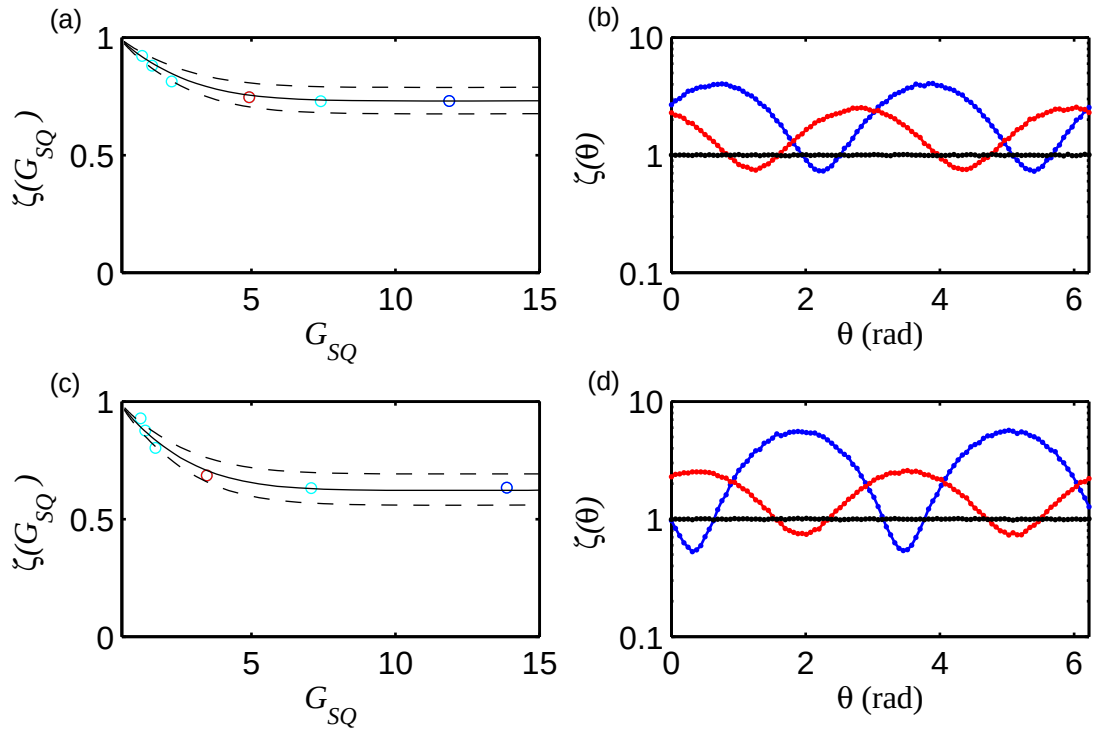

Figure 7.11: (a) Measured real squeezing ζ (circles) as defined by Eq. (7.39) and prediction (lines) using Ref. [38] as a function of squeezer gain. The solid line is assuming an incident noise of 0.65 quanta, while the dashed lines represent the uncertainty on this value. (b) Squeezing ζ as a function of phase for two different gains. The gains shown in (b) correspond to the same colors as the circles shown in (a). (c) and (d) are same as (a) and (b) but for a JPA gain of 180.

gains is shown in figure 7.11d. In general, we observe the expected behavior and the disagreement with theory observed is of the order of a 1 % for high gains and up to 4% at lower gains. The maximum observed real squeezing is $\zeta = 37\%$ as observed in figure 7.11c, which is close to the estimated squeezing. We were unable to go further in squeezer gain for two main reasons. The observed squeezing stops growing for higher squeezer gains, as was shown in the previous chapter.[13] And in the case of high JPA gain we observed a small saturation (reduction of the JPA gain by 0.1 dB) that we believe was not related to a poor cancelation of the squeezer pump but caused due to

[13] In this particular cooldown, the maximum squeezing happens at a gain of about $G_{\mathrm{SQ}} = 10$ as shown in appendix B, not at $G_{\mathrm{SQ}} = 30$ as observed in the previous cooldown described in chapter 6.

saturation from the large amplified noise coming from the squeezer.[14]

So far, our analysis of the time traces has not been very different from the previous chapter as comparing the variance of the calibration and the squeezed state histograms is effectively the same as comparing its power spectral density. The only difference has been that by using a JPA as a preamplifier for our HEMT amplifier, our effective efficiency has been increased from 2% to 38%, which allow us to have an observed real squeezing of $\zeta = 37\%$. However, this increment in efficiency can allow us to start reconstructing quasiprobability distribution functions. Note, though, that since our efficiency is only $\eta \simeq 0.4$, the reconstructed distribution is really an s-parameterized function, with $s = 1 - 1/\eta \simeq -1.5$. But for simplicity I will call this reconstruction, Wigner function reconstruction.

7.3.3 Quasiprobability distribution reconstruction

For the reconstruction of the Wigner function based on the histograms, we need to first consider if the number of phases and the number of points are enough for a reliable reconstruction. In this case, since we are analyzing squeezed state, which has a Gaussian Wigner function, the reconstruction is very forgiving.

What is the effect of only using d phases for the Wigner function reconstruction? One first consequence is that using a phase resolution of π/d would prevent us from properly discerning details with phase oscillations in the quadrature distribution $\mathrm{pr}(x, \theta)$ with frequencies higher than d as they would be aliased. In our case, the phase-dependant variance of the Gaussian distribution of a quadrature squeezed state only oscillates once in a π period, so this possible error of aliasing certain details of the Wigner function is not a concern. Leonhardt in Ref. [76] derives a rule-of-thumb for the minimum amount of phase values d in order to reconstruct the density state based on

[14] In the previous section I estimated that a squeezer gain of 15 dB or $G_{\mathrm{SQ}} = 30$ could start saturating the JPA. This was assuming the saturation point as the 1 dB compression point. This estimation is not far from the observed gain that started showing saturation behavior.

quantum tomography. This rule-of-thumb reads "the number of phase must be equal to the minimum dimension to accurately approximate density matrix of the measured state." However, although this a sufficient condition, it is not a requirement [76], especially for Gaussian states such as squeezed states. In any case, even with this constraint, figure 7.12 shows that the 50 phases taken over a range of π are more than enough.

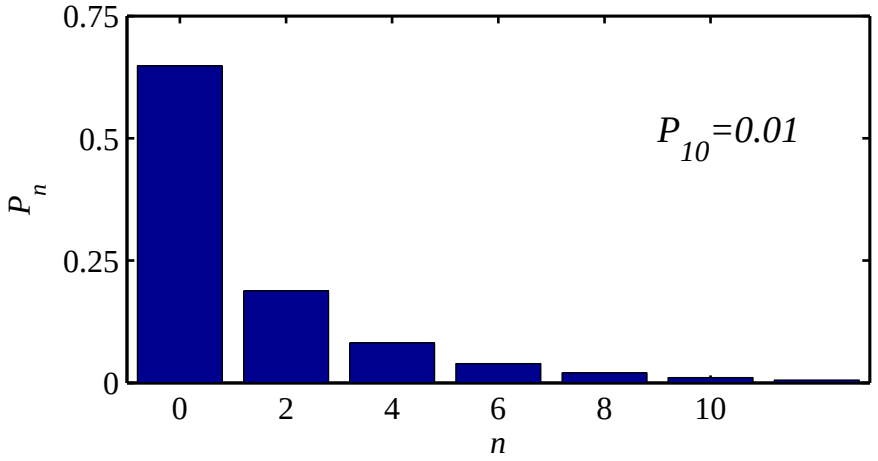

Figure 7.12: Probability distribution for and ideal squeezed state with $\Delta x_1^2 = 1/4e^{-2}$, or squeezing of 84 %. Setting an accuracy for the tomography detection of $P_n > 0.01$, suggest that a density matrix of dimension $n = 10$ would be sufficient for an accurate Wigner function reconstruction.

Regarding the statistical error due to finite samples of length N for a given phase θ, how much confidence do we have in the reconstruction of the quasiprobability distribution. Dividing the measurements in bins of size δx, the rate at which the quadrature values fall into that bin are governed by the expectation value $\mathrm{pr}(x, \theta)$. This process is a Poisson counting process, with the measured $\mathrm{pr}_{\mathrm{meas}}(x, \theta)$ being a fluctuation quantity. As a Poisson process, I expect the value of the histogram representing the bin δx_j to have fluctuations σ_j^2 of the order of N_j. For the measured distribution $\mathrm{pr}_{\mathrm{meas}}(x, \theta)$ which is formed by the histogram normalized by the total number of measured samples and

the uniform bin size δx, I expect then its variance to be given by

$$\sigma^2_{\mathrm{pr}_{\mathrm{meas}}(x_j,\theta)} = \frac{\mathrm{pr}(x_j,\theta)^2}{N\delta x}, \tag{7.40}$$

showing the expected result that the fluctuations in the measured marginal distributions $\mathrm{pr}_{\mathrm{meas}}(x,\theta)$ will have a $1/N$ dependance. The question is, though, how are these fluctuations going to affect the reconstruction of a Wigner function. Again Ref. [76] gives a rule-of-thumb based on Eq. (7.40) but using the photon number distribution $\rho_{n,m}$. There it is shown that the variance of $\rho_{n,n}$ is bounded by

$$\sigma^2_{nn} \leq \frac{4}{N}$$

and since for an experiment we want the statistical error to be smaller than the measured quantity,

$$\sigma_{nn} < \rho_{nn}.$$

This estimate implies that the required number samples per phase interval scales with the inverse of the photon-number probability squared

$$N_{\min} \sim \frac{4}{\rho^2_{n,n}}.$$

If I want to resolve states with an accuracy of $P_n > 0.01$ (Fig. 7.12), this implies a total number of samples per phase interval of $N = 40000$ over a phase range of π. Each of our time traces have this amount of samples per phase, and in order to make the reconstruction better, we took 10 time traces making a total of 400000 samples per phase interval.

Once we have decided that we have enough phase resolution and samples for a reliable construction of the quasiprobability distribution we can use the inverse radon algorithm to reconstruct it. We first need to scale the measured quadratures accordingly. Assuming again that our incoming noise is a thermal state with $\langle n \rangle = 0.15$, then the variance of the Gaussian histogram measured with η efficiency is given by

$$\Delta x^2_{\mathrm{meas}} = \frac{1}{4}(1-\eta) + \eta \Delta x^2_{\mathrm{therm}} \tag{7.41}$$

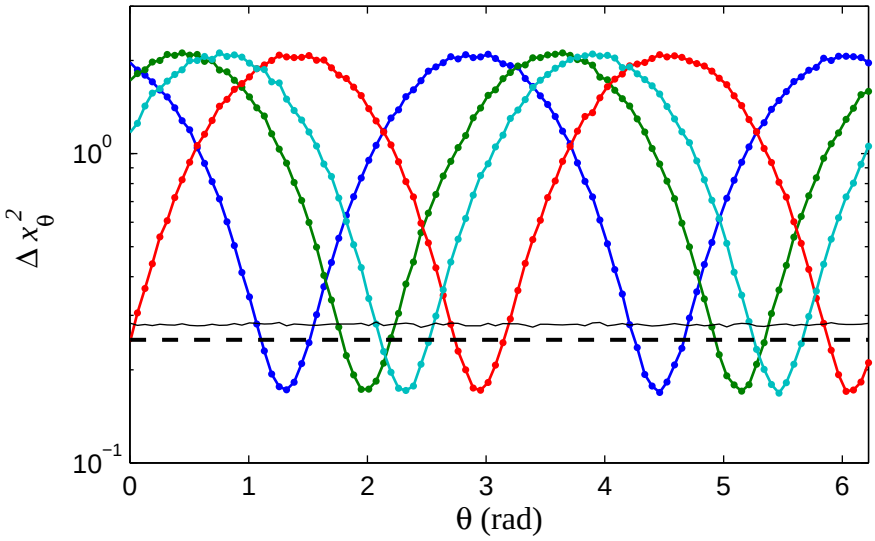

Figure 7.13: Assuming the $S_{\rm in} = 0.65$ quanta and an efficiency of $\eta = 0.38$, we use the the noise calibration to estimate the real quadrature values of the time traces measured with our microwave homodyne detector. The solid line represents our calibration noise ($\Delta x^2_{\rm meas} = 0.28$) the dashed line represent our estimate of the shot noise limit. From the squeezed traces, we observe a minimum real squeezing of $\zeta = 37\%$ which represents 30% below the vacuum level.

where

$$\begin{aligned} \Delta x^2_{\rm therm} &= \frac{1}{4}\coth\left(\frac{\hbar\omega}{2k_BT}\right), \\ &= \frac{1}{4}(1+2\langle n\rangle), \\ &= 0.33. \end{aligned}$$

In our case, because our calibration noise has a variance of $\Delta x^2_{\rm therm} = 0.33$, our measured variance is equivalent to $\Delta x^2_{\rm meas} = 0.28$. Note that if we had been able to use a vacuum state, Eq. (7.41) would have given us the "shot-noise" limit $\Delta x^2_{\rm meas} = 1/4$. The calibrated squeezing then looks like shown in figure 7.13. Based on this normalization, we estimate that the maximum *real* squeezing is 30% below the vacuum level. Compared with the 2% of *real* squeezing that was observed using only the HEMT amplifier (Fig. 6.34b), we then can conclude that using the JPA as a preamplifier has increase significantly our detection efficiency.

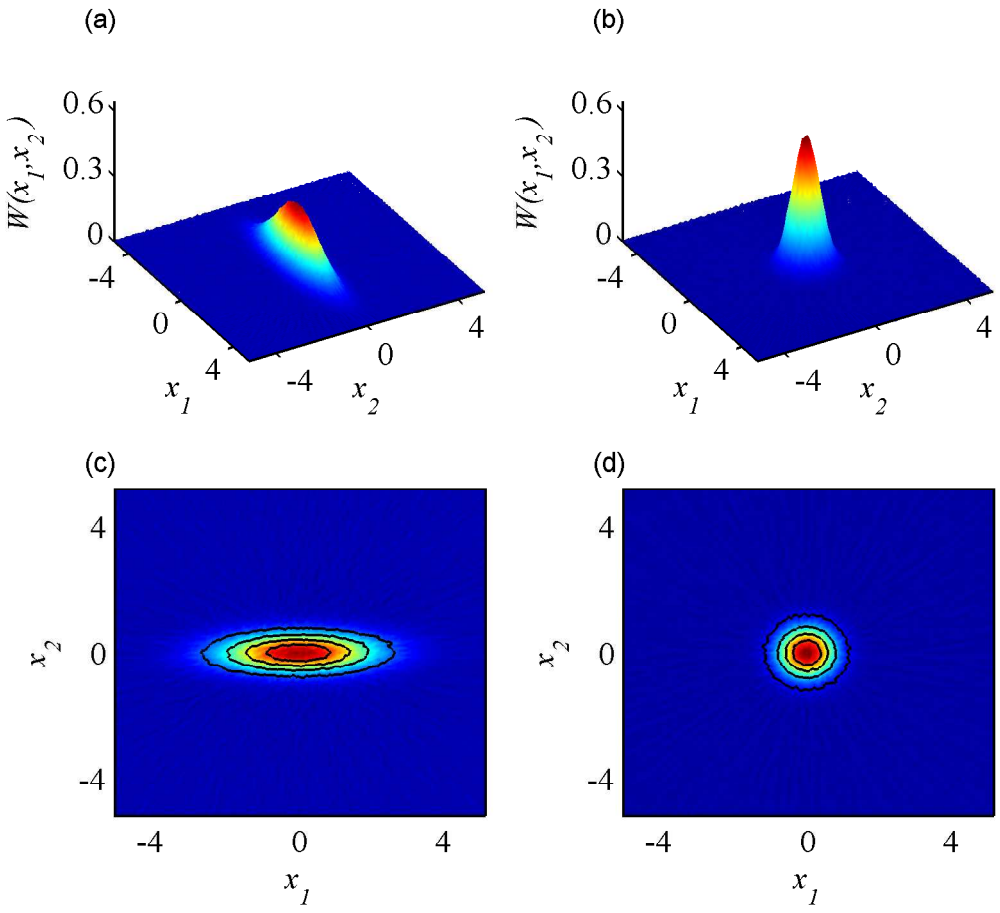

Figure 7.14: Wigner function reconstructed from the data for the squeezed state (a) and the calibration noise (b). The projection of the Wigner functions are shown in (c) and (d) including contour plots.

With calibrated histograms now, I use the MATLAB function *iradon* to obtain the Wigner functions of the prepared states. This is shown in figure 7.14 for the "calibration noise" and squeezer gain of $G_{\mathrm{SQ}} = 14$ and a JPA gain of $G_J = 180$. Both distributions were calculated by averaging the distributions reconstructed from each of the 10 time traces in the case of the squeezed state, and the 4 time traces in the case of the calibration noise. In the case of the squeezed states, the phase offset for each time trace was different so we first did a fitting to the variance as a function of phase using an expression similar to 7.12 but without assuming intelligent states (the variances $\langle \Delta x_i^2 \rangle$ do not fulfill the

equality $\langle \Delta x_1^2 \rangle \langle \Delta x_2^2 \rangle = 1/16$). Once the phase offsets are calculated for each trace, then this phase offset is included in the reconstruction of the Wigner function by providing the appropriate phase vector to the MATLAB *iradon* algorithm.

Chapter 8

Applications II. Increasing the sensitivity in the detection of mechanical motion of a nanomechanical wire.

In this chapter I will discuss the use of a Josephson parametric amplifier in order to increase the sensitivity of the detection of motion of a nanomechanical wire. The coupling of light and mechanical degrees of freedom is the underlying principle of many techniques to measure mechanical displacement and sits at the core of the research field called Optomechanics. Explaining all the interesting possibilities that emerge from these coupling of optical and mechanical degrees of freedom would take far from the main goal of this thesis. Instead, I will first give a very brief description of the concepts that will helps us understand the importance of using a JPA in the detection of motion of a nanomechanical harmonic oscillator. This will be done in the first part of this chapter. Sometimes I will be using a language that seems closer to that used in optics. The reason for this is that, as it is obvious from the name, optomechanics is a field that has been dominated by implementations that use light at optical frequencies to probe the motion of mechanical oscillators. However, in the case of our group, the implementation is all done with microwave circuit elements. In the second part of this chapter I will describe some features of this implementation, specifically the use of microwave cavities and the way we implement the coupling of the mechanical oscillator to the microwave-light degrees of freedom. In the last section I will discuss the results, specifically how the imprecision of our measurement was below the imprecision at the Standard Quantum

Limit (SQL).

One point that I want to emphasize is that I am not part of the group that performs the microwave-cavity optomechanics experiments. In the experiments that I will describe in this chapter, I only helped in the implementation of the JPA in the measurement scheme and some of the experimental work. For this reason, I will not discuss details such as the fabrication of the devices, or the specific decisions regarding the design of the sample. For those details, I refer the reader to the paper published by our group regarding this experiment [104].

8.1 Optomechanics

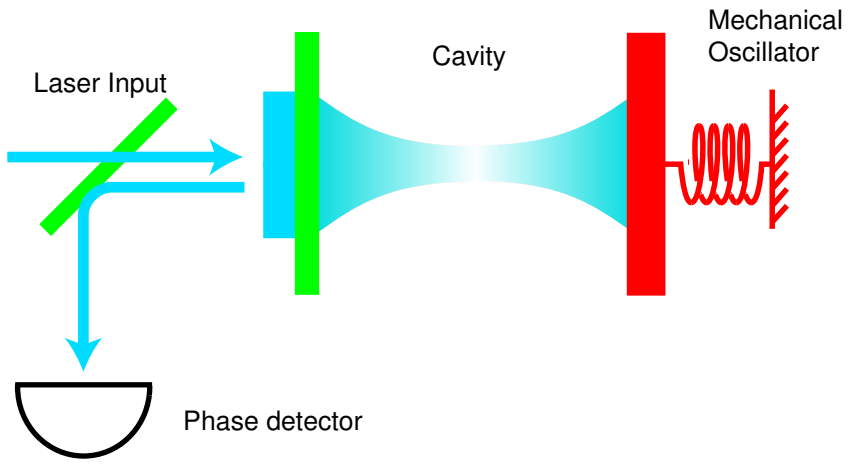

Figure 8.1: Schematic of a typical optomechanical setup. An optical cavity is formed by two parallel mirrors, one of which is attached to a mechanical oscillator (red). Light entering the cavity (cyan) induces radiation pressure that affects the motion of the mechanical oscillator, which in turn alters the mode frequency relative to the frequency of the incident light. The effect on the reflected light is measured with a phase detector, for example a Mach-Zehnder interferometer.

Optomechanics is concerned with the effects that emerge from having a coupling between mechanical and electromagnetic degrees of freedom, such as the effects of radiation pressure on a mechanical object. We are mostly concerned with those in connection with micro- and nanomechanical structures coupled to a resonant cavities

(cavity-optomechanics). A standard setup of cavity-optomechanics used to measure displacement is a Fabry-Perot interferometer such as the one shown in figure 8.1. It consists of on optical cavity driven by a laser impinging on the cavity through a fixed mirror. The other mirror of the cavity is movable (for example, it may be attached to a cantilever). In such a setup, the mechanical effects of light are enhanced, as the light field inside the cavity is resonantly increased and each photon interacts with the movable mirror in each of the multiple (of the order of Q) reflections it undergoes before leaving the cavity. The coupled nanomechanical-cavity system is described by a Hamiltonian of the form

$$H = \hbar\omega_0(a^\dagger a + \frac{1}{2}) + \hbar\omega_m(b^\dagger b + \frac{1}{2}) - \hbar g_c a^\dagger a(b^\dagger + b)\delta x_{\mathrm{zp}}, \tag{8.1}$$

where the cavity and mechanical modes are described respectively by a and b, ω_0 is the bare cavity resonance, ω_m is the mechanical resonance, and $g_c = \partial\omega_c/\partial x$ is the coupling between the mechanical harmonic oscillator displacement $x = (b^\dagger + b)\delta x_{\mathrm{zp}}$ and the perturbed cavity's resonance frequency ω_c. δx_{zp} is the oscillator zero point motion $\delta x_{\mathrm{zp}} = \sqrt{\hbar/2m\omega_m}$. In Eq. (8.1) I have left out the additional terms that describe the driving of the cavity by an outside light source (see section 2.3.3).

In terms of mirror displacement measurement, it is possible to show that a single-port cavity described by Eq. (8.1) will have a linear dependance between the the phase shift ϕ of the reflected signal from the cavity and the position x of the oscillator:

$$\phi \approx 4Q\frac{g_c}{\omega_0}x. \tag{8.2}$$

The previous expression can be derived using the tools of IOT on the Hamiltonian given by Eq. (8.1) [3]. Two fundamental sources of imprecision exist for the measurement of ϕ and hence x. First, there is the detector noise that, for an ideal coherent light source (emitting a coherent state) and an ideal detector, is given by the random arrival of photons at the detector; i.e., shot noise (Fig. 8.2). The phase imprecision expressed

in terms of single-sided power spectral densities is given by [3]:

$$S_{\phi,\phi}^{\rm imp} = \frac{1}{2\dot{N}} \tag{8.3}$$

where $\dot{N}$ is the photon flux at the incident on the detector. An interferometer with a phase uncertainty given by Eq. (8.3) is said to be shot-noise limited. We can find an expression for the imprecision of our measurement of the position[1] x, by multiplying Eq. (8.3) by a transducing factor $\partial\phi/\partial x$ that relates the displacement x in the mechanical oscillator and the phase ϕ of the signal at the output of the cavity (Eq. (8.2), for example). Hence the imprecision of our measurement for x is given by [104]

$$S_{x,x}^{\rm imp} = \frac{1}{2\dot{N}}\frac{1}{(\partial\phi/\partial x)^2} \tag{8.4}$$

$$= \frac{1}{2P_{\rm in}/\hbar\omega_c}\frac{1}{(\partial\phi/\partial x)^2} \tag{8.5}$$

where in the second line, I have expressed the phase imprecision in terms of the incident power in the detector rather than the photon flux.

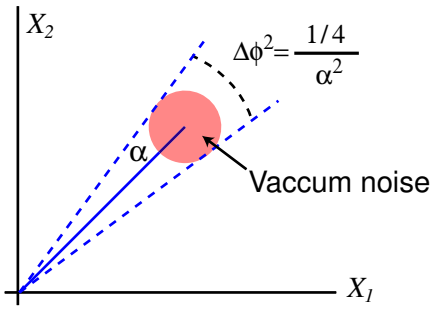

Figure 8.2: A coherent state contains a Poisson distribution of the number of photons. Thus the fluctuations and the mean number of photon are related as $\Delta N = \sqrt{\langle N\rangle} = |\alpha|$. This means that there is an uncertainty in any measurement of the phase given by $\Delta\phi = 1/2\sqrt{\langle N\rangle}$. The equivalent of this statement in terms of spectral densities associated with a real experiment is given by Eq. (8.3), where $(\Delta\phi)^2 \rightarrow S_{\phi,\phi}$ and $(\Delta N)^2 \rightarrow S_N = 2\dot{N}$ [3]. Note, however, that we use a single-sided spectral density.

In order to land some of these ideas, let's consider what it is actually measured.

[1] It is important to point out that the measurement discussed here is what it is known as a *weak continuous measurement* which means that the position x of the mechanical oscillator undergoes multiple cycles before we can acquire significant information [3].

According to the fluctuation-dissipation theorem, a mechanical oscillator with a mechanical damping rate of γ_m will experiment a random force with a power spectral density of

$$S_{F,F}^{th} = 4\hbar\omega_m(n_T + \frac{1}{2}) \tag{8.6}$$

$$\approx 4k_BTm\gamma_m, \tag{8.7}$$

where $n_T = 1/(e^{\frac{\hbar\omega_m}{k_BT}} - 1)$. In the second line, I have done the classical approximation, consistent with the equipartition theorem, since our mechanical resonator will behave classically due to a high occupancy n_T ($k_BT \gg \hbar\omega_m$). The response of the resonator is given by

$$S_{x,x} = S_{F,F}|H(\omega)|^2 \tag{8.8}$$

$$= S_{F,F}\left|\frac{1}{m(\omega^2 - \omega_m^2 - i\omega\gamma_m)}\right|^2 \tag{8.9}$$

where $H(\omega)$ is called the mechanical susceptibility. We use a single-sided convention such that

$$\int_0^\infty \frac{d\omega}{2\pi} S_{x,x} = \frac{k_BT}{m\omega_m^2} \tag{8.10}$$

In our experiments, when the spectral density of the phase of the reflected light Eq. (8.2) is measured by an interferometer, what will be measured is the Lorentzian response of the mechanical oscillator to the thermal force $S_{F,F}^{th}$ on top of a background imprecision noise floor (Fig. 8.3). Such measurement will allows us to calibrate the coupling of the mechanical oscillator to the cavity and assuming we know the temperature, we will be able to calibrate the imprecision of our measurement (the background noise floor).

As can be deduced from Eq. (8.2), the detector imprecision decreases with larger incident power. Increasing power, however, comes at the expense of increased intracavity power, causing a back-action onto the mirror: every time a photon reflects off the movable mirror, it will transfer momentum to it. This leads to a second source

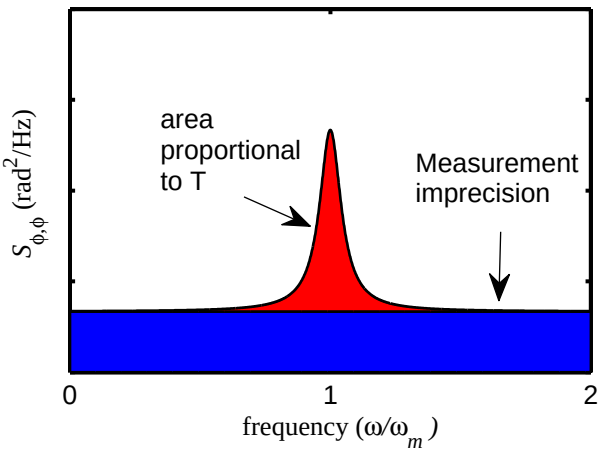

Figure 8.3: Example of the phase spectral density at the output of an interferometer used to measure a systems such as the one shown in figure 8.1. The Lorentzian peak corresponds to the thermal motion of the mechanical oscillator, while the background is our imprecision of the measurement, ideally just given by photon shot-noise.

of imprecision: the resulting momentum kicks of reflected photons create a mirror displacement noise, causing the mechanical oscillator to be driven and thus effectively heated. Although this noise can contain classical contributions due to uninteresting sources of noise (excess phase or amplitude noise, in the driving light, for example), it is ultimately limited by the quantum nature of light. Hence, it is termed quantum back-action [105]. Since the back-action does affect the quantity being measured (position), there is a limit on the accuracy on the measurement. This limit is described by the Heisenberg uncertainty limit, which ensures that an increasingly precise measurement of a harmonic oscillator's displacement is accompanied by an increasingly large force acting back on that oscillator [106]. This principle limits the total noise energy added in a measurement of displacement to be at least half a quantum $\hbar\omega_m/2$. The limit between the imprecision of the measurement and its back-action is better described, in spectral density units, as $S_{x,x}^{\mathrm{imp}} S_{F,F}^{b.a.} \geq \hbar^2$, where $S_{x,x}^{\mathrm{imp}}$ is the displacement imprecision and $S_{F,F}^{b.a.}$ the back-action force spectral density, both specified as single-sided spectral densities. A measurement reaches this limit, called the standard quantum limit (SQL)

when the imprecision and the driven motion from the back-action force each add precisely one quarter of a quantum of energy $\hbar\omega_m/4$. Therefore, the imprecision at the SQL provides a natural scale (which we will be using) to which to compare the noise of the measurement. On resonance, and in units of displacement spectral density, a noise energy $\hbar\omega_m/4$ corresponds to a displacement noise of $S_{x,x} = \hbar/(m\omega_m\gamma_m)$. It is worth noting that although the total added noise of the measurement has a minimum $S^T_{x,x} = S^{\rm imp}_{x,x} + S^{b.a.}_{x,x} = 2\hbar/m\omega_m\gamma_m$, the imprecision can be made arbitrarily small compared to that at the SQL, $S^{SQL}_{x,x} = \hbar/m\omega_m\gamma_m$. A system described by the Hamiltonian (8.1) can in principle reach the SQL. Physically, at the SQL, our knowledge of the mirror position is limited equally by shot-noise in the measured signal and by the motion of of the mirror due to the random kicks the mirror receives from the photons. On the other hand, if the strength of the drive used to probe the cavity is too small, the imprecision of the measurement is dominated by the photon shot-noise $\dot{N}$. If the drive is too big, the back-action noise perturbs the oscillator so strongly that the position uncertainty increases beyond the minimum.

Although the concept of quantum back-action is very interesting and its observation is a goal pursued in our lab, I will not discuss it here. For the effects of quantum back-action to become most apparent, we would need two things: first we would need to enter the regime where quantum fluctuations (zero-point motion) become the dominant fluctuations felt by the mechanical oscillator ($k_BT \ll \hbar\omega_m$), or equivalently a thermal occupation less than unity (something our lab is working on to achieve [107, 108]). And second, we would need a quantum-limited light detector, such as for example a Josephson parametric amplifier.

Most experimental implementations of such optomechanical systems are made using light at optical frequencies. Photons at optical frequencies are very well suited to measure mechanical displacement for several reasons. For example, because of the high energy of optical photons ($\sim$ 1 eV), thermal occupation is negligible at room

temperature, present-day laser sources are available that offer noise performance that is limited only by quantum noise, and detectors which a high efficiency allow to measure at the quantum-level, that is being only limited by the vacuum noise of the light used. However, devices in the microwave domain such as a nanomechanical resonator coupled to a superconducting microwave resonator have an advantage in some regards. For example, for such microwave implementations, the measurement setup is compatible with dilution-refrigerator temperatures, automatically cooling the mechanical motion by four orders of magnitude. Next I will discuss our implementation of the Hamiltonian given by Eq. (8.1).

8.2 Nanomechanical resonators inside microwave resonators

The microwave analysis of the resonator is similar to the ones done in chapter 5. The implementation of the experiment is shown in figure 8.4a. For simplicity we model the microwave resonator as a lumped element resonator (Fig. 8.4b). The geometry used to excite the resonator is also somewhat different from the ones we have described. Instead of measuring the resonator in reflection, or in transmission by using a two-port resonator, we place the microwave resonator as a shunt across a transmission line. This geometry (referred to as the feedline geometry), allows us to measure more than one cavity by putting several of them in the feedline. Each resonator is designed to have a slightly different resonant frequency. As long as the resonance frequencies of each of the microwave cavities are separated in the frequency axis by several linewidths, then it is possible to individually address them [69, 70].

We measured the transmission coefficient from port 1 to port 2, S_{21} which is given by [16]:

$$S_{21} = \frac{2}{2 + Z_c/Z_r} \tag{8.11}$$

where Z_r is the impedance of the circuit shunting the feedline. For now let's assume a

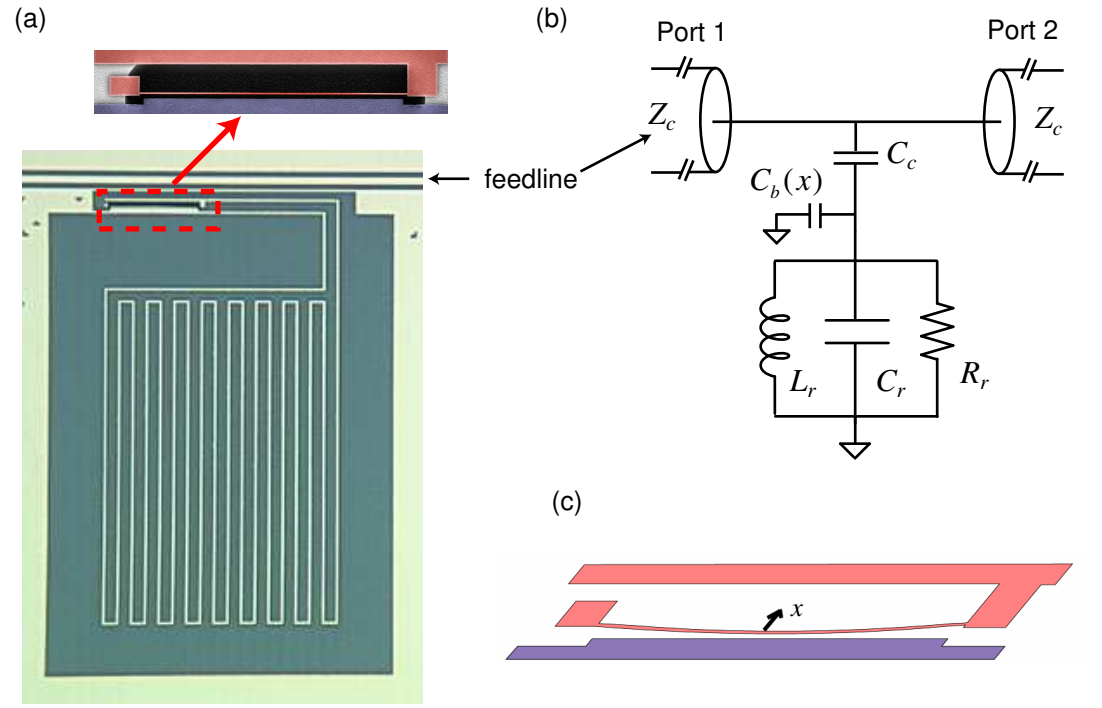

Figure 8.4: (a) Optical image of the inductor-capacitor (LC) resonant circuit, which behaves as a microwave cavity with $\omega_c = 2\pi \times 7.49$ GHz. The cavity linewidth is given by $\gamma_c = 2\pi \times 2.88$ MHz. The microwave-cavity was fabricated from superconducting aluminum on top of a silicon substrate. The nanomechanical oscillator consists of nanowire embedded in the microwave resonator near the CPW feedline used to excite the resonator. The wire has dimensions of 150μm $\times$ 170nm $\times$ 160 nm, yielding a total mass $m = 11 \pm 2$ pg and a mechanical resonance frequency $\omega_m = 2\pi 1.04 MHz$. (b) Electrical diagram of the device. The resonator is coupled to the feedline by a capacitor C_c. The effect of the nanowire on the circuit is equivalent to that of a small capacitor C_b in parallel to the LC resonator. (c) The mechanical degree of freedom is the fundamental mode of the freely suspended aluminum nanowire.

lossless cavity ($R_r \to \infty$). The bare cavity resonance is given by

$$\omega_0 = \frac{1}{\sqrt{L_r C_r}}.$$

However, by finding the location of the minimum of $|S_{21}|$, we can find the new resonance frequency of the cavity loaded by both capacitors:

$$\omega_c = \omega_0 (1 - \frac{C_c}{2C_r} - \frac{C_b}{2C_r}). \tag{8.12}$$

If we now consider finite loss R_r, but still working in the high-Q limit, we find that the

quality factors associated with internal losses and the coupling capacitor:

$$Q_c = \frac{2C_r}{\omega_0 C_c^2 Z_c}$$

and

$$Q_l = \omega_0 R_r C_r.$$

Based on this expression, Eq. (8.11) reduces to

$$S_{21} = \frac{S_0 + 2iQ(\omega - \omega_c)/\omega_c}{1 + 2iQ(\omega - \omega_c)/\omega_c} \tag{8.13}$$

where Q is the total quality factor given by Eq. (5.27)

$$Q = \frac{Q_c Q_l}{Q_c + Q_l}$$

and

$$S_0 = \frac{Q_c}{Q_c + Q_l}.$$

From the measurements of the scattering parameter S_{21}, the internal and coupling quality factors of the cavity used for the experiment were $Q_c = 3.0 \times 10^3$ and $Q_l = 2.6 \times 10^4$. Yet, in the case of Q_l, it varies by as much as 20% for the range of temperatures and powers used in the experiment.

Eqs. (8.12) and (8.13) and figure 8.4c allows us to understand how it is that we can infer the motion of the beam from the information encoded in the measured S_{21}. For that, let's plot the phase and amplitude we expect for some usual parameters (Fig. 8.5). As it can be seen in those plots, the amplitude is rather insensitive to small changes of resonance frequency. However, the phase depends linearly to changes in the resonance frequency (to first order). Therefore, the motion of the beam (Fig. 8.4c) will generate changes in the resonance frequency, Eq. (8.12) due to changes in the capacitor $C_b(x)$. When measuring a cavity of the kind shown in figure 8.4a, usually the frequency of the microwave probing tone remains constant. Hence, the motion of the beam will be encoded in the phase of the transmitted signal (Fig. 8.5c).

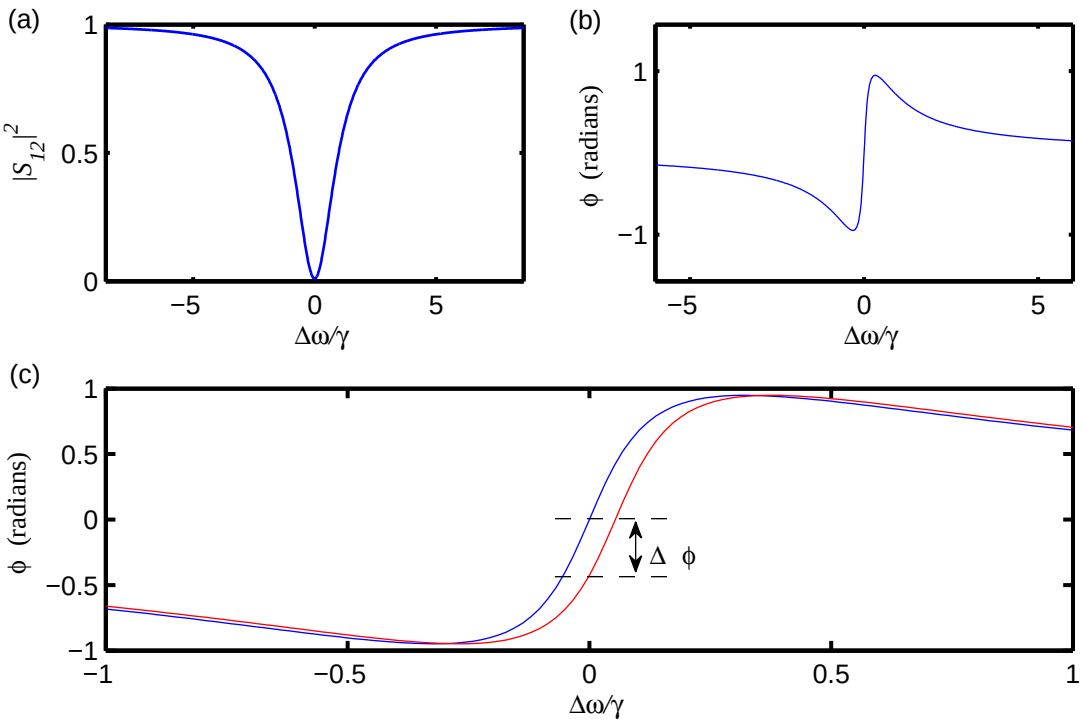

Figure 8.5: (a) Magnitude $|S_{21}|$ and (b) phase ϕ of the transmission coefficient as a function of frequency for the feedline geometry used to probe the microwave resonators. The values used for the quality factors were the same as the ones found from the measurement of S_{21}, $Q_c = 3000$ and $Q_l = 26000$. (c) The phase is a very sensitive function of the resonance frequency. Small changes in ω_c, correspond to large changes in phase $\Delta\phi$.

The simplified diagram of the microwave setup used in shown in figure 8.6. It is essentially the microwave analog of a Mach-Zehnder interferometer (MZI) typically used to measure phase-shifts. However, at microwave frequencies, from the same reasons there is not a commercial mixer with quantum-limited sensitivity (sect. 6.3.3), there is not such a thing as a shot-noise limited phase detector. As shown in figure 8.6, the signal at the output of the cavity is actually amplified by a chain of commercial amplifiers (same as explained in chapter 6) before entering the RF-port of the mixer. Calling A_N the noise floor of the amplifier chain (including the mixer) , the equivalent of Eq. (8.2) for a microwave interferometer that is not shot-noise limited because of this

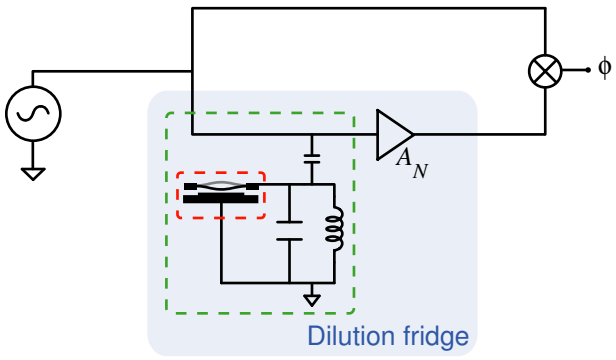

Figure 8.6: Simplified diagram of measurement setup. We detect the motion of the oscillator with a microwave analog of a Mach-Zehnder interferometer. A microwave tone is split and injected into the two arms of the interferometer. One arm forms the phase reference (LO of an IQ-mixer), and the other arm contains the cavity optomechanical system shown as an LC-microwave resonant circuit with an embedded nanomechanical oscillator. Displacement of the oscillator changes the capacitance of the electrical circuit and therefore its resonance frequency, Eq. (8.12). The microwave tone excites the circuit and acquires a phase shift proportional to the mechanical motion. That phase-modulated microwave signal is first amplified by a chain of microwave amplifiers and then mixed with the phase reference.

extra added noise A_N is

$$S_{x,x}^{\mathrm{imp}} = \frac{A_N + 1/2}{P_{\mathrm{in}}/(\hbar\omega_c)} \frac{1}{(\partial\phi/\partial x)^2} \tag{8.14}$$

Although the sensors for the applications mentioned above are governed by classical physics, the imprint of quantum phenomena upon them can be readily seen in the laboratory if care is taken in preparing the mechanical oscillator in the ground state. As I said before, there is an ongoing effort in the field (and in our lab) to accomplish this endeavor. But, even if we were able to do it, in order to reach this quantum limit, the detector must be quantum limited. Here is where the use of a quantum-limited amplifier becomes necessary in experiments used at microwave frequencies. The signal that comes from the cavity is just a phase-modulated (PM) signal, and all we want to do is to measure it with the best sensitivity possible. Since, the signal consists of a linear combination of fourier frequencies around a carrier tone (Fig. 3.14), I have shown that the most efficient way to measure such a tone is by using a degenerate parametric

amplifier like the JPA. As long as the phase between the pump of the JPA and carrier of the PM-modulated signal is chosen appropriately, we could ideally amplify that signal with no added noise, and could recover the ideal case for the imprecision in Eq. (8.2).

8.3 Experimental results. Increasing the sensitivity and getting closer to a shot-noise limited detection.

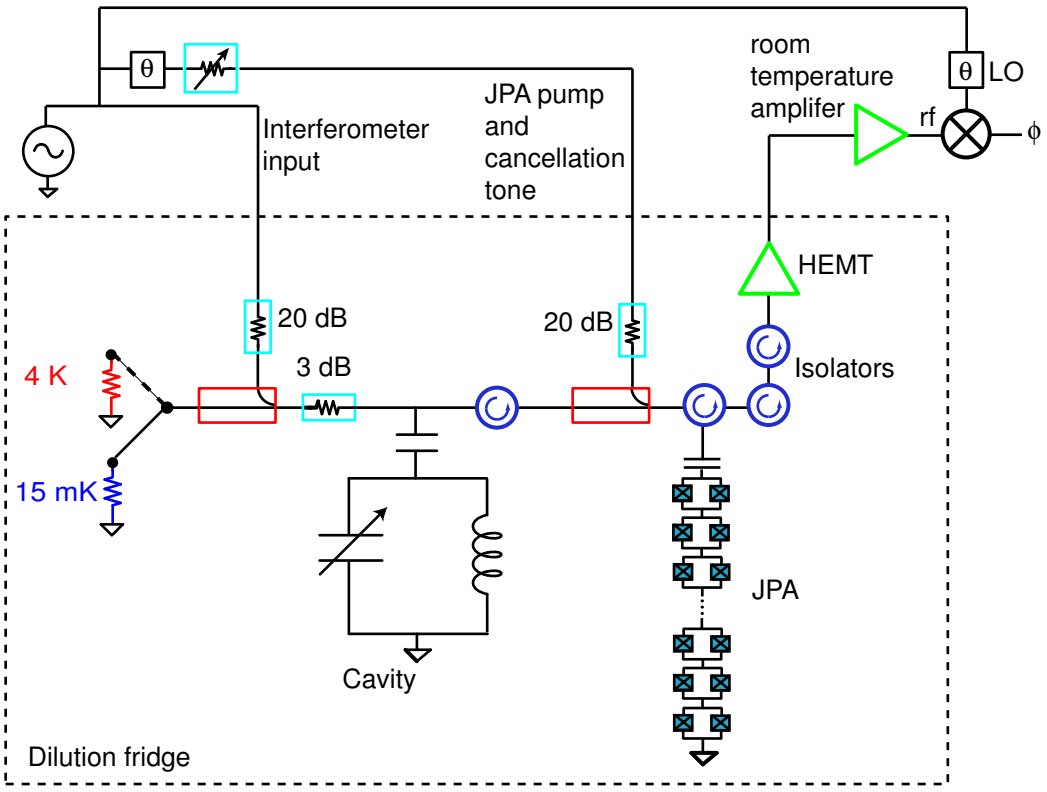

Figure 8.7: Detailed diagram of the measurement setup. A microwave generator is used to generate a tone that gets split into three main arms plus one carrier-cancelation arm. The first is used to excite a microwave cavity with a coupled nanomechanical oscillator. The second arm is used to pump the JPA and the third arm provides a phase reference for the mixer at room temperature. The carrier-cancelation arm is used to suppress the tone from the first arm in order to prevent saturation of the JPA. The setup for the Y-factor measurement (switch plus two terminations held at two different temperatures) is connected to the main port of the first directional coupler.

The detailed diagram of the setup used is shown in figure 8.7. A large microwave tone is used to probe the cavity, and only a fraction $(1 - S_0^2)$ is transmitted. The

transmitted power has the information regarding the motion of the nanomechanical oscillator in the form of phase modulation. Before reaching the JPA (a $\lambda/4$ resonator), a carrier-cancelation similar to that described in chapter 7 needs to be done in order to prevent saturation of the JPA. Once the carrier-cancelation is performed, the JPA pump phase is chosen appropriately so that the phase-modulation information is amplified. The gain of the JPA was chosen close to $G_s(0) = 14$ dB, or equivalently, a quadrature gain 6 dB higher, $G_{X_1} = 20$ dB (higher gains were used for some measurements but a proper carrier cancelation was too hard to achieve for the highest incident power on the cavity-optomechanics system). After the JPA, the measurement setup is similar to the one described in section chapter 6. The amplified signal emerging form the cryostat is down-converted using an IQ-mixer (as a homodyne detector, $\omega_c = \omega_p = \omega_{LO}$). We can convert voltage spectral density at the output of the mixer into spectral density of cavity fluctuations from the following expression,

$$S_{\omega_c}(\omega_m) = \frac{1 + 4\omega_m^2/\gamma_c^2}{(\partial V/\partial \omega_c)^2} S_{V,V}(\omega_m) \tag{8.15}$$

where the factor $1 + 4\omega_m^2/\gamma_c^2$ is included to account for the fact that since $\omega_m/\gamma_c \sim \mathcal{O}(1)$, the cavity field cannot respond instantaneously to the changes in ω_c due to the mechanical-motion of the nanowire. Hence, the frequency fluctuations $S_{\omega_c}(\omega_m)$ are filtered by the Lorentzian response of the cavity, the filtering factor being $1/(1+4\omega_m^2/\gamma_c^2)$ [109]. The voltage V at the output of the mixer will be given by $V = V_0 \mathrm{Im}(S_{21})$, where V_0 is a function of the incident power on the cavity as well as the attenuation and amplification through the whole signal path. It can be found by measuring the transmission $|S_{21}|$ far from resonance.

Once we know how to convert the voltage fluctuations at the output of the mixer into cavity frequency fluctuations, we can use the thermal motion of the nanowire (Eq. 8.10) to estimate the optomechanical coupling $g_c = \partial\omega_c/\partial x$ used in Eq. (8.1). This is shown in figure 8.8. The thermal sweep shown in figure 8.8b yields a value of $g_c =$

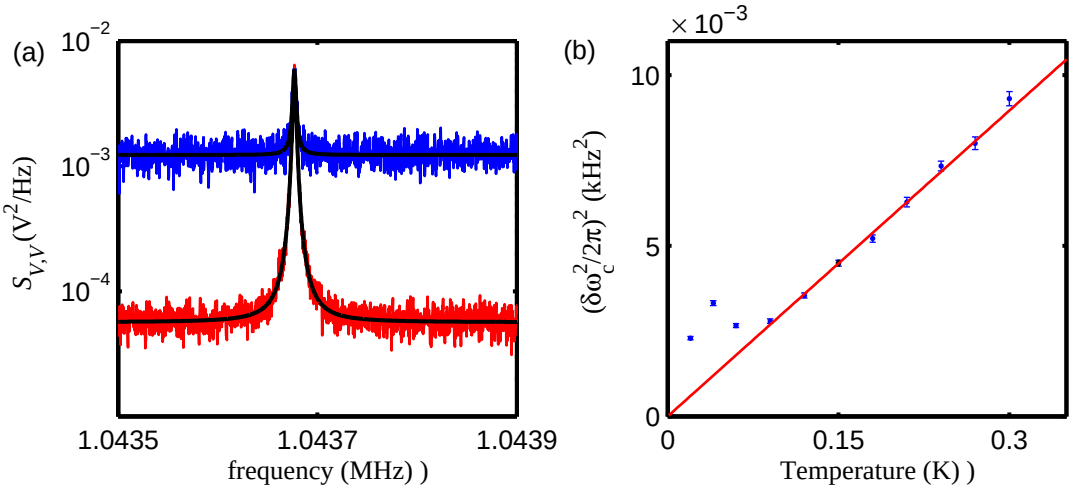

Figure 8.8: Fluctuations at the output of the mixer in arbitrary units (V^2/Hz) for a fridge temperature of $T = 0.150$ K. The red data was taken using the JPA and the blue only using the HEMT. By using the JPA, we observe an improvement in the sensitivity of over 13 dB with respect to the HEMT for similar incident powers. With Eqs. (8.10) and (8.15), we can calibrate the interferometer and convert the voltage fluctuations at the output of the mixer into fluctuations in the cavity's resonance frequency due to the thermal motion of the mechanical oscillator as shown in (b). From a linear fit to these fluctuations as they vary with temperature, we can determine the optomechanical coupling constant g_c. The lowest three temperature points are excluded from the fit as the mechanical mode is no longer in thermal equilibrium with the cryostat.

$2\pi \times 32 \pm 3$ kHz/nm. One thing to notice is that at the lowest temperature of the fridge, the beam is no longer in thermal equilibrium with the cryostat. Knowing the value of g_c will let us directly measure the temperature on the mode from the area under the Lorentzian curve in the displacement spectral density $S_{x,x}$. Also, it will help us determine the imprecision of the measurement. This can can be shown by using the expected dependance of ϕ from Eq (8.13). Then, Eq. (8.14) becomes [109]

$$S_{x,x}^{\text{imp}} = \frac{A_N + 1/2}{P_{\text{in}}/(\hbar\omega_c)} \left(\frac{S_0 \omega_c}{2Q(1-S_0)g_c} \right)^2 \left(1 + 4\omega_m^2/\gamma_c^2\right) \tag{8.16}$$

Eq. (8.16) demonstrates that the absolute imprecision is reduced by measuring with a larger power, a stronger coupling g_c and minimum added noise A_N.

However, even with the JPA, the microwave interferometer is not shot-noise limited. We estimate the noise-floor of the amplifier chain as explained in section 6.3.3

using a cryogenic switch that can toggle between two 50 Ω terminations held at two different temperatures. However, in order to accurately refer the noise to the output of the cavity, we need to measure the microwave loss. This is done by doing a thermal sweep and measuring the output noise of the mixer as a function of T_{fridge}, when the switch is connected to hot-load. The thermal sweep calibration is similar to the one used to estimate the microwave losses in the experiment explained in chapter 7, and it is explained in appendix B. We estimate that there is 6 dB of total loss between the switch and the JPA (that includes the 3 dB-attenuator placed at the output of the switch) of which 2 dB is between the cavity and the JPA, and 1.5 dB from the JPA to the HEMT. From a Y-factor measurement, we infer that the JPA adds $A_J = 0.3$ microwave quanta and that the HEMT adds $A_H = 24.5$ microwave quanta of noise. The effective added noise of the HEMT to our measurement is obtained by referring its noise number to the output of the cavity, that is by dividing its noise number A_H by G_{X_1} and multiplying by the loss between the the HEMT and the cavity output. Including all the losses, we estimate that the interferometer adds 1.16 microwave quanta of noise. Yet, in addition to the noise added by the amplifier chain, there is a small amount of thermal noise from the input signal. The signal line is attenuated by about 50 dB, reducing the larger room-temperature thermal noise to about 0.17 quanta on top of the vacuum noise. In total, we estimate the number of noise quanta added to be $A_N = 1.3$.

Once all the optomechanical-system and interferometer parameters have been determined, we can estimate the displacement fluctuations of the nanomechanical wire from the phase fluctuations at the output of the mixer. I display the main result of this chapter in figure 8.9a. There we demonstrate that this setup is capable of achieving $S_X^{\text{imp}} < S_X^{SQL}$. The minimum measured imprecision is $(0.8 \pm 0.03) \times S_X^{SQL}$, or 0.2 mechanical quanta. From the Lorentzian peak, we can infer the temperature of the wire's thermal motion, which corresponds to $T = 130$ mK, or thermal occupancy of $n_{th} = 2600$ mechanical quanta.

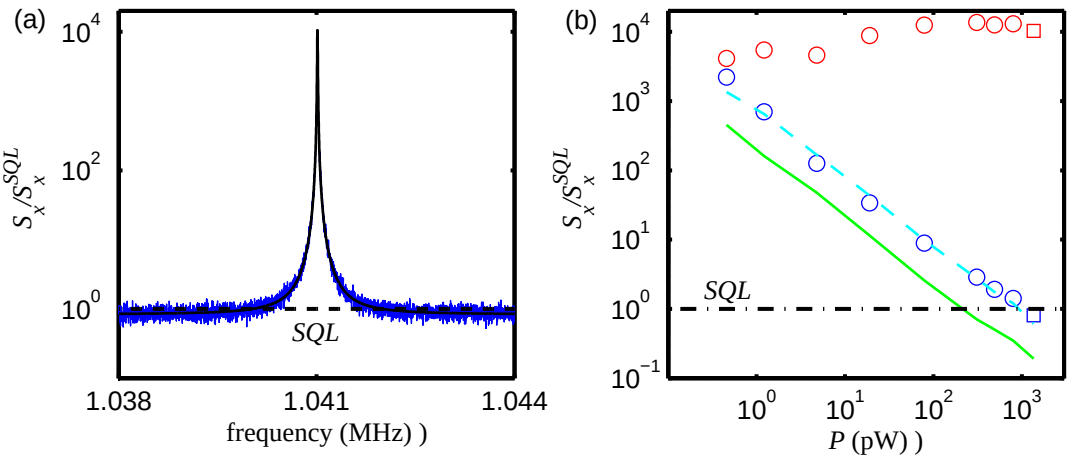

Figure 8.9: (a) Displacement sensitivity below that at the Standard Quantum Limit. The data shown is the spectral density of the displacement fluctuations $S_{x,x}$ in units $S_{x,x}^{\mathrm{SQL}}$ versus fourier frequency. In black, we show a fit to the Lorentzian thermal-response plus a frequency-independent background. This background represents the imprecision of our measurement, and lies below $S_{x,x}^{\mathrm{SQL}}$ (black dashed line). (b) Imprecision $S_{x,x}^{\mathrm{imp}}$ (blue circles) and total noise $S_{x,x}$ (red circles) in units of $S_{x,x}^{\mathrm{SQL}}$ as a function of incident microwave power at the resonator. The data points at the highest power shown as a square were extracted from the data shown in (a). The statistical error is smaller than the size of the symbols. Two theoretical predictions are shown, one for a shot-noise limited interferometer (solid-green) and for an interferometer with $A_N = 1.3$. This value was independently measured as explained in appendix B.

The quoted imprecision is estimated based on the measurement of the thermal motion of the wire. However, we can compare it with the predictions from Eq. 8.16 assuming an interferometer with $A_N = 1.3$. This is done in figure 8.9b, where we plotted our measured imprecision and the expected imprecision based on Eq. 8.16, for different incident powers. We also display the predictions for shot-noise-limited interferometer $A_N = 0$. Figure 8.9b shows that our model accurately predicts the observed imprecision. The predictions shown are not straight lines since they take into consideration changes in both the cavity and the mechanical oscillator parameters (γ_c and γ_m) as a higher incident power is applied. Also, the temperature of thermal motion of the wire increases with incident power. Therefore, a quantum efficient measurement which minimizes the power needed to reach a given imprecision is always desirable. To quantify how close we

are to a shot-noise limited interferometer, we can estimate the effective efficiency of the detector using Eq. (7.28) for $A_N = 1.3$. This gives an efficiency of $\eta = 0.28$, comparable to the one observed in chapter 7, for a similar JPA gain.

In conclusions, in this chapter I have shown the JPA can be used to boost the sensitivity in the detection of motion of a nanomechanical oscillator embedded in a microwave cavity. It has allowed us to get to the SQL by using a much lower power than if were only using the HEMT amplifier. The use of the JPA has also made our microwave interferometer only a factor of ~ 4 from being shot-noise limited.

Chapter 9

Conclusions and future directions.

In this thesis, I described our approach to develop an ultra-low noise microwave amplifier. Even though our results show great experimental progress, they also revealed areas that require further research. We achieved our overall goal of characterizing the performance of a new design of Josephson parametric amplifiers for a microwave signal. After the characterization, we used it for two specific applications: microwave homodyne tomography for quantum state reconstruction and improving the sensitivity of a microwave interferometer used in the detection of mechanical motion of a nanomechanical oscillator. In this chapter I will review some of the more interesting results presented in previous chapters and discuss the possible future directions for JPA in our lab.

9.1 Conclusions

Although the focus of the initial measurements of a microwave cavity with a series SQUID array as the center conductor of the transmission line was different, the experiments done with the first device were very encouraging. With our first JPA we demonstrated that a Josephson parametric amplifier based on a coplanar waveguide resonator whose inner conductor is made from a SQUID array could be operated with good performance and that it was tunable over a full octave of bandwidth. We observed gains as high as 28 dB and although the resonator is composed of discrete elements, its behavior is well described by a continuum theory of parametric amplification [38].

In this first experiment, we did not have a calibrated noise source that would allow us to estimate the added noise of the JPA. Nonetheless, compared to the measurement of a weak microwave signal using only a low-noise HEMT, we observed that the JPA was 16 dB more sensitive than a HEMT amplifier. From this improvement of the signal-to-noise ratio we estimated a total noise at the output of the JPA referred to the input of slightly less than 1 quanta of noise, suggesting that the JPA added an amount of noise comparable to the vacuum noise. One very important difference with previous implementations was that in our case we were able to operate the JPA with high enough gain that the very small amount of noise at its input, after amplification, overwhelmed the noise of the following amplifier chain. Therefore, the JPA set the noise-floor of the measurement.

This first device showed very promising performance, but also some problems, specifically some strange behavior in the magnetic-field dependance of the resonance frequency. It also had very low power-handling capacity, which was good enough for some applications (for example for amplifying the signals generated by superconducting qubits), but not for some of the applications we were intended to use it for. Also, its gain-bandwidth product was rather small. Hence, we decided to modify the design to increase both the power-handling capacity and the bandwidth. In the second implementation of this amplifier we used niobium instead of aluminum for the superconducting resonant structure as well as a larger SQUID current. The coupling quality factor Q was also increased by a factor of 10. All these changes increased the critical powers, and hence the power-handling capacity, by about 20 dB. For this new design, we collaborated with Kent Irwin's group at NIST. The fabrication of these devices was done using a more industrial-like procedure, which would give us a more homogeneous array of SQUIDs, hoping to avoid issues such as the non-ideal magnetic-field dependance of the first resonator.

We tested two different kinds of niobium JPAs. A quarter-wavelength and an

asymmetrically-coupled half-wavelength resonator. With these new devices, we also implemented a setup to measure the added noise of the JPA by using a microwave switch that could toggle between two noise sources (50 Ω resistors) held at two different temperatures. From these noise measurements, we estimated that the added noise of the amplifier was as low as 0.23 quanta. This is a very important result as it makes these JPA the lowest-noise microwave amplifiers ever reported. Again, we were able to operate the amplifier with high gains (G_s as high as 40 dB) and set the noise floor of the measurement. The larger critical powers also gave us a better power-handling capacity. The amplifier showed at 8 GHz a 1-dB compression point of -130 dBm with a gain of 27 dB. We also tested their squeezing performance: being a degenerate parametric amplifiers, the JPA can amplify one quadrature with less added noise than that of a quantum-limited amplifier, while it squeezes the fluctuations at the other quadrature. We measured squeezing of noise of as much as 10 dB.

Once we characterized the performance of the JPA we decided it was possible to use it for two particular applications. For most measurements, the low added noise of the JPA is helpful, but for some measurements it is crucial. For example, to fully characterize the quantum state of non-Gaussian states, such as the Fock states generated by superconducting qubits [110], a subquantum limited amplifier is a necessity [111]. Hence, we decided to use the JPA to implement what, in optics, is called homodyne-tomography for the Wigner function reconstruction of quantum-states of light. In our case, those quantum states were squeezed states generated by a second JPA. Using the JPA as an integral part of microwave homodyne tomography lead to a dramatic increase of the performance of the Quantum State Tomography. It has enabled us to reconstruct the Wigner function of a squeezed state of the microwave field and observe real squeezing of the input noise of 37%, compared to the 2% real squeezing observed using only the HEMT amplifier. In this case, the quantum efficiency of the state tomography detector was 38%.

In addition to characterizing non-Gaussian states of microwave fields, the JPA is also well suited to amplifying the signal generated by a nanomechanical beam moving in a microwave cavity [11], enabling a quantum-limited measurement of position, which lead us to the second application I discussed in this thesis. Here, I presented displacement measurements of a nanomechanical oscillator with an imprecision below that at the standard quantum limit. We infer the motion from the phase modulation imprinted on a microwave signal by that motion. The modulation is enhanced by embedding the oscillator in a high-Q microwave cavity. We achieve the low imprecision by reading out the modulation using a JPA, realizing a microwave interferometer that operates near the shot-noise limit. The apparent motion of the mechanical oscillator, due to the interferometer's noise, is now less than its zero-point motion, making future detection of quantum states feasible. In addition, the phase sensitivity of the demonstrated interferometer is 30 times higher than previous microwave interferometers, providing a critical piece of technology for many experiments investigating quantum information encoded in microwave fields.

9.2 Future directions

Although the good performance of the JPAs described here have let us improve the detection of squeezed states and the detection of mechanical motion, we still need to improve certain things about the setup in general. First, the amplifiers added noise is higher from what we would expect from a model that only includes loss as the contributor of added noise. The 0.23 quanta of added noise already sets the maximum efficiency of a homodyne detector using these amplifiers at about 70%. As we do not know where this extra added noise is coming from, it is hard to decide what the next step is. However, since we have had some yielding problems during fabrication, one obvious step would be to reduce the number of SQUIDs in the resonator as shown in figure 9.1. This would mostly affect the range of tuning for the resonance frequency.

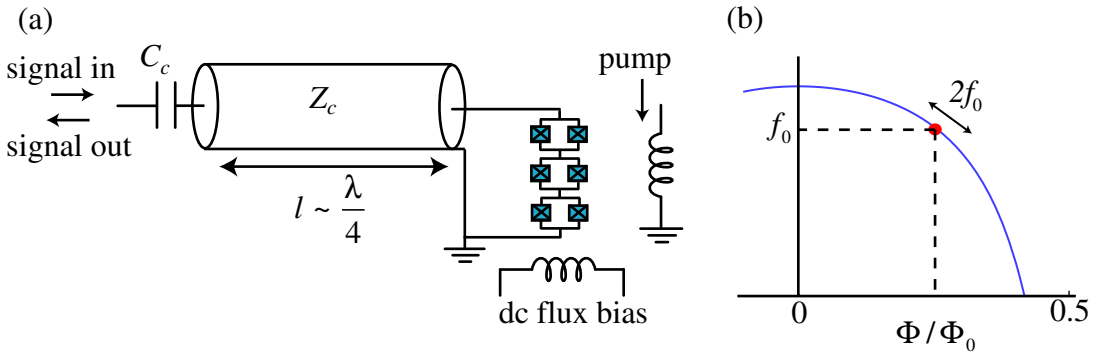

Figure 9.1: (a) In our new devices, we reduce the number of SQUIDs to increase the yield of devices per wafer. (b) In these new devices, we will study the possibility of implementing a 3-photon mode parametric amplifier, applying the pump as a 2-ω tone on the magnetic flux line, in order to eliminate the necessity of doing carrier-cancelation when multiple JPAs are used.

However, for the applications we are planning on doing, we do not need a full octave of tuning. Treating the small SQUID-array as a lumped element [48], in this case the change in resonance frequency comes from a change in the boundary-condition of the resonator rather than from a change in the phase velocity of the metamaterial [72, 73]. Another point our group will study is the possibility of implementing a three-photon mode Josephson parametric amplifier by using the magnetic-coupling line to apply a microwave pump close to twice the resonance frequency of the resonator [59]. The main reason to attempt this is that although the carrier cancelation works, it would be rather hard to implement it when more than two JPAs are used. This will be the case in the future experiments our group is planing on doing for certain quantum communication protocols.

Another issue we want to eliminate is the low-frequency noise observed in these amplifiers (Fig. 6.33c). One hypothesis is that it consists of current noise present in any closed-loop of metal (like for example the circular walls of the sample box), which inductively couples noise to the SQUID loop. One way to test this hypothesis is to use dc-SQUID gradiometers (Fig. 9.2). In the gradiometer configurations shown in figure

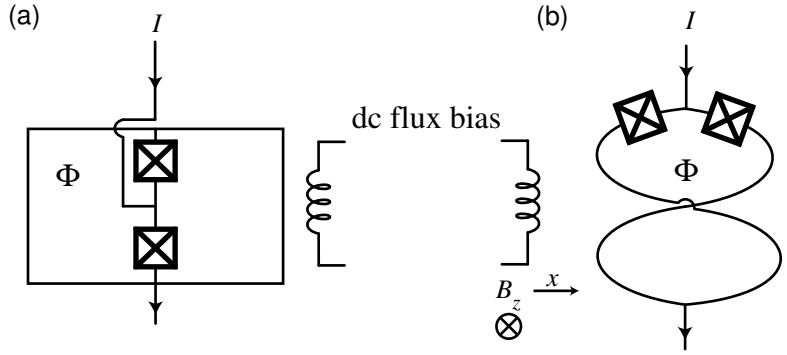

Figure 9.2: One strategy we will implement to reduce the low-frequency noise observed in the JPA is to use dc-SQUID gradiometers. (a) Parallel and (b) series gradiometer. Due to their geometry they will not couple to space-homogeneous magnetic fields but rather to the first derivative $\partial B_z/\partial x$ of the field.

9.2, the dc-SQUIDs would not couple to space-homogeneous magnetic fields, but rather to the first derivative $\partial B_z/\partial x$. If our hypothesis is right, we should see a significant reduction of the low-frequency noise. The only disadvantage of using gradiometers is that, due to the more complicated fabrications, they tend to be larger and hence have larger loop-inductance, limiting the suppression of the supercurrent and hence the tuning of the effective Josephson inductance. However, as I said before, the amount of resonance frequency tuning we are trying to achieve is much less than the one obtained in the devices described in this thesis.

Another modification in the setup is to use a better calibration. Due to the unknown losses in the microwave components at 4.1 K that are used to toggle between the two calibrated noise sources, the uncertainty in the added noise is too large. If we want to really nail down the origin of the extra added noise observed we need to reduce this uncertainty. For that we are planing on implementing a varying temperature resistor which is thermally weakly coupled to the fridge using a superconducting coaxial cable. By removing the need of going back and forth between the 4K plate and mixing chamber plate, we will be able to reduce the uncertainty in the losses between the noise source and the JPA.

Thinking ahead in terms of applications for degenerate parametric amplifiers, our group is planing on using the squeezed states at the output of the JPA as building blocks for quantum information experiments. These states, which are highly non-classical, form EinsteinPodolskyRosen (EPR)-states when combined together and thus are the basis of a complete quantum information processing strategy, known as Continuous Variables Quantum Information [112]. Quantum information processing aims to exploit entanglement, the unique feature of quantum mechanics, to enhance our abilities for communication and computation. In the strategy of continuous-variables quantum information processing, an entangled state of the electromagnetic field, can be generated by combining two squeezed states on a beam splitter. In this thesis, I showed that we have the ability to generate squeezed states at microwave frequencies using a Josephson Parametric Amplifier. However, generating EPR states is more demanding. Passive elements, like directional couplers and 90-degree-hybrid couplers using superconducting elements have to be developed such that they can be integrated on the same chip as the JPA, as the loss in the coaxial cables and commercial microwave components can really degrade the entanglement. Our group is also starting to test these passive components' performance (Fig. 9.3).

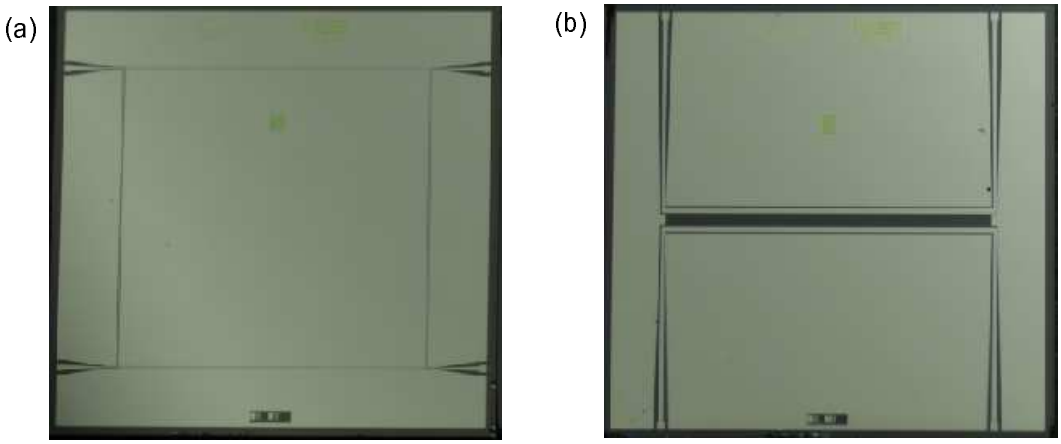

Figure 9.3: Passive microwave components being developed by our group for applications in continuous-variables quantum information processing. (a) 90-degree-hybrid coupler and (b) directional coupler.

Bibliography

[1] Haus, H. A. and Mullen, J. A. Phys. Rev. **128**(5), 2407–2413 Dec (1962).

[2] Caves, C. M. Phys. Rev. D **26**(8), 1817–1839 Oct (1982).

[3] Clerk, A. A., Devoret, M. H., Girving, S. M., Marquardt, F., and Schoelkopf, R. J. Review of Modern Physics (Accepted), (2008).

[4] Stenholm, S. Annals of Physics **218**, 233–254 (1992).

[5] Takahasi, H. Adv. Comm. Syst. **1**, 227 (1965).

[6] Movshovich, R., Yurke, B., Kaminsky, P. G., Smith, A. D., Silver, A. H., Simon, R. W., and Schneider, M. V. Phys. Rev. Lett. **65**(12), 1419–1422 Sep (1990).

[7] Yurke, B., Kaminsky, P. G., Miller, R. E., Whittaker, E. A., Smith, A. D., Silver, A. H., and Simon, R. W. Phys. Rev. Lett. **60**(9), 764–767 Feb (1988).

[8] Yurke, B., Corruccini, L. R., Kaminsky, P. G., Rupp, L., Smith, A., Silver, A. H., Simon, R. W., and Whittaker, E. A. Physical Review A **39**, 2519–2535 (1989).

[9] Wallraff, A., Schuster, D. I., Frunzio, A. B. L., Huang, R.-S., Majer, J., Kumar, S., Girvin, S. M., and Schoelkopf, R. J. Nature **431**, 162 (2004).

[10] Schuster, D. I., Houck, A. A., Schreier, J. A., Wallraff, A., Gambetta, J. M., Blais, A., Frunzio, L., Majer, J., Johnson, B., Devoret, M. H., Girvin, S. M., and Schoelkopf, R. J. Nature **445**, 515 (2007).

[11] Regal, C. A., Teufel, J. D., and Lehnert, K. W. Nat Phys **4**, 555–560 (2008).

[12] Devoret, M. H. In Les Houches, Session LXIII, Renaud, S., Giacobino, E., and Zinn-Justin, J., editors, 351–386. Elsevier Science, (1995).

[13] Louisell, W. H. Coupled mode and parametric electronics. John Wiley & Sons, Inc., (1960).

[14] Louisell, W. H. Radiation and Noise in Quantum Electronics. MacGraw Hill, (1964).

[15] Yurke, B. and Denker, J. S. Physical Review A **29**, 1419–1437 (1984).

[16] Pozar, D. M. Microwave Engineering. John Wiley & Sons, Inc., second edition, (1998).

[17] Yurke, B. Quantum Squeezing, chapter 3, Input Output Theory, 53–96. Springer (2004).

[18] Vijayaraghavan, R. Josephson Bifurcation Amplifier: Amplifiying quantum signals using a dynamical bifurcation. PhD thesis, Yale University, (2008).

[19] Nyquist, H. Phys. Rev. **32**(1), 110–113 Jul (1928).

[20] Caldeira, A. O. and Leggett, A. J. Annals of Physics **149**(2), 374 – 456 (1983).

[21] Courty, J.-M., Grassia, F., and Reynaud, S. arXiv:quant-ph/0110021v1.

[22] Walls, D. and Milburn, G. Quantum Optics, chapter 7, 121–136. Springer (1994).

[23] Gardiner, C. W. and Collett, M. J. Phys. Rev. A **31**(6), 3761–3774 Jun (1985).

[24] Collett, M. J. and Gardiner, C. W. Phys. Rev. A **30**(3), 1386–1391 Sep (1984).

[25] Collett, M. J. and Walls, D. F. Phys. Rev. Lett. **61**(21), 2442–2444 Nov (1988).

[26] Gerry, C. C. and Knight, P. L. Introductory Quantum Optics. Cambridge University Press, (2006).

[27] Yamamoto, Y. and Mukai, T. Optical and Quantum Electronics **21**, S1–S14 (1989).

[28] Leonhardt, U. and Paul, H. Progress in Quantum Electronics **19**, 89–130 (1995).

[29] Enns, R. H. and McGuire., G. C. Nonlinear Physics with Mathematica for Scientist and Engineers, chapter 8, 293–353. Birkhauser (2001).

[30] Novak, S. and Frehlich, R. G. Phys. Rev. A **26**(6), 3660–3663 Dec (1982).

[31] Manucharyan, V. E., Boaknin, E., Metcalfe, M., Vijay, R., Siddiqi, I., and Devoret, M. Physical Review B (Condensed Matter and Materials Physics) **76**(1), 014524 (2007).

[32] Josephson, B. D. Rev. Mod. Phys. **36**(1), 216–220 Jan (1964).

[33] Duzer, T. V. and Turner, C. W. Superconductive Devices and Circuits. Prentice Hall, Inc., (1998).

[34] Feldman, M. J., Parrish, P. T., and Chiao, R. Y. Journal of Applied Physics **46**(9), 4031–4042 (1975).

[35] Barone, A. Physics and applications of the Josephson effect. Wiley-Interscience, (1982).

[36] Landau, L. D. and Lifshitz, E. M. Mechanics, chapter 5, 58–95. Butterworth Heinemann (2000).

[37] Yurke, B. J. Opt. Soc. Am. B **4**, 1551–1557 (1987).

[38] Yurke, B. and Buks, E. Lightwave Technology, Journal of **24**(12), 5054–5066 Dec. (2006).

[39] Babourina-Brooks, E., Doherty, A., and Milburn, G. J. New Journal of Physics **10**(10), 105020 (14pp) (2008).

[40] Milburn, G. and Walls, D. F. Optics Communications **39**, 401–404 (1981).

[41] Yurke, B. Phys. Rev. A **29**(1), 408–410 Jan (1984).

[42] Smith, A. D., Sandell, R. D., Burch, J. F., and Silver, A. H. IEEE Transactions on Magnetics **21**, 1022–1028 (1985).

[43] Mygind, J., Pedersen, N. F., Soerensen, O. H., Dueholm, B., and Levinsen, M. T. Applied Physics Letters **35**(1), 91–93 (1979).

[44] Feldman, M. J. and Levinsen, M. T. IEEE Transactions on Magnetics **17**, 834–837 (1981).

[45] Feldman, M. J. and Levinsen, M. T. Applied Physics Letters **36**(10), 854–856 (1980).

[46] Parrish, P. T. and Chiao, R. Y. Applied Physics Letters **25**(10), 627–629 (1974).

[47] Feldman, M. J. Journal of Applied Physics **48**(3), 1301–1310 (1977).

[48] Wahlsten, S., Rudner, S., and Claeson, T. Journal of Applied Physics **49**(7), 4248–4263 (1978).

[49] Huberman, B. A., Crutchfield, J. P., and Packard, N. H. Applied Physics Letters **37**(8), 750–752 (1980).

[50] Pedersen, N. F. and Davidson, A. Applied Physics Letters **39**(10), 830–832 (1981).

[51] Chiao, R. Y., Feldman, M. J., Peterson, D. W., Tucker, B. A., and Levinsen, M. T. AIP Conference Proceedings **44**(1), 259–263 (1978).

[52] Miracky, R. F. and Clarke, J. Applied Physics Letters **43**(5), 508–510 (1983).

[53] Bryant, P., Wiesenfeld, K., and McNamara, B. Journal of Applied Physics **62**(7), 2898–2913 (1987).

[54] Bryant, P. H., Movshovich, R., and Yurke, B. Phys. Rev. Lett. **66**(20), 2641–2644 May (1991).

[55] Calander, N., Claeson, T., and Rudner, S. Journal of Applied Physics **53**(7), 5093–5103 (1982).

[56] Sweeny, M. and Mahler, R. IEEE Transactions on Magnetics **21**, 654–655 (1985).

[57] Yurke, B., Roukes, M. L., Movshovich, R., and Pargellis, A. N. Applied Physics Letters **69**(20), 3078–3080 (1996).

[58] Bergeal, N., Vijay, R., Manucharyan, V. E., Siddiqi, I., Schoelkopf, R. J., Girvin, S. M., and Devoret, M. H. arXiv:0805.3452v1.

[59] Yamamoto, T., Inomata, K., Watanabe, M., Matsuba, K., Miyazaki, T., Oliver, W. D., Nakamura, Y., and Tsai, J. S. Applied Physics Letters **93**(4), 042510 (2008).

[60] Abdo, B., Suchoi, O., Segev, E., Shtempluck, O., Blencowe, M., and Buks, E. EPL (Europhysics Letters) **85**(6), 68001 (6pp) (2009).

[61] Siddiqi, I., Vijay, R., Pierre, F., Wilson, C. M., Metcalfe, M., Rigetti, C., Frunzio, L., and Devoret, M. H. Phys. Rev. Lett. **93**(20), 207002 Nov (2004).

[62] Siddiqi, I., Vijay, R., Pierre, F., Wilson, C. M., Frunzio, L., Metcalfe, M., Rigetti, C., Schoelkopf, R. J., Devoret, M. H., Vion, D., and Esteve, D. Phys. Rev. Lett. **94**(2), 027005 Jan (2005).

[63] Tholén, E. A., Ergül, A., Stannigel, K., Hutter, C., and Haviland, D. B. arXiv:0906.2744v1.

[64] Dahm, T. and Scalapino, D. J. Journal of Applied Physics **81**(4), 2002–2009 (1997).

[65] Tholén, E. A., Ergül, A., Doherty, E. M., Weber, F. M., Grégis, F., and Haviland, D. B. Applied Physics Letters **90**(25), 253509 (2007).

[66] Likharev, K. K. Rev. Mod. Phys. **51**(1), 101–159 Jan (1979).

[67] Gupta, K., Garga, R., Bahl, I. J., Garg, R., and Bhartia, P. Microstrip Lines and Slotlines 2nd Ed. Artech House Antennas and Propagation Library, (1996).

[68] Stan, G., Field, S. B., and Martinis, J. M. Phys. Rev. Lett. **92**(9), 097003 Mar (2004).

[69] Mazin, B. A. Microwave Kinetic Inductance Detectors. PhD thesis, California Institute of Technology, (2004).

[70] Lehnert, K., Irwin, K., Castellanos-Beltran, M., Mates, J., and Vale, L. Applied Superconductivity, IEEE Transactions on **17**(2), 705–709 June (2007).

[71] Metcalfe, M., Boaknin, E., Manucharyan, V., Vijay, R., Siddiqi, I., Rigetti, C., Frunzio, L., Schoelkopf, R. J., and Devoret, M. H. Physical Review B (Condensed Matter and Materials Physics) **76**(17), 174516 (2007).

[72] Sandberg, M., Wilson, C. M., Persson, F., Johansson, G., Shumeiko, V., Bauch, T., Duty, T., and Delsing, P. volume 1074, 12–21. AIP, (2008).

[73] Palacios-Laloy, A., Nguyen, F., Mallet, F., Bertet, P., Vion, D., and Esteve, D. Journal of Low Temperature Physics **151**, 1573–7357 (2008).

[74] Haviland, D. B. and Delsing, P. Phys. Rev. B **54**(10), 6857 Sep (1996).

[75] Wallquist, M., Shumeiko, V., and Wendin, G. arXiv:cond-mat/0608209v2.

[76] Leonhardt, U. Measuring the Quantum State of Light. Cambridge University Press, (1993).

[77] Leonhardt, U. Phys. Rev. A **48**(4), 3265–3277 Oct (1993).

[78] Martinis, J. M., Cooper, K. B., McDermott, R., Steffen, M., Ansmann, M., Osborn, K. D., Cicak, K., Oh, S., Pappas, D. P., Simmonds, R. W., and Yu, C. C. Phys. Rev. Lett. **95**(21), 210503 Nov (2005).

[79] Teufel, J. D. and Donner, U. T.

[80] Teufel, J. D. Superconducting Tunnel Junctions as Direct Detectors for Submillimeter Astronomy. PhD thesis, Yale University, (2008).

[81] Agilent. Agilent E8257D PSG Microwave Analog Signal Generator.

[82] Martinis, J. M., Devoret, M. H., and Clarke, J. Phys. Rev. B **35**(10), 4682–4698 Apr (1987).

[83] Gao, J. The Physics of Superconducting Microwave Resonators. PhD thesis, California Institute of Technology, (2008).

[84] Yurke, B. Phys. Rev. A **32**(1), 300–310 Jul (1985).

[85] Yurke, B. Phys. Rev. A **32**(1), 311–323 Jul (1985).

[86] Kamal, A., Marblestone, A., and Devoret, M. Physical Review B (Condensed Matter and Materials Physics) **79**(18), 184301 (2009).

[87] Dolan, G. J. Applied Physics Letters **31**(5), 337–339 (1977).

[88] Sauvageau, J., Burroughs, C., Booi, P., Cromar, M., Benz, R., and Koch, J. Applied Superconductivity, IEEE Transactions on **5**(2), 2303–2309 Jun (1995).

[89] Mates, J. A. B., Hilton, G. C., Irwin, K. D., Vale, L. R., and Lehnert, K. W. Appl. Phys. Lett. **92**(2), 023514 (2008).

[90] Castellanos-Beltran, M. A., Irwin, K., Vale, L., Hilton, G., and Lehnert, K. Applied Superconductivity, IEEE Transactions on **19**(3), 944–947 June (2009).

[91] Castellanos-Beltran, M. A. and Lehnert, K. W. Applied Physics Letters **91**(8), 083509 (2007).

[92] Castellanos-Beltran, M. A., Irwin, K. D., Hilton, G. C., Vale, L. R., and Lehnert, K. W. Nat Phys **4**, 929–931 (2008).

[93] Wigner, E. Phys. Rev. **40**(5), 749–759 Jun (1932).

[94] Bertrand, J. and Bertrand, P. Foundations of Physics **17**, 397–405 (1987).

[95] Case, W. B. American Journal of Physics **76**(10), 937–946 (2008).

[96] Vogel, K. and Risken, H. Phys. Rev. A **40**(5), 2847–2849 Sep (1989).

[97] Smithey, D. T., Beck, M., Raymer, M. G., and Faridani, A. Phys. Rev. Lett. **70**(9), 1244–1247 Mar (1993).

[98] Beck, M., Smithey, D. T., and Raymer, M. G. Phys. Rev. A **48**(2), R890–R893 Aug (1993).

[99] Yuen, H. P. and Chan, V. W. S. Opt. Lett. **8**(3), 177–179 (1983).

[100] Dicke, R. H. Review of Scientific Instruments **17**(7), 268–275 (1946).

[101] Kak, A. C. and Slaney, M. Principles of Computerized Tomographic Imaging. IEEE Press, (1988).

[102] Leonhardt, U. Phys. Rev. A **49**(2), 1231–1242 Feb (1994).

[103] Furusawa, A., Sorensen, J. L., Braunstein, S. L., Fuchs, C. A., Kimble, H. J., and Polzik, E. S. Science **282**, 706–709 (1998).

[104] Teufel, J. D., Donner, T., Castellanos-Beltran, M. A., Harlow, J. W., and Lehnert, K. W. Nature Nanotechnology **4**(1), 820–823 Dec (2009).

[105] Kippenberg, T. J. and Vahala, K. J. SCIENCE **321**, 1172–1176 (2008).

[106] Braginsky, V. B. and Khalili, F. Y. Quantum Measurement. Cambridge University Press, (1992).

[107] Teufel, J. D., Regal, C. A., and Lehnert, K. W. New Journal of Physics **10**(9), 095002 (2008).

[108] Teufel, J. D., Harlow, J. W., Regal, C. A., and Lehnert, K. W. Phys. Rev. Lett. **101**(19), 197203 Nov (2008).

[109] Regal, C. Corrected notes on beam in cavity calculations, March 2007 (Unpublished), (2007).

[110] Houck, A. A., Schuster, D. I., Gambetta, J. M., Schreier, J. A., Johnson, B. R., Chow, J. M., Frunzio, L., Majer, J., Devoret, M. H., Girvin, S. M., and Schoelkopf, R. J. Nature(London) **449**(328), 328–331 (2007).

[111] Yurke, B. and Stoler, D. Phys. Rev. Lett. **57**(1), 13–16 Jul (1986).

[112] Braunstein, S. L. and van Loock, P. Rev. Mod. Phys. **77**(2), 513–577 Jun (2005).

[113] Caves, C. M. and Schumaker, B. L. Phys. Rev. A **31**(5), 3068–3092 May (1985).

Appendix A

Multimode fields

In this appendix we discuss the broadband analysis of signals and the necessary corrections on the single-mode analysis done in chapter 2. These correction will set new limits on amplification and squeezing of vacuum noise. For a more in-depth explanation of the results quoted here, I refer the reader to Refs. [2, 84, 112, 113].

A.1 Multimode signals

The idea is to find the corrections to the single-mode analysis which results from the nonzero bandwidth that any real signal and real amplifier have. In general, the input and output mode frequencies do not have to be the same. However, in our experiments this is usually the case so I will not make a distinction between the input and output mode frequencies. Consider a broadband signal whose voltage, according to Eq. (2.39) can be expressed as

$$V(t) = V_0 \int_{B_\omega} \frac{d\omega'}{2\pi} \sqrt{\omega'} [a(\omega') e^{-i\omega' t} + a^\dagger(\omega') e^{i\omega' t}] \tag{A.1}$$

where I assume $\omega' > 0$ only. The limits of the integral are labeled by B_ω which represents the bandwidth of integration of the measuring instrument used. Here the annihilation and creation operators (now, no longer dimensionless but each in units of root of time, $\sqrt{t}$) satisfy the commutation relation given by Eqs. (2.23) and (2.24):

$$[a(\omega'), a^\dagger(\omega'')] = 2\pi\delta(\omega' - \omega'')$$

and

$$[a(\omega'), a(\omega'')] = 0.$$

I assume that associated with the signal, there is a carrier with frequency ω_0. The carrier frequency ω_0 is essentially some preferred frequency, say the pump of a degenerate Josephson parametric amplifier, or the local oscillator of a homodyne detector (a mixer). The quadrature phases are to be defined relative to this frequency. The quadrature operators $X_1(t)$ and $X_2(t)$ of the field amplitude components can be introduced by writing our expression for the input signal $V(t)$ in the follwing form

$$V(t) = 2\sqrt{\omega_0}V_0 \left[X_1(t)\cos(\omega_0 t) + X_2(t)\sin(\omega_0 t)\right]. \tag{A.2}$$

Using Eqs. (A.1) and (A.2), we obtain explicit expression for the quadrature operators $X_1(t)$ and $X_2(t)$ deriving what essentially is a continuum generalization of the quadrature operators

$$X_1(t) = \int_{B_\omega} \frac{d\omega}{2\pi}\frac{1}{2}\sqrt{\frac{\omega_0+\omega}{\omega_0}}[a(\omega_0+\omega)e^{i\omega t} + \text{H.c.}] \tag{A.3}$$

$$X_2(t) = \int_{B_\omega} \frac{d\omega}{2\pi}\frac{1}{2}\sqrt{\frac{\omega_0+\omega}{\omega_0}}[-ia(\omega_0+\omega)e^{i\omega t} + \text{H.c.}] \tag{A.4}$$

where now the fields are described as functions of the modulation frequency ω which consists of an offset frequency respect to ω_0, $\omega' = \omega_0 \pm \omega$. The previous expressions can be simplified significantly in the case where the bandwidth of the signal is symmetric about ω_0, and if we also define the operators in the rotating frame about the central frequency ω_0 as it was done in section 2.3.2:

$$b(t) = a(t)e^{i\omega_0 t}.$$

We use the following definition of the fourier transform

$$b(\omega) = \frac{1}{2\pi}\int dt b(t)e^{i\omega t}.$$

In this case, the rotating frame operators follow the commutation relation

$$[b(\omega), b^\dagger(\omega')] = 2\pi\delta(\omega-\omega')$$

Based on the steps described above, we obtain from Eqs. (A.3) and (A.4)

$$X_1(t) = \int_0^{B_\omega/2} \frac{d\omega}{2\pi}[X_1(\omega)e^{-i\omega t} + \text{H.c.}] \tag{A.5}$$

$$X_2(t) = \int_0^{B_\omega/2} \frac{d\omega}{2\pi}[X_2(\omega)e^{-i\omega t} + \text{H.c.}] \tag{A.6}$$

where

$$X_1(\omega) = \frac{1}{2}\left[\sqrt{\frac{\omega_0+\omega}{\omega_0}}b(\omega) + \sqrt{\frac{\omega_0-\omega}{\omega_0}}b^\dagger(-\omega)\right] \tag{A.7}$$

$$X_2(\omega) = \frac{1}{2i}\left[\sqrt{\frac{\omega_0+\omega}{\omega_0}}b(\omega) - \sqrt{\frac{\omega_0-\omega}{\omega_0}}b^\dagger(-\omega)\right] \tag{A.8}$$

Eqs. (A.5-A.8) are the multimode generalization of the single-mode quadrature operators, Eq. (2.73). The generalization to a rotated-quadrature operator $X_\theta(\omega)$ is similar to the single-mode quadrature, Eq. (2.86)

$$X_\theta(\omega) = \frac{1}{2}\left[\sqrt{\frac{\omega_0+\omega}{\omega_0}}b(\omega)e^{i\theta} + \sqrt{\frac{\omega_0-\omega}{\omega_0}}b^\dagger(-\omega)e^{-i\theta}\right] \tag{A.9}$$

where it is easy to show that $X_1 = X_{\theta=0}$ and $X_2 = X_{\theta=-\pi/2}$.

Although the multimode generalization $X_1(t)$ and $X_2(t)$ can have reduced fluctuations (squeezing) just like in the single-mode case, it can be shown [2] that those fluctuations cannot be reduced to zero as in the single-mode case. There are also corrections to the minimum amount of of the noise that a linear amplifier adds, which are bandwidth dependant and emerge naturally from the multimode analysis. These new limits and corrections can be inferred by calculating the spectral density for the fluctuations of the quadratures $S_{X_i,X_i}(\omega)$ $(i = 1, 2)$ of the mean-square fluctuations of $X_i(t)$ from

$$\langle\{X_i(\omega), X_i^\dagger(\omega')\}\rangle = 2\pi S_{X_i,X_i}(\omega)\delta(\omega-\omega') \tag{A.10}$$

where we are using a single-sided spectral density convention. Then, it can be shown that

$$S_{X_i,X_i}(\omega) \geq \frac{1}{2}\frac{\omega}{\omega_0} \tag{A.11}$$

Eq. (A.11) is the limit I mentioned, and it will be the origin of the new limits on added noise for a phase-sensitive amplifier and the minimum squeezing it can generate.

A.2 Squeezed states

The transformation of a single mode degenerate parametric amplifier, Eq. (2.83), to create squeezed states can be generalized to the broadband case. Consider the vacuum state for the operator $b(\omega)$

$$b(\omega)|0\rangle = 0.$$

Squeezed states can be generated from this vacuum state via a mode transformation similar to the single-mode case

$$b'(\omega) = \mathcal{G}(\omega)b(\omega) + \mathcal{M}(\omega)b^{\dagger}(-\omega) \tag{A.12}$$

Under this transformation, $|0\rangle$, which is a vacuum state for the $b(\omega)$ operator, becomes a squeezed state for the $b'(\omega)$ operator. Since both operators $b(\omega)$ and $b'(\omega)$ must satisfy commutation relations of the form (2.61), the quantities $\mathcal{G}(\omega)$ and $\mathcal{M}(\omega)$ need to fulfill the following relations

$$|\mathcal{G}(\omega)|^2 - |\mathcal{M}(\omega)|^2 = 1$$

and

$$\mathcal{G}(\omega)\mathcal{M}(-\omega) = \mathcal{G}(-\omega)\mathcal{M}(\omega).$$

Substituting Eq. (A.12) into Eq. (A.9), the transformed quadrature operator is given by

$$\begin{aligned} X_\theta(\omega) = &\frac{1}{2}\left(\sqrt{\frac{\omega_0+\omega}{\omega_0}}\mathcal{G}(\omega)e^{i\theta} + \sqrt{\frac{\omega_0-\omega}{\omega_0}}\mathcal{M}^*(-\omega)e^{-i\theta}\right)b(\omega) \\ &\frac{1}{2}\left(\sqrt{\frac{\omega_0+\omega}{\omega_0}}\mathcal{M}(\omega)e^{i\theta} + \sqrt{\frac{\omega_0-\omega}{\omega_0}}\mathcal{G}^*(-\omega)e^{-i\theta}\right)b^{\dagger}(-\omega) \end{aligned} \tag{A.13}$$

Hence, from Eq. (A.13), we obtain that

$$S_{X,X}(\omega,\theta) = \frac{1}{2}\left[|\mathcal{G}(\omega)|^2 + |\mathcal{M}(\omega)|^2 + 2\sqrt{1-\left(\frac{\omega}{\omega_0}\right)^2}\,\mathrm{Re}(\mathcal{G}(\omega)\mathcal{M}(-\omega)e^{2i\theta})\right] \tag{A.14}$$

The term $\sqrt{1-(\omega/\omega_0^2)^2}$ consist of the correction due to the multimode analysis, and it sets a fundamental upper bound on how small $S_{X,X}(\omega,\theta)$ can be made [2, 84]. It is possible to show that

$$S_{X,X}(\omega,\theta) \geq \frac{1}{2}\frac{\omega}{\omega_0}.$$

as it was mentioned above, Eq. (A.11).

A.3 Quantum limits for multimode linear amplifiers

The correction from the multimode analysis in the case of amplifiers is very different whether is phase-sensitive or phase-insensitive. In the case of phase-insensitive amplifiers, the only real change is that rather than specifying an added number of quanta, what it's specified is an added number of quanta per unit bandwidth. The fundamental theorem for phase-insensitive linear amplifiers is then given by [2]

$$S_A(\omega) \geq \left|1 \mp \frac{1}{G(\omega)}\right| \tag{A.15}$$

where the upper (lower) sign holds for phase-preserving (phase-conjugating) amplifiers. $S_A(\omega)$ is the added noise single-sided spectral density (in units of number-quanta per unit-bandwidth). If the input signal has phase-independent noise, then the output spectral density is given by

$$S_O(\omega) = G(\omega)[S_I(\omega) + S_A(\omega)]$$

where the superscripts I and O are used to designate the spectral densities of the input and output signals.

In the case of a phase-sensitive amplifier such as a degenerate parametric amplifiers, the situation is different. In this case, it can be shown that the multimode-correction to the single mode result is

$$S_{X_i,A} = \frac{1}{2}\frac{\omega}{\omega_0}\left|1 - \frac{1}{G_i(\omega)}\right|$$

where the subscript i is used to designate the quadrature, and G_i is the gain for the quadrature X_i. Note that unlike the single-mode case, there is a fundamental limit on amount of noise for modulation-frequencies $\omega > 0$. The purpose of this limit is to ensure that the output mode still follows Eq. (A.11) [2].

Some literature uses a different convention for the spectrum of an operator $\hat{Y}$, where the symmetrized noise $S_{Y,Y}$ is actually defined as

$$\frac{1}{2}\langle\{Y(\omega), Y^\dagger(\omega')\}\rangle = 2\pi S_{Y,Y}(\omega)\delta(\omega - \omega').$$

With this definition, the limit for phase insensitive amplifiers S_A becomes 1/2 quanta per unit bandwidth (just like the single mode case). Also the numerical factor in Eq. (A.11) becomes 1/4 as opposed to 1/2. We do not use this convention, except for in Eqs. (3.80-3.82) where the extra factor of 1/2 was added to compare the added noise of the JPA with and ideal single-mode phase-insensitive amplifier. However, for the rest of the thesis I have used the convention of Eq. (A.10). In this convention, then the added noise per unit bandwidth in each quadrature of a quantum-limited phase-insensitive amplifier is 1/2 quantum, which is the value we compare the added noise of our JPA.

A.4 Approximation

Although this fundamental limit is important from a theoretical point of view, from an experimental point of view $\omega \ll \omega_0$. In the rotating frame, using $a(\omega_0 \pm \omega) = b(\pm\omega)$, the frequency resolved quadrature amplitudes may be written in a form more reminiscent of the discrete quadratures:

$$X_1(\omega) \simeq \frac{1}{2}(b(\omega) + b^\dagger(-\omega)) \tag{A.16}$$

$$X_2(\omega) \simeq \frac{1}{2i}(b(\omega) - b^\dagger(-\omega)) \tag{A.17}$$

These are the definitions I used for the quadrature operators in the frequency domain in this thesis. They are also the definitions usually used to analyze the experimentally

measured quadrature noise [8, 38]. In our case, for all the noise spectral densities that were measured $\omega/\omega_0 < 1/1000$, and it is justified to use the approximated quadrature operators. Within this approximation, the term $\sqrt{1-(\omega/\omega_0^2)^2}$ from Eq. (A.14) disappears and we obtain Eqs. (3.74) and (3.75).

Appendix B

Thermal sweep and loss calibration

As described in section 6.3.3, we use a cryogenic switch to toggle between two terminations held at two different temperatures to estimate the added noise of the HEMT and the JPA. However, in order to accurately refer this noise to the input of the different amplifiers, one must also measure the microwave loss of the components between the calibrated noise sources and the input of the amplifiers. Knowing the amount of loss between the different sections of the experiment is also very important in order to accurately predict the amount of squeezing observed. The determination of the amount of loss is accomplished by measuring the change in the measured noise at the output of the amplifier chain as a function of the cryostat temperature T_c when the switch is connected to the hot load at $T_h = 4.1$ K. In the presence of loss the noise from the hot termination at T_h will be partially absorbed. In addition, this loss will emit noise with a spectrum given by the temperature of the loss (T_c). In this appendix, I will describe a set of thermal-sweep measurements that help us estimate the loss between the switch and the amplifiers. From the thermal sweeps, we can also estimate the added noise of amplifiers and compare it with what we measure using the Y-factor measurement described in section 6.3.3 to make sure both methods give similar answers.

In the following calculations, I will assume that the HEMT sets the noise floor of the measurement. For this reason and for simplicity I label with a subindex H the gain and added noise of the commercial amplifier chain, starting with the HEMT and

ending at the digitalization card used to measure the output of the mixer.

B.1 HEMT

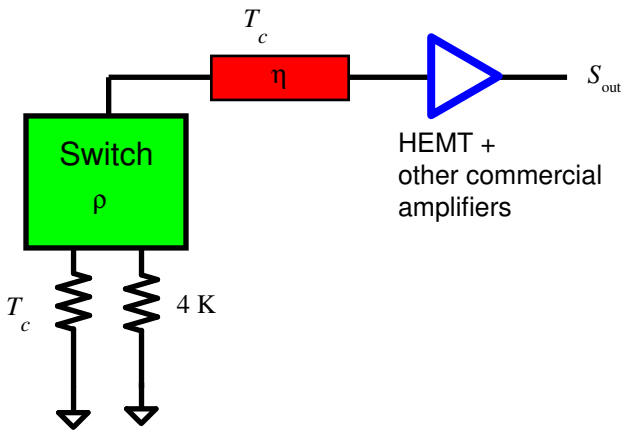

Figure B.1: Simplified diagram of the measurement when only the HEMT is used. By measuring the noise at the output of the amplifier chain for both loads, as we change the temperature of the fridge T_c, we can estimate the loss η.

During the thermal sweeps we do a Y-factor measurement on the amplifiers, in this case the HEMT. This means that we have access to two possibilities for S_{out} (Fig. B.1). One is when we are observing at the "cold load" which sits at a temperature of T_c and the second when we are observing at the hot load with a temperature of $T_h = 4.1$ K. When we measure the cold load at a temperature T_c, we can estimate the HEMT's noise (assuming a few approximations I will describe below). Then, when we measure the hot load. If there was no loss between the switch and the HEMT, ideally we would not see any change of S_{out} when we change the temperature of the fridge. Thus, when measuring the the hot load, it is the change we measure in S_{out} that allows us to estimate the loss η. The ouput of the HEMT is given by S_{out},

$$S_{\text{out}} = G_H \left[A_H + (\rho S_{\text{load}} + (1-\rho)S_\rho)\eta + (1-\eta)S_\eta\right] \tag{B.1}$$

where A_H is the added noise of the HEMT in noise quanta, G_H is the gain of the HEMT (more accurately is the gain of all the amplifier chain, but for simplicity let's

call it the HEMT gain), S_{load} is the noise coming from the load (it can be at the fridge temperature or at 4.1 K), ρ is the loss in the switch, η is the loss from the switch to the HEMT. S_ρ is the noise attributed to the switch loss, and S_η is the noise attributed to the loss between the switch and the HEMT. S_{load}, S_η and S_ρ are in units of noise quanta and are given by:

$$S_i = \frac{1}{2}\coth(\frac{hf}{2k_B T_i}) \tag{B.2}$$

Unfortunately, with the following analysis, we will not be able to estimate the loss of the microwave components that sit at 4.1 K. This consists of the loss of the switch as well as the loss from a bias-tee used to heat sink the center-conductor of the superconducting cables and the switch. Thus, I will do fits assuming worst and best case scenario based on the factory specifications of the microwave components: a total insertion loss of -0.8 dB for the worst case, or $\rho \simeq 0.83$, and for the ideal case $\rho = 1$.

B.1.1 Hot load

In this case when we are measuring the hot load, then $S_{\text{load}} = S_\rho$, and Eq B.1 yields

$$S_{\text{out}} = G_H[A_H + S_\rho\eta + (1-\eta)S_\eta] \tag{B.3}$$

where $S_\eta = \frac{1}{2}\coth(\frac{hf}{2k_B T_c})$ is the term that will change with the fridge temperature. Now, this expression could be used to do a fits to obtain the HEMT's added noise and the loss. However, since we do not know exactly the gain of the amplifier chain, the variable G_H in the fitting expression is also a fitting parameter. This means that there is one too many fitting parameters which give us too much freedom in the fits. So, I do first a fitting to the cold load measurement, which sets (approximately) G_H and A_H.

B.1.2 Cold load

In this case, $S_{\rm load} = S_\eta$, and then Eq B.1 reduces to

$$S_{\rm out} = G_H[A_H + (1-\eta+\eta\rho)S_\eta + (1-\rho)\eta S_\rho] \tag{B.4}$$

If the switch and bias-tee at 4.1 K did not have any loss ($\rho = 1$), then this expression would be much simpler $S_{\rm out} = G_H\{A_H + S_\eta\}$ and the fitting to a simple expression with only 2 fitting parameters (G_H and A_H) would work fine. However, since I cannot assume that there is no loss at 4.1 K, things are slightly more complicated. In order to simplify the expression I will regroup some of the terms in Eq. (B.4):

$$\begin{aligned} S_{\rm out} &= G_H[A_H + (1-\eta+\eta\rho)S_\eta + (1-\rho)\eta S_\rho] && \text{(B.5)} \\ &= G_H(1-\eta+\eta\rho)\left[\frac{A_H + (1-\rho)\eta S_\rho}{(1-\eta+\eta\rho)} + S_\eta\right] && \text{(B.6)} \\ &= G_{\rm fit}\{A_{\rm fit} + S_\eta\} && \text{(B.7)} \end{aligned}$$

with

$$G_{\rm fit} = G_H(1-\eta+\eta\rho) \tag{B.8}$$

$$A_{\rm fit} = \frac{A_H + (1-\rho)\eta S_\rho}{(1-\eta+\eta\rho)} \tag{B.9}$$

Now I have a simple expression with only 2 fitting parameters. The procedure to estimate the loss is the follwing:

(1) I do a fit to the cold load, from which I get $G_{\rm fit}$ and $A_{\rm fit}$;

(2) Using $G_{\rm fit}$ and $A_{\rm fit}$, I do a fit to the hot load, where I replace G_H and A_H using Eqs. (B.8) and (B.9) assuming $\rho = 1$ from which I get a value of the attenuation η;

(3) Then I do a fit to the hot load assuming $\rho = 0.83$ from which I get another value of the attenuation η.

Since ρ is close to one and $\eta < 0.1$, $(1-\eta+\eta\rho) \simeq 1$ this will make $G_{\rm fit} \simeq G_H$ and $A_{\rm fit} \simeq A_H$.

B.2 JPA

We can try to do a similar analysis when we operate the JPA to estimate the added noise of the JPA and the attenuation between the different locations of the circuit shown in figure B.1. The output of the amplifier chain (again labeled by the subindex H) and including the JPA is given by the following expression:

$$S_{\text{out}} = G_H \left[A_H + (1-\eta_2)S_c + \eta_2 G_J \left(A_J + (1-\eta_1)S_c + \eta_1\{(1-\rho)S_\rho + \rho S_{\text{load}}\}\right)\right] \tag{B.10}$$

where η_1 is the attenuation between the switch and the JPA, η_2 is the attenuation between the JPA and the HEMT, and $S_i = \frac{1}{2}\coth(\frac{hf}{2k_B T_i})$. For simplicity, since the noise from both losses η_1 and η_2 are the same and are function of the fridge temperature, I have used S_c to label their noise. S_{load} is the load thermal noise, which can be at the fridge temperature T_c or at 4.1 K, and S_ρ is the thermal noise (with T=4.1 K) from the loss at 4.1 K (switch and bias-tee).

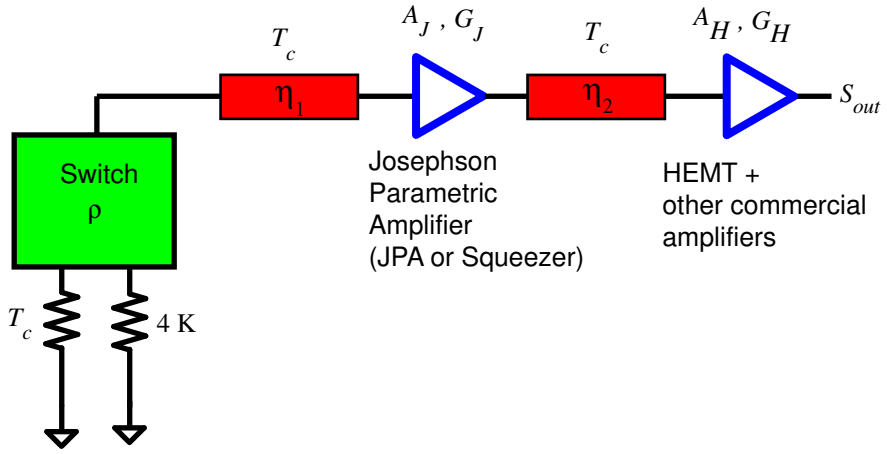

Figure B.2: Simplified diagram of the measurement when both the HEMT and a Josephson parametric amplifier (either the one labeled the squeezer or the JPA) are used. By measuring the noise at the output of the amplifier chain for both loads, as we change the temperature of the fridge T_c, we can estimate the loss η_1. From the measurement done only with the HEMT where we estimate $\eta = \eta_1 + \eta_2$ we can then know η_2.

B.2.1 Cold load

In this case $S_{\rm load} = S_c$ and equation B.10 reduces to:

$$\begin{aligned} S_{\rm out} &= G_H\{A_H + (1-\eta_2)S_c + \eta_2 G_J(A_J + (1-\eta_1)S_c + \eta_1[(1-\rho)S_S + \rho S_c])\} \\ &= G_H[g(1-\eta_1(1-\rho)) + (1-\eta_2)]\{\frac{A_H + gA_J + g\eta_1(1-\rho)S_\rho}{g(1-\eta_1(1-\rho)) + (1-\eta_2)} + S_c\} \\ &= G'(A' + S_c) \end{aligned}$$

where $g = G_J\eta_2$. Now, for reasonable values for η_1, ρ and η_2, then A' can be simplified:

$$A' = \frac{A_H + gA_J + g\eta_1(1-\rho)S_\rho}{g(1-\eta_1(1-\rho)) + (1-\eta_2)} \tag{B.11}$$

$$\simeq \frac{A_H}{g} + (1-\rho)\eta_1 S_\rho + A_J \tag{B.12}$$

Finally, when taking the data, we are modifying not only the temperature of the fridge and the cold-resistor but also the temperature of the JPA. We do not know the temperature dependance of the added noise of the JPA. Although our model includes some temperature dependance of the added noise, Eq. (5.56), the measured added noise is larger than what theory predicts. I know that the added noise of the amplifier is (ideally) of the order of $A_J = \frac{\gamma_{loss}}{\gamma_{coupling}}\frac{1}{2}\coth(\frac{hf}{2k_BT_c})$. So, for these fits, I will assume that at least this much of the added noise of the JPA must depend with temperature. Then I can use the following expression to fit the data:

$$A_J = A_J^0 + \kappa\left[\frac{1}{2}\coth(\frac{hf}{2k_BT_{cryo}})\right] \tag{B.13}$$

where $\kappa = \frac{\gamma_{loss}}{\gamma_{coupling}}$ is calculated from fits to the reflection coefficient and A_J^0 is assumed temperature independent. Hence, my fitting function for the cold-load noise measurement is:

$$S_{\rm out}^{\rm cold} = G^{\rm fit}\left[A_{\rm fit} + (\kappa+1)S_c\right] \tag{B.14}$$

where $A_{\rm fit} = \frac{A_H}{g} + (1-\rho)\eta_1 S_\rho + A_J^0$.

B.2.2 Hot load

In this case $S_{\rm load} = S_\rho$, so equation B.10 reduces to

$$\begin{aligned} S_{\rm out} &= G_H\{A_H + (1-\eta_2)S_c + \eta_2 G_J(A_J + (1-\eta_1)S_c + \eta_1[(1-\rho)S_\rho + \rho S_\rho])\} \\ &= G_H[g + (1-\eta_2)]\{\frac{A_H + gA_J}{g + (1-\eta_2)} + \frac{g\eta_1}{g + (1-\eta_2)}S_\rho + (1 - \frac{g\eta_1}{g + (1-\eta_2)})S_c\} \\ &= G''(A'' + \eta_1' S_{\rm load} + (1-\eta_1')S_c) \end{aligned}$$

With some approximations that are valid for high gain g and reasonable values of η_1, ρ and η_2, this expression can be written as follows:

$$S_{\rm out}^{\rm hot} = \frac{G_{\rm fit}}{1-\eta_1(1-\rho)}\{A_{\rm fit}(1-\eta_1(1-\rho)) - \eta_1(1-\rho)S_\rho + \eta_1' S_\rho + (1-\eta_1')S_c\} \quad \text{(B.15)}$$

where $G_{\rm fit}$ and $A_{\rm fit}$ will not be fitting parameters in this case but are obtained from the fit to the cold-load data. Finally, the last thing to do is to notice that η_1' can be approximated by:

$$\begin{aligned} \eta_1' &= \frac{g\eta_1}{g + (1-\eta_2)} \\ &\simeq \eta_1 \end{aligned}$$

Therefore, expression B.15 reduces to

$$S_{\rm out}^{\rm hot} = \frac{G_{\rm fit}}{1-\eta_1(1-\rho)}\{A_{\rm fit}(1-\eta_1(1-\rho)) + \eta_1\rho S_\rho + (1-\eta_1+\rho(1-\eta_1(1-\rho)))S_c\} \quad \text{(B.16)}$$

which is the expression I use to fit to the hot load with one single fitting parameter, η_1.[1]

The procedure for the fits of the data in the case of the JPA is similar to the HEMT amplifier case.

(1) I do a fit to the cold load, from which I get $G_{\rm fit}$ and $A_{\rm fit}$;

(2) Using $G_{\rm fit}$ and $A_{\rm fit}$, I do a fit to the hot load assuming $\rho = 1$ from which I get a value of the attenuation η_1;

[1] The term $(1-\eta_1(1-\rho)))$ is a number very close to one, so this extra terms does not affect the results of the fits.

(3) Then I do a fit to the hot load assuming $\rho = 0.83$ from which I get another value of the attenuation η_1;

(4) η_2 can be obtained from the value of $\eta = \eta_1 + \eta_2$ given by the fits to the HEMT amplifier thermal sweep data.

B.2.3 Low-frequency noise

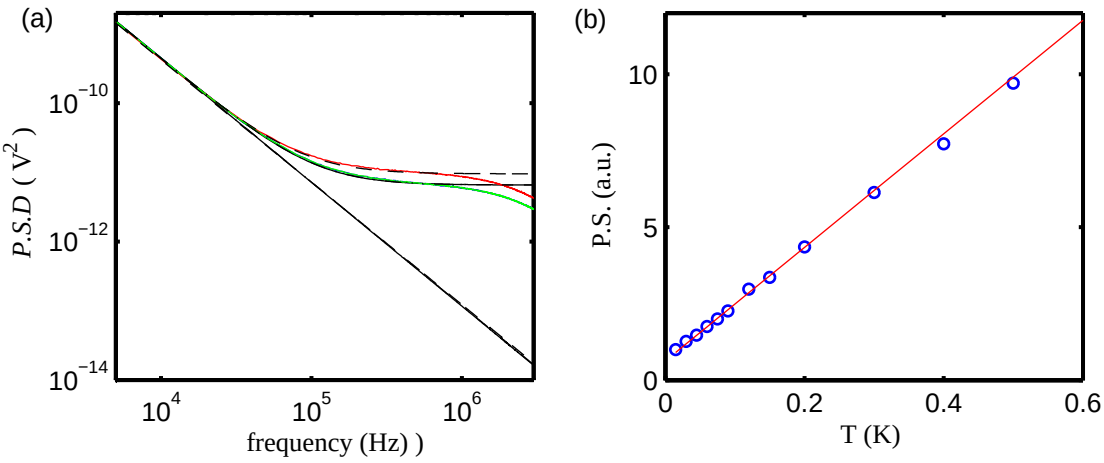

Figure B.3: (a)Spectral density of the output of the mixer when the JPA is used. Below 100 kHz there is an extra contribution from an unknown source. (b) This extra noise has a linear dependance with temperature which, unless avoided, would interfere with our fits to Eqs. (B.14) and (B.16).

Before we move into fitting the data to Eqs. (B.14) and (B.16), there is something I need to discuss which is the low frequency noise we observe in the spectral density at the output of our amplifier chain (fig. B.3). If we integrate over only the low frequency part (below 100 kHz), then we obtain a linear T-dependance as shown in figure B.3b. Thus, if I want to fit to the expressions (B.14) and (B.16) then I can not integrate over the whole band measured but at least above 200 kHz. What I actually do is I fit to the low frequency part which gives a dependance of $\sim 1/f^{1.8}$. Then I compare how much of the total noise at, for example, 500 kHz comes from the $1/f^{1.8}$ part. For this case, it

is less that 5%, and since I integrate over a band bigger than 1 MHz, at the end, after integrating above 500 kHz, the part of the noise that comes from the $\sim 1/f^{1.8}$ part is negligible.

B.3 Chapter 7 calibration

In all the data that I will show, we used a calibration tone that allowed us to remove drifting in the gain of the whole amplifier chain (as the measurements took several hours).

B.3.1 HEMT

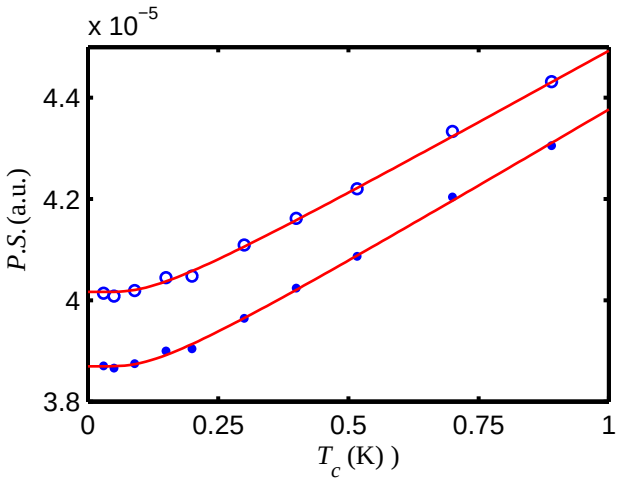

Figure B.4: Thermal sweep using only the HEMT amplifier. The JPA and the squeezer resonances have been tuned far from the frequency of interest by applying a current to the coil. Thus, the resonators behave as mirrors reflecting all the incident power. The data shown consist of the power spectrum over a 5 MHz bandwidth when the switch is connected to the cold load (dots) and the hot load (circles) as well as their fits to Eqs. (B.16) and (B.14) (red lines). The error bars are smaller than the data points.

The fits to the data taken with the HEMT are shown in figure B.4. In order to avoid the losses of the resonators, we applied a current to the coil that move the resonance frequency of both the JPA and squeezer far from the frequency at which we were measuring ($f = 7.44$ GHz). Thus, both resonators behaved as mirrors, reflecting all the noise incident on them. By doing a fit to Eqs. (B.3) and (B.4), we estimate that the added noise of the HEMT is $A_H = 17.3 \pm 0.2$, where the uncertainty is predominantly from the unknown loss of the microwave components at 4.1 K. Regarding the loss η from figure B.1, our estimate is $\eta = -11.7 \pm 0.3$ dB.

B.3.2 JPA

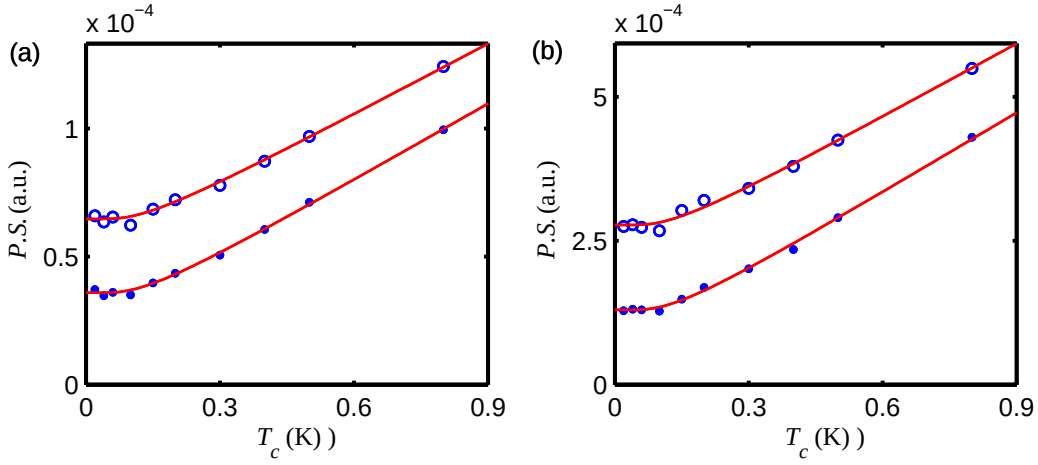

Figure B.5: Thermal sweep with a JPA gain of (a) $G_J = 60$ and (b) $G_J = 250$. These values of the JPA gain consist of the average gain over the integrated band. The data shown consist of the power spectrum over over a 2.5 MHz bandwidth (from 500 kHz to 3 MHz), when the switch is connected to the cold load (dots) and the hot load (circles) as well as their fits to Eqs. (B.16) and (B.14) (red lines).

In this experiment we have two different parametric amplifiers one as a squeezer (and hence will be only referred as the squeezer) and one as an amplifier (JPA). We

first analyze the one that is used as an amplifier. When we took this data we took thermal sweeps with 2 different gains. All through the thermal sweep we kept the gains the same. From the fits to the data (Fig. B.5) we estimate the following parameters: $A_J = 0.24 \pm 0.03$, where again the largest contribution to the uncertainty comes from the unknown losses at 4.1 K. Regarding the losses, we obtain, $\eta_1 = 10.4 \pm 0.2$ dB and $\eta_2 = 1.3 \pm 0.3$ dB. In order to obtain A_J, η_1, η_2, we used the results obtained from the HEMT-thermal-sweep analysis.

One important point that is still under discussion is that I have assumed that the noise of the JPA is formed by one part that is constant with temperature and one part that depends in temperature as shown in Eq. (B.13). This is a somewhat arbitrary model. The second part $\kappa(\frac{1}{2}\coth(\frac{hf}{2k_BT_c}))$ is what I expect from theory, and since we see extra noise I have added a constant, but this "constant" A_J^0 could very well be a function of temperature, which would then change the results previously shown. However, the obtained attenuation is compatible with measurements of the attenuation of the microwave components when measured at 77 K. Also, assuming the estimated attenuation from the fits, we can do Y-factor measurements on the JPA and the obtained added noise of $A_J \simeq 0.25 \pm 0.05$ is compatible with the estimated from the fits. So I will use these values to analyze the data in chapter 7.

B.3.3 Squeezer

In the case of the squeezer, the analysis from the fits shown in figure B.6 yields $A_J = 0.26 \pm 0.03$, $\eta_1 = -8.7 \pm 0.3$, and $\eta_2 = 3.0 \pm 0.2$ dB (note that η_1 and η_2 in this case will be different from the ones obtained for the JPA). Just as in the previous case, by performing a Y-factor measurement, we have observed consistency between the measured loss and the measured added noise from the thermal sweeps, and the measured added noise from the Y-factor measurement.

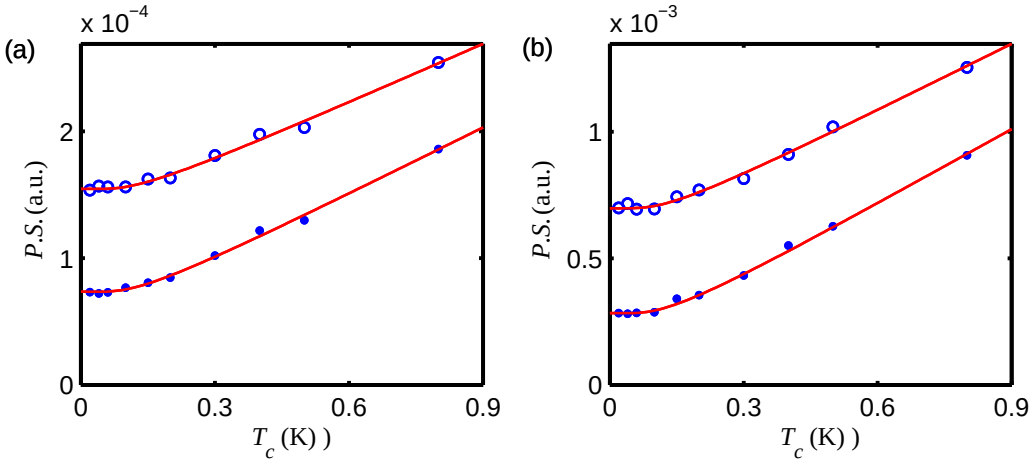

Figure B.6: Thermal sweep with a squeezer gain of (a) $G_J = 70$ and (b) $G_J = 350$. These values of the JPA gain consist of the average gain over the integrated band. The data shown consist of the power spectrum over over a 2.5 MHz bandwidth (from 500 kHz to 3 MHz), when the switch is connected to the cold load (dots) and the hot load (circles) as well as their fits to Eqs. (B.16) and (B.14) (red lines).

The estimated values of η for the HEMT, and η_1 and η_2 for both the JPA and the squeezer can be used to estimate the losses between all the three amplifiers, as shown in figure B.7. For the analysis done in chapter 7, we assumed $\alpha = 1.7 \pm 0.1$, $\beta = \eta_2^{\text{JPA}} = 1.3 \pm 0.3$ and $S_{\text{in}} = 0.65 \pm 0.15$.

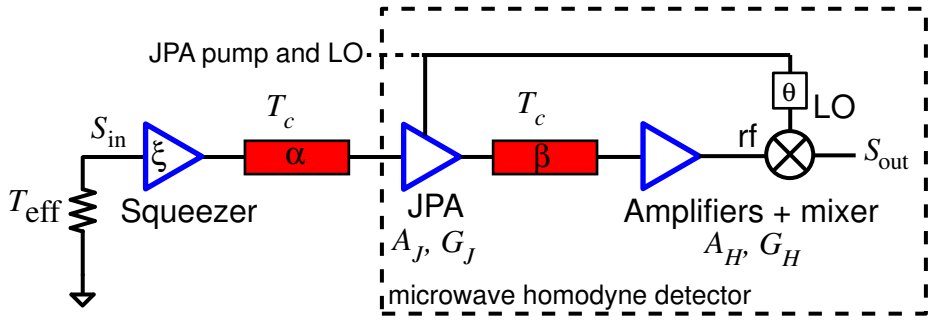

Figure B.7: From the thermal sweeps then we can estimate the loss between the squeezer and the JPA (α), and the loss between the JPA and the HEMT (β).

Squeezing

We also measured the squeezing just using the HEMT to observe whether the squeezer behave as in the previous experiments. The observed squeezing as a function of gain is shown in figure B.8 and compared with theory. We observe a similar behavior as in figure 6.34b. The squeezing increases as a function of gain up to gains of $G_J \simeq 10$ dB, and the it decreases for higher gains. The maximum estimated observed squeezing is 80%.

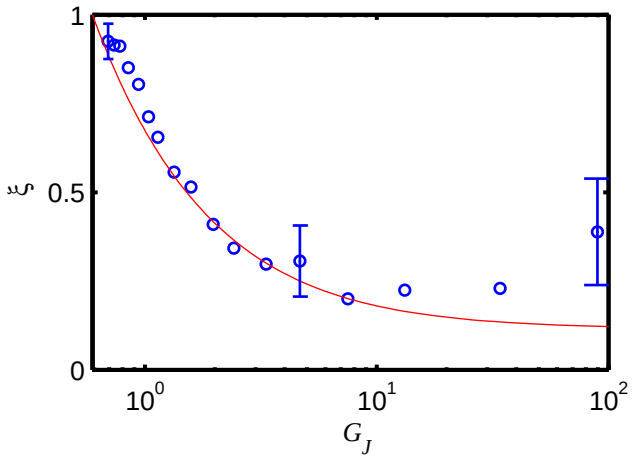

Figure B.8: Squeezing as a function of the squeezer gain. The maximum squeezing observed is 80%.

B.4 Chapter 8 calibration

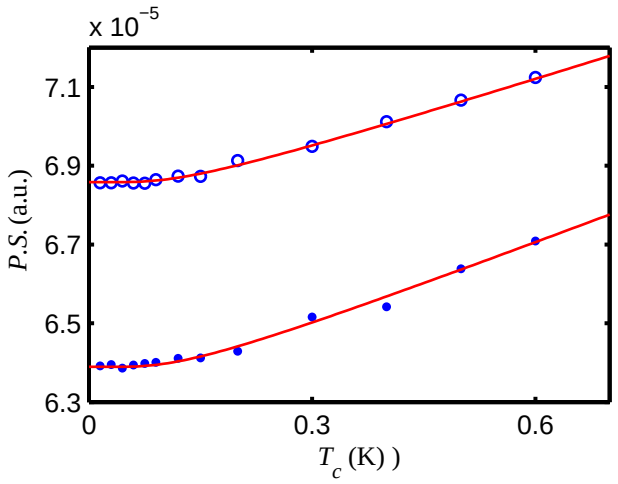

Figure B.9: Thermal sweep using only the HEMT amplifier. Only one JPA is used in this experiment and its resonance has been tuned far from the frequency of interest by applying a current to the coil. The data shown consist of the power spectrum over a 5 MHz bandwidth when the switch is connected to the cold load (dots) and the hot load (circles) as well as their fits to Eqs. (B.16) and (B.14) (red lines).

We also performed a thermal sweep for the experiment described in chapter 8. Following are the plots with the results from the fits using the procedure previously described. Based on the thermal-sweep data for the HEMT and other commercial amplifiers (Fig. B.9), we get the following results for the effective added noise of the commercial amplifier chain and attenuation η between the switch and the HEMT amplifier. $A_H = 24.5 \pm 0.5$, and $\eta = 7.6 \pm 0.2$.

In the case of the JPA, we took the thermal-sweep data for two different gains. From the fits shown in figure B.10, we estimate the following values: $A_J = 0.33 \pm 0.04$ and $\eta_1 = 6 \pm 0.3$ dB. The values of the estimated added noise of both the JPA and the HEMT are consistent with the values from Y-factor measurements assuming the

given values of attenuation of $\eta_1 \simeq -6$ dB and $\eta = \eta_1 + \eta_2 = -7.6$ dB. These are the values assumed for the estimate of the effective added noise A_N in the microwave interferometer for figure 8.9.

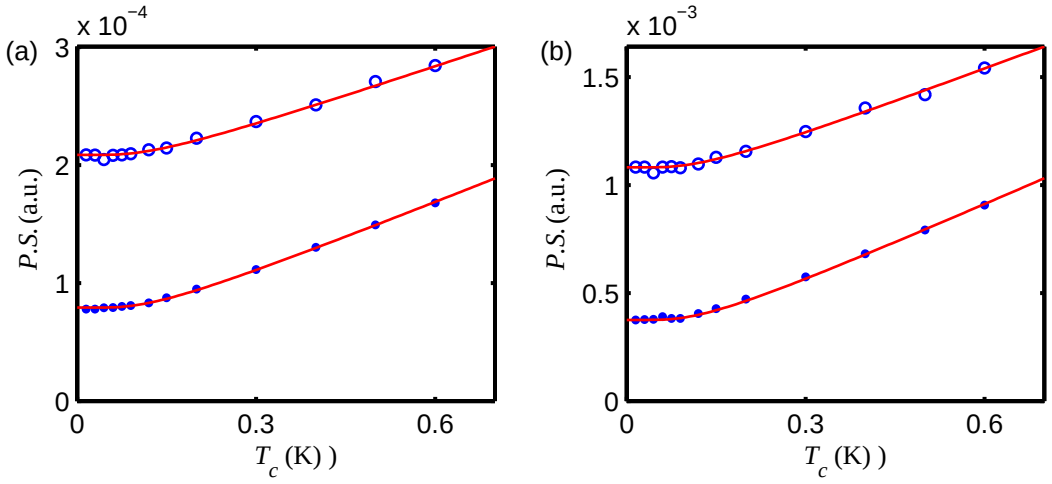

Figure B.10: Thermal sweep with a JPA gain of (a) $G_J \approx 115$ and (b) $G_J \approx 400$.

Appendix C

Sample Fabrication

In this appendix I discuss some details regarding the fabrication of the samples. First I will describe in some detail the fabrication of the aluminum samples which I did in the JILA cleanroom. Then I will only briefly describe the process involved in the fabrication of the niobium samples done by our collaborators at NIST.

C.1 Aluminum resonators

This sample was fabricated with electron beam (e-beam) lithography. The first step is choosing a substrate. We used a 300 μm thick silicon substrate with a thermally grown oxide. The thickness of the oxide was 150 nm. On the wafer, we deposit a protecting layer resist. At this point, the wafer was diced into individual 1/4 in^2 chips. Then individual chips are prepared for the fabrication of the devices. Each chip is thoroughly cleaned with acetone and isopropanol before depositing the layers of photoresist. First, a thick ($\sim$ 5000 Å) layer of polymethylglutarimide (PMGI) SF-9 from Micro-Chem is spun at 3000 rpm for 40 seconds and baked for 10 minutes on the substrate using a hot plate at 190°C; then a second thinner ($\sim$ 3000 Å) layer of polymethyl methacrylate (PMMA-A5.5) is spun at 4000 rpm and baked at 180°C for 30 minutes. These two layers form a resist bilayer necessary to create suspended structures (Fig. C.1). Then the chip is exposed to an e-beam using a scanning electron microscope (SEM) as shown in figure C.2a. The PMMA is then developed for 1:20 minutes using PMMA-developer

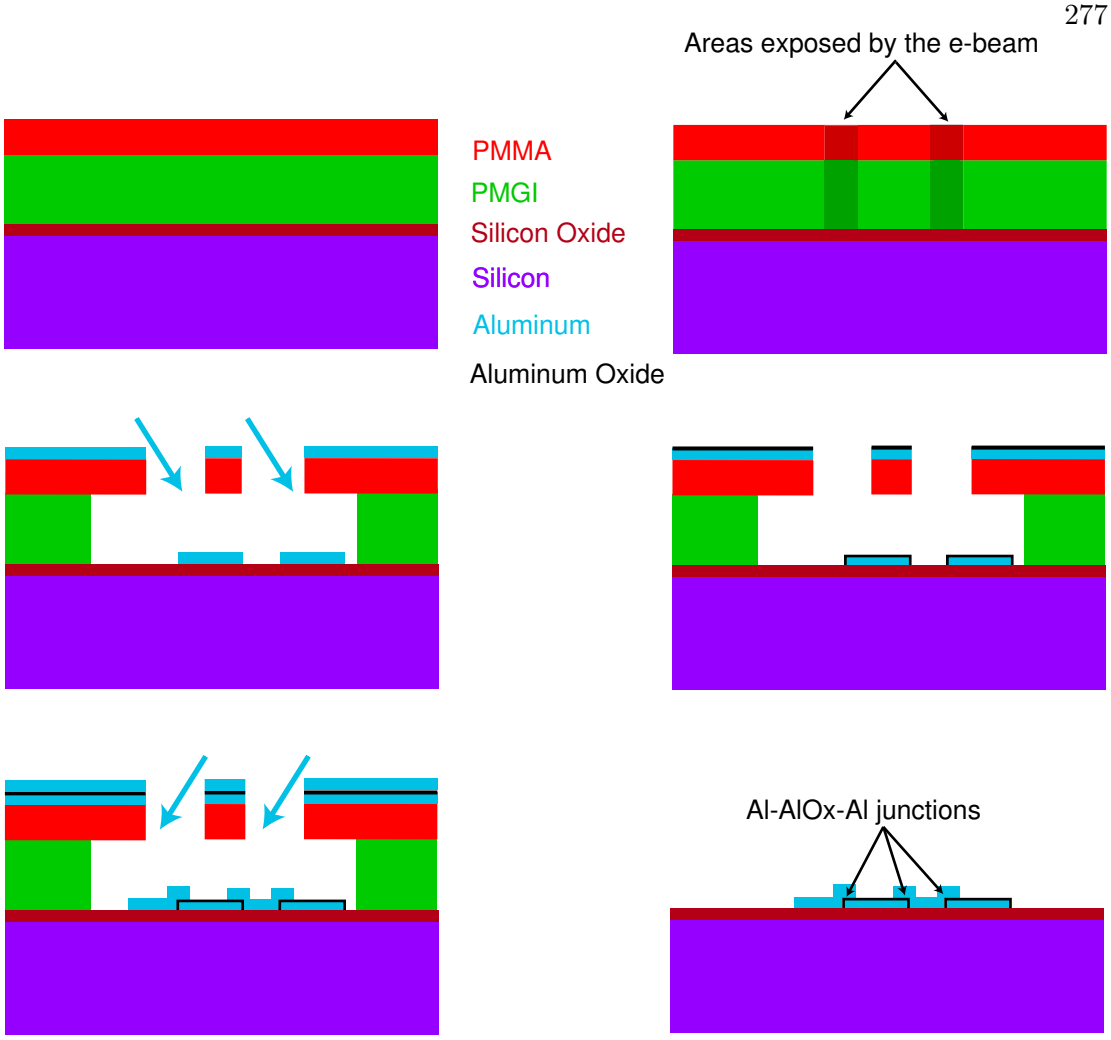

Figure C.1: Dolan bridge technique. A bilayer of PMGI/PMMA resist is spun and baked on a silicon chip with a thermally grown oxide. The pattern is written with a scanning electron microscope, exposed and developed to create the suspended pattern shown in cross section. Then a layer of aluminum is evaporated at an angle to create the bottom electrode of the tunnel junction. The next step is to create an oxide layer by introducing oxygen into the evaporation chamber. Next, a second layer of aluminum is evaporated to form the counter electrode. Finally, the resist pattern is lifted to leaving the finished tunnel junction and other structures of the device.

(MIBK). The areas of PMMA exposed are then removed and the PMGI is developed for 3:00 minutes using PMGI developer. This creates a the suspended pattern as shown in cross section in figure C.1. After that the sample is placed in an evaporator (Fig. C.2b). I evaporate aluminum at two different angles and allow an oxide to form in between.

This oxidation is accomplished by letting oxygen into the evaporating chamber causing the aluminum to oxidize. The thickness of each of the layers of evaporated aluminum was 100 nm. The region of overlap results in a tunnel junction. This technique is called Dolan-bridge technique [87]. Finally, the resist pattern is lifted using acetone and PMGI-remover leaving the tunnel junctions and the resonator structure.

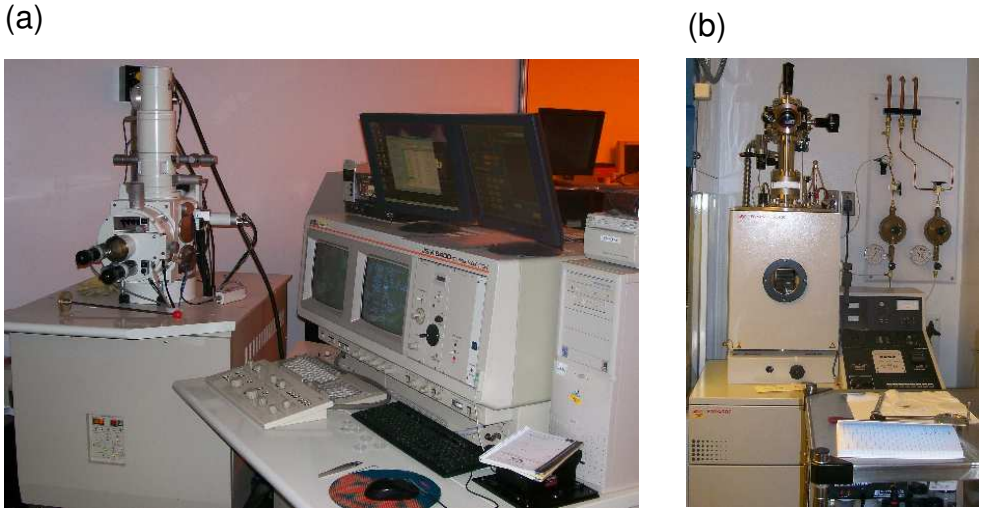

Figure C.2: (a) Scanning electron microscope, JEOL JSM-6400, used in the fabrication of the aluminum devices. (b) Oxford evaporator. It is set up to do both thermal and e-beam evaporation. The device described in chapter 6 was thermally evaporated.

C.2 Niobium resonators

Niobium devices were fabricated at NIST Boulder using optical-lithography with a standard NbAlOxNb trilayer process [88], modified by eliminating the shunt resistor layer and minimizing deposited oxides [89]. Trilayers are deposited in a dedicated load-locked vacuum system. The first base-electrode layer consist of a 200 nm thick Nb film; then a 6-10 nm thick Al film is deposited and oxidized. Finally a 50-100 nm thick Nb counter-electrode deposition completes the trilayer process. The pattern of the resonator is done by performing an etch process in a load-locked reactive-ion-etch system (Fig. C.3).

Our role in the fabrication of the Niobium resonator consist of designing the structures. For that, we used commercial software named Xic Graphical Input Editor, from Whiteley Research Inc. In there we plot all the structure including the layers used in the fabrication. Beside the trilayer described in the previous paragraph, which only creates the junctions, we also used two extra layers, a dialectric insulating layer (SiO_2) and a niobium wiring layer used to connect the multiple junctions. The dialectric SiO_2 layer is deposited using plasma-enhanced-chemical-vapor-deposition (PECVD) with an electron-cyclotron-resonance (ECR) reactor. Before depositing the wiring-layer, vias are etched in the SiO_2 layer. For more details in the fabrication process of these devices, contact Leila Vale at NIST.

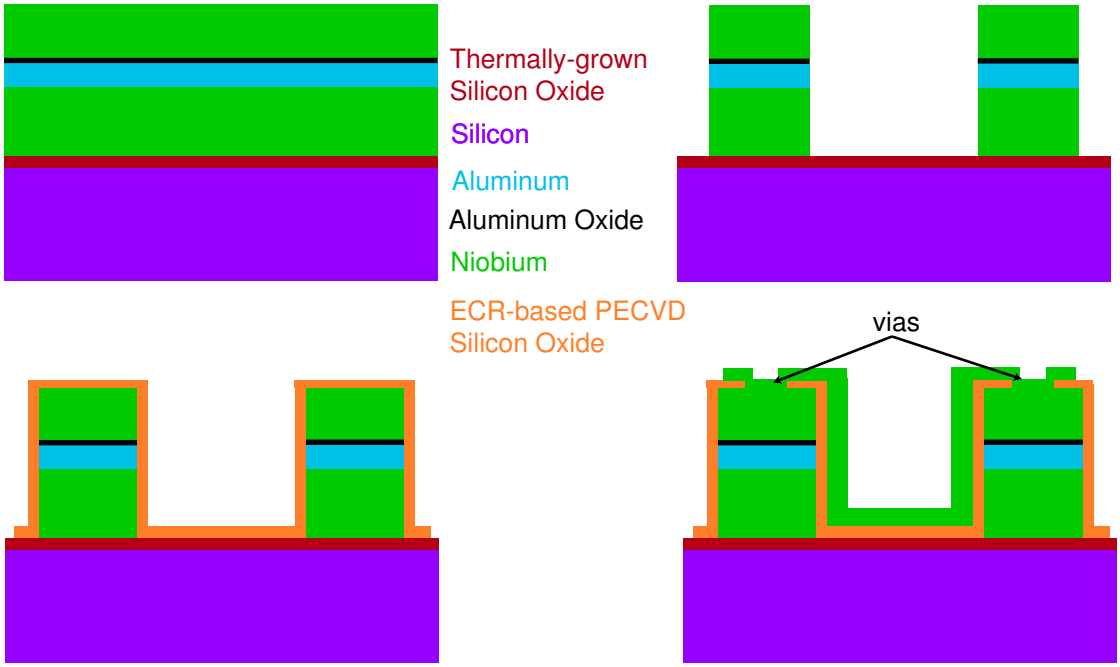

Figure C.3: Niobium trilayer process. First a layer of niobium is deposited followed by an aluminum layer which is oxidized and finally another niobium layer completing the trilayer process. However, this creates the junctions as well as the other resonator structures, but leaves the junctions disconnected from the rest of the device. Hence, a layer of SiO_2 is deposited followed by an etch to creates vias and the deposition of a niobium-wiring layer that connects the junctions to form the SQUIDs and to connect them to the rest of the resonator circuitry.

Appendix D

List of symbols and abbreviations

Δ	Superconducting gap
γ	linewidth defined as the amplitude decay rate, or half width at half maximum (HWHM). $\gamma = \omega_0/2Q$
ζ	Real squeezing observed at the output of the homodyne detector.
η	Transmission coefficient of a beam splitter.
η	Efficiency of the homodyne measurement modeled by a beam-splitter at the input of an ideal homodyne detector.
ξ	Squeezing at the output of the JPA
Φ	Flux
B_ω	Bandwidth
C	Capacitance
C_l	Capacitance per unit length
CPW	Coplanar waveguide
EOM	Equations of motion
DPA	Degenerate parametric amplifier
g_c	Coupling between the mechanical harmonic oscillator displacement and the cavity's resonance frequency, $g_c = \partial\omega_c/\partial x$.
G_1	Maximum quadrature power gain
G_2	Maximum de-amplification. In an ideal degenerate parametric amplifier $G_2 = 1/G_1$
G_θ	Phase-dependant quadrature power gain
G_i	Image power gain
G_J	JPA gain, defined as the maximum quadrature gain. $G_J = G_1$
G_s	Signal power gain
HEMT	High electron mobility transistor amplifier
I	Current
I_0	Critical current of a Josephson junction
I_0^S	Critical current of a SQUID
IOT	Input Output Theory
JPA	Josephson parametric amplifier
L	Inductance
L_l	Inductance per unit length

L_J	Nonlinear Josephson inductance
L_{J0}	Linear part of the Josephson inductance
Q	Charge
Q ,$\mathcal{Q}$	Quality factor
SHO	Simple Harmonic Oscillator
S/N	Signal-to-noise ratio
SQL	Standard Quantum Limit
$S_{y,y}$	Single-sided spectral density for an operator $\hat{y}$, $S_{\hat{y},\hat{y}} = \langle\{\hat{y},\hat{y}\}\rangle$
S_z	Quadrature single-sided spectral density, where z defines a location in the experiment setup. This variable-naming scheme is only used in chapter 6, 7 and appendix B.
T	Temperature
v_{ph}	Phase velocity of a transmission line
$W(x_1, x_2)$	Wigner function
X_i	Quadrature operator, $i = 1, 2$
x_i	Quadrature variable, $i = 1, 2$. The Wigner function is a function of x_i.
X_θ	Phase-dependant quadrature
Z_c	Characteristic impedance of a transmission line